Università degli Studi di Perugia

Dottorato in Fisica e Tecnologie fisiche - Ciclo XXVIII

Time dependence of electron and positron fluxes measured with the AMS-02 spectrometer

Relatore:
Bruna Bertucci

Autore:
Maura Graziani

Correlatore:
Matteo Duranti

Coordinatore del Corso di Dottorato: Maurizio Busso

Anno Accademico 2014 - 2015

Contents

Introduction

The Alpha Magnetic Spectrometer, AMS-02, is a general purpose high energy particle physics detector. It was launched into space with the Space Shuttle STS-134 mission and installed onboard the ISS in 2011, on May 19*th*, to conduct a unique long duration mission of fundamental physics research in space. The experimental challenge of this spectrometer is the accurate measurement of the Cosmic Rays (CR) composition and energy spectra, up to the TeV energy scale, that could reveal the presence of primordial anti-matter or give the signature of exotic sources, as for example secondaries from dark matter annihilation.

In this thesis, we present the precision measurement of the time dependency induced by solar activity on electrons and positron fluxes at energies below 40 GeV based on the analysis of the first 30 months of AMS-02 collected data.

Electrons (e^-) and positrons (e^+) are a rare component of the cosmic radiation since they represent only a $\sim 1\%$ and $\sim 0.1\%$ of the total CR flux, which is dominated by protons (90%) and alpha particles (8%). From the experimental point of view is therefore a challenge to select their signals and to collect an adequate statistics. In spite of this, a constant effort has been put in their measurement since decades due to the unique knowledge that they can bring on CR astrophysical sources and InterStellar Medium (ISM) properties as well as for their potential in probing new exotic sources.
Due to their low mass, $e^{\pm}$ suffer of dramatic energy losses due to the interactions with the magnetic field and background photons in the ISM: high energy $e^{\pm}$ observed near earth are therefore of galactic origin and their sources are mostly located within few kpc. In the most common astrophysical models, e^- are mainly of primary origin, i.e. produced and accelerated in astrophysical sources, whereas e^+ are mostly produced in the interactions of protons and nuclei with the ISM material: their flux is faint and expected to extinguish more rapidly with increasing energy with respect to that of e^-. These features make the e^+ a sensitive channel for indirect Dark Matter detection or to search for new astrophysical sources.

However, $e^{\pm}$ spectra, when measured near Earth, are significantly affected by the solar activity and subject to the so-called *solar modulation* (SM) effect. The solar activity has a cycle which period is ~ 11 years, during which it increases reaching a maximum and then decreases again. The intensity of cosmic ray radiation is correlated (or rather anticorrelated) with the activity of the sun.

In order to have a correct understanding of spectra of $e^{\pm}$ out of the heliosphere, the SM should be well known and taken into account. A detailed study of the $e^{\pm}$ fluxes evolution with time is needed in order to develop and test different models of the SM effects based on the interaction of cosmic rays with the heliosphere and to study the charge-sign dependent modulation effects. Most of previous studies on charge-sign dependence of the solar modulation compared the combined $e^{-} + e^{+}$ flux time behaviour with that of CR protons and helium of the same rigidity. However, only simultaneous measurements of e^{-} and e^{+} (or protons and anti-protons) over a complete solar activity cycle can represent a sound test of the current charge-sign dependent modulation models.

AMS-02 can provide the most accurate measurements of the time dependence of electron and positron fluxes since 2011 thanks to its high acceptance and the excellent performances of the detector. In this work, we fully take advantage of the AMS-02 performances to carry out the first precision measurement of charge sign dependent effects in e^{+} and e^{-}.

After an overview on the Cosmic Rays physics (Chapter 1), the main characteristics of the AMS-02 instrument will be introduced (Chapter 2). The event selection and the techniques used to distinguish $e^{\pm}$ signal from proton background will be then presented in detail (Chapter 3). All the elements that will enter in the flux definition will be then discussed as well as the time-dependent analysis (Chapter 4). Discussion of the results and their measurement uncertainties (Chapter 5) will conclude this dissertation.

Chapter 1

Cosmic Rays

Cosmic Rays are high energy charged particles originated in outer space reaching the Earth atmosphere from all directions. Mainly constituted in particle number density by protons ($\sim$ 90%), alpha particles ($\sim$ 8%), electrons and nuclei ($\sim$ 1% each), the CR reaching the Earth can have different origins: solar, galactic or extra-galactic. This reflects into peculiar features in their composition and spectrum, which extends over 15 decades in energy . Interactions with matter, radiation and magnetic fields of the interstellar medium, as well as with the heliosphere and the Earth's magnetosphere, significantly modify the spectrum of the CR from their sources to the Earth and generate secondary components, as positrons ($O(10^{-3})$) or anti-protons ($O(10^{-4})$).
Accurate measurement of the CR composition and energy spectrum then gives a valuable access to open problems in understanding the energetics of their sources and in the dynamics of their propagation as well as in the search for new *exotic* sources, e.g. dark matter annihilations contributing to the flux of CR particles.

In the following, we will first give an overview of the current understanding of the CR spectrum. We will then address the main effects of the propagation process on the $e^{\pm}$ energy spectra: energy losses in the interstellar medium, solar modulation effects in the heliosphere and geomagnetic cutoff effects near Earth. A review of the experimental measurements of the $e^{\pm}$ fluxes will close this chapter.

1.1 The CR composition and energy spectrum

The Cosmic Rays reaching the Earth atmosphere include all stable charged particles and nuclei with lifetimes of order 10^6 years or longer. As sketched in figure1.1,

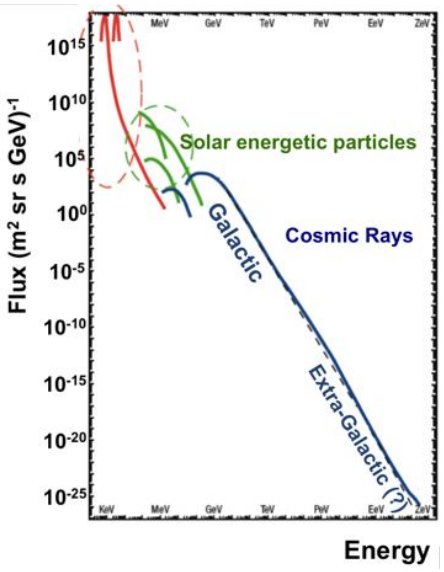

FIGURE 1.1: An overall view of the CR spectrum and its origin as a function of energy. Adapted from [1]

their energy spectrum spans over 15 decades in energy and 40 decades in intensity. At low energy, solar particles are mostly dominating the flux, whereas the galactic component starts to be relevant above few hundreds of MeVs. Below few MeV, the flux is dominated by the solar wind, a steady expanding flux of plasma, from the Sun corona. Transient events due to the variable solar activity, as solar flares or Coronal Mass Ejections (CME), inject energetic particles in the heliosphere, which superimpose and perturb the steady solar wind and that can reach the Earth. In the following, we address the features of the CR spectra where the solar particle contribution can be neglected, the so called *Galactic* spectrum. The galactic CR spectrum observed at the top of the atmosphere, is constituted by *primary* cosmic rays (i.e. particles accelerated at astrophysical sources) and by *secondaries* cosmic rays (i.e. particles produced in interaction of the primaries with interstellar medium). Electrons, protons and helium, as well as carbon, oxygen, iron, and other nuclei synthesized in stars, are primaries. Nuclei such as lithium, beryllium, and boron (which are not emitted during stellar nucleosynthesis since they act as catalyzers of nuclear reactions in the stars) are secondaries, produced by nuclear reactions of primaries during the propagation with the InterStellar Medium (ISM). Antiprotons and positrons are also in large part secondary, according to the standard picture. Whether a fraction of these particles may be primary is a open question of great interest.

CR belong to a *non-thermal* class particles which energy spectra follow a power law:

$$\frac{dN}{dE} \propto E^{-\gamma} \tag{1.1}$$

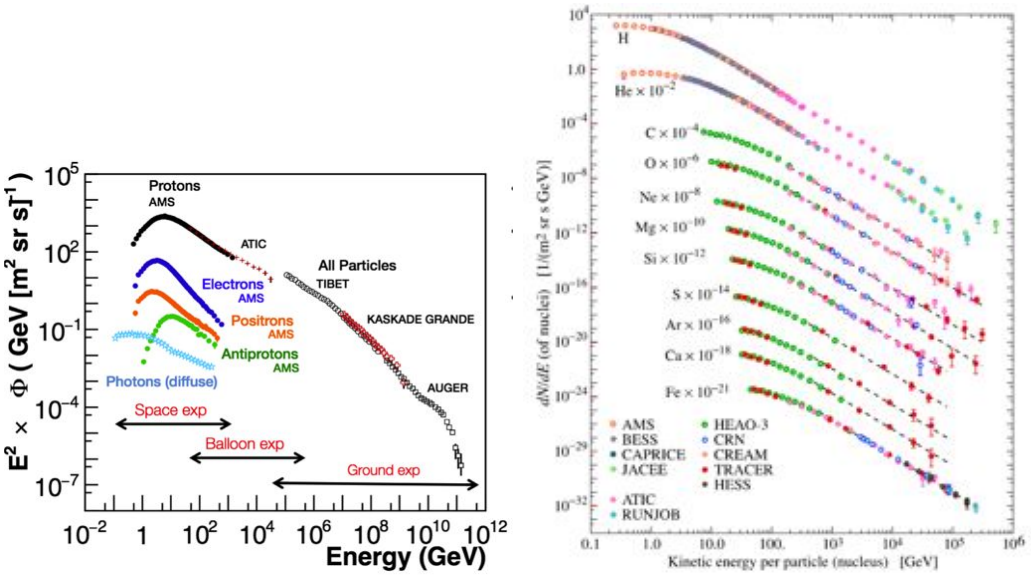

FIGURE 1.2: The CR spectrum as a function of Energy. Left: In the energy range accessible to direct measurement the different components of the spectrum are detailed, at energies above 10^5 GeV only the inclusive spectrum from ground based arrays is shown. (from [2]). Right: Flux of nuclei in the CR as a function of their kinetic energy per nucleon from direct measurements from [3]

Where dN is the number density of particles with kinetic energy per nucleon between E and $E + dE$. A wide range of energies, ranging from 10^8 eV/nucleon to 10^{20} eV/nucleon has been observed. Figure 1.2 (left) shows the differential energy spectrum multiplied by E^2 in order to display the features of the steep spectrum that are otherwise difficult to discern: it is clearly visible that the spectral index is not the same for the whole energy range. The first change of the spectral index from 2.73 to 3.0 is observed between 10^{15} and $10^{16}\,eV$, the break-point is known as the *knee* of the spectrum. The second change in slope is around $10^{18.5}$ eV is called the *ankle* of the spectrum. Above this break, the index is ∼2.7 again. The change in the spectral index is believed to reflect differences in the acceleration processes and propagation, as will be discuss in the following section.

At low energies (E<10–20 GeV), the intensity of the incoming charged particles is modulated by the solar wind. As will be extensively discuss in section 1.2.1 there is a significant anti-correlation between solar activity and the intensity of the cosmic rays. In addition, the lower-energy cosmic rays are affected by the geomagnetic field, which they must penetrate in order to reach the top of the atmosphere. Thus the intensity of any component of the cosmic radiation in the GeV range depends both on the location and time (see section 1.2.2).

1.1.1 Origin and acceleration of Cosmic Rays

The sources and acceleration mechanisms of CRs are still open problems. The total, stationary, power carried by galactic CRs is of the order of 10^{41} erg/s, as the result of a dynamical equilibrium between injection and loss processes within our galaxy. Any source model must explain this feature. From this point of view, it is quite convincing that SuperNova Explosions (SNE) are sources of galactic CRs. In fact, given the energy released in a SNE -of the order of 10^{51} erg- and the estimated SNE frequency in our galaxy of about three per century, the total energy from a SNE is of the order of 10^{42} erg/s. A mechanism to transfer a fraction of a $\sim 10\%$ of the SNE energy to the particles is then needed to explain the observed flux.

The stochastic Fermi mechanisms [4] of first and second order are able to explain how the shockwave produced by a SNE transfers energy, i.e. *accelerates*, to CRs up to the knee, i.e. to energies of $\sim 10^{15}$ GeV. This mechanism is very appealing since it reproduces, without ad hoc hypothesis, the CR spectrum at the sources, before it is modified by the propagation. Convincing evidences of this process for both electrons and protons are the observed synchrotron radiation from electrons accelerated at the shockwave fronts in Supernova Remnants (SNR) and the π_0 lines produced by the interactions of accelerated protons with nearby molecular clouds, as in the case of IC273 and W44 SNRs observed by the Fermi satellite [5]. At higher energies, other mechanisms must be invoked for the acceleration of the CRs as shocks in AGN jets, galactic and extragalactic halos, magnetar, since the Fermi mechanism is limited by the lifetime of the cosmic accelerator. However, for the highest energies, above the ankle, no suitable sources have been yet observed or modelled, so that their origin is still a mistery.

An important clue to the CRs origin is whether they come from within the Milky Way or from outside of it. Our galaxy is a disc-shaped spiral galaxy with a barred central bulge and a disc diameter of $\sim 30kpc$ with thickness of $\sim 300 - 1000pc$. It is permeated by an average galactic magnetic B field with an intensity of $1 - 3nT$, both in disc and the halo, where, however, the B field weakens and fades away. Superimposed to the average B field are present random turbulent irregularities both in intensity and direction, which make the local galactic field essentially random, with a coherence scale of the order of 10 kpc.

Most of the luminous mass of the galaxy is made of stars and dust, concentrated in the disc. A fraction of the galactic mass is made by cold and hot gas, mainly hydrogen (HI, HII and H+) with traces of complex molecules as CO, NH3, etc. The average matter density of the ISM is $\sim 1\,\mathrm{proton/cm^3}$ in the disc and much less in the halo and it is a relevant parameter for the CR propagation. CR play

an important role in the energetics of the galaxy since their energy density $u \sim 1\,\mathrm{ev/cm^3}$ is comparable to the B field energy density ($\sim 0.2\,\mathrm{eV/cm^3}$) and Cosmic Microwave Background energy density, present everywhere ($u \sim 0.4\ \mathrm{eV/cm^3}$) and for the starlight energy density ($u \sim 10^{-2}\,\mathrm{eV/cm^3}$). The CR propagation is modelled by the combined action of the galactic B field, that bends particle trajectories and scatters them randomly on the field irregularities, and of the interactions of energetic CR particles with particle and fields in the ISM, that modify both the energy distribution and the composition of CR. These include radioactive decays in lighter particles of unstable species, ionization energy loss, inelastic interactions loss, bremsstrahlung emission due interactions of CR with ISM and radiative losses as synchrotron or inverse Compton emission due to interactions with magnetic fields and photons.

A CR is therefore accelerated at the source or created by some inelastic interaction in the ISM, propagates with a random walk in the ISM magnetic field until either it escapes the galaxy after a characteristic average residence time or gets absorbed, destroyed or it looses all its energy, becoming part of the ISM. Neglecting to a first approximation the random scatterings in the B field irregularities, it is possible to demonstrate [6], that protons with energies $< 10^{15}\,\mathrm{GeV}$ are fully contained into the galactic disc since their Larmor gyro-radius $r = R/Bc$[1] is smaller than the galactic disc thickness and therefore are produced within the galaxy.

At rigidities R above $\sim 10^{15}\,GV$, the gyro-radius r becomes of the same order as the thickness of the galactic disc, therefore the confinement starts to be less and less efficient. This may lead to a spectral break in the flux. Another possibility is that assuming the cosmic ray spectrum below $10^{18}\,\mathrm{eV}$ is, at least partly, of galactic origin, the *knee* might reflect the fact that most of the cosmic accelerators in the galaxy have reached their maximum energy.

For rigidities $> 10^{18}\,GeV$, CRs cannot be contained in the disc since r is much greater than its thickness and therefore they are believed to be of extra-galactic origin. The second break, the ankle, is the result of a higher energy population of particles that overtakes a lower energy population, for example an extragalactic flux starts to dominate over the galactic flux. Another possibility is that the dip structure in the region of the ankle is due to $\gamma p \rightarrow e^+ + e^-$ energy losses of extragalactic protons on the 2.7 K cosmic microwave radiation (CMB) [7].

The energy loss processes limit the average lifetime of the CR in the galaxy and therefore the distance of the source they come from. All the particles undergo to

[1] being $R = p/Ze$ the magnetic rigidity of the particle

energy losses but the relative importance of each process depends on the particle species. Since radiative cross sections depends on mass, m, as m^{-2}, radiative processes are important only for light particles, namely electrons, while ionization collisions in the ISM, independent of the CR mass, are present for all the species.

So protons and nuclei undergo only to ionization (weakly depending on energy) and inelastic interactions, while for high energy electrons radiative losses are most important. From simple considerations, it can be seen that, since synchrotron and inverse Compton depend on E^2, high energy electrons must come from nearby sources. Different situation for the protons and nuclei: they probe a much larger distance since not affected by radiative loss. For instance, the CMB radiation permeates all space and therefore all the relativistic electrons are subject to *Inverse Compton* losses. For a E=100 GeV electron, if we take into account only the *Inverse Compton* energy losses, the source cannot be distant more than $30\,kpc$. For 1 TeV electrons, the source cannot be located more than few kpc away from the point of observation. This is much smaller distance than the nearest galaxy or even the disc, so that we may infer that the origin of the high energy electron is galactic. Instead protons and nuclei can travel distances comparable to dimensions of the local supercluster.

The maximum distance that a charged can come from is limited by the so called Greisen-Zatsepin-Kuzmin (GZK) mechanism [8]: CRs start to interact with the CMB photons through the Δ^+ resonance formation ($p + \gamma_{CMB} \rightarrow \Delta^+ \rightarrow$ anything and their path-length in the ISM steeply decreases above the energy threshold for the reaction. Cosmic rays are not expected to be observed above this limit without invoking exotic explanations, and the flux measured by ground experiments above 10^{19} eV shows a significant suppression as predicted by this model.

1.1.2 Cosmic Rays propagation

As outlined in the previous section, CR are injected in the ISM by astrophysical sources, where they are accelerated by some mechanism, as Fermi mechanism at the shockwave fronts of SNRs or the unipolar inductor in pulsars. CR leave the source after some time characteristic of the source and diffuse in the ISM, with a random motion in the turbulent interstellar magnetic field. While diffusing, they may interact with radiation fields and matter in the ISM through all the possible processes allowed by the conservation laws. CR contain all the elements of the periodic table, stable or long-lived particles as electrons, positrons, antiprotons and

radioactive isotopes. The composition and energy distribution of each species is determined by the equilibrium of all the processes that can modify them.

In this approach, the propagation of all the CR species is generally described by a system of Fokker-Planck type equations [9]. For every species, it must be included source distribution, particle diffusion in the galactic magnetic field, energy losses, nuclear interactions, decays and re-acceleration processes. According to this equation, the number density evolution per momentum units p for the i^{th} species (ψ_i), can be written as:

$$\begin{aligned}\frac{\partial \psi_i(\overrightarrow{r},p,t)}{\partial t} = q(\overrightarrow{r},p,t) + \overrightarrow{\nabla}\cdot(D_{xx}\overrightarrow{\nabla}\psi_i - \overrightarrow{V}\psi_i) + \frac{\partial}{\partial p}p^2 D_{pp}\frac{\partial}{\partial p}\frac{1}{p^2}\psi_i + \\ -\frac{\partial}{\partial p}[\dot{p}\psi_i - \frac{p}{3}(\overrightarrow{\nabla}\cdot\overrightarrow{V})\psi_i] - (\frac{1}{\tau_f}+\frac{1}{\tau_r})\psi_i\end{aligned} \tag{1.2}$$

This is a system of coupled differential equations that must be solved simultaneously. Many astrophysical parameters are needed, as the source distribution, the ISM gas density distribution, the magnetic field map, Milky Way halo shape and so on.

Infact, the temporal, spatial and energetic evolution of the CR densities is ruled by several factors:

Source term, $q(\overrightarrow{r},p,t)$
$q(\overrightarrow{r},p,t)$ represents any possible production mechanism for particles of a given species i. The source term includes primary source, spallation, and decay contributions. The first describes the astrophysical source distribution in the galaxy, where CR are accelerated and emitted in the ISM with a given energy spectrum (the *source spectrum*), the second and third describe the production of particles i by the interactions of heavier species j with the protons of the ISM and the production of particles i from the decay of heavier species j, respectively. The spatial distribution of CRs sources is usually assumed to be correlated with the density of known pulsars or SNRs. The energy injection spectrum of the source term is modelled as a power law spectrum $\frac{\partial}{\partial p}q \propto p^{\gamma}$, according to the assumed Fermi acceleration mechanism. For some sources, as pulsars, a broken power law (power law with an exponential cutoff) is assumed.

Diffusion in the galactic cosmic rays, D_{xx}**,** D_{pp}
The concept of CR diffusion explains why energetic charged particles have highly isotropic distributions and why they are well retained in the Galaxy. The terms D_{xx}, D_{pp} describe the diffusion of the particles in the turbulent magnetic field. The galactic magnetic field that tangles the trajectories of particles plays a crucial role in this process.

The cosmic rays propagate through the Galaxy from their sources to the Earth, under the influence of the galactic magnetic field B_{gauss}, which curves their trajectories. The curvature depends, in addition to the intensity of galactic magnetic field ($B_G \sim 6\mu G$ [10]), by the particle rigidity R. Different particles with the same rigidity are equally affected by the magnetic fields.
The galactic magnetic field can be decomposed in a regular average component, which follows the distribution of the arms of the Galaxy, and a turbulent component in the form of perturbations of the regular field. The resonant scattering of charged CRs with these random small fluctuations $\delta B << B$ leads to a diffusive motion.
Typical values of the diffusion coefficient found from a fit to CR data are $D_{xx} \sim (3-5) \times 10^{28}\,\mathrm{cm}^2 s^{-1}$ at energy $\sim$1 GeV/n.
In addition to the spatial diffusion, the interaction with the turbulent galactic fields induces a stochastic acceleration, also known as re-acceleration [11]. This process is modelled by a diffusion in momentum space with a coefficient $D_{pp} \propto |\overrightarrow{V}|^2 |D_{xx}$, where the Alfvén velocity $\overrightarrow{V}$ is the characteristic propagation speed of the random fluctuations in the magnetic field.

Convection with galactic wind, $\overrightarrow{\nabla} \cdot \overrightarrow{V}\psi_i$
CRs may not only diffuse in our Galaxy: the existence of galactic winds in many galaxies suggests that convective (or advective) transport may be important. Winds are common in galaxies and can be CRs driven. The effect of this galactic wind is to dilute the energy of the particles located in the disc in a larger volume, so that the propagation in a adiabatically expanding gas results in a kind of energy loss (*adiabatic deceleration*), depending on the wind velocity $V = V(t, r)$. The topology, the speed and the evolution of the galactic winds are highly constrained by measurements of secondary to primary CR ratios, like the boron to carbon ratio (B/C), and of the unstable isotope ratios, like the ^{10}Be/^{9}Be ratio.

Nuclear processes, τ_f and τ_r
The terms τ_f and τ_r indicate respectively the timescale for loss by fragmentation and the timescale for radioactive decay.

Unstable nuclei decay into other nuclear products with a probability per unit of time $\Gamma = (1/\tau_r)$, thus the net rate of loss is -ψ_i/τ_r. Long lived ($O(Myr)$) unstable isotopes are usually used to measure the residence times of CR in the galaxy by measuring the relative abundance with respect to their decay products, e.g. ^{9}Be/^{10}Be.

Spallation processes of CRs nuclei with the ISM, namely $N_j + p_{ISM} \rightarrow N_i + anything$, also contribute to the evolution of the density of a species i. The time scale for the fragmentation is given simply by $\tau_f = 1/n_{ISM}\sigma_f$, where n_{ISM} is the ISM proton

density and σ_f is the total inelastic cross section of the nuclei on protons. Thus the net rate of loss is -ψ_i/τ_f. The total time scale for nuclear loss can be written as $1/\tau = (1/\tau_f + 1/\tau_r)$, so that the smallest scale dominates the process.

Fragmentation processes are responsible also for the production of *secondary* species that are not produced in astrophysical sources, as Li, Be, B and the sub-Fe elements. The net rate of production is given by $\Sigma_{j>i} P_{ji}/\tau_f$, where P_{ji} is the probability that a nucleus j produces a nucleus i in the process. Only heavier nuclei than the given species i can contribute. The measurement of the secondary CRs is very important since from it we can deduce the total grammage crossed by the particle from the source to the Earth as a function of the energy and the spatial diffusion coefficients in the galaxy.

Continous energy losses, $-\frac{\partial}{\partial p}(\dot{p}\psi_i)$
The term $\frac{\partial}{\partial p}(\dot{p}\psi_i)$ describes the continuous energy losses suffered by CR through various processes that occur during the propagation in the ISM.

Protons and nuclei mainly loose their energy due to the Bethe-Bloch specific energy loss when a charged particle travels in the ISM. Instead, as will be shown in the next chapter, the electrons and positrons loose their energy mainly for synchrotron and Inverse Compton processes.

In the case of a steady-state, $\frac{\partial \psi_i(\vec{r},p,t)}{\partial t} = 0$, the solution of the equation 1.2 completely describes the Local Interstellar Spectrum (LIS) for each species before entering in the region dominated by the Sun's activity, the heliosphere. The equation can be solved both in the semi-analytical and numerical way, using dedicated packages like GALPROP [12] or DRAGON [13].

1.1.3 Electrons and positrons propagation

For of electrons (e^-) and positrons (e^+), in the equation 1.2 all the terms related to nuclear process and decays can be neglected. The $e^\pm$ propagation can be described by a simplified equation:

$$\frac{\partial \psi_{e^\pm}(\vec{r},p,t)}{\partial t} = q(\vec{r},p,t) + D_{xx} \cdot \vec{\nabla}^2 \psi_{e^\pm} - \frac{\partial}{\partial p}(\dot{p}\psi_{e^\pm}) \tag{1.3}$$

It is possible to solve the equation under some simplifying assumptions. Thus, many of the relevant features of the electron propagation in the galaxy can be easily outlined.

Let consider a steady state, where $\frac{\partial \psi_{e^\pm}(\overrightarrow{r},p,t)}{\partial t} = 0$.

Assuming an infinite, uniform distribution of sources, each injecting CR electrons with a power law spectrum $N(E) \propto E^{-\gamma}$ ($q(\overrightarrow{r}, E, t) = KE^{-\gamma}$), the diffusion is not important and the equation 1.3 can be written as:

$$q(\overrightarrow{r}, p, t) = \frac{d}{dp}(\dot{p}\psi_{e^\pm}(\overrightarrow{r}, p, t)) \quad \rightarrow \quad \int_0^\infty q(\overrightarrow{r}, p, t)\, \mathrm{d}p = \int_0^\infty \mathrm{d}[\dot{p}\psi_{e^\pm}(\overrightarrow{r}, p, t)] \tag{1.4}$$

Assuming $\psi_{e^\pm}(\overrightarrow{r}, p, t) \rightarrow 0$ for $p \rightarrow \infty$, taking into account that for ultrarelativistic particles $E \simeq p$ and putting $dE/dt = b(E)$, equation 1.4 gives:

$$\psi_{e^\pm}(\overrightarrow{r}, p, t) = \frac{Kp^{-(\gamma-1)}}{(\gamma-1)\cdot(-\frac{dE}{dt})} = \frac{Kp^{-(\gamma-1)}}{(\gamma-1)\cdot b(E)} \tag{1.5}$$

The spectral index at the source is changed by the energy loss $b(E) = -\frac{dE}{dt}$ suffered by the electrons during the propagation, so that the spectrum measured at the Earth is not the same as the source spectrum. One advantage of electrons is that they emit radiation by various processes, so that by measuring the emission spectra at source, their population spectrum can be deduced and compared with the one measured at Earth. This allows for a measurement of the effect of the propagation of the electrons in the galactic environment.

In order to know how the energy losses modulate the source energy spectrum, we need to know the form of $b(E)$. The electrons interact with matter, magnetic fields and radiation trough the *Ionization*, *Bremsstrahlung*, *Synchrotron radiation* and *Inverse Compton*. The dominant processes are usually Synchrotron and Inverse Compton, but in some environments (as the central regions of AGN or the space within galaxy custers) bremsstrahlung is also important.

Ionization losses

The ionization energy loss for electrons is described by the Bethe-Block formula:

$$-\frac{dE}{dx} = \frac{e^4 NZ}{8\pi\epsilon_0^2 m_e v^2}[ln\frac{\gamma^2 m_e v^2 E}{2I^2} - (\frac{2}{\gamma} - \frac{1}{\gamma^2}) \times ln2 + \frac{1}{\gamma^2} + \frac{1}{8}(1-\frac{1}{\gamma})^2] \tag{1.6}$$

Since it is a process $\propto 1/\gamma$, for protons and electrons of the same kinetic energy, the energy loss rate is greater in the case of protons. The energy loss per time unit is proportional to $ln\, E$:

$$-\left(\frac{dE}{dt}\right)_{ionization} \propto ln\, E \tag{1.7}$$

Generally the Ionization losses are of little importance for high energy electrons, compared to other processes, while they become the dominant energy loss below few tens of MeV.

Bremsstrhalung

The *bremsstrahlung* radiation emission occurs when a charged particle enters in an electric field, such as the Coulomb field of a nucleus. The particle is accelerated or decelerated due to the Coulomb force and it emits electromagnetic radiation. The energy loss rate for *bremsstrahlung* emission in the relativistic case, can be written as:

$$-\left(\frac{dE}{dt}\right)_{brem} = \frac{Z^2 z^4\, e^2\, E}{12\,\pi^3\,\epsilon_0^3\, M^2\, c^4 \hbar}\, ln\left(\frac{192}{Z^{1/3}}\right) \tag{1.8}$$

Where Z is the charge of the target and z and M are respectively the charge and the mass of the incident particle. The cross section of the process depends strongly on the mass of the incident particle ($\propto 1/M^2$). For this reason is much more important for electrons than for protons. The rate of energy loss is proportional to E: at low energies electrons and positrons primarily loose energy by ionization. While ionization loss rate rises logarithmically with energy, the bremsstrahlung losses rise nearly linearly with energy and dominate above a few tens of MeV.

Synchrotron

The *synchrotron emission* is the radiation of a high energy charged particle bending in a magnetic field. This process dominates the high energy astrophysics. This mechanism is responsible for the radio emission from the Galaxy, from supernova remnants and extragalactic radio sources, of gamma emission from AGN and pulsars. It was first discovered in the early betatrons when electrons were accelerated at relativistic energies. The energy loss rate can be written as:

$$-\left(\frac{dE}{dt}\right)_{sync} = \frac{4}{3}\sigma_T c \left(\frac{E^2}{(mc^2)^2}\right) U_{mag} \tag{1.9}$$

where σ_T is the Thomson cross-section and U_{mag} is the energy density of the magnetic field. The energy loss is $\propto E^2$, thus at high energy the *synchrotron emission* gives the main contribution to the energy loss for ultra-relativistic electrons and positrons, compared to ionization and bremsstrahlung losses.

Inverse Compton scattering

The *Compton scattering* is a collision between a charged particle and a photon.

When a high energy photon collides on a low energy electron, it gains energy from the photon. In the *Inverse Compton scattering* (IC) high energy electrons collide with low energy photons that gains energy at the expense of electrons.

The situation most often encountered in astrophysical conditions is the limit in which the energy of the photon in the center of mass frame of the collision is much less than the rest mass of the electron ($\gamma h\nu \ll m_e c^2$), the so called Thomson limit. The energy loss rate is:

$$\left(\frac{dE}{dt}\right)_{IC} = \frac{4}{3}\sigma_T c U_{rad}\left(\frac{E^2}{(mc^2)^2}\right) \tag{1.10}$$

Equations 1.9 and 1.10 have the same form and dependence on particle energy. The reason for this is that in both cases, the particle is accelerated by the electric field induced by the relative motion of the particles. *Inverse Compton scattering* of cosmic ray electrons in our Galaxy is important for the following reasons. First, there is an average energy density of optical photons due to the light of all the stars which amounts to $U_{rad} \sim 0.6\, eV\, cm^{-3}$. Second, there is the CMB radiation which fills the whole Universe. Its energy density is about $0.25\, eV\, cm^{-3}$.

Comparing equations 1.9 and 1.10 and putting $B = 3{\times}10^{-6}\, G$ and $U_{rad} = 0.6\, eV\, cm^{-3}$:

$$\frac{(dE/dt)_{IC}}{(dE/dt)_{sync}} = \frac{U_{rad}}{U_{mag}} \simeq 3 \tag{1.11}$$

The energy loss due to IC turns out be higher than the synchrotron and unavoidable. Inverse Compton losses are bound to be important for CR electrons. Electrons outside the Galaxy would have very little energy loss due to synchrotron radiation, because we can set very low limits on the intergalactic magnetic field. However, the microwave background is present everywhere and therefore the electrons loose all their energy in the scattering with photons of the microwave background. In the galactic environment, the IC loss limit drastically the distance of the sources which the electrons can come from.

Energy loss for cosmic electrons and positrons

Taking into account all the energy losses described above, the term $b(E)$ in the equation 1.5 can be written as:

$$b(E) = -\left(\frac{dE}{dt}\right) = A \cdot (ln\, E) + B \cdot E + C \cdot E^2 \tag{1.12}$$

where the first term ($\propto ln\, E$) is due to the ionization losses, the second one ($\propto E$) to the Bremsstrahlung and the third one ($\propto E^2$) is due to Synchrotron and Inverse Compton losses.

From equation 1.5 follows that:

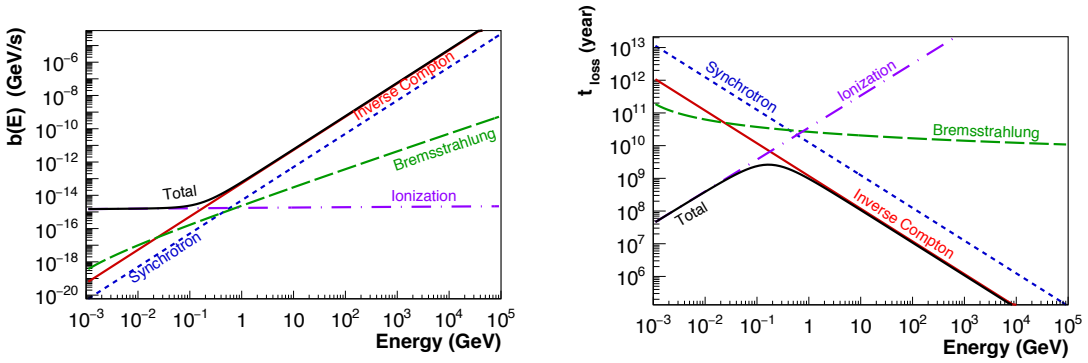

FIGURE 1.3: Left: Values of the loss functions 1.12 as a function of the energy of the electron for an intercluster medium (ICM) electron density of $n_e = 1.0 \times 10{-}3\,\mathrm{cm}^{-3}$ and a typical ICM magnetic field of $B = 1\,\mu\mathrm{G}$ [14]. Right: Instantaneous loss timescale ($t_{loss} = \frac{E}{b(E)}$) as a function of energy of the electron for an intercluster medium (ICM) electron density of $n_e = 1.0 \times 10{-}3\,\mathrm{cm}^{-3}$ and a typical ICM magnetic field of $B = 1\,\mu\mathrm{G}$ [14].

- if ionization losses dominate $\rightarrow$ $\psi_{e^\pm}(\overrightarrow{r}, p, t) \propto E^{-(\gamma-1)}$;
- if Bremsstrahlung or adiabatic losses dominate $\rightarrow$ $\psi_{e^\pm}(\overrightarrow{r}, p, t) \propto E^{-\gamma}$
- if Synchrotron or IC losses dominate $\rightarrow$ $\psi_{e^\pm}(\overrightarrow{r}, p, t) \propto E^{-(\gamma+1)}$;

Figure 1.3 (left) shows the values of the loss function 1.12 as a function of the energy of the electron for an inter-cluster medium (ICM) electron density of $n_e = 1.0 \times 10{-}3\,\mathrm{cm}^{-3}$ and a typical ICM magnetic field of $B = 1\,\mu\mathrm{G}$ [14].

From the figure is clear that the IC losses are dominant for energies $> 0.1\,GeV$ while Coulomb losses dominate for sufficiently small energies ($E < 0.1\,GeV$) or for higher densities. Bremsstrahlung losses are unlikely to be dominant unless the density is higher than the typical one in the bulk of the ICM. Similarly, synchrotron losses are unlikely to be dominant unless the magnetic field is much stronger than $1\,\mu\mathrm{G}$. For each loss process, a characteristic timescale can be defined as the time needed to loose all (or half of) the energy $t_{loss} = \int \frac{E}{b(E)}$, Figure 1.3 (right) shows the timescale t_{loss} calculated with the same conditions of figure 1.3.

The maximum loss time ($\sim 10^9$ years) is reached for energies 0.1–0.5 GeV.

The solution of Equation 1.5 shows that the typical gyro-radius of $e^\pm$ with energies above $\sim 1\,\mathrm{GeV}$ is smaller than the galactic halo thickness. Therefore, $e^\pm$ detected in the CRs at Earth above the GeV energies must have galactic origin. Since the Synchrotron and IC are omni-present in the galactic environment, differently from hadrons, the propagation volume they span during the propagation drastically decreases with increasing energies. In the galaxy, a 100 GeV $e^\pm$ has to originate from a distance $d < 30\,\mathrm{Kpc}$. At 10 TeV, the distance decreases to 3 pc.

This is remarkable, as the measurement of high energy $e^{\pm}$ could potentially improve the knowledge of the galactic neighbourhood with important consequences on the phenomenological interpretation of the measurements of all the CR species.

1.2 Local environment effects on CRs spectrum

To reach the Earth, the CRs must penetrate the heliosphere (HS) of the Solar System and the magnetosphere (MS) of the Earth. The first is a void in the interstellar medium where the solar activity dominates the environment, the latter is a void in the heliosphere due the Earth's magnetic field. Both HS and MS influence the interstellar spectrum which is observed nearby the Earth below ∼20–30 GeV. In the following the influence of HS and MS on the CR flux will be discussed.

1.2.1 Cosmic rays in the heliosphere

The heliopshere is a cavity in ISM where there is a variable supersonic solar wind with an embedded a *frozen-in* magnetic field, originating from the Sun's corona. The solar wind consists of a plasma, made mainly of protons, electrons and ionized atoms from the solar corona, expanding at supersonic speed with respect to the speed of sound in local interstellar medium.

The magnetic field embedded in the plasma can be described as formed by a regular, large-scale component with superimposed random irregularities.

The average IMF lines in the HS form archimedean spirals, given by the combination of the expanding solar wind and the 27 days Sun rotation, as shown in figure 1.4 .

The IMF field has a defined polarity, defined by the direction of magnetic field in the northern and southern hemispheres of the HS, measured by A, the projection of the solar magnetic dipole on the solar rotation axis, shown in figure 1.5. This is true during the periods when the activity of the Sun is low, around the minimum. In the phases close to a maximum, the field polarity is much less defined and the average, large-scale magnetic field has not a well defined polarity .

A can be either positive or negative. At each sunspot maximum, the dipole reverses direction, leading to alternating magnetic polarity in successive solar cycles as shown in figure 1.6.

Superimposed to the average structure of the IMF field, random perturbations of the IMF field are present, due to transient, random solar events, as flares, CMEs.

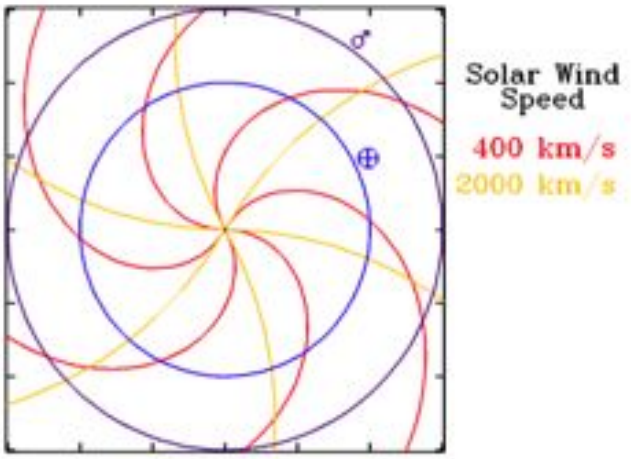

FIGURE 1.4: Archimedean spirals of the IMF field at different speeds of the solar wind.

A solar flare is a sudden, large, localized increase of brightness near the Sun's surface. Flares are often, but not always, accompanied by CME[15]. The flare ejects clouds of electrons, ions, and atoms through the Sun corona. Particles can get accelerated by the magnetic energy released during the flare at relativistic energies and form Solar Energetic Particles events. These clouds typically may reach Earth a day or two after the event, if they are directed along the field lines intersecting Earth. The frequency of occurrence of solar flares varies, from several per day when the Sun is particularly "active" to less than one every week when the Sun is "quiet". Large flares are less frequent than smaller ones. Coronal mass ejections are huge explosions of magnetic field and plasma from the Sun's corona. CMEs originate from

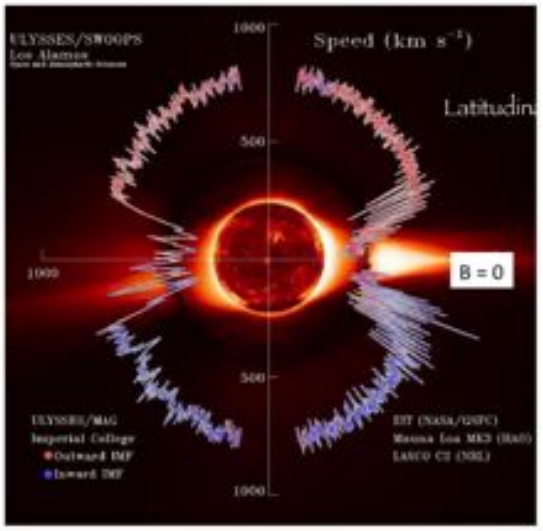

FIGURE 1.5: Speed profile of the solar wind as a function of latitude. In the northern hemisphere the polarity A is positive, while in the southern is negative. The neutral sheet is the surface that separates the two hemispheres

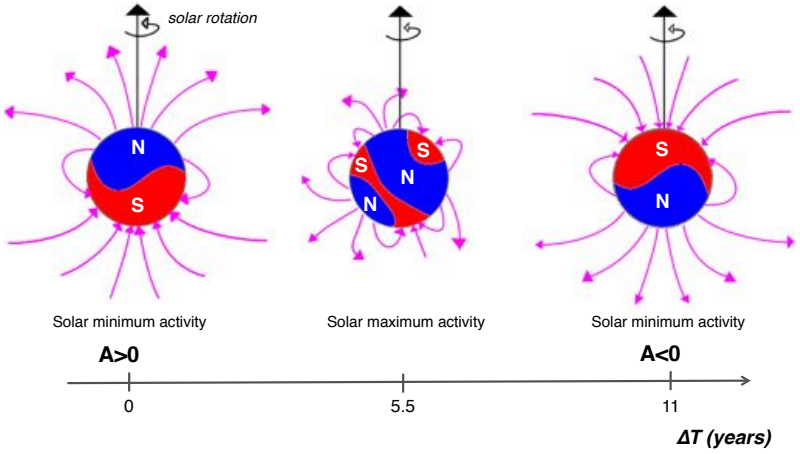

FIGURE 1.6: Configuration of the coronal solar magnetic lines (magenta lines) during an entire solar cycle of 11 years starting from a minimum of solar activity with positive polarity (A>0) and reaching the next solar minimum with negative polarity (A>0).

twisted magnetic field lines ("ropes") on the Sun surface, often coupled to associated *filaments* or *prominences*, made of plasmas trapped in the field in the corona. When these flux ropes erupt from active regions on the Sun (regions associated with sunspots and very strong magnetic fields), they are often accompanied by large solar flares. CMEs travel with speeds ranging from 100 km/s to 3000 km/s, with typical speeds of 300 km/s The fastest CMEs erupt from large sunspot active regions on the Sun. The fast CMEs can reach Earth in as little as 14-17 hours and when they impact the Earth magnetosphere, geomagnetic storms and enhanced aurora occurs. The size, speed, direction, and density of a CME are important parameters to determine when trying to predict if and when it will impact Earth. The intensity and distribution of the CMEs depend on the solar activity.

The so called neutral sheet is the surface where the intensity of the IMF is equal zero, so that the IMF field reverts its polarity. It is the surface that separates the northern and southern magnetic hemispheres of the Sun. The tilt of the Sun magnetic field, combined with the Sun's rotation, makes the neutral sheet wavy, as shown in figure 1.7.

The Sun is an active star, where both the speed of the solar wind, its pressure, density and temperature, together with the intensity and direction of the embedded Interplanetary Magnetic Field (IMF) vary considerably over characteristic timescales, called "cycles". The main cycles relevant to the CR flux measurement in the heliosphere are: the 11-year cycle, reflected by sunspots number reaching a max and the

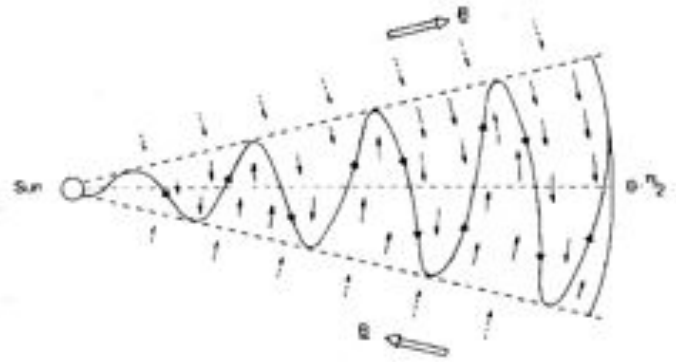

FIGURE 1.7: Wavy neutral sheet, where the sun's magnetic field reveres polarity.

22-year cycle, related to the Interplanetary Magnetic Field (IMF) reversal during each period of maximum solar activity.

Additional short-term periodicities are the 25-27 days variation, due to solar rotation and the daily variation due to Earth rotation (small: O(1%)). Corotating Interacting Regions (CIR) caused when slow SW catches up with the fast stream, may merge and form Global Merged Interaction Region (GMIR) that may cause a decrease similar in magnitude to the 11-year cycle but on scales of several months (as happened in 1991 and may be from May 2012). There are indications of periodicities of 50-65 and 90-130 years and also of about 220 and 600 years.

A good indication of the solar activity is the sunspot number, which has been observed almost continuously for the last century. During each *solar cycle*, which

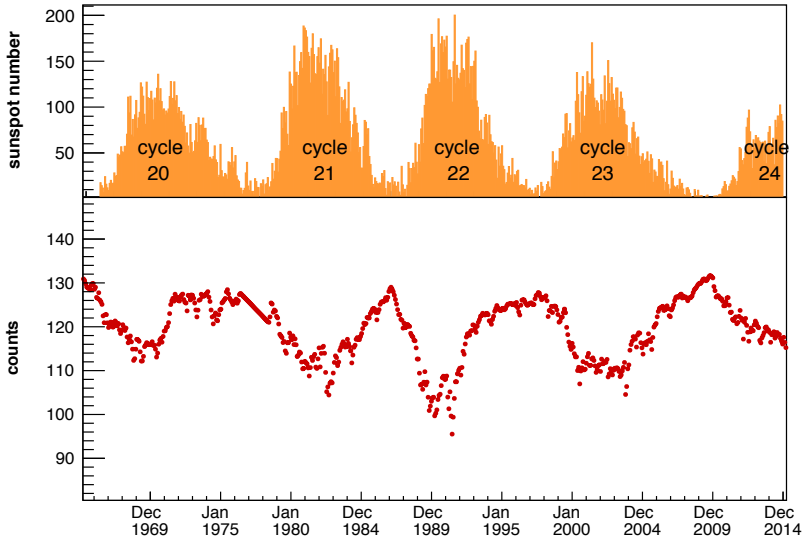

FIGURE 1.8: Sunspot number as a function of time (data from http://www.sidc.be/silso/datafiles) compared with neutron monitor counters as a function of time (data from http://neutronm.bartol.udel.edu/Welcome.html).

period is $\sim$ 11 *years*, the sunspot number rises from a low level (<10/week at minimum) to a large value (>100/week at maximum) and then comes down again. There is a clear correlation (or rather anti-correlation) with the cosmic ray intensity and solar activity, seen by ground-based detectors as the *neutron monitor*, a very stable counter which measures the total flux of neutrons or muons, produced by the interactions of the CR with nuclei of the atmosphere. There is a worldwide network of neutron monitors recording the flux. Figure 1.8 shows the neutron counts compared with the solar activity as a function of time and it is clear that the cosmic ray flux is very well anti-correlated with solar activity.

The solar magnetic field reverses at each solar activity maximum resulting in the 22-year cycle as well [16, 17]. The field orientation (polarity) is defined positive when the field is outward from the Sun in the northern hemisphere (e.g.,during the 1970's and 1990's) and negative when the field is outward in the southern hemisphere (e.g., during the 1960's and 1980's). A positive polarity field is denoted by the A>0 epoch and a negative field by the A<0 epoch [18, 19], as shown in figure 1.9 . Another good indicator of the solar activity is the tilt angle, the inclination of the neutral sheet with respect to plane of ecliptic. It varies form a minimum of 10^o at solar minimum to 75^o at solar maximum.

CR particles, that enter the HS must flow in the solar wind plasma and in the magnetic field of the heliosphere and are subjected to four distinct transport effects. (a) An outward convection caused by expanding solar wind velocity, i.e convection, (b) the magnetic field varies over large scales, so there are curvature and gradient

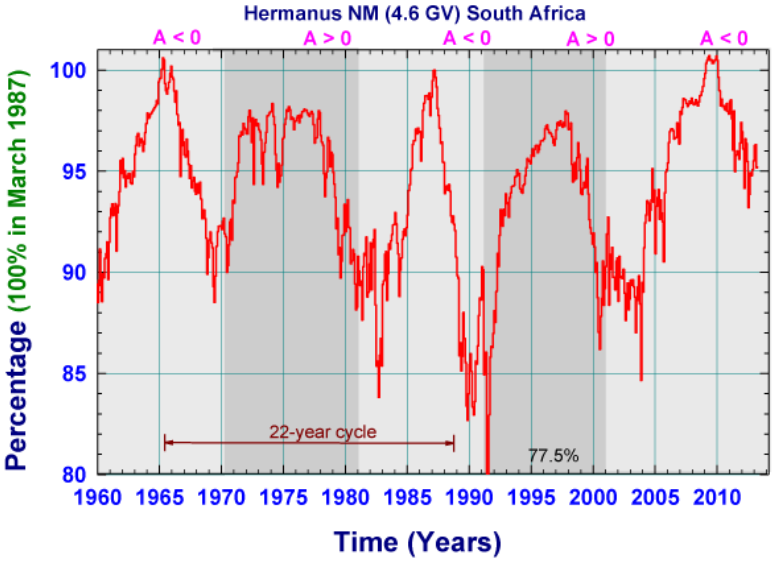

FIGURE 1.9: The 11-year and 22-year cycles in the solar modulation of CRs as observed by the Hermanus NM in South Africa at a cut-off rigidity of 4.6 GV in terms of percentage with March 1987 at 100%.

drifts (drifts), (c) depending on the sign of the divergence of solar wind velocity, there will be energy loss (adiabatic energy loss), (d) the spatial diffusion is caused by the scatterings by random magnetic irregularities (diffusion) ([20] and references therein). The resulting transport is a superposition of these coherent and random effects and it is described by the Parker's equation, that gives an approximate description of the cosmic rays solar modulation, considering a spherically symmetric configuration in which the solar wind carries magnetic irregularities radially with speed $V(r)$ [21]. This magnetic irregularities are assumed to act as "magnetic scattering centers" for the cosmic rays. In this situation the motion of the CRs can be described by the equation:

$$\frac{\partial f}{\partial t} = \frac{\partial}{\partial x_i}\left[k_{ij}^{(S)}\frac{\partial f}{\partial x_j}\right] - \overrightarrow{U}\cdot\overrightarrow{\bigtriangledown} f - \overrightarrow{V_d}\overrightarrow{\bigtriangledown} f + \frac{1}{3}\overrightarrow{\bigtriangledown}\overrightarrow{U}\cdot\left[\frac{\partial f}{\partial lnp}\right] + Q \tag{1.13}$$

where $f(p, r, t)$ is the CR density, U is the SW speed, V_D is the gradient and curvature average drift velocity, k_{ij}^{S} is the diffusion tensor and p is the particle momentum. The first term in the right side represents the diffusion in the irregularities of the IMF field, the second the outward convection due to the SW, the third is the curvature and drift motion on the large-scale average field and the fourth represents the adiabatic energy loss of the CRs in the expanding SW flux. In the guiding center approximation, the curvature and gradient drift velocity is given by:

$$\overrightarrow{V_d} = \frac{pcw}{3q}\overrightarrow{\bigtriangledown}\times\left[\frac{\overrightarrow{B}}{B^2}\right] \tag{1.14}$$

All the mentioned processes are important [22, 23], but their relative importance changes during the solar cycle. In the period near solar minimum, drifts may play an important role in the transport of cosmic rays in the heliosphere, since there is a well defined field polarity. In the complex magnetic structure characteristic of solar maximum, it is likely that drifts play only a small role and that the transport is determined by large-scale disturbances in the solar wind, since the IMF field is irregular and without a defined polarity [24], as can be seen in figure 1.6.

The diffusion and convection components of cosmic-ray transport equation are independent of the solar polarity and will only vary with the solar activity cycle. Conversely, the drift components will have opposite effect in each activity cycle following the field reversal around each solar maximum. Positively-charged cosmic-ray particles would essentially enter the heliosphere along the helio-equator and exit via

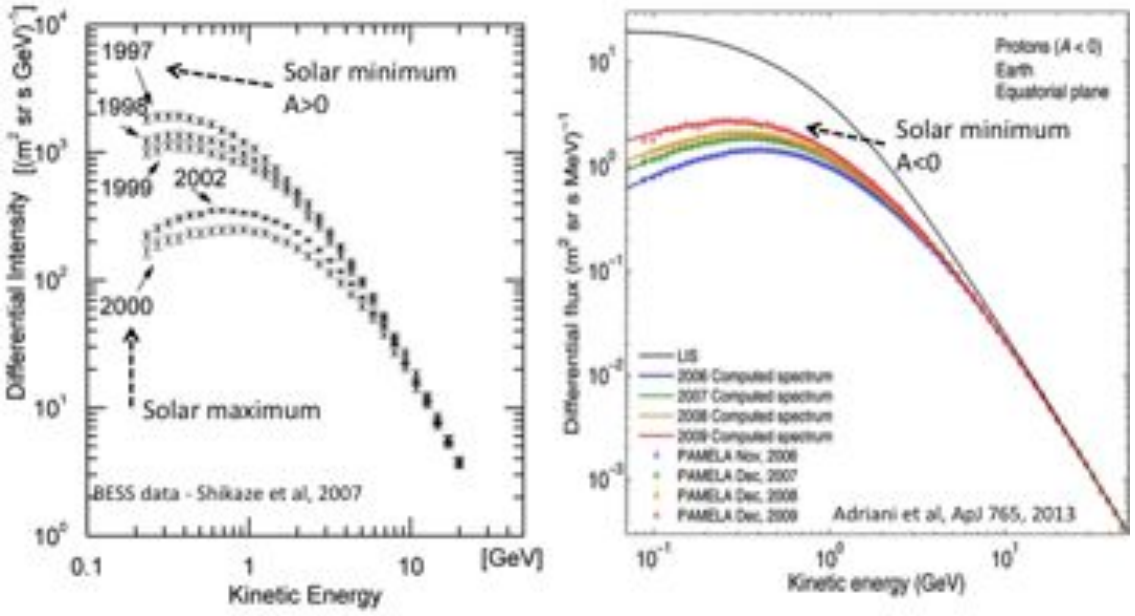

FIGURE 1.10: Proton flux at different epochs, measured by the BESS and Pamela experiments. The solar modulation is clearly visible. It is also visible its dependence on IMF field polarity A.

the poles in the A<0 polarity state. In the A>0 polarity state the flow would be reversed, with particles entering over the poles and exiting along the equator.

Thus, it may be expected that the response of GCR intensity to the changes in solar activity during the A<0 epochs is different from that in the A>0 solar polarity epochs, which has been observed in a long-term record of cosmic ray intensity. Differences in the response of solar activity to GCR intensity variations [25] and to the tilt angle of the HCS [26] during the increasing phases of solar cycles 21, 23 (A>0) and 20, 22 (A<0) have been noted.

The opposite holds for negatively charge CR.

This leads to different path-lengths and trajectories for positively and negatively charged CR during their propagation in the HS and thus to different effects and attenuation of the flux.

All these effects lead to global and temporal variations in the intensity of CR as a function of position inside the heliosphere since the CR interact with IMF. This process is identified as the *solar modulation* of the CR. Modulation plays a role for the LIS CR flux up to 30 GeV. It is fundamental to deconvolve the LIS spectrum of CR at low energy, because the spectra at Earth location below $\sim 30GeV$ are not representative of the LIS spectrum, as can be seen in figure 1.10

Thus it will be interesting to study the Galactic CR intensity during different polarity epochs (A<0 and A>0) when solar activity is decreasing i.e. in the declining (including minimum) phases of different solar cycles, where different modulation may be expected for positively and negatively charged CR, as in the case of electrons and positrons.

AMS02 offers the unique opportunity to study these effects over a long period of time, during the solar cycle 24, in particular at solar maximum and during the descending phase, where the polarity changes.

Infact, the Parker field [27] has opposite magnetic polarity above and below the helioequator, but the spiral field lines themselves are mirror images of each other. This antisymmetry produces drift velocity fields that (for positive particles) converge on the heliospheric equator in the A>0 state or diverge from it in the A<0 state. Negatively charged particles behave in the opposite manner, and the drift patterns interchange when the solar polarity reverses.
This effect is expected to be maximum during the minimum solar activity when the solar magnetic field is regular. During the maximum of the solar activity, because of the irregularity of the IMF field lines, the diffusion processes dominate over the magnetic drift and the effect of the solar modulation is the same both for negative and positive charges.

1.2.1.1 Force field approximation

An analytical solution to the Parker's equation can be given under some simplifying assumptions as solar wind speed V and diffusion tensor K constant with r, a steady state without sources, a spherically symmetric geometry of the heliosphere [21]. This approximation accounts for cosmic ray diffusion through the magnetic field carried by and the convection by the outward motion of the solar wind, the adiabatic deceleration of the galactic cosmic rays in this flow. In this approximation, called *force field approximation*, the diffusion tensor becomes isotropic and reduces to a scalar coefficient κ which can be written as a separable function of r and the rigidity R of the particle as $k = \beta\kappa_1(r,t)\kappa_2(R)$ with k_2 independent from time t [28].

The solar modulation is expressed in terms of this single parameter $Z\phi$, which represents the energy spent by an incoming particle of charge Z to reach a given position in the heliosphere from outside against the expanding SW flux. Under the assumptions above, the modulation parameter turns out to be

$$\phi(E) = \frac{1}{3}\int_{r_1}^{r_h} \frac{V}{K} dr \tag{1.15}$$

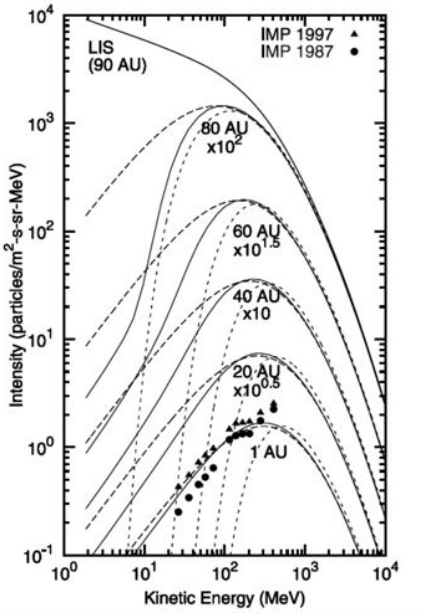

FIGURE 1.11: Galactic cosmic ray modulation in different parts of the Solar system (H. Moraal). The solid lines show the numerical solutions, while the dashed lines show the force field solutions at different distances from the Sun. The end of the heliosphere here is at 90 AU.

where r_1 is the radial distance of the observation position (e.g. 1 AU) and r_h is the distance from Sun of the heliosphere boundaries. It has the same units of a rigidity, GV.

A particle of energy E_{LIS} in interstellar space would reach Earth with $E = E_{LIS} - |Z|\phi$. Only particles with energy greater than $Z\phi$ can reach 1 UA. This leads to a suppression of the LIS flux during the propagation of CR that depends on the position within the heliosphere: the more it is close to Sun, the higher is the suppression of the flux, as shown in Figure 1.11.

The flux of galactic CR measured at 1 AU with energy E is related to the interstellar spectrum by the relationship:

$$\Phi(E) = \frac{E^2 - m^2}{(E + |Z|e\phi)^2 - m^2} \cdot \Phi_{LIS}(E + |Z|e\phi) \tag{1.16}$$

Usually is assumed to be r_h ∼90 AU, even if the recent data from voyager suggest a higher value (may be a factor 2). The solar wind speed varies during the solar cycle and therefore ϕ changes accordingly. The best values of ϕ are deduced by best fits to the data and vary from 400 GV at solar minimum to 1400 GV at solar maximum, as shown in Figure 1.12.

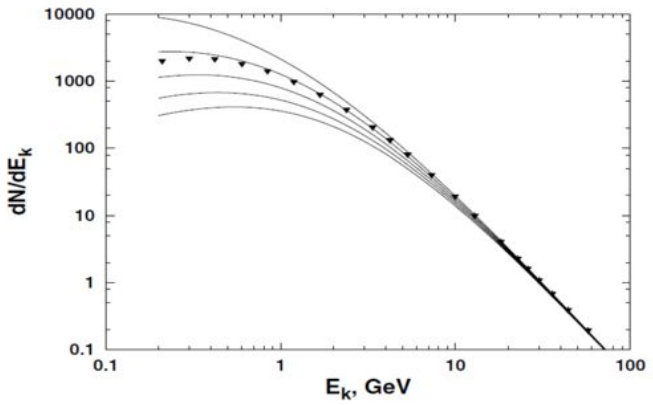

FIGURE 1.12: Comparison of the proton flux measured above 20 GeV with the LEAP experiment with solar modulation using ϕ=200, 400, 600, 800 and 1000 MV

The *Force field approximation* doesn't take into account possible charge-sign dependent effects (that are discussed in section 1.2.1), since the drift is neglected here. This means that it leads to same modulation for positively and negatively charged CR, independently of the solar phase and polarity of the IMF field. This holds when Sun's activity is close to maximum since it is expected that drift plays a minor role in the perturbed IMF field at this phase. When solar cycle is at minimum, where polarity is well defined, it could be expected a different modulation parameter for positively and negatively charged CR since diffusion becomes less important and the propagation might be dominated by the large scale drifts, which do depend on the particle charge.

1.2.2 Geomagnetic Cutoff

After a GCR has crossed the heliosphere or a solar particle reached the Earth orbit, there is another obstacle they have to pass through before the detection around the Earth becomes possible. This is created by the magnetic field of the Earth against the streaming solar wind from the Sun in a very similar way as it happens for the heliosphere in the interstellar wind. The relevant difference is that for HE the pressure against the surrounding ISM medium is given by the kinetic (or ram) pressure of the solar wind (nmV^2), while around the Earth the energy pressure is provided by the magnetic energy density ($B^2/2\mu$) of the Earth magnetic field against the SW ram pressure.

The Earth's magnetic field is generally modelled as composed by two components. One is due to the internal dynamo of the Earth, the other is generated by the complex system of currents circulating around the Earth, made of plasma particles

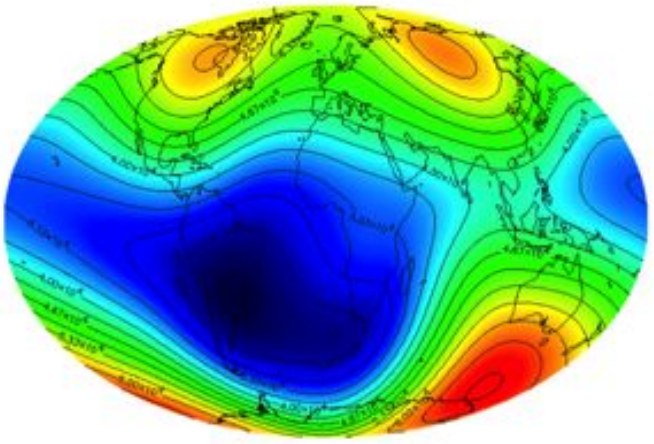

FIGURE 1.13: Map of the internal component of the geomagnetic field at Earth's surface. Units in the map are Gauss.

fed by the SW, as the equatorial ring current and the currents at the polar cusps. The Inner Field is described by a shifted multipole expansion, as written in Eqn. 1.17 and shown in figure 1.13.

$$V = \sum_{n=1}^{\infty} \frac{1}{r^{n+1}} \sum_{m=1}^{n} [g_n^m cos(m\phi) + h_n^m sin(m\phi)] P_n^m (cos\theta) \tag{1.17}$$

where g and h are normalization coefficients, P Legendre functions and θ, ϕ geomagnetic coordinates, n gives the order of the multipole, and m the harmonics order. The International Geomagnetic Reference Field (IGRF) [29] gives a worldwide estimation by using n=15 terms in the multipole expansion. To take into account the secular variations of field (it decreases of $\sim 5\%$/year), the multipole coefficients are updated every five years. The dipole center is located at 320 km, 21.6 N, 144.3 E in GTOD (geographic coord.) The magnetic poles are inverted with respect to geographic ones, dipole axis is tilted of 11.3^o. The IGRF accuracy is $\sim$0.5% close to Earth surface, $\sim$6% at 3 R_E. Typical values of the field near the Earth surface are 0.3 G at equator and 0.7 gauss at poles (a small fridge magnet has 100 G). The *external* field is exposed to the SW and varies according to the heliospheric conditions. It is described by a phenomenological semi-empirical model, such that it reproduces quite accurately ($\sim 20-30\%$ accuracy at few Earth's radii) the observed geomagnetic field as a function of time. A widely accepted model is the Tsyganenko Model [30], that takes into account accurately the effect of the solar wind, as shown in figure 1.14

Since the geomagnetic is not uniform and increases as distance from dipole center decreases, the Larmor radius of an incoming CR gets smaller and smaller or equivalently particle deviation gets larger. This may result in a reflection of the

particle, such that it cannot reach a given position in the magnetosphere. This results in a screening effect for particles having a magnetic rigidity ($R = p/eZ$) below a threshold -called *cutoff rigidity* R_c, which depends on the position in the field and on the arrival direction of the particle. The access from infinity to any position is described by a set directions of approach: at any point we can define a cone dependent on rigidity- which encloses all the trajectories from infinity reaching the point (allowed) and the cone enclosing those not reaching the position (forbidden) for the given rigidity.

The cutoff rigidity or the forbidden/allowed cones can be calculated analytically in a dipolar field [31, 32]. Nevertheless, the geomagnetic field is much more complex than a dipole field (see Figure 1.14) and some allowed trajectories become forbidden because of presence of solid Earth that intercepts them. Thus the transition from allowed to forbidden trajectories and viceversa is not sharp and the rigidity interval is called *Earth penumbra*, The most accurate way to take into account these effects is usually to trace the particle orbit while it moves in the geomagnetic field [33].

In a dipole field approximation, R_c is given by the classical Stormer cut-off. In this approximation, the geomagnetic field is represented as an offset and tilted dipole field with moment $M = 8.1 \cdot 10^{25}\,\mathrm{G\,cm^3}$. R_{cutoff} was analytically evaluated by Støermer [34, 35]:

$$R_{cutoff} = \frac{M\,cos^4\lambda}{d^2[1 + (1 \pm cos^3\lambda cos\phi sin\xi]^2} \tag{1.18}$$

where M is the dipole moment. The arrival direction is defined by ξ and ϕ, respectively the polar angle from local zenith and the azimuthal angle counted clockwise form local magnetic East. The $\pm$ sign applies to negatively/positively charged particles. The arrival location is defined by the geomagnetic coordinates (d, λ), a commonly used coordinate system relative to the dipole axis. d is the distance from

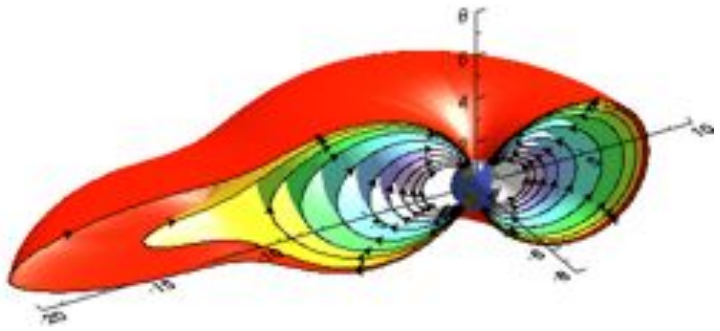

FIGURE 1.14: Semi-empirical model of the Tsyganenko geomagnetic field model, derived from observations on satellites. The Sun is to the right. The units are in Earth radii. (from http://www.ucalgary.ca/above/science/mag_field).

the dipole center, usually expressed in Earth radii units ($d = r/R_{Earth}$), and λ is the latitude along the dipole.

Because of the factor $\pm sin\phi$, a charged particle from ϕ has a lower cut-off with respect to a particle coming from $\phi + \pi$ and a charge Q has a lower cut-off rigidity compared to a charge -Q from the same direction (East-West effect).

For vertically incident particles ($\xi = 0$) the azimuthal dependence of the cut-off simply vanishes, putting in evidence the cutoff behavior as a function of the geomagnetic latitude:

$$R_{cutoff}(\xi = 0) = \frac{M}{4\,d^2}\, cos^4\lambda \tag{1.19}$$

The cut-off is maximum at the geomagnetic equator, with a value of $\sim 15\,\mathrm{GV}$, and vanishes at the poles.

1.3 Experimental measurements of CR $e^{\pm}$

Due to the steep descent in the flux intensity with energy, different experimental techniques are needed to detect CR particles in different portions of their spectra. Direct CR measurements are those where the single CR particle is positively identified and its kinematical properties are measured by means of its interactions in the experimental apparatus. Direct measurements must be performed in space or in the upper layers of the atmosphere to minimize contaminations from secondary particles produced in the interaction of the CRs with the atmosphere. Stratospheric balloons, satellites or the space station are the platforms needed to host the instruments, and this imposes severe constraints on the weight, dimension and electric consumption of the experimental apparatus. Exposure times of several years can be achieved in space, whereas only few months of flight is the current limit for stratospheric balloon operations.
The combination of a limited acceptance and/or reduced exposure time, effectively sets a limit to the achievable energy in direct measurements which depends to the abundance of the species under study and the characteristics of their spectrum. As of today, direct measurements of nuclear components have been performed up to $\sim 10^5$ GeV, the inclusive ($e^+ + e^-$) spectrum has been measured up to 1 TeV, whereas e^- and e^+ separate components have been only recently measured up to 700 e 300 GeV respectively by AMS. The most recent $e^{\pm}$ measurements are reported in figures 1.15, 1.16 and 1.17 and will be discussed later in this section.
At higher energies, detection of the energetic air showers of particles generated by the interactions of the CR with the atmosphere is used to indirectly measure their

properties. Showers characteristics are measured in ground detectors by means of particle counting or revealing the associated emission of fluorescence or Cherenkov light. From the reconstructed shower topology, the energy and the nature of the primary CR particle are inferred from the different characteristics expected for electromagnetic ($e^{\pm}$ or γ) and hadronic (light or heavy nuclei) components of the CR flux. A clear advantage of these techniques is the large acceptance: the particle footprint of the highest energetic showers can be measured over wide area, as in the Auger observatory where particle detectors arrays are arranged on a surface ∼3000 km^2. The use of hybrid techniques, as particle counting in conjunction with detection of the fluorescence light from the excited atmospheric nitrogen, can provide a cross calibration of the energy scale, however, large uncertainties are induced by the accuracy of the models describing showering processes in atmosphere for different particles.
As of today, ground measurement of the inclusive e^++e^- spectrum have been performed by Cherenkov telescopes ([36, 37]) at hundreds of GeV up to 4 TeV, large systematic uncertainties in the hadronic background subtraction and on the energy scale ((O(15-20%)) completely dominate the experimental error. In the following, we will therefore concentrate our discussion on direct $e^{\pm}$ measurements.

The key issues in the $e^{\pm}$ measurements are the low flux intensity and the large background from the nuclear CR components, mainly from protons. A systematic experimental effort in the direct detection of CR $e^{\pm}$ started in the sixties with different experimental strategies, based on the scientific objectives of the specific instrument and the available platforms to host them.
For both balloon and space born experiments, we can broadly identify two categories of experiments based on their capability to distinguish the charge sign of the incoming particles, i.e. magnetic spectrometers or calorimetric experiments. This directly reflects, even if with some noticeable exception, on the capability of performing the study of the inclusive $(e^+ + e^-)$ flux or of the separate components.

1.3.1 $e^+ + e^-$ flux measurement

The main advantage of the calorimetric approach is the possibility to achieve a large acceptance with a relatively compact design. This approach has been then extensively used by experiments aiming to test the global features of the electron spectrum and probe its sensitivity to local astrophysical sources, thus having as a goal the reach of highest energies in their measurement. A large variety of detection techniques have been adopted along the years, making use of combined time of flight, transition radiation detectors and shower counters, emulsion chambers and

calorimeters [38–44]. A review of historical measurements can be found in [45], we should however explicitly mention the recent results from ATIC [46] and Fermi [47] that in the last few years, before the precise measurements from AMS-02, were intriguing the scientific community. The Advanced Thin Ionization Calorimeter (ATIC) is a balloon borne experiments with the broad scientific goal of measuring the composition and energy spectrum of CR up to 100 TeV. A pixelated silicon matrix (SiM) detector measures the charge of the incident particle, followed by three layers of scintillator hodoscopes embedded within a 30-cm-thick graphite target (corresponding to 0.75 nuclear interaction lengths and 1.5 radiation length X_0) and a $18X_0$ radiation length BGO calorimeter. The e/p separation is achieved by the different shower topology and profile in the calorimeter, which insures a good containment of the electromagnetic induced showers. Based on the statistics collected during flights carried in 2000-2003, ATIC reported in fall 2008 the presence of 70 electrons with energies in the range 300-800 GeV, largely in excess with respect to the expected CR electron flux, opening the scientific debate wether this excess could be related to close pulsar emissions or more exotic Dark Matter signals. Within few months, measurement of the inclusive electron spectrum from Fermi was excluding that excess. Fermi is a satellite γ-ray telescope in orbit since 2008: a pair conversion silicon tracker (1.5 X_0) is followed by a CsI calorimeter with 8.6 X_0 depth. Even if much thinner than ATIC in terms of X_0, and thus with a reduced shower containment, Fermi measurements could benefit of an impressive data sample thanks to its wide acceptance and long exposure time which allowed to apply tighter selection cuts for e/p separation. For both experiments, the results were mainly relying on the direct calibration of the detector with beam tests on ground at lower energies, and on a detailed Monte Carlo simulation of the detector response to $e^{\pm}$ and p signals. Indeed, this is one of the experimental limits unavoidable in the purely calorimetric approach. There the accuracy in e/p separation is limited by the accuracy of the modelling in the detector response, without the possibility to verify the Monte Carlo simulation by a simultaneous measurement performed with a different technique. Redundancy in the measurement of particles is insured by the AMS experiment, which we will discuss at length later in this work, which has performed a purely calorimetric measurement of the $e^+ + e^-$ flux up to 1 TeV based however on the e/p discrimination achieved by three independent detectors. The AMS-02 results definitively disconfirmed the ATIC excess, but with a clear systematic difference with respect to Fermi measurement. Recent results of direct $e^+ + e^-$ spectrum measurement are reported in figure 1.15 together with the ground based results from HESS[48, 49].

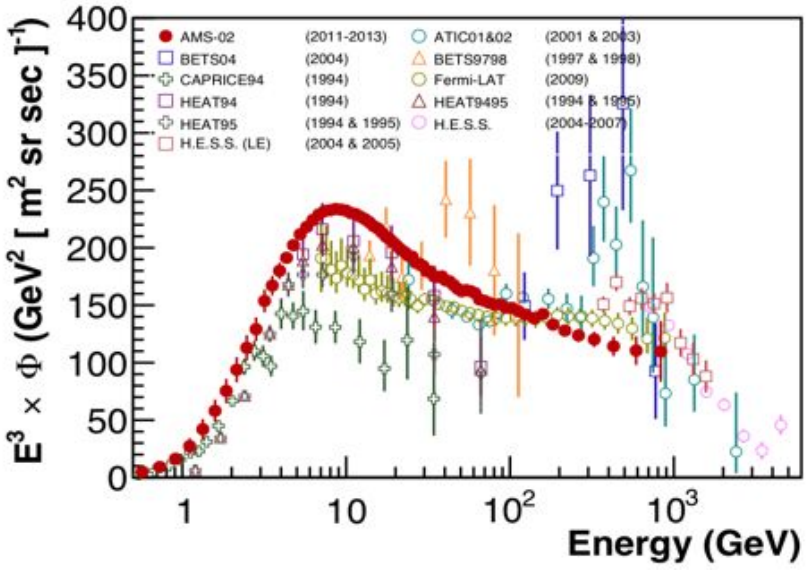

FIGURE 1.15: Recent experimental measurements of the $e^+ + e^-$ flux from balloon [46, 50–57], space [47, 58–62] and ground [48, 49] experiments. The flux is multiplied by E^3 in order to better appreciate features in the spectrum over several decades. At high energies, the differences of previous experimental results with respect to AMS-02 are mostly related to their systematic errors and uncertainties on the energy scale (not shown in figure). Below 30 GeV, a direct comparison should instead take into account solar modulation effects which are related to the period of data taking.

1.3.2 e^-, e^+ measurements

A magnetic field is needed in order to positively separate e^+ and e^- components. The Earth magnetic field induces an asymmetry in the arrival directions of oppositely charged particles (see section 1.2.2) and this was exploited in the pioneering experiments in the '60s [63] and most recently by Fermi experiment [62]. This approach is naturally limited in energy to $\sim 300GeV$ by the geomagnetic field intensity and must rely on the external input of a magnetic field model which takes into account of internal (earth) and external (sun) contributions and is continuously evolving in time.

A magnetic spectrometer is indeed the natural choice to perform such studies and, starting in the early 70's, a series of instruments was launched with stratospheric balloons to address the effective content of CR anti-particle fluxes (e^+ and $\bar{p}$) generated during the primary CR propagation in the galaxy as well as to search for anti-nuclei ($\bar{\text{He}}$) of primordial origin.

The key issue to measure rare particle fluxes up to a given rigidity ($R = p/Ze$) with magnetic spectrometers is related to the conflicting requirements of maximising the detector acceptance, which determines the statistical limit to detection, and the spectrometer resolution, which determines the effective power of separating

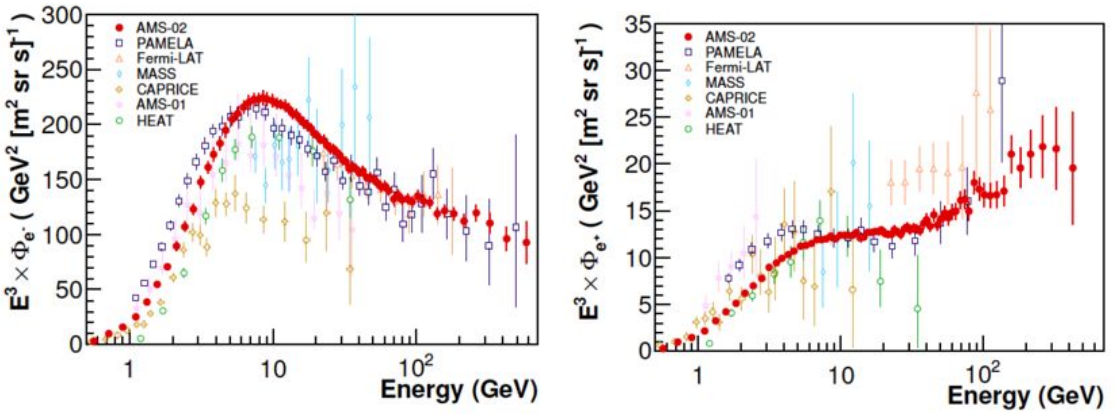

FIGURE 1.16: Recent measurements of the e^- (left) and e^+ flux (right) by balloon [50, 51, 54–57] and space borne experiments [47, 58–62]. The flux is multiplied by E^3 in order to better appreciate features in the spectrum over several decades. The latest results from AMS-02 not only significantly reduce measurement uncertainties, but are also extending towards energies never reached before. The direct comparison of different experimental results below 30 GeV should take into account the different solar modulation effects corresponding to the specific experiments data taking periods.

different charge signed particles of the same species. The bending power of the instrument scales in fact as BL^2, where L is the length of the particle trajectory in the B field of the magnet. Given the limits in size/weight of the apparatus and in the achievable B field value, in a cylindrical geometry[2] the transversal dimension of the apparatus must be reduced with respect to its height in order to maximise the L factor, thus leading to an effective reduction of the angular field of view and of the overall acceptance. Use of superconducting magnets can increase the B values, and this has been extensively exploited in balloon-borne programs [46, 50–57, 64] with different geometries, but the same technology is not viable - as of today - for missions of several years in space. The other way round, space experiments offer two main advantages in anti-particle flux measurements with respect to balloon borne instruments: at least one order of magnitude longer exposure time and no atmospheric background, i.e. particles generated by the interaction of CR in the residual atmosphere which corresponds to ~ 5 gr cm^{-2} of passive material on top of the instrument.

Figure 1.16 reports the e^+, e^- fluxes as measured as a function of energy by the most recent balloon-borne and space experiments. The corresponding positron fraction $e^+/(e^+ + e^-)$ measurements are separately reported in figure 1.17.

Energy reach of balloon borne experiments is limited below 100 GeV with larger uncertainties with respect to space experiments even at the lowest energies. An exception in this concern is the space based AMS-01 result, limited to 30 GeV.

[2] the axis of the cylinder corresponding to the zenith direction of the incoming particle trajectories

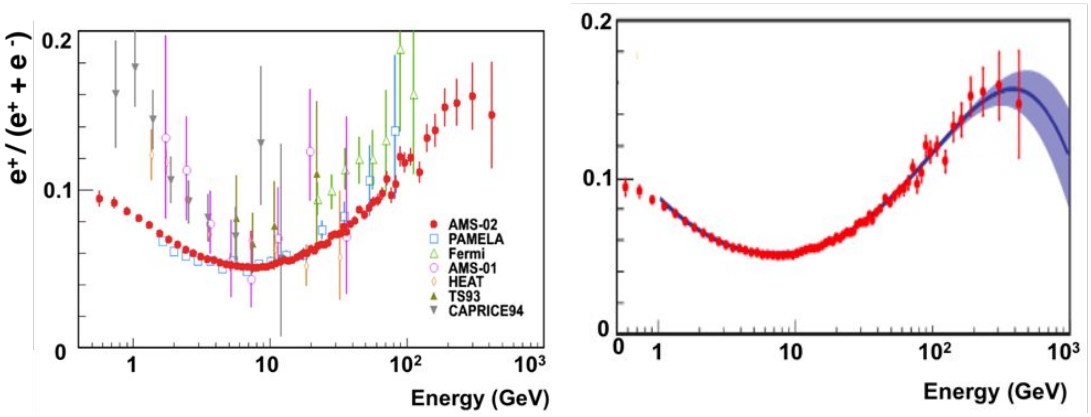

FIGURE 1.17: Left: experimental measurements of the positron fraction by balloon [50, 51, 54–57] and space [59, 61, 62] experiments. The latest measurements provided by the AMS experiment [65] increased the accuracy of the data and reached energy ranges never explored so far. As discussed in the text, the accuracy and extended energy range of the AMS-02 measurement allow an empirical description of the observed positron fraction with a common source of primary e^- and e^+ at high energy. The fitted model and its uncertainty band is superimposed to the AMS-02 data in the right panel.

This result, however, corresponds to a 10 days technical flight on Space Shuttle in 1998 whose main goal was to test for the first time in space the silicon tracking technology, at that time used only in ground based High Energy Physics detectors. This successful flight enabled this technology for space, and it has been then used in Fermi, PAMELA and AMS-02 experiments.

The most noticeable measurements come from the PAMELA and AMS-02 experiments. The Payload for AntiMattEr and Light nuclei Astrophysics (PAMELA) is a multipurpose spectrometer orbiting since 2006 onboard of a Resurs-DK1 Russian satellite. Its spectrometer core, with a geometrical acceptance of $20.5 cm^2 sr$, is made of a permanent magnet ($B = 0.4T$) equipped with six silicon tracker planes for a MDR$\sim$ 1 TV. It is surrounded by different sub-detectors, a time-of-flight, an anti-coincidence system, an electromagnetic calorimeter and a neutron detector, in order to perform a sound e/p discrimination and a measurement of nuclear components up to Z=6. A long debate about a possible excess in the positron CR component with respect to what foreseen from its secondary production was carried before the PAMELA results, based on possible structures of the positron fraction measured by HEAT and AMS-01 experiments. The first publication on this subject from PAMELA, in early 2009, clearly showed a steady increase of the positron fraction [61] and - in conjunction with the ATIC measurement of the anomalous peak in the $e^+ + e^-$ flux - this opened the road to a world-wide effort to account for new e^+ sources contributing to the flux. Measurements from Fermi were confirming the trend shown by PAMELA, even if the dispersion of the FERMI data with respect to the PAMELA and the following AMS-02 measurements clearly shows the limits of the indirect charge measurement technique. The real breakthrough in these

measurements came however with AMS-02 results [65–67]. Thanks to the large acceptance and the high e/p discriminating power, AMS-02 has provided precise measurements in an extended energy range. This allowed to study in detail how the positron fraction increase evolves with energy, giving the first indication that around 275 GeV its attaining to its maximum. The detailed study of the spectral index of e^- and e^+ positron fluxes demonstrated at the same time an hardening of the e^+ spectrum with respect to the e^-, which fully justifies the positron fraction increase in terms of *additional* positrons and not in a lack of e^- in the same energy range.

In fact, as described in figure 1.17, the AMS-02 measurements can be described by a minimal model in which Φ_{e-} and Φ_{e+} are parametrized as the sum of its individual diffuse power law spectrum ($A_{e^\pm}E^{-\gamma_{e^\pm}}$) and a common source term ($C_{CS}E^{-\gamma_{CS}}e^{-E/E_{cutoff}}$) with an exponential cutoff parameter, E_{cutoff} [65, 66]:

$$\begin{aligned}\Phi_{e^-} &= A_{e^-}E^{-\gamma_{e^-}} + C_{CS}E^{-\gamma_{CS}}e^{-E/E_{cutoff}} \\ \Phi_{e^+} &= A_{e^+}E^{-\gamma_{e^+}} + C_{CS}E^{-\gamma_{CS}}e^{-E/E_{cutoff}}\end{aligned} \tag{1.20}$$

Many interesting interpretations have been formulated about the common source of electrons and positrons [68–71]. Among these, two possible models are shown in figure 1.18. In the first, depicted on the left, the excess of positrons comes from pulsar: after a flattening out with energy, the positron fraction will begin to slowly decrease and a dipole anisotropy should be observed. In the second, reported on the rightmost plot, the shape of the positron fraction is due to dark matter collisions: after the flattening out, the fraction will decrease rapidly with energy due to the finite and specific mass of the dark matter particle, and no dipole anisotropy will be observed.

In order to discern between different hypotheses on the origin of the e^+ excess not only new experimental observations of $e^\pm$ at higher energies are needed, but - more in general - a more accurate model of the underlying fluxes of *standard* origin and the influence of the heliosphere on the Local Interstellar Spectrum (LIS). Constraints on the the still poorly known parameters of primary CR propagation in the galaxy can be obtained by the accurate measurements of all secondary CR species; this includes nuclear species as B, Li which are mainly produced in the fragmentation of the most abundant C,N,O nuclei, as well as anti-protons. Connecting the spectrum observed near Earth to the true LIS can be achieved by detailed measurements of the changes in the fluxes as a function of the solar activity, i.e. in time. As discussed beforehand in this chapter (see section 1.2.1) modelling of the heliospheric effects is a complex matter, as of today there are very few direct measurements of CR fluxes to correlate with continuos changing solar activities along the extended period of a

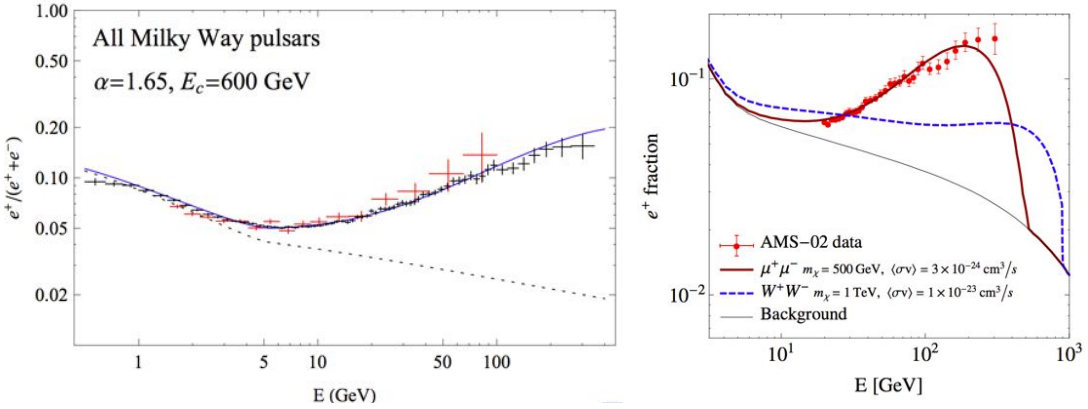

FIGURE 1.18: Left: The predicted cosmic ray positrons fraction (blue line) from the sum of all pulsars throughout the Milky Way, for an injected spectrum of $dN_{e^\pm}/dE_{e^\pm} \propto E_{e^\pm}^{-1.55} exp(-E_{e^\pm}/600\,GeV)$[68]. The dashed line represent the result expected by the standard model of CRs propagation. The black points are the data from AMS-02 [66] and red points from PAMELA [61]. Right: Comparison of the positron fraction measured by AMS-02 [66] to two different dark matter models. [69]

solar cycle. Due to this lack of experimental data, charge dependent effects are often modelled comparing variations of p and e^- fluxes, and never measured directly on the same species. The AMS-02 experiment will allow to simultaneously measure the time dependence of nuclear fluxes as well as $e^\pm$ fluxes over more than 11 years and with % accuracy in reduced time windows. The analysis presented in this thesis is aimed to demonstrate the capability of AMS-02 in this field and provided the time dependence measurement of the $e^\pm$ fluxes over the first 30 months of AMS-02 operation. Results and comparison with existing data will be presented in chapter 5.

Chapter 2

The Alpha Magnetic Spectrometer

The Alpha Magnetic Spectrometer (AMS-02) is a large acceptance ($0.45\,\mathrm{m}^2\,\mathrm{sr}$) instrument installed on the International Space Station (ISS) in May 2011 to conduct a long term observation of cosmic rays in near earth orbit. AMS-02 has been conceived as a multi-purpose detector and its design takes full advantage of the state-of-the art detector technology developed for high energy experiments operating at particle accelerators. The AMS proposal dates back to 1994 [72] introducing for the first time the use of a large area tracker based on silicon micro-strip detectors in space. A ten days precursor flight of the AMS-01 apparatus was carried on board of the space shuttle in June 1998 to validate its innovative design: the successful end of that mission, which also produced relevant physics results [73], effectively started the AMS-02 detector design.
In this chapter a general overview of the AMS-02 instrument and its operation in space will be presented. A brief introduction to the AMS-02 apparatus and the scientific objectives of its mission starts our discussion that will continue with a description of its different detectors, that allow a clear separation of different CR species by means of redundant measurements of their charge, energy and velocity. Design of electronics, trigger and data acquisition system will be then discussed. Operation in space is a daily challenge: an overview of the AMS-02 operation on ISS will conclude our brief journey in AMS-02.

2.1 AMS-02 detector

AMS-02 has been conceived to address open questions in fundamental physics and astrophysics by means of accurate measurements of cosmic rays.

The apparent absence of anti-matter in the Universe is still a mystery which questions the foundations of elementary particle physics and our current understanding of the origin and evolution of the cosmos. From cosmological data, we know that primordial antimatter is subdominant to matter in the Universe by about one part in a billion, however this experimental evidence requires bariogenesis models with baryon non-conservation and large levels of CP-violation not supported by particle physics experimental data. Theories which predict the existence of anti-matter in segregated domains have not found any experimental support as well. The detection of even a single anti-nucleus in the cosmic radiation, such a nucleus of $\overline{\mathrm{He}}$ or $\overline{\mathrm{C}}$, could be a direct proof of the existence of antimatter domains, since the probability of their generation via spallation processes in the interstellar medium is very low [74] due to their high mass. Searches for nuclear anti-matter has been carried by now since more than 30 years with increasing sensitivity in continuously extending energy ranges, with no positive detection [75] . The large amount of CR particles that AMS will be able to collect during its mission (as of today more than 70 billion particles) will allow to search for anti-nuclei with unprecedented sensitivity.

Another primary discovery potential for AMS concerns the *indirect dark matter detection*. Precision cosmological observation in the last decades have shown that only a small fraction of the energy density of the universe, around $\sim 5\%$, is made of baryonic matter. Structure formation requires $\sim 26\%$ of the energy to be in an unknown form of matter, the so-called *Dark Matter*. The dominant component of the energy density, generically referred as *Dark Energy*, brings the total close to the critical density and is responsible for the recent phase of accelerated expansion. Dark matter could be detected in CR through its annihilation into standard particles and γ resulting in deviations or structures to be seen in the cosmic ray spectra. Due to the low intensity of fluxes coming from DM annihilation, detection of an excess can be possible only in the rarest CR components, i.e. anti-protons, positrons or anti-deuteron (never observed so far) which are not routinely produced at astrophysical sources. As already discussed in Sec.1.3, an unexpected rise has been already observed in the positron component: AMS has the potential to shed light on the origin of these observed features by extending the e^+ measurements to higher energy while performing a simultaneous study of the anti-proton component.

Accurate knowledge of *all the charged species of the cosmic rays*, including chemical species up to Iron and isotopes up to Carbon, is needed to address open questions in the origin and propagation of CR in our galaxy. The AMS-02 measurements of P and He spectra [76, 77] have already shown a gradual change of their spectral indexes above $\sim$ 200 GeV which questions the current understanding of the underlying

processes at their origin. The measurement of the nuclear and isotopic composition of cosmic rays can be used to improve the models for particle propagation in the ISM, e.g. the accurate determination of the Boron to Carbon ratio over a wide range of energies is crucial to determine propagation parameters like the thickness of the galactic halo or the galactic wind velocity [78]. This will improve our knowledge of the Interstellar Medium (ISM) in which cosmic rays propagate and will allow to firmly assess the expected fluxes of light anti-particles.

The understanding of the origin and propagation of cosmic rays requires knowledge of the cosmic ray energy spectra in the ISM, i.e. uninfluenced by the Sun's magnetic field. The measurements of low energy CR fluxes during an entire solar cycle will help in the understanding of solar physics and the dynamics of CR in the Heliosphere. Thanks to its long duration mission, AMS will be able to perform a precise measurements of low energy CR fluxes (few hundred MeVs to tens of GeVs) along a whole solar cycle ($\sim$11 years) providing a precious input not only on the absolute flux intensity but also on charge dependent effects as needed to tune current models of CR propagation in the heliosphere.

To fulfill its ambitious scientific objectives, AMS-02 has been conceived as a particle physics experiment, with a high degree of redundancy in measuring the characteristics of the incident particles, satisfying at the same time the stringent requirements in reliability that are needed to survive to the hostile environment in space.

Figure 2.1 shows a schematic view of AMS-02: the core of the instrument is the magnetic spectrometer composed of a permanent magnet, which produces a magnetic field with an intensity of 0.15 T, and of 9 layers of double-sided silicon micro-strip sensors. The task of the spectrometer is the reconstruction of the particle trajectory and the measurement of its rigidity ($R = P/eZ$, momentum/charge ratio).
Above and below the spectrometer two planes of time of flight counters (ToF) provide the main trigger of AMS-02 and distinguish between up-going and down-going particles. This information, combined with the trajectory curvature given by the spectrometer, is used to reconstruct the sign of the charge. A Transition Radiation Detector (TRD) is located at the top of the instrument. The detector ends with a Ring Imaging Cherenkov detector (RICH) and an electromagnetic calorimeter (ECAL).The central part of AMS-02 is surrounded by an anti-coincidence system (ACC) that provides the veto signal in the trigger for the particles detected outside the field of view of the instrument.

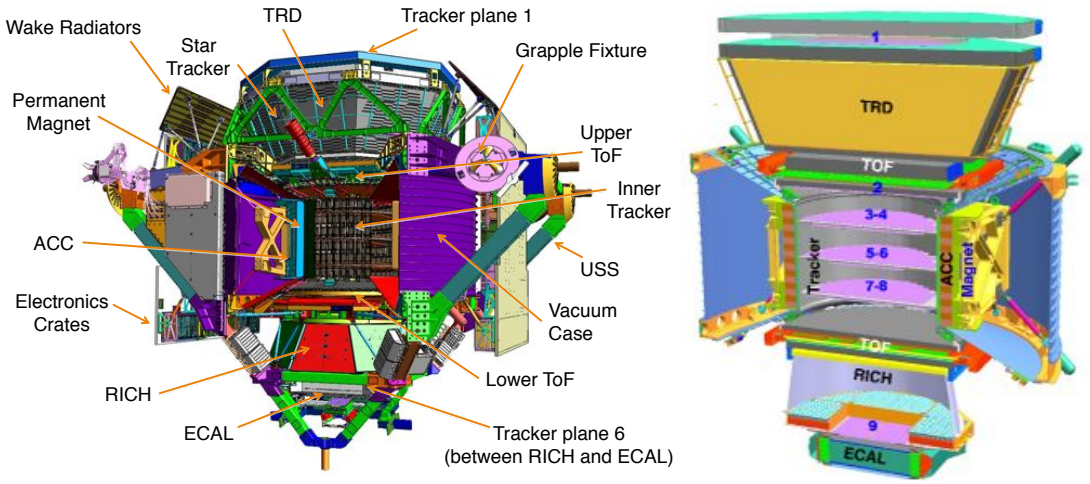

FIGURE 2.1: Two schematic views of AMS. The various detectors are labelled.

2.1.1 The Permanent Magnet

Figure 2.2 shows a picture of the magnet. It is composed by 64 sectors arranged in a cylindrical shape with inner radius of 115 cm, outer radius of 129.9 cm and a height of 80 cm. Each sector is assembled from 100 high grade Nd–Fe–B blocks glued together with epoxy. This arrangement results in a dipole magnetic field of 0.15 T in the magnet center, with a negligible dipole moment outside the magnet case ($\sim 10^{-2}$ T). The permanent magnet also defines the natural reference frame for AMS with its origin at the center of the magnet, as can be observed in figure 2.3. The Z axis runs along the cylinder's axis of symmetry, with positive values in the direction of the top of the instrument. The X axis is aligned to the magnetic field lines while the Y coordinate describes the bending direction. With this choice of reference system, the bent trajectories of all charged particles traversing the magnet are contained in the Y–Z plane.

2.1.2 The Silicon Tracker

The Silicon Tracker is made of 2264 double-sided micro-strip silicon sensors distributed over 9 layers [79, 80] disposed on 6 planes for a total active area of $\sim 6.4\,\mathrm{m}^2$. As shown in figure 2.4, 3 of the 9 layers are located outside the magnetic field of the permanent magnet: layer 1 is located on top of the TRD,layer 2 above the magnet, and layer 9 between the RICH and the ECAL. The others 6 layers constitute the inner Tracker which is contained in the permanent magnet field volume.

Each plane located inside (outside) has a composite structure with two 220

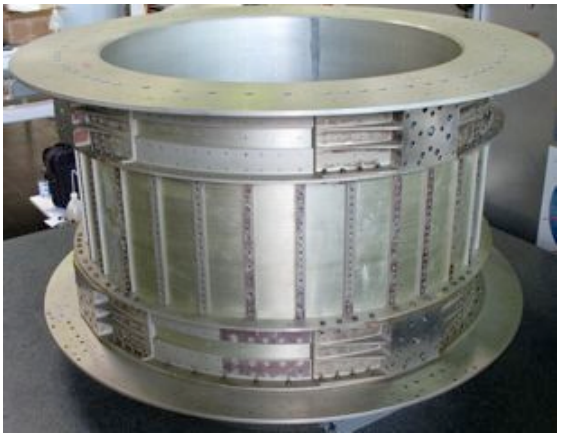

FIGURE 2.2: AMS permanent magnet, already employed for AMS-01 experiment on board of Space Shuttle Discovery [73].

(700) μm thick layers of Carbon fiber surrounding a 12 (40) mm thick, low density Aluminum honeycomb interior of density $\rho = 16.02$ (32.0) Kg/m^3. The diameter of the interior (exterior) planes is 1.0 (1.4) m (upper photos of Figure 2.5). A Carbon fiber cylindrical shell, supporting planes 3 to 5 located inside the magnet, and two Carbon fiber flanges, supporting the exterior layers 1, 2 and 9 provide a high precision Silicon sensor positioning and the mandatory structure resistance for vibrations due to the Shuttle launch (lower photo of Figure 2.5). Layers 1-8 have a diameter of ~ 1 m and contain approximately 24 read-out units, the *ladders*. Layer 9 is the smallest one and is constituted only by 16 ladders. Each ladder is composed by a variable number of double–sided silicon sensors (from 7 to 15) grouped along the x direction and coupled to a read out chain characterized by a low power consumption (~ 0.7 mW per channel), a low noise and a large dynamic range. The basic Tracker element, the double-sided Silicon sensor, has dimensions of $\sim 72.045 \times 41.360 \times 0.300$ mm^3. Biasing of n-type high resistivity 300 μm thick Si

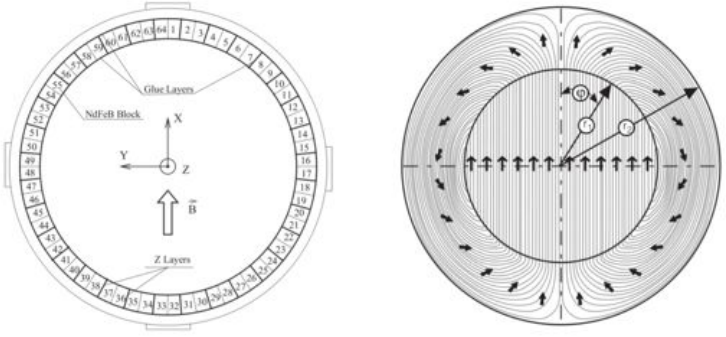

FIGURE 2.3: Left: AMS magnet configuration. 64 Nd-Fe-B blocks are distributed in the toroidal structure to provide a uniform dipole field in the magnet inner volume. Superimposed in the picture is the AMS coordinate reference frame. Right: Magnetization vector. Its flux is confined in the magnet volume, providing a negligible leaking field.

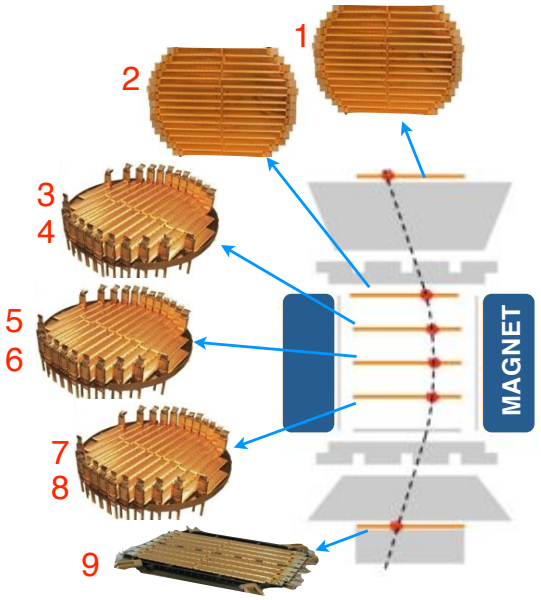

FIGURE 2.4: Layout of the 9 Silicon Tracker layers: Layer 1, 2 and 3 are located outside the magnetic field. The others 6 layers constitute the inner Tracker which is contained inside the permanent magnet field volume.

sensors is made with a dynamic resistive coupling, as punch-through and surface-through techniques. On the two surfaces p^+ strips with an implantation (readout) pitch of 27.5 (110) μm and n^+ strips, along the orthogonal direction, with implantation (readout) pitch of 104 (208) μm are placed. The finer pitch p-side strips is used to measure the bending, or y, coordinate while the orthogonal n-side strips measure x. When a ionizing particle crosses a silicon detector electron/hole pairs ($\sim 10^4$) are produced. Charges are rapidly drifted ($\tau \sim 10$ ns) by the sensor electric field, generated by the inverse bias regime, toward the segmented electrode strips. The measured signal is proportional to the energy deposit and identifies the coordinate of the traversing particle. The AMS-02 Tracker is able to detect the crossing points of particles with high accuracy ($\sim 10\,\mu$m in the bending direction and $\sim 30\,\mu$m along the non-bending one). The crossing points provide the information to reconstruct the particle trajectory and to measure its curvature and, therefore, the particle rigidity. The AMS-02 Tracker has a Maximum Detectable Rigidity, MDR[1], of $\sim$2 TeV for single charged particles as presented in figure 2.6 reporting the rigidity resolution for proton particles estimated with a Monte Carlo simulation of the full detector and validated with beam test (red point in the figure) before launch. Rigidity measurement allows AMS to measure the momentum of all the non-electromagnetic particles, such as protons and nuclei, up to TeV energies. Together with the information about the direction of the particle provided by the

[1]The Maximum Detectable Rigidity is the maximum value of Rigidity that can be measured by a Tracker before that the error on the rigidity itself becomes 100%.

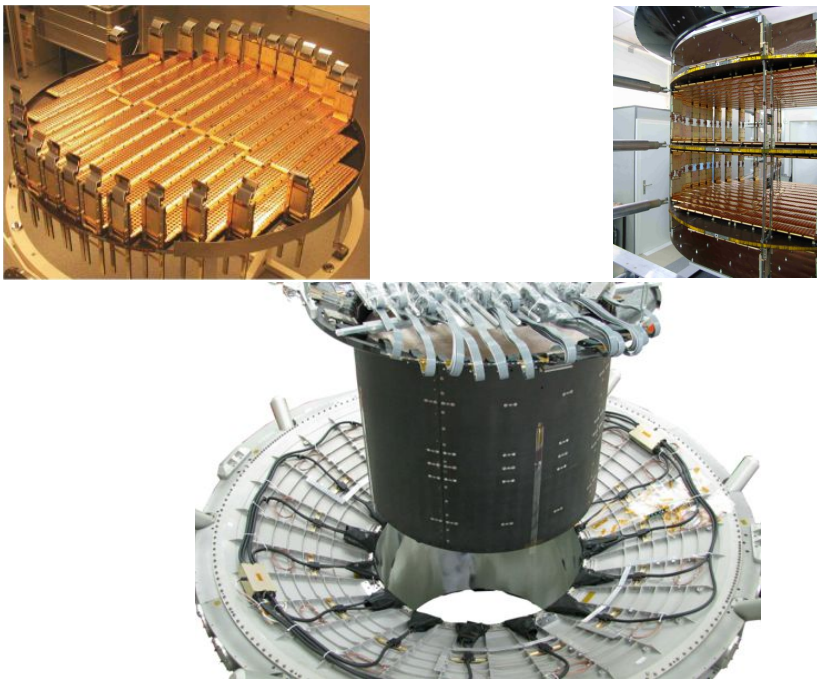

FIGURE 2.5: Some of the steps of the Tracker integration. Top left: an assembled layer. Top right: the assembling of the inner Tracker layers with the 6 layers arranged on 3 supporting planes. Bottom: the pre-integration of the Silicon Tracker in the AMS vacuum case

ToF (down-going or up-going particle) the Tracker is able to measure the sign of the charge of cosmic ray. The Tracker system is completed by two sub-systems: the Tracker Thermal Control System (TTCS), a two phase (liquid, gas) CO_2 heat exchanging system that chills the Tracker electronics minimizing the heat conduction toward the cryogenic magnet [81]; and the Tracker laser Alignment System (TAS) that provides optically generated signals in the Inner Tracker layers that mimic straight (infinite rigidity) tracks and that allows therefore to monitor tracker geometry with a position accuracy better than $5\,\mu$m. The Silicon Tracker performances in terms of calibration stability, spatial resolution and charge discrimination have been studied with several beam using electron, photon, proton and ion beam lines.

2.1.3 Time of Flight (ToF)

The AMS-02 Time of Flight (ToF) system measures the particle velocity ($\beta = v/c$), flight direction and charge, and provides the main trigger to the whole experiment (see section 2.1.9). It is composed by 4 planes of scintillation counters 2 above (*upper ToF*)and 2 below (*lower ToF*) the magnet (Figures 2.1 and 2.7). The four planes contain, from top to bottom, 8, 8, 10 and 8 scintillator paddles. The fibers

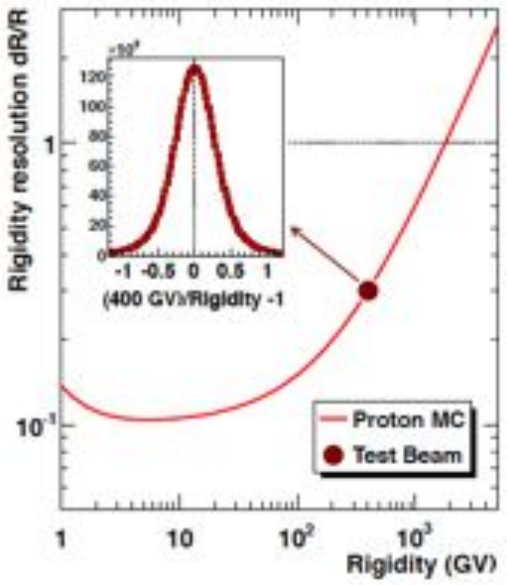

FIGURE 2.6: Rigidity resolution as estimated by Monte Carlo protons. The MDR is ∼2 TeV. The result from 450 GeV Test Beam protons is superimposed (full red circle) validating the simulation.

of upper ToF and the lower ToF planes runs alternatively along the x and y coordinates providing a granularity of $12\times12\,\mathrm{cm}^2$ cells. The ToF single counter consists of 1 cm thick polyvinyltoluene scintillator of trapezoidal (18.5–26.9×117–$134\,\mathrm{cm}^2$) or rectangular (12×117–$134\,\mathrm{cm}^2$) shape, at both ends coupled, via plexiglass light guides, to 4 (rectangular) or 6 (trapezoidal) photo-multipliers (PMTs). A particular class of PMTs, the fine mesh, with a compact dynodes structure and high operating voltage (∼1600 V) has been selected in order to reduce the dependence of the photo-induced multiplication by the stray magnetic field. Tilted and bent light guides have been used to optimized the angle between PMT along the y-axis and

FIGURE 2.7: The upper and lower ToF assembled before the final shielding. The scintillator paddles, the bent light guides and the PMT are exposed.

the magnetic field [82]. The particle velocity $\beta = \frac{\Delta l}{c\Delta t}$ is measured using the time of flight Δt between Upper-Tof and Lower-Tof and the trajectory length Δs. The time measurements resolution on the ToF is ∼160 ps for protons and ∼100 ps for particles with Z⩾2. The resulting resolution on velocity β is $\sigma/\beta \sim 3\%$ for protons and $\sigma_\beta/\beta \sim 1\%$ for ions. The energy deposition in a single ToF counter is also used to measure the particle charge exploiting the proportionality between the the energy loss by ionization and the charge ($\frac{dE}{dx} \propto Z^2$).

2.1.4 Anti-Coincidence Counter (ACC)

The highest analyzing power is reached for particles traversing the detector from top to bottom, with redundant measurements of the particle properties along the trajectory. For this reason is important to identify and reject the particles entering the detector sideways. Such particles do not contribute to valuable information and can cause spurious triggers by interacting with the detector material. This is illustrated in figure 2.8 where the type of events accepted and rejected based on the ACC information are shown. The ACC is made by 16 scintillating paddles arranged on a cylinder that surrounds the permanent magnet (Figure 2.9). The light coming from the scintillation panels is collected in wavelength shifter fibers of 1 mm diameter, embedded in grooves milled into the scintillation panels. At

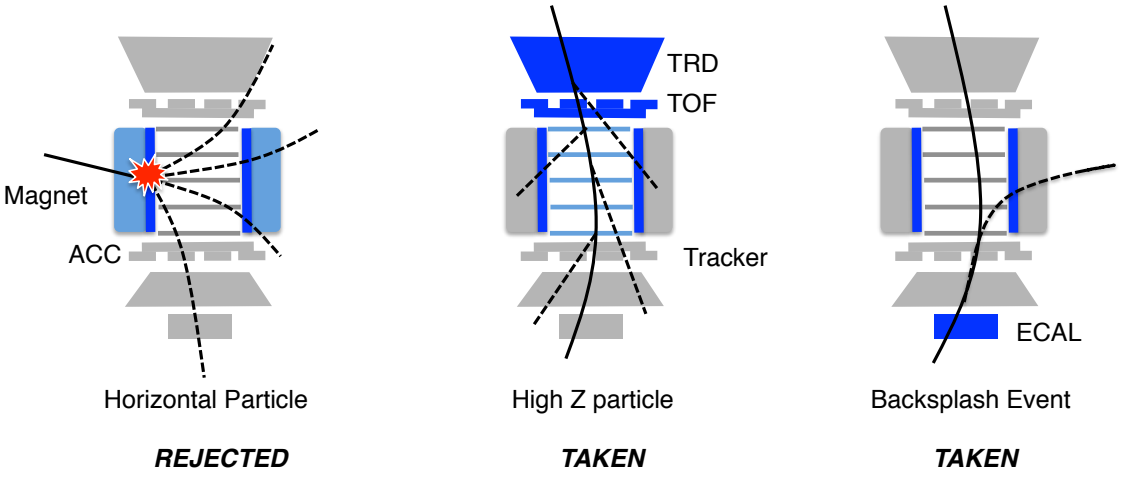

FIGURE 2.8: *Left*: A particle entering the detector sideways may give a signal on ACC and not in ToF. This kind of events are rejected. *Center*: an incoming ion (high-Z particles): when an ion traverse matter it is accompanied by electron production, the so called δ–rays. These electrons can easily fire the ACC. In order to keep ion events the ACC veto is disabled. *Right*: an electron/positron converting on the ECAL: when an electon/positron passes through the ECAL backsplash particles are produced (rightmost case in the figure). These particles may exit from the calorimeter surface and hit the ACC. In this case the trigger condition should be ToF and not more than 4 ACC paddles fired.

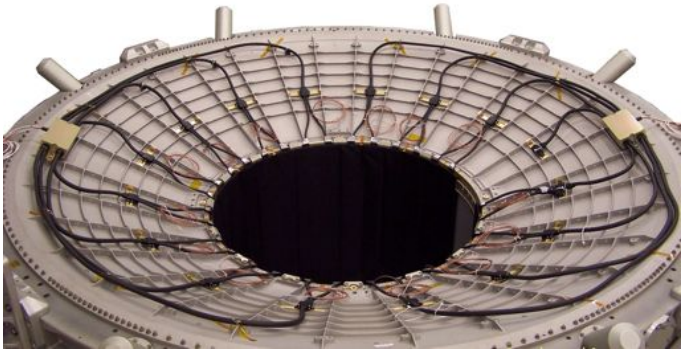

FIGURE 2.9: The ACC system mounted inside the vacuum tank. The signals from the 16 scintillation paddles, arranged on the inner cylinder of the vacuum case, are guided and coupled by wavelength shifter fibers to 8 PMTs on the border of the toroidal structure. A similar fiber/PMT readout scheme is repeated on the other side of the vacuum case in order to provide redundancy of the veto system.

both ends of the counters, the fibers are routed in 2 bunches of 37 fibers each to transition connectors located on the conical flanges of the magnet vacuum case. From these connectors the light is routed through clear fibers up to the 8 PMTs mounted on the rim of the vacuum case. The ACC PMTs, similar to the ToF ones, are placed approximately 40 cm from the racetrack coils and are oriented with their axes parallel to the stray field. The very high efficiency and the high degree of homogeneity of the scintillating fibers will ensure a reliable and fast ACC veto trigger signal (see section 2.1.9) for the high inclination particles [83].

2.1.5 Transition Radiation Detector (TRD)

The Transition Radiation Detector (TRD) is placed on top of AMS-02, just below the Tracker plane 1 and above the upper ToF. The main purpose of the TRD is to identify electrons and positrons among the overwhelming flux of protons and nuclei traversing the detector. The identification principle is based on the electromagnetic transition radiation (TR) emitted when a charged particle traverses the boundary between two media with different dielectric constants, as the result of the particle's field reformation. The AMS-02 TRD (Figure 2.10), is made by 328 modules. The modules are arranged in 20 layers supported by a conical octagon made of aluminum-honeycomb walls with carbon-fiber skins and bulkheads. To provide 3D tracking capabilities, the lower and upper four layers are oriented parallel to the AMS-02 magnetic field while the middle 12 layers run perpendicular.
Each modules contains:

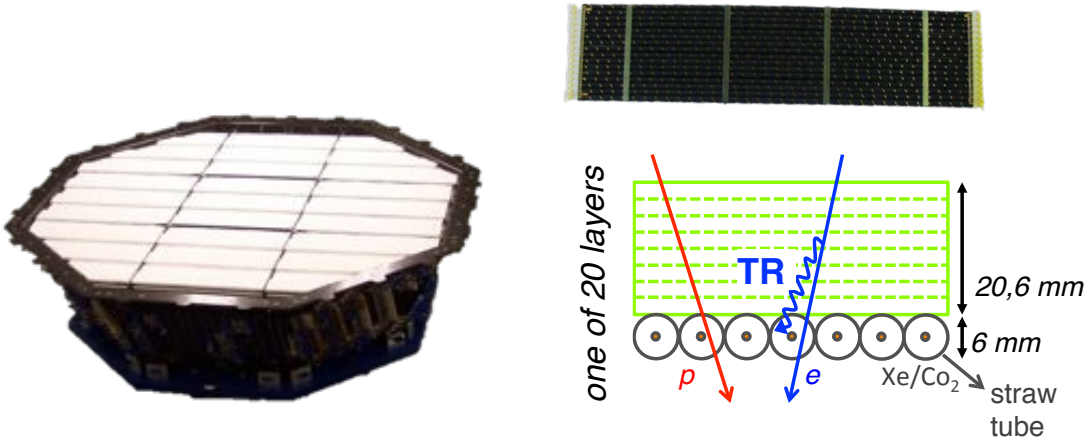

FIGURE 2.10: *Left*: The truncated octagonal pyramid AMS-02 TRD. *Right*: one of the 328 modules (top) and the principle of measurement of one TRD layer (bottom): the TR X-rays produced by electrons in the fleece are efficiently absorbed in the straw tubes, producing a signal significantly larger with respect to the only ionization of protons.

- 22 mm thick polypropylene/polyethylene fiber fleece radiators, corresponding to a density of 0.06 g/cm^3. A large number of interfaces increases the probability of TR X-rays production (up to 50% for 5 GeV electrons);
- 6 mm straw tubes filled with a Xe:CO_2 (90%:10%) gas mixture operating in full–avalanche mode (1500 V). The wall of the straw tubes, made of 72 mm thick double–layered kapton–aluminum foil, works as cathode. A 30 m thick fine gold plated wire in the center of the tube works as anode for the proportional chamber.

Highly relativistic particles crossing the TRD may produce TR X-rays in the radiators. Such photons are efficiently absorbed and detected in the proportional chambers using Xe as absorber. The CO_2 works as quencher for charge multiplication. The combined measurement of the energy deposit in the 20 layers allows the TRD to discriminate $e^{\pm}$ from hadrons up to 1 TV making it a fundamental tool for $e^{\pm}$ analyses. The electron/proton separation capabilities of the TRD are summarized in figure 2.11. The energy deposit in each tube is read out and digitalized by a 12-bit ADC converter. The dynamic range of the read out has been set to resolve the low energy deposits for ionizing protons and to consequently maximize the electron/proton separation. The measurement of the direct ionization from nuclei $dE/dx \propto Z^2$ is used to infer the charge of the crossing particle up to carbon (Z = 6). Above this charge, the ADC saturates. Nevertheless, techniques based on γ–rays detection can be used to extend the identification up to iron (Z=26) [84]. In

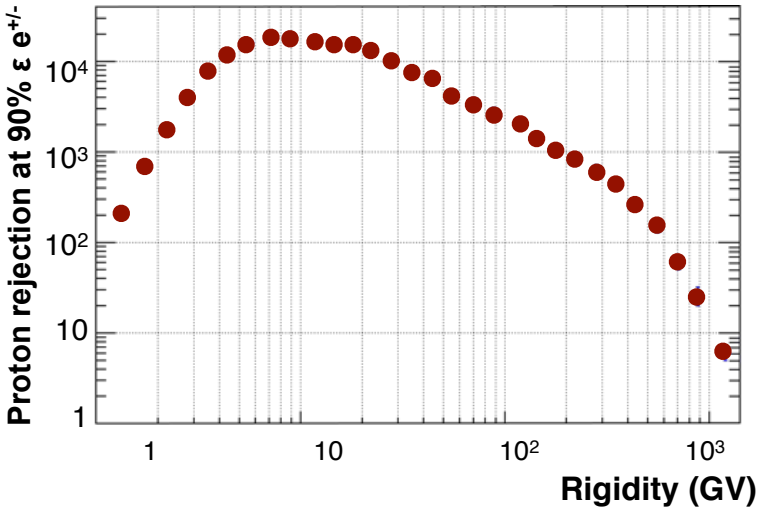

FIGURE 2.11: Electron/proton (e/p) rejection measured with data collected by AMS. The e/p separation is achieved by combining the measurements of the energy deposit in the 20 layers of the TRD detector. The efficiency of the selection on e is 90%. The proton rejection is well above 10^3 up to 200 GV. At 400 GV, protons start to produce transition radiation and the TRD rejection capabilities drastically decrease.

the vacuum of space, gas continuously diffuses out of the straw tubes. Since CO^2 molecules are smaller than Xe molecules, they are the component leaking the most, with a total measured average leak rate of 4.5 mbar/day. In order to operate the detector at stable parameters, the TRD is coupled to a gas supplier system (see Figure 2.12).

At the time of the launch, the TRD gas system was equipped with 49 Kg Xe and 5 Kg CO_2. It is composed of the two supply boxes, a mixing vessel and a circulation box. This latter is responsible to transfer the freshly mixed gas to the gas network system with the help of a pump. The complete proportional chamber gas volume amounts to 230 L. The TRD modules are connected in series in groups of 8 to form a gas circuit. The gas is circulated in a total of 41 gas circuits. After the first commissioning phase, monthly gas refills have been regularly performed since the start of the data acquisition in order to maintain an optimal gas composition for the detector performances. Moreover, daily HV adjustment are applied to correct the straw tubes gas gain change due to the continuously changing gas composition [85].

2.1.6 Ring Imaging Detector (RICH)

The AMS-02 Ring Imaging Cherenkov detector (RICH) is placed below the lower ToF plane and provides a very precise measurements of β. The detection principle

is based on the Cherenkov electromagnetic emission produced by a charged particle with velocity larger than the phase velocity of the electromagnetic field in the material. A cone of emission is created along the particle trajectory. The opening angle of this cone is related to the particle velocity through $\beta = \frac{1}{n \cdot cos\theta}$ where n is the refraction index. Moreover, for a particle of charge Ze, the number of radiated photons per frequency unit and length unit is given by $d^2N/(d\omega dx) = \alpha Z^2 sin^2\theta$. The RICH therefore also provides an independent measurement of the particle charge. The RICH detector consists of a radiator plane, a conical mirror and a photon detection plane. The radiator is composed by a dodecahedral polygon with a 118.5 cm internal tangent diameter. It consists of an array of 2.7 cm thick aerogel tiles with a refractive index between 1.03–1.05, which surrounds a central $35 \times 35\,cm^2$ region equipped with 5 mm thick sodium fluoride (NaF) radiator (nNaF = 1.335). This radiators combination optimizes the overall counter acceptance ($0.4\,m^2sr$) since the Cherenkov photons radiated by the NaF in large cones will fall within the detection area. In fact the detector plane has an empty $64 \times 64\,cm^2$ area in its center, matching the active area of the electromagnetic calorimeter located below. Outside the "ECAL hole", 680 4×4-multi-anode PMTs are arranged to cover the circular 134 cm diameter surface at the basis of the conical mirror. The radiator and the detection plane are enclosed in the volume of a conical reflector multi-layer structure on a Carbon fiber reinforced composite substrate of height 47 cm. The mirror increases the RICH acceptance reflecting high inclination photons and provides the necessary photon drift ring expansion (Figure 2.13). RICH provides the β measurement with

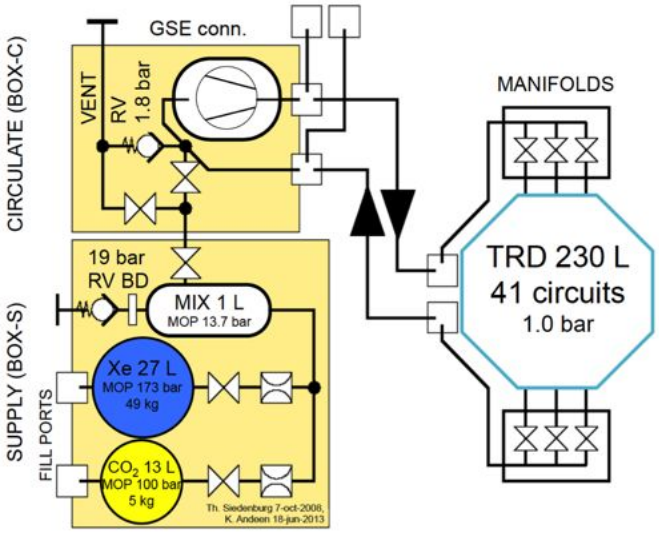

FIGURE 2.12: TRD gas system schematic. The gas in the supply boxes is first mixed (BOX-S). A pump (BOX-C) helps the circulation of the gas through 41 gas circuits, feeding the whole TRD detection volume. Each gas circuit connects 8 TRD modules in series. Ten separate manifolds with a shut-off valve control a variable number of gas circuits. Single gas groups can be isolated in case of a gas leak in a tube [85].

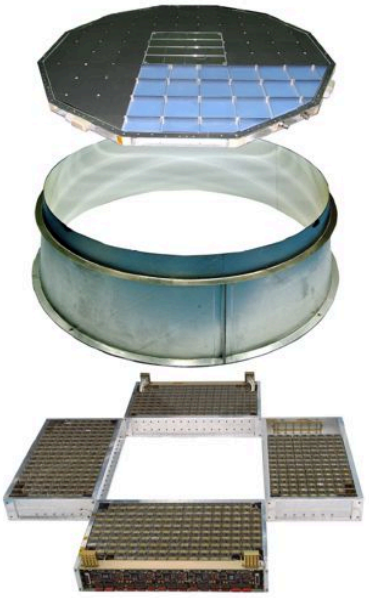

FIGURE 2.13: Exploded view of the RICH detector. It is composed by three parts: the radiators layer, the conical mirror and the detection plane (the angular sectors of the detection plane are not shown).

a resolution $\sigma_\beta/\beta \sim 0.1\%$ for unitary charge particles, and $\sigma_\beta/\beta \sim 0.01\%$ for ions. It also provides a particle charge measurement with a charge confusion of the order of 10 %.

2.1.7 Electromagnetic Calorimeter ECAL

The AMS ECAL is a lead-scintillating fiber sampling calorimeter [86]. Particles crossing the active volume release their energy and produce light collected by PMTs at the fiber end. The detector concept [87, 88] has been developed to maximize the X_0/λ ratio (X_0 is the electromagnetic interaction length and λ the nuclear interaction length). It consists in a lead-fiber-glue volume ratio of 1:0.57:0.15, an average density of $\sim 6.8\,\mathrm{g/cm^3}$ and a radiation length X_0 of about 1 cm. The total ECAL length corresponds to $\sim 17\,X_0$ and to $\sim 0.6\lambda$. The active volume (*pancake*) is built up by a pile of 9 *superlayers* (SL) consisting of 11 grooved 1 mm lead foils interleaved by 1 mm plastic scintillating fibers. The fibers are glued by means of optical cement and they run alternatively, in each superlayer, in one direction only (Figure 2.14).

Each SL is designed as a square parallelepiped with 68.5 cm side and 1.85 cm height, for a total active dimension of $68.5\times68.5\times16.7\,\mathrm{cm^3}$. The pancake has a weight of 496 Kg, for a total weight of the calorimeter of 638 Kg (including mechanical structures and readout cables). Each SL is read out on one end only by 36

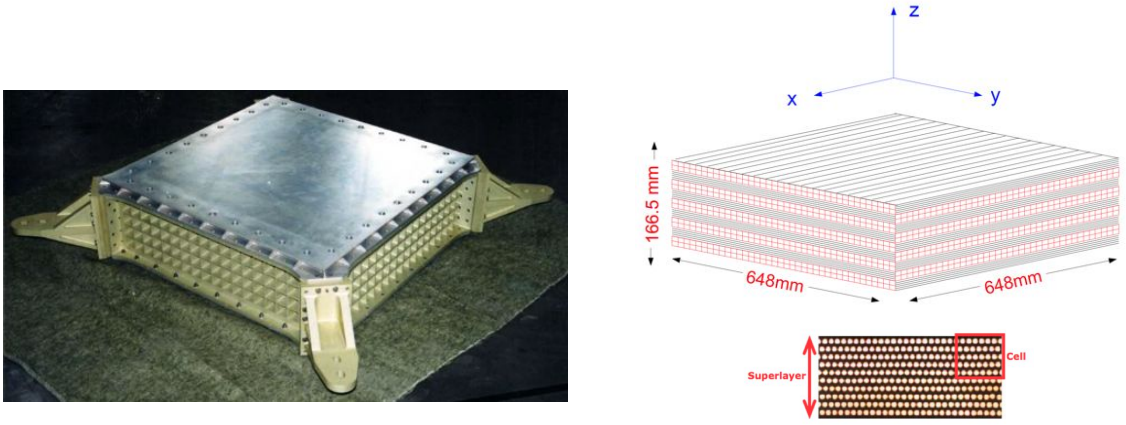

FIGURE 2.14: A picture of ECAL before the installation of PMTs (left). The scintillating fibers and lead foils structure of the 9 assembled super-layers (top right). Picture of one cell on a superlayers (bottom right.

PMTs, alternately arranged on the two opposite sides to avoid mechanical interference. The PMTs are shielded from magnetic field by a 1 mm thick soft iron square parallelepiped tube, which also acts as mechanical support for the light collection system. Each PMT accommodates four $8.9\times8.9\,\mathrm{mm}^2$ anodes. The anodes define the ECAL granularity, for a total of 1296 readout cells. The 3D imaging of shower development is achieved by alternating 5 SLs with fibers along the x axis and 4 SLs with fibers along the y axis. The ECAL Moliére radius, measured to be $\sim 2\,\mathrm{cm}$, corresponds approximately to 1 PMT width. In order to obtain the necessary sensitivity on minimum ionizing particles ($\sim$7 MeV/cell) and to measure energies up to 1 TeV ($\sim$60 GeV/cell) using standard 12-bit ADCs, the digitization is performed by the front-end readout system at two different gains, with a gain ratio of about 33. Besides the eight signal from anodes, each PMT's last dynode signal is also read out to build up the ECAL trigger (see Section 2.1.9). The ECAL PMT response is equalized by setting the PMT HV to minimize the spread gain. The residual differences are equalized for each anode using the response of each cell to minimum ionizing particles (MIP) in flight [89]. Electrons, positrons and photons reaching ECAL start an electromagnetic shower. The mean longitudinal profile of the energy deposit by an electromagnetic shower is usually described by a gamma distribution [90]:

$$\langle \frac{1}{E}\frac{dE(t)}{dt} \rangle = \frac{(\beta t)^{\alpha-1} e^{-\beta t}}{\Gamma(\alpha)} \tag{2.1}$$

where $t = x/X_0$ is the shower depth in units of radiation length, $\beta \sim 0.5$ is the scaling parameter and α the shape parameter. The total thickness of the ECAL ($\sim 17\,X_0$) allows the containment of 75% of the shower energy deposit for 1 TeV

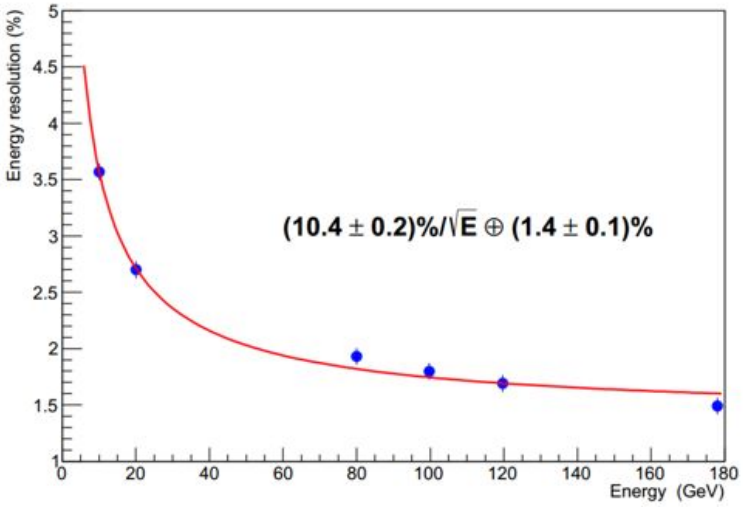

FIGURE 2.15: ECAL energy resolution measured using e^- test beams for perpendicularly incident particles [91].

$e^{\pm}$. The energy of the incoming particle is measured applying corrections for the rear and lateral energy leakages, and for the anode inefficiency, to the deposited energy. These corrections ensure the energy linearity to better than 1% up to 300 GeV. The calorimeter energy resolution $\sigma(E)/E$ has been measured during the test beams [91] (see Figure 2.15) to be:

$$\frac{\sigma(E)}{E} = \frac{10.4 \pm 0.2}{\sqrt{E(GeV)}}\% \oplus (1.4 \pm 0.1)\% \tag{2.2}$$

The fine ECAL 3D readout granularity allows to reconstruct the shower axis and direction with high precision. The ECAL pointing accuracy is an extremely important parameter for gamma ray astrophysics. The ECAL angular resolution has been measured to be better than 1^o for energies above 50 GeV [92]. The ECAL standalone trigger, whose efficiency for non-interacting photons is better than 99% at energies above 5 GeV, allows to measure photons inside the AMS field of view and which did not interact before the calorimeter. Given the amount of radiation length X_0 in front of the calorimeter, more than 60% of photons crossing the detector from the top reach directly the calorimeter without interactions. Photons that interact in the material before the ECAL are instead measured by the detection of $e^{\pm}$ pairs in the Silicon Tracker.

One of the main purposes of the ECAL is the identification of electrons and protons. The electromagnetic shower starting point, its shape and the matching between the deposited energy in the ECAL and the rigidity measured by the Tracker are used to identify $e^{\pm}$ while rejecting the hadronic background. The ECAL proton rejection capabilities, measured directly from data, are shown in figure 2.16.

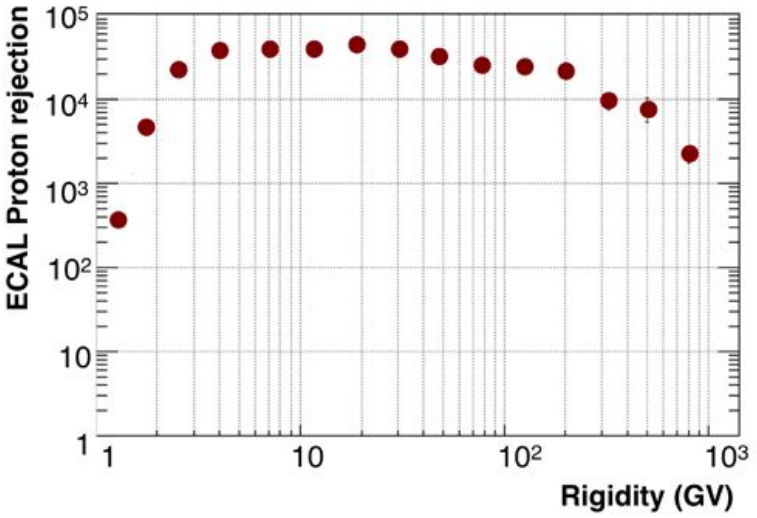

FIGURE 2.16: Electron/proton rejection measured from data collected in space using the ECAL shower topology analysis and the matching between the deposited energy in the ECAL and the rigidity measured by the Silicon Tracker. The efficiency of the selection for e^- is 90%. The proton rejection is above 10^4 in almost the whole energy range.

2.1.8 AMS electronics

The main challenge faced by the design of the AMS-02 electronics was to adapt well-known particle physics electronics to the requirements of space operations especially for a mission with a foreseen duration greater than 10 years. The requirements for the AMS-02 electronics demanding than those for usual space electronics due to the level of expectations in terms of performances, complexity and resource constraints. One must also consider the fact the AMS-02 mission will operate in excess of 10 years with respect to the initial design of the experiment. The durability of the electronics over the years will therefore be of important concern. All the electronics has been tested to be radiation hard.

For the best physics performances, the various sub-detectors must meet clear operational constraints : the gas gain of the TRD must be carefully controlled, the relative timing accuracy of the ToF must be of the order of 100 ps, signals as small as a few fC must be detectable in the silicon tracker and single photons must be measurable in RICH and in the ECAL requiring a very wide operational dynamic range. All these requirements and many more add up to more than 300K electronic channels out of which 200K are dedicated to the Silicon Tracker readout.

2.1.9 The trigger logic

The main purpose of the AMS-02 trigger logic is to take a fast and efficient decision to start the data acquisition of the signals in the subdetectors due to the crossing of a particle. The decision is tuned to the particle properties, such as its type (photon, lepton, hadron), its charge, potentially its energy and, to some extent, its trajectory through the detector (for example, if the particle is in the acceptance of a specific tracker configuration or not). The AMS trigger uses the combined information coming from the ToF, ACC and ECAL sub-detectors, which are analyzed inside a dedicated electronics board, the JLV1 [93]. The processing of all the different signals takes about 200 μs which represents a significant contribution to the dead time of the experiment. This is the time interval during which the detector is set in a "busy" state and cannot detect new particles. In order to minimize this dead time, a complex decision tree architecture is adopted with 2 different stages : the *Fast* and *Level1* trigger logics. Only if the conditions of the *Fast trigger* stage are satisfied, the *Level1* is evaluated. Following the lines of the presentation given in [94], we give below a brief description of the two trigger levels.

Fast Trigger
The Fast Trigger (FT) logic is used to make extremely fast decisions that do not contribute to any dead time and eventually activate the Level-1 trigger logic evaluation. It is based on the signals received by ToF and ECAL. The ToF FT signals are constructed from combination of the digital signals received from the ToF paddles (six signals per plane) and correspond to three different categorical information about the particle:

- Charged Particle (CP) : signal constructed from the ToF paddles above a High Threshold value (HT).
- Charged Particle in Tracker Acceptance (CT) : the signal uses only the signals from the paddles inside the Tracker acceptance.
- High Z Particle (BZ-TOF) : same as CP but the digital signals must be above a so called Super-High Threshold (SHT), which is normally associated to heavier particles (nuclei) traversing the detector.

ECAL produces only two signals based on signal detection in the x or y SL. The signals from the two views are logically combined with OR and AND giving ECAL-F_or and ECAL-F_and signals. The detection requires a minimum number of neighboring cells with energy deposit above a given threshold value. The ToF and ECAL signals

can then be combined in different logics to produce three different FT categories that can eventually be combined to produce a general FT signal :

- FTC: set if any of the CP or CT conditions are set.
- FTZ: this a dedicated trigger for the detection of potential stangelets, particles expected to have a very high charge but to be very slow with respect to ions with the same charge and rigidity. The FTZ uses the combination of the top and bottom ToF planes in a extended decision time window.
- FTE: ECAL-F_and and ECAL-F_or are multiplexed to generate a Fast Trigger ECAL (FTE) signal.

Level 1
Based on the existence of a FT, the JLV1 board enters the Level 1 (LVL1) logic evaluation, which takes exactly 1 μs. The following conditions are tested

- Charged Particles : the FT opens a 240 ns gate to latch the CP and CT charged particle signals. Events with 3 out of 4 ToF planes and 4 out of 4 ToF planes are accepted. The first condition is used to construct the unbiased trigger sample.
- High Z Particles : builds the trigger for ions with looser conditions on the ACC than in the standard Charged Particle trigger.
- ACC : the signals coming from anti-coincidence counters are used to veto triggers associated with particles traversing horizontally the AMS detector. ACC signals are also associated with high activity in the detector, typical of heavy nuclei interactions with the detector material.
- ECAL-F signals : FTE signals are used to build the unbiased electromagnetic trigger.
- ECAL-A signals : angular information used for non converting photons detected in the ECAL only.

These LVL1 triggers are added to FTE and FTZ signals to produce 8 different LVL1 sub-triggers. The LVL1 is built only if one LVL1 triggers fulfill the requirements. Among the various combinations offered by the trigger flexibility, 7 sub-triggers were carefully chosen for data taking on ISS :

- Unbiased charged : ToF 3/4 (HT) with a 100 pre-scaling factor.

- Single charged : ToF 4/4 (HT), NACC[2]=0.
- Normal ions : ToF 4/4 (SHT), NACC<5.
- Slow ions : ToF 4/4 (SHT), extended gate to latch the signals to account for slow strangelet particle.
- Electrons : ToF 4/4 (SHT), both x and y ECAL super-layers.
- Photons : an ECAL shower.
- Unbiased EM : ECAL signal over threshold, pre-scaling factor of 1000.

Live-Time

The constraint of minimizing the experiments dead-time depends on several factors. As we have seen, the FT initiates a 1 μs time window for the LVL1 evaluation to take place. Based on a LVL1 trigger, the various sub-detectors start the digitization of the signals. Although carried out in parallel, a 200 μs additional dead-time is introduced. Finally, the compression of the collected signals can take up t0 300 μs. The associated dead-time is kept as low as possible by allowing the compression to take place in parallel to the digitization of the following event. To precisely evaluate the live-time[3], a 20 ns scaler is used to sample continuously the status (busy/not-busy) of the data acquisition.

2.1.10 The Data Acquisition System

When a charged particle crosses the top and bottom plane of the ToF instrument, or when a particle produces a shower in the ECAL, a trigger signal is initiated and sent to the various sub-detectors to record the potential associated detections. All sub-detectors in AMS-02 are equipped with dedicated Front-End electronics (FE) with a maximum readout time of 90 μs. The DAQ system has been developed to efficiently collect the signals from the 300K FE channels and minimize the dead time introduced by the signal digitalization. A schematic view of the DAQ architecture is represented in figure 2.17. A dedicated simplified nomenclature has been adopted to identify uniquely each sub-detector: U stands for the TRD, S for the ToF and Anti-Coincidence Counters, E for the ECAL, T for the Tracker, R for the RICH, and $LV1$ for the Level-1 trigger module. The architecture adopts a tree-like structure with roughly 300 computational nodes : 264 xDR nodes (DR for Data Reduction and x specifying a sub-detector) that collect the signals from the detector

[2]ACC= number of ACC counts

[3]The live-time of a detector, is defined as (1-dead time)

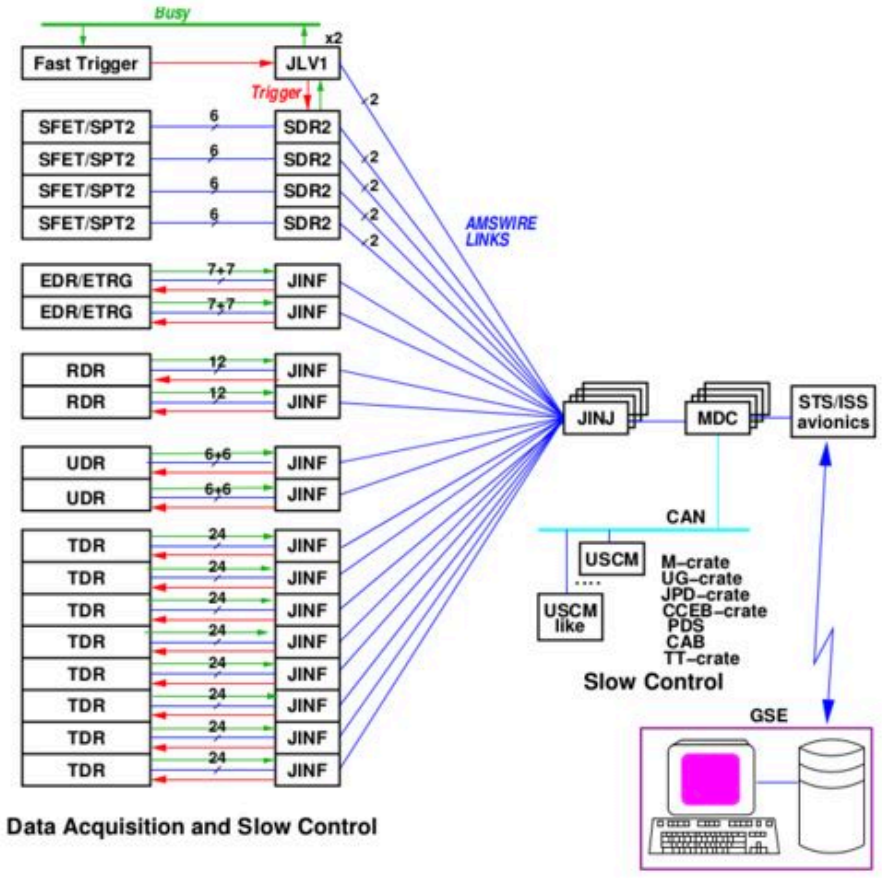

FIGURE 2.17: AMS data acquisition system. About 300,000 analog channels are processed by about 300 DSP computers in a Master-Slave based architecture. Due to the impossibility of any repair, the system has been designed allowing maximal redundancy of boards and cable connections: in case of any failure, the detector performance is not degraded [95].

Front-End electronics and perform a first reduction of the data, 28 JINF nodes that collect the data from the $xDRs$; 8 SDR nodes that produce the trigger signal based on ToF and ACC information as well as 2 JLV1 nodes that collect both analog and digital information to produce the LV1 trigger. Finally, 4 JINJ nodes collect the data from the JINF, SDR and JLV1 nodes [95].

All nodes are interconnected through serial wired links and a dedicated communication protocol is used, based on a master-and-slave hierarchy. Data is sent from a slave to its master only upon the master's request. The typical transmission speed is about 7.6 Mbytes/s. Upon a LV1 trigger signal generated by the JLV1 module, and delivered to the xDRs via the JINFs, each xDR node collects, processes and stores in a internal buffer all the information related to the event. The content of this buffer is further retrieved by the master node upon request. To minimize the dead-time, event buffering is performed at each level of the architecture. The 4 JMDCs are the main computers on-board the experiment. The JMDC provides the

monitoring and the control of the entire AMS instrument. It also contains a large buffer (called JBUX) to store the data, avoiding any science loss when interruptions in the transmission between the ISS and the ground take place. All the data is sent to ground through dedicated NASA interfaces (see section 2.2), the communication with AMS-02 from ground is mediated through the JMDC software and operation procedures can thus be constantly uploaded to the experiment if needed. This flexibility, together with the high transmission bandwidth provided by NASA for transferring the collected data to ground, makes the AMS mission a truly unique space experiment. The data acquisition is organized in 23 minute runs, 4 runs are recorded each orbit. A full calibration of the various sub-detectors is performed every 2 runs. Twice per orbit, a dedicated procedure is used to identify and correct single electronic upsets (bit flips) in all acquisition nodes.

2.2 AMS on ISS

On the 16th of May 2011, NASA's Space Shuttle Endeavour was launched from Cape Canaveral at the Kennedy Space Center (KFC). Few hours later, the first successful power-on of the AMS-02 electronics inside the shuttle was performed from the Johnson Space Center (JSC, Houston Texas) with a first monitoring on ground of various temperatures and electrical currents. On May 19th, AMS-02 was powered off for installation on the International Space Station. At 4:46 a.m. the same day, AMS-02 was attached to its mission site and the first activation of the full detector in space took place less than an hour later, with the first science data arriving to ground. No damage on any of the sub-detectors due to the shuttle launch was found and all the functions are proven to be as expected. Since then, AMS-02 has been collecting cosmic ray data at a rather steady rate of about 10^{10} particles per month, 90% of which correspond to completely ionized hydrogen. The operation of AMS-02 in space is extremely challenging due to the very harsh and constantly changing thermal conditions. Whether AMS-02 is directly facing the sun or deep space results in significant temperature variations, sometimes within a single ISS orbit. The ISS completes 15.7 orbits per day at an altitude ranging from 330 km to 410 km. The performance of the various sub-detectors strongly depends on the precise understanding and control of the effects caused by such important temperature excursions.

NASA provides 3 different electrical interfaces to AMS-02 on ISS. After AMS was physically attached to its mission site, all connectors were attached to the payload. The first interface provides the power to the AMS payload. The other two interfaces

are data transmission links: the Low Rate Data Link (LRDL) and the High Rate Data Link (HRDL) [96].

Power Interface

The power on the ISS is provided by the eight large solar array panels. The power is distributed to the AMS-02 payload through two feeds with a maximum power draw allocation of 2000 W. To meet the severe constraints imposed by NASA in terms of isolation, grounding, inrush current, etc., a dedicated power distribution system (PDS) was developed to distribute the ISS power input to the various sub-detectors. It has been designed to minimize the number of units directly attached to the ISS feeds and to provide the best monitoring, control and protection of the power delivered to each sub-system.

Low Rate Data Link (LRDL)

The LRDL is a dual serial bus link that is split to each of the four JMDCs. To avoid single point failures, there are two such splitters which can be selected by an astronaut by swapping a cable at the bottom of the experiment during an extra-vehicular activity (EVA). Data sent from JMDC to ground using the LRDL proceeds through various units of NASA and then via radio beam to Earth using Tracking and Data Relay Satellites (TDRS). Around 20 KBits/s of data bandwidth on the LRDL is allocated to AMS-02. The expected duty cycle is about 70%. In nominal conditions, all commands to operate AMS-02 originate from the POCC and follow the inverse path. The maximum command rate is about 1 Kbit/second.

High Rate Data Link (HRDL)

A parallel path of data transmission is organized throughout the HRDL and represents the main path for the data out of AMS-02. The transmission is based on fiber optics communication. Transmission speeds up to 90 MBits can be reached on-board the ISS, and the radio down link supports up to 43 Mbits, with a duty cycle of about 70%. The HRDL is crucial for the proper operations of AMS-02 considering the high event acquisition rate of the experiment. The average trigger rate is about 600 Hz, but can reach up to 2kHz in regions of low Earth magnetic field. The resulting average event size is about 2kBytes which represents a substantial amount of data to be downlinked to ground. The needed downlink rate is on average 10 Mbits/s. AMS currently operates with a steady value of 13 Mbits/s which can be increased upon request depending on ISS activities.

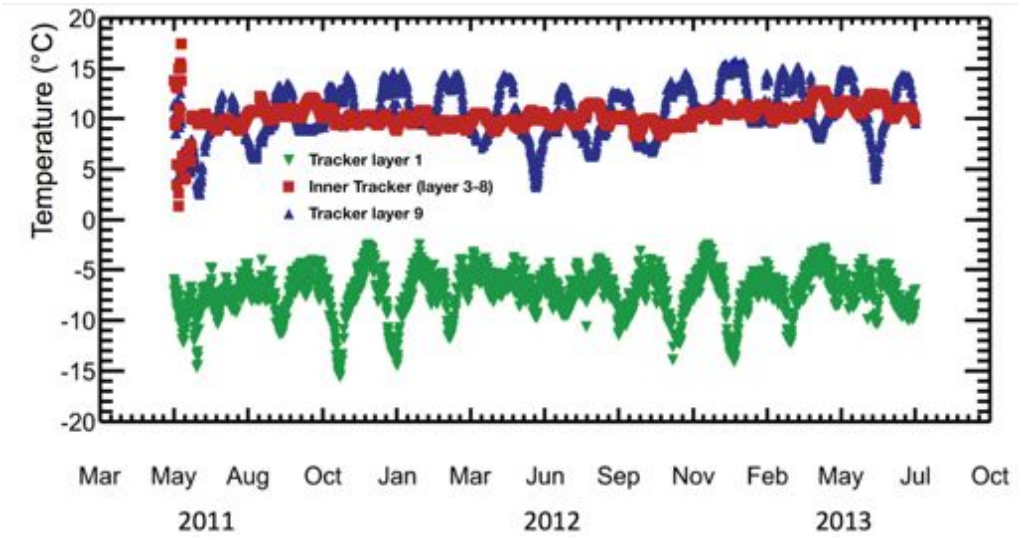

FIGURE 2.18: Time evolution of the temperature measured in different sensors thermally connected to the tracker front-end electronic of the Inner Tracker, layer 1 and layer 9.

2.2.1 Thermal environment and TTCS system

On board of the ISS, AMS orbits around the Earth with a period of ∼93 minutes and is subjected to extreme thermal variations due to day/night effect during its orbits and seasonal Sun exposure variation or due to changes of the attitude of the ISS, as in the case of berthing/unberthing of visiting vehicles [81]. Since each AMS sub-detector has its own warning, operational and no-operational temperature range, AMS requires constant alertness in order to avoid damage to its electronics. For this purpose, several sensors are placed on each sub-detector and the temperatures of AMS are constantly monitored all around the clock.

In particular, the Tracker electronics, that produces almost the whole quantity of the AMS electronics heat, has its own temperature control system: the TTCS (Tracker Thermal Control System). The AMS-02 TTCS is a mechanically pumped two-phase CO_2 cooling loop. It is able to remove 140 W of heat by means of two dedicated radiators facing outer space located on the top of AMS-02. TTCS provides also stability with respect to the environmental temperature described above.

Figure 2.18 shows the average temperature of the Tracker layer 1, Inner Tracker and Tracker layer 9 during the first two years of operation. Since the Inner Tracker and layer 9 are cooled by the TTCS system, their temperature has a small variation with respect to the orbital thermal environment changes. The wide temperature variations that can be observed at the beginning of AMS-02 operations in 2011 were due to the commissioning of the TTCS system on orbit. Since the Tracker layer 1

is facing outer space, it has no need of a cooling system but a system of heaters has been installed on this layer to warm it up in the case of low temperatures.

2.2.2 The Data Flow from ISS

Two categories of data are buffered into the main JMDC computer: science data (SCI), the data associated to the measurement by the various sub-detectors of a traversing particle, and housekeeping data (HS), consisting of various informations such as temperature readings and memory program checks (upsets and bit flips) related to the general health and status of the experiment. The latter information is crucial for fast reaction against potential damage of the payload in case of unexpected events. This is why the HS data, in parallel to being buffered in the JBUX, is also directly transferred to ground through the LRDL for real-time assessment of the payloads condition. The buffered SCI and HS data are transferred to ground through the HRDL based on the First In First Out logic (FIFO). This stream can thus be few hours late due to low bandwidth availability or loss of satellite connection. NASA delivers a schedule of available satellite connections for each orbit of the ISS. This schedule is loaded inside the JMDC which automatically enables the playback from the buffer. Unexpected losses of transmission from the ISS are unavoidable contingencies of space operations. To avoid any loss of science data, a final copy of the data is sent to a laptop computer on-board the ISS through a wired link. The laptop has a 500 GB hard memory capacity, which allows to buffer approximately one continuous week of data if needed. The data from the laptop are downloaded weekly. The system is flexible enough such that the buffering in JMDC can be by-passed if real-time data is needed on ground. The data are received on ground by high rate radio frequency antennas and directed to the Marshall Space Flight Center (MSFC). The data is then copied to CERN and a copy of the HS data is sent to the Taiwan control center.
Data from the AMS-02 sub-detectors are collected by the JMDC in blocks of information. These blocks are separated into frames for transmission to ground. One frame corresponds to approximately 4kbytes of information. At ground, the frames are merged into packets before being copied to the CERN location. A dedicated de-framing program then recovers the original block files. These are fed to the event reconstruction software that produces the standard Root [97] files for the analysis. The reconstruction is a time consuming process and new arriving data is queued to already running processes on available computing resources at CERN. In parallel to this standard production, a special reconstruction is immediately started on dedicated machines to provide fast reconstruction of high-level event variables for a close to real-time monitoring of the detectors.

2.2.3 AMS Payload Operation Control Center

The Payload Operation Control Center, the POCC, is located on the French border side of CERN, in Prevessin. It is a single building fully dedicated to the control of AMS-02 operations on-board the ISS. The control center was certified by NASA authorities prior to starting operations. The POCC is occupied every single day of the year, day and night, by a team of experts that monitor the health and status of the payload in successive shifts of 8 hours. A picture of the CERN POCC is shown in figure 2.19. Five positions are occupied:

FIGURE 2.19: Picture of the AMS POCC at Cern Prevessin. A big central screen displays the position of the ISS at any moment in time.

- **LEAD**: is the main responsible for the operations inside the POCC. LEAD deals with direct communication with NASA collaborators responsible for ISS activities management (Debris Avoidance Maneuver, astronaut crew activity, etc.). LEAD is the only authority in the POCC to allow commanding actions to the payload.

- **DATA**: the DATA shifter controls the flow of data from the ISS to ground and to the various locations on earth, primarily the CERN POCC.

- **THERMAL**: monitors the hundreds of temperature readings provided by sensors placed in various places in the detector. It continuously assesses potential risks due to up-coming events associated with unexpected temperature excursions.

- **PM**: controls the proper functioning of the RICH, the ECAL and the ToF subdetectors.

- **TEE**: controls the proper functioning of the TRD and the Silicon Tracker.

Two years after the beginning of the science activities on the ISS, a second POCC center was opened in Taiwan. During CERN night time, the PM and TEE positions tasks are covered by shifters in the Taiwan POCC. The LEAD and THERMAL positions remain at all time occupied at CERN, which remains the only location allowed to communicate with NASA teams through the official International Voice Loop System (Ivods).

2.2.4 Data Processing and Event Reconstruction on Ground

The data taken on board of the ISS by AMS are *raw events* and each event is a collection of the information coming from the various AMS subdetectors. The raw events are grouped into *runs*. Each *run* includes all events taken during a quarter of ISS orbit ($\sim$23 min) and contains in average 7×10^5 events. Usually the AMS environmental characteristics are uniform during one run.

Since physics analysis cannot be performed directly on the *raw files*, a *reconstruction* is required to convert the original detector read outs to *physics events*, containing all necessary parameters of the particles crossing the detector and being ready for the further analysis. The AMS recontructed data format is based on `CERN ROOT` package [97] and each reconstructed event is represented by a `ROOT tree object` that contains high level information such as particle trajectory finding and association with other detectors.

A dedicated AMS offline software is designed to serve both reconstruction and simulation. The AMS data are reconstructed in two steps. A first reconstruction, which is constantly running on the freshly arrived data, is the initial data validation and indexing. It proceeds data summary files and event tags for fast event selection and quick evaluation of the detector performance. The first production is used to produce the calibration for the various subdetectors, which are required for the second production.

The second reconstruction uses all the available calibrations and additional data from the ISS as well as monitoring values (temperatures, pressures and voltages) to produce analysis ready dataset. Unlike the first reconstruction, the second production usually runs every 3-6 months.

The simulations of the AMS detector performance is done by producing the simulated events using all available information about AMS geometry, its environmental conditions and electronics characteristics and is based on the Geant4 package [98]. As knowledge of particles interaction with media is evolving with time, the AMS software needs to be regularly validated with the latest available Geant4 software version.

The chosen computing strategy of the AMS experiment allowed reliable running of the AMS data reconstruction and simulation during over 4 years of operations of AMS on ISS, resulting more than 1 PB of reconstructed data and simulated events available for the AMS Collaboration [99].

Chapter 3

Electron and positron identification with AMS

The identification of electrons and positrons in the primary cosmic ray flux is very challenging. The signal should be extracted from a huge background constituted mainly by protons ($\sim 90\%$ of background) and nuclei. In this chapter, the technique applied to select $e^{\pm}$ with the AMS detector will be discussed.

The key AMS sub-detectors used in the $e^{\pm}$ analysis are the electromagnetic calorimeter and the TRD. Both give an high e/p separation power and the calorimeter perform the measurement of the $e^{\pm}$ energy with very high accuracy. The information coming from the other sub-detector are combined with the signal from ECAL and TRD in order to completely identify the particles. For example, the sign of the rigidity measured by the tracker is used to distinguish between e^{+} and e^{-} and the direction of the particle given by the ToF is used to distinguish between upward going and downward going particles.

3.1 Data sample

In this work the term DATA will refer to the data collected by AMS-02. The data that have been used for this analysis correspond to a total of 41×10^9 events that have been collected in the first 30 months of the AMS-02 data-taking mission (May 20, 2011 – Nov 29 2013). These data are the same used for [65, 67, 100].

In order to fully understand the behaviour of the detector and of the reconstruction applied to its raw signals, a set of simulated data has been used. The term "MC"

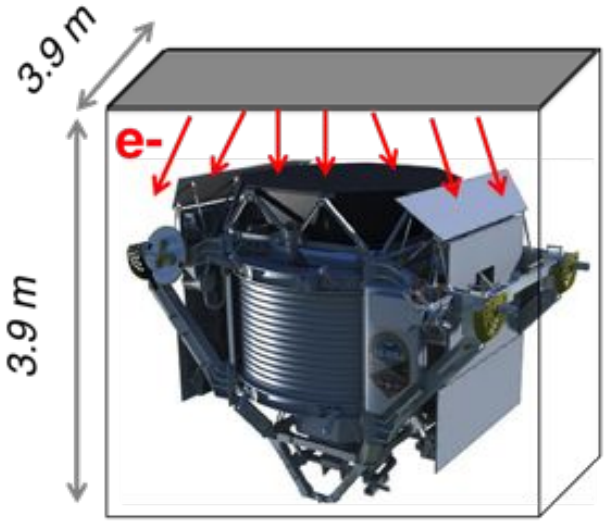

FIGURE 3.1: Sketch of the MC simulation. An isotropic flux (electrons but also protons) is generated from the top plane of a cube of side 3.9 m that surrounds AMS-02, and concentric to it.

will refer to events simulated with the Monte Carlo method. The MC data are based on the Geant4 package as discussed in section 2.2.4 and the same reconstruction software of the data is used. Both electron and proton MC data have been used. Since the response of the detectors for electrons and positrons is the same, the electron MC is valid also for positrons.

For this purpose three dataset of electrons, generated in three different energy ranges, for a total of 4.96×10^{10} events, have been used:

- 37.0×10^9 events simulated in the energy range 0.25–5 GeV;
- 11.8×10^9 events simulated in the energy range 5.–100. GeV;
- 0.07×10^9 events simulated in the energy range 100.–2000. GeV;

The simulated electrons have been generated from the top plane of a cube of side 3.9 m that surrounds AMS-02, and concentric to it, as shown in figure 3.1. The incoming direction of the simulated events has been generated in order to simulate an isotropic flux in the detector [101].

The electron MC sample has been also used for the calculation of the detector acceptance, A_{MC}, as more detailed in section 4.3.

In addition, a proton MC sample has been used to study the systematic uncertainty introduced by the "irreducible background", which, as discussed in section

3.2.3, is mainly constituted by protons, interacting with the AMS material, that are producing secondary electrons. These electrons, being genuine electrons inside the detector, can be misidentified as primary cosmic rays and counted in the flux measurement. For this purpose three dataset of protons, generated in three different energy range, for a total of 1.2×10^{11} events, have been used:

- 0.1×10^9 events simulated in the energy range 0.5–10 GeV;
- 0.15×10^9 events simulated in the energy range 10.–200. GeV;
- 122.0×10^9 events simulated in the energy range 200.–4000. GeV;

Similarly to the electron MC sample, the simulated protons have been generated from the top plane of the cube shown in figure 3.1 and with an isotropic distribution of the incoming directions.

3.2 Sample definition

In general two different methods can be followed to extract the signal: a cut-based method and a template fit based one.
In the first case a selection is applied on the variables reconstructed by the detector. Following this method electrons and positrons can be selected applying requirements to the events based on ECAL and TRD reconstructed quantities. The selection applied can be chosen to have the most advantageous combination of $e \setminus p$ rejection power and efficiency on electrons and positrons. However this method presents some problems in particular for the measurement discussed in this work. Since electrons and positrons constitute a rare component of CRs, the selection should contain several cuts. However, each cut applied introduces a systematic that should be taken into account, as will be described in section 4.4. In addition, is not possible to obtain a high e\p rejection power together with a high efficiency on signal. This introduces a statistical limitation, since the natural low number of electrons and positrons is further reduced.
In the fitting method, instead, a template fit on one of the key variables, in terms of e\p rejection power, is performed. The signal and the background are extracted by the fit procedure using two reference distributions. The fit procedure allows to extract the signal without any cut. For this work the second method has been followed. However a minimal preselection on DATA should be first applied in order to define a good sample on which to perform the fit.

The preselection contains a minimal set of cuts that allow to reject the events that are not useful for a $e^{\pm}$ analysis and in order to define a clean sample of downward going unitary charge particles from which extract the signal. At the end of this preselection, the sample will contain mainly protons and a low fraction of $e^{\pm}$ (e/p$\sim$1%–10% depends on energy). From the preselected sample, the signal has been statistically separated from proton background through a template fit on TRD distribution. For the definition of the electron and proton templates, the variables reconstructed by the ECAL have been used.

The amount of events taken during the period in which the analysis has been performed, is 41×10^9. The preselection cuts, can be divided into four categories, according to the purpose with which were applied:

- Good data taking: first of all it should be assured that the events used for the analysis are without any problems during the DAQ and that have been taken in a nominal conditions.
- Geometric selection and nominal conditions reconstruction: it is not possible to have for each event coherent information coming from the various sub–detectors. This is mainly due to the interactions of the events with the material of AMS and to the fact that some of the triggered events could be outside the geometrical acceptance of the detector. Only events that satisfy some geometrical requests and for which it is possible to have consistent information coming from the various detectors have been taken into account.
- Unitary charge particle: since the signal in this analysis is constituted by $e^{\pm}$, only the event with unitary charge have been taken;
- Above cut-off: in order to take only primary cosmic rays and not to take into account the secondary particles trapped in the geomagnetic field, a cut on the geomagnetic cutoff has been applied.

3.2.1 Good data taking

Since AMS is installed on ISS it is not a free flyer orbital satellite. The orbit parameters cannot be decided and moreover the AMS field of view can be modified by the ISS operations. This first part of preselection concerns only parameters related to the data acquisition and to the position of AMS. All the information regarding the orbit and DAQ parameter are stored every second in the RTI (Real Time Information), a developed tool inside the AMS collaboration, mainly used for

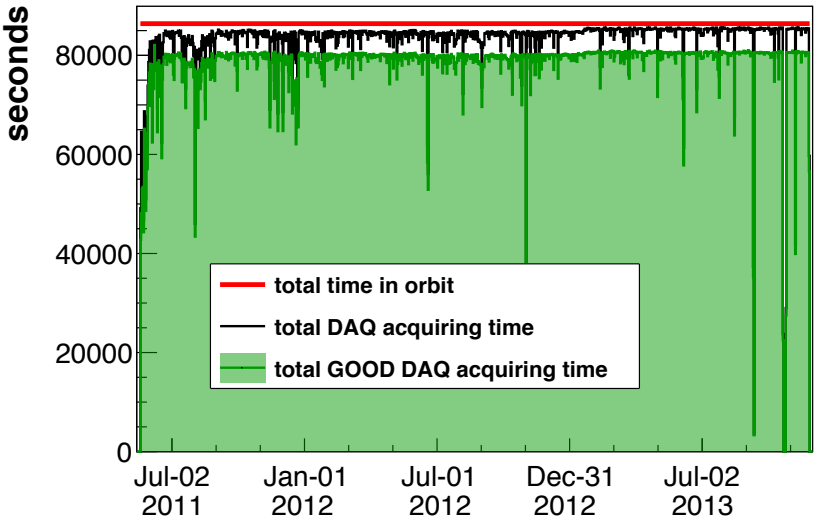

FIGURE 3.2: Seconds as a function of time (each bin=1 day=86400 s) during which: AMS was in orbit (red line), DAQ was acquiring (black line) and DAQ was acquiring in good conditions (green line).

exposure time calculation for flux and detector performance [102]. This tool has been used for the selection of the data taking periods with good conditions.

First of all, if some errors have occurred in the hardware or if DAQ failures arisen, the events are rejected. The events in which raw data block are missing because of an unexpected loss of signal from ISS to ground, have been removed also. Figure 3.2 shows the total time of AMS in orbit compared with the DAQ acquiring time and to the good fraction of it.

For the DAQ rate, is requested to not exceed a maximum value (1800 Hz) in order to have an efficient DAQ, and only events with DAQ *livetime*[1]>0.4 have been selected. As shown in figure 3.3 this cut automatically removes the events taken when the ISS is in the SAA[2]. It is also important assure that the events to be analyzed were not taken when the material of ISS intercepts the field of view of AMS. Moreover, due to special ISS operations like a docking/undocking of the Soyuz, the AMS can be tilted with respect to the zenith. Since the field of view of AMS is $\sim 40^{o}$ the events taken during periods where the deviation from the zenith was greater then 40^{o} have been rejected.

The runs that are not good for the analysis (tests, TRD gas refills, etc..) have been removed.

[1]The live-time of a detector, is the contrary of the dead time, the time after each event during which the system is not able to record another event

[2]SAA = South Atlantic Anomaly

This part of preselection is important to ensure that the data on which the analysis is performed are not affected by DAQ or hardware problems or are not taken in the SAA anomaly and has an efficiency of 90% over all the data acquired by AMS.

3.2.2 Geometric selection and nominal conditions reconstruction

Even for events taken in naïve data taken condition, it is not possible to reconstruct clear and univocal information. For one single event, two or more different particles can be reconstructed by the detector. This can be due to the presence of secondary particles produced by the cosmic rays interaction with AMS material or can be due to the *pile-up* effect (i.e. when two genuine cosmic rays are triggered together). In order to have a clean event reconstruction, the kind of events described above should be removed.
In order to do that, the sample to be analyzed can be reduced without any loss of good electrons, applying some geometrical cuts. The purpose of these cuts is to obtain only events in which the information coming from the various sub-detectors are matching between each other. Moreover, all the events that are not geometrically contained in a volume that is suitable for a $e^{\pm}$ analysis (for example, the events outside the calorimeter) should be rejected.

The first request that has been applied in this part of preselection is the presence of a physics trigger (see section 4.5). As will be shown, this cut has an efficiency of 100% for energies above 3 GeV and decreases up to ∼70% for lower energies.

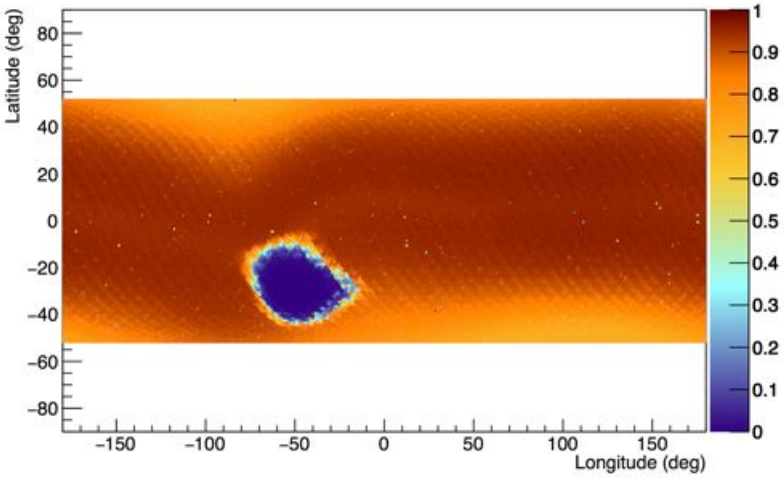

FIGURE 3.3: Value of AMS livetime as a function of the ISS orbit position in geographical coordinates. The request livetime> 0.4 automatically removes the events taken when the ISS is over the SAA.

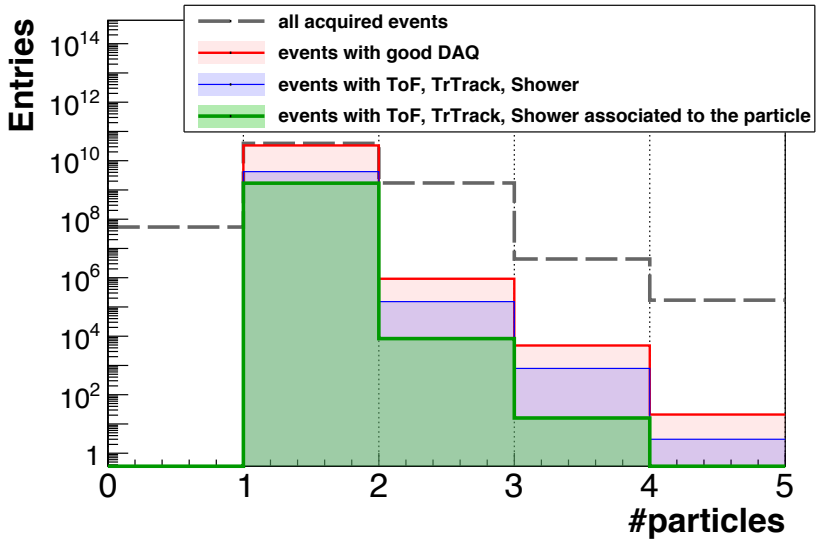

FIGURE 3.4: Number of reconstructed `Particle` objects for each event at different levels of preselection.

For each sub-detector the raw data are clustered together in order to build an high-level physics object: The hits on Tracker layers are grouped to build the `Tracker Track` object, the hits in the calorimeter to build the `ECAL Shower` and the hits in the ToF paddles to build the `ToF Track`.

The high-level physics objects are combined into the higher level physics object: the `Particle`. The basic criteria to have a `Particle` defined for an event is the presence of the `ToF Track`. Since the energy used in the $e^{\pm}$ analysis is the one reconstructed by the ECAL, only events that have at least one `Particle` with an associated `ToF Track`, `Tracker Track` and `ECAL Shower` have been taken into account. Figure 3.4 shows the distribution for the number of reconstructed `Particle` objects for each event at different levels of preselection. For the events in which are present `Tracker Track`, `ToF Track` and `ECAL shower`, the percentage in which these object are associated to a `Particle` object is ∼40%.

The information coming from the `ToF Track` have been used to select *downward going* and relativistic particles applying a cut on the value of the reconstructed velocity $\beta = v/c$. The β is reconstructed using the time measured by the ToF and the known distance between the upper and lower ToF. The quantity $1/\beta$ follows a gaussian distribution and in the case of electrons is a gaussian which peak is ~ 1. A symmetric cut $0.8<1/\beta<1.2$ has been applied that correspond to a 5 σ (where σ ∼4% is the ToF resolution). As shown in figure 3.5 this request ensures that only downward going particles are taken and moreover this cut has an efficiency ∼100% on electrons.

Further requests have been applied on `Tracker Track` and `ECAL shower`, both of them associated to the `Particle` object.
First of all only events with the `Tracker Track` inside the ECAL fiducial volume have been taken. This is a fundamental request in order to use a good reconstructed energy value. The particles that cross the border of ECAL, as Figure 3.6 shows, have a bad energy resolution[3]. This is due to the lateral leakage of the shower and to the presence of the PMTs and read-out electronics. The bad resolution that can be observed around x_{ECAL}=∼18 cm is due to a dead PMT on layers 6 and 7.

The definition of the ECAL fiducial volume has be carefully studied. If only particles with showers fully contained in ECAL are kept, the energy resolution improves but the ECAL acceptance is significantly reduced (as shown in figure 3.7). In order to choose the fiducial volume a good compromise between a good ECAL resolution and a minimum loss of ECAL acceptance should be found. The cut that has been applied is the following. Only `Tracker Tracks` that cross the top and the bottom of calorimeter inside 32.4 cm (both in x and y side) are taken. This cut removes all the border of the ECAL where the PMTs are mounted and the read-out electronics. Furthermore, also the `Tracker Tracks` that arrived at the ECAL crossing vertically the border of calorimeter (defined as $x(y)$ >31.4 cm) are removed, in this way only the showers with a significant lateral leakage are removed.

[3]The ECAL resolution has been evaluated on MC electrons and defined as:

$$\frac{E_{\mathrm{gen}} - E_{\mathrm{rec}}}{E_{\mathrm{gen}}}$$

where E_{gen} is the MC generation energy and $E_{\mathrm{rec}} is the reconstructed energy by ECAL$.

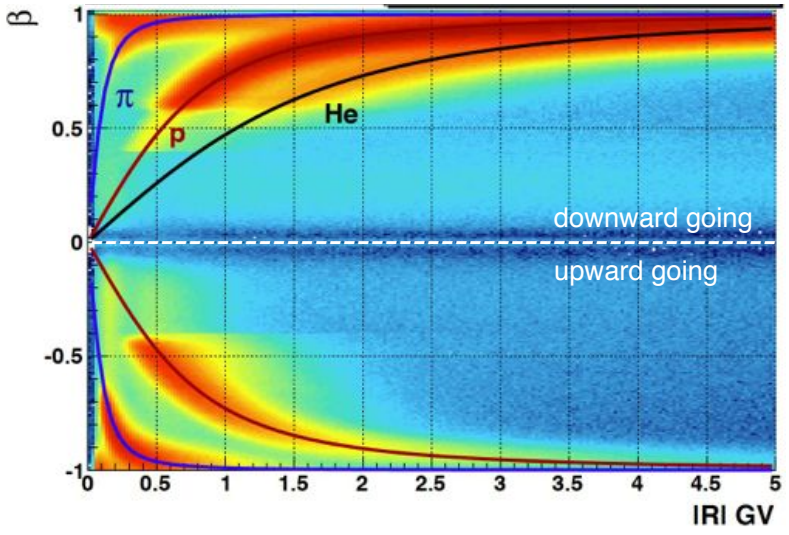

FIGURE 3.5: β measured by the ToF as a function of rigidity.

Also the matching between the `Tracker Track` and `ECAL shower` has been checked. Figure 3.8, show the distance between the `Tracker Track` and the `ECAL shower` in x (Δx) and in y (Δy).

The distance has been evaluated with respect to *Center of Gravity* of the shower. Both the distributions show larger tails at low energies, due to the multiple scattering effect but only (Δx) is a symmetric distribution. The (Δy) distribution has an asymmetric tail due to the bremsstrahlung effect. An electron (positron) that

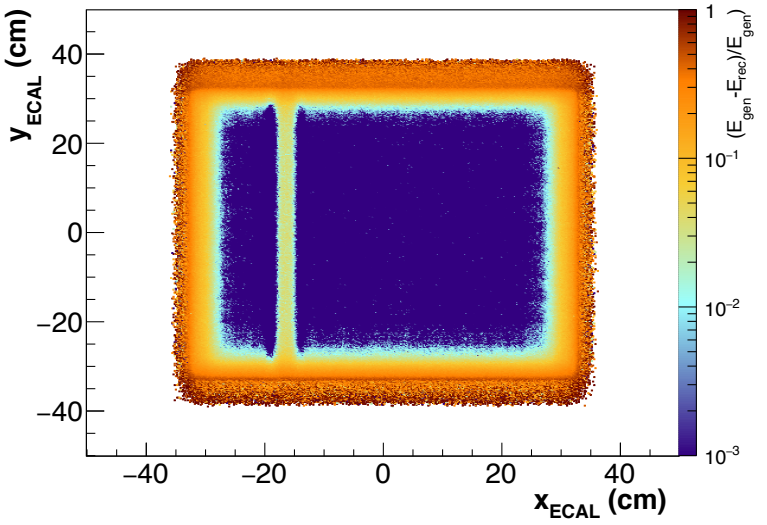

FIGURE 3.6: ECAL energy resolution defined on MC electrons, as a function of the impact position of the crossing particle.

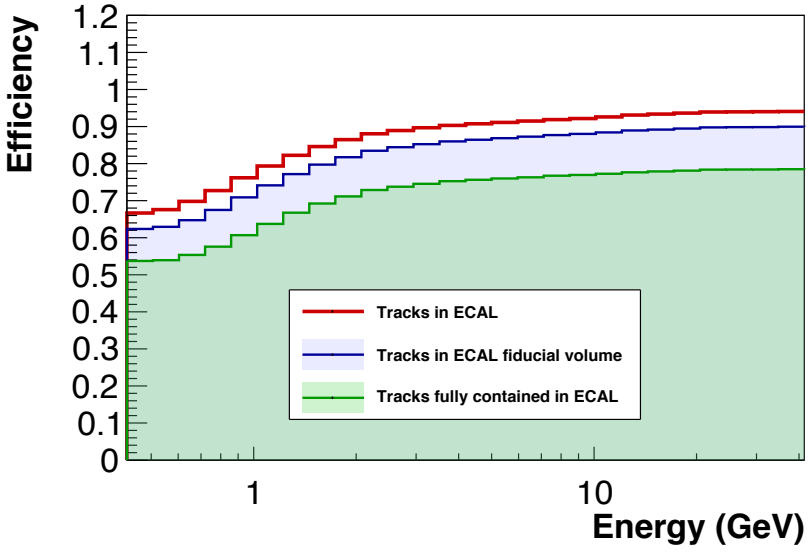

FIGURE 3.7: Efficiencies on electrons obtained for three different definitions of ECAL fiducial volume.

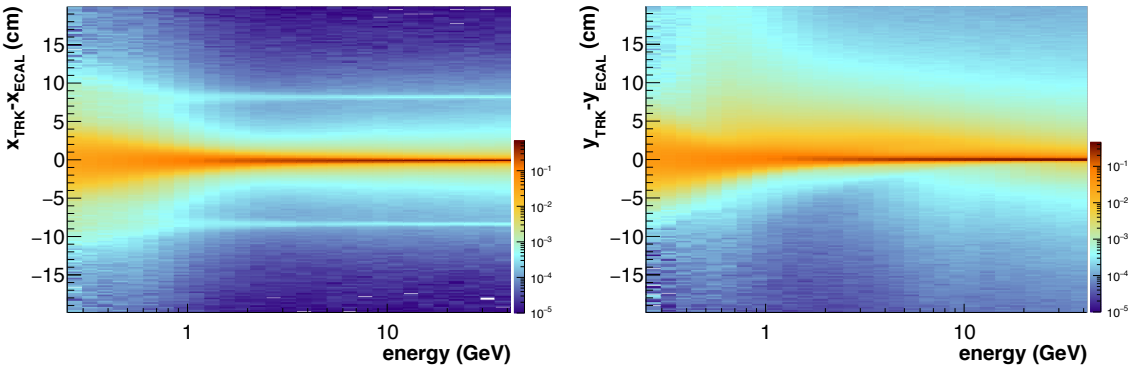

FIGURE 3.8: Distance between the `Tracker Track` and the `ECAL shower` in x (left) and y (right) evaluated at the Center of Gravity of the shower.

goes through the tracker has an high probability to emit bremsstrahlung photons that follow the direction in which they are emitted and reach the ECAL, starting an electromagnetic shower. The electron, after the emission of the photon, decreases its energy and the curvature of the trajectory increases. As consequence, when the track reaches the calorimeter will be shifted respect to the shower axis, that will be a combination of the shower started by the electron and the shower started by the photon. This effect is schematically represented in figure 3.9. Only events with Δx <3.6 cm have been taken. Since the effect of bremsstrahlung should be taken into account the cut applied on Δy is wider and only events with Δy <7.2 cm have been taken.

A fundamental tool for the electrons and positrons analysis, is the TRD estimator

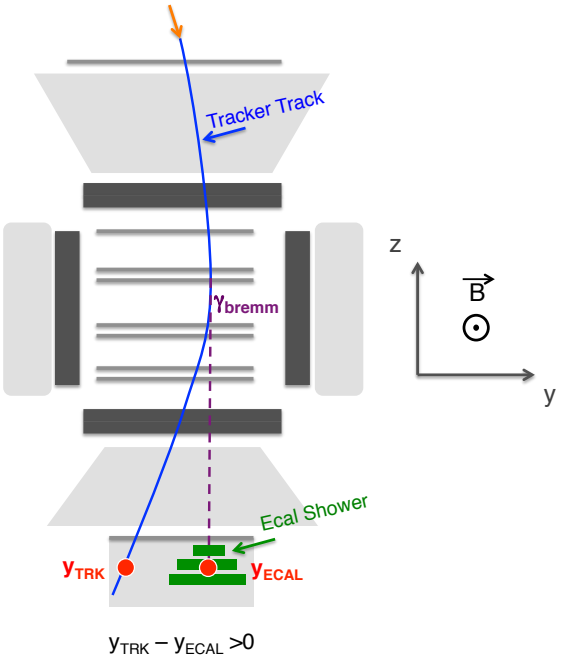

FIGURE 3.9: Bremsstrahlungs effect on Δy for an electron.

built through the information coming from the different energy deposits per unit length for electrons and protons. The `Tracker Track` has been extrapolated inside the TRD volume and only the TRD hits that are along the `Tracker Track` are taken into account while building the TRD estimator. This contributes to reject the events with a wrong reconstruction of `Tracker Track` and the events that are affected by the multiple scattering. Moreover only the events with a number of TRD hits > 9 have been taken. This ensures a good reconstruction of the TRD classification tools. This cut has a total efficiency of 99.2 % and is less efficient at low energies due to the multiple scattering effect.

3.2.3 Unitary charge sample

At the end of the first step of preselection, the sample contains only events with downward going relativistic particles which have an associated `Tracker Track` and `Ecal Shower`. Moreover the `Tracker Track` of the particles is inside the TRD and ECAL volume and it is geometrically matched with `Ecal Shower`. However, the sample still contains CRs nuclei and secondary particles produced by the primary event through the interaction with AMS materials. The rejection of these kind of events is the purpose of this part of selection.

The charge reconstructed by the inner tracker (layers 2-8) using the ionization signal in each layer was used in order to select the unitary charge particles. Only the events with the inner tracker charge (Z_{inn}) <1.5 have been taken. As will be discussed in details in section 4.6, the efficiency of this cut is high and doesn't represent a problem in the calculation of systematics. However it shows a slight decrease with the energy due to an asymmetric shape of the Z_{inn} distribution for electrons sample when the energy starts to increase, as shown in figures 3.10. The asymmetric tail is due to secondary particles produced before the inner tracker or due to Bremsstrahlung events. This behavior is confirmed also by MC simulation.

AMS can provide multiple redundant charge measurements from the various sub-detectors. In figure 3.11 the charge reconstructed through the energy deposition on the ToF paddles (Z_{ToF}) versus the charge obtained from del energy deposition on the inner tracker layers is shown. However a request on Z_{ToF} introduces one more cut in the systematics calculation. Moreover, it doesn't significantly remove the residual nuclei after the request (Z_{inn}) <1.5 since the resolution of (Z_{ToF}) is worst respect to (Z_{inn}).

Another tool used for the unitary charge selection is the TRD. Thanks to the

different energy deposition between electrons and Helium released in the various TRD layers , it is possible to build a TRD estimator to separate electrons from Helium (*TRD estimator e/He*). A cut of TRD estimator e/He<0.8 has been applied. This cut helps in removing Helium from the sample with an efficiency of $\sim 100\%$ over electrons: it doesn't enter in the systematic calculation.

More cuts should be applied in order to remove the number of the interacting events

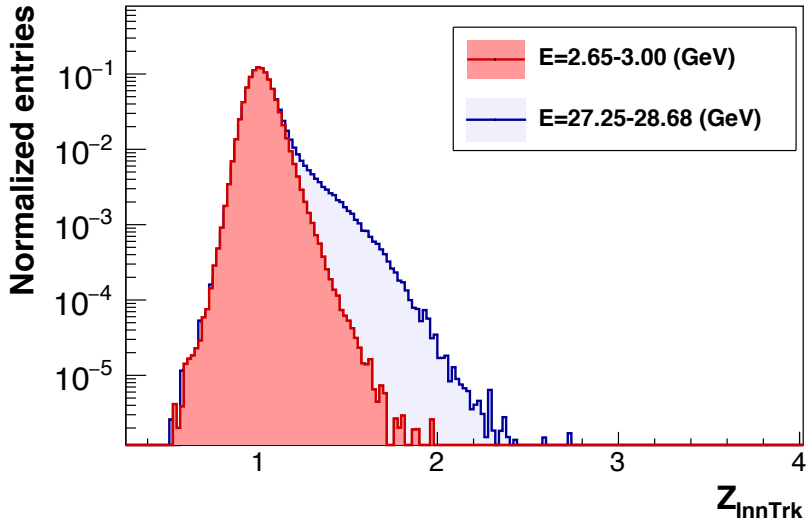

FIGURE 3.10: Distribution of charge reconstructed using the energy deposit on the Inner tracker Layers (Z_{InnTrk}) for 2 different energy bin. The distribution starts to become asymmetric with the increase of energy.

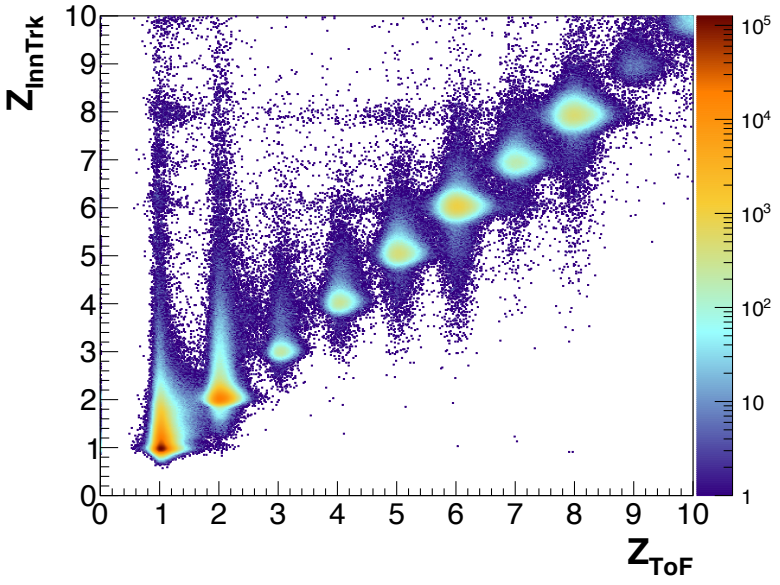

FIGURE 3.11: Charge measured by the Inner Tracker (Z_{InnTrk}) versus the charge measured using the energy deposition on ToF paddles.

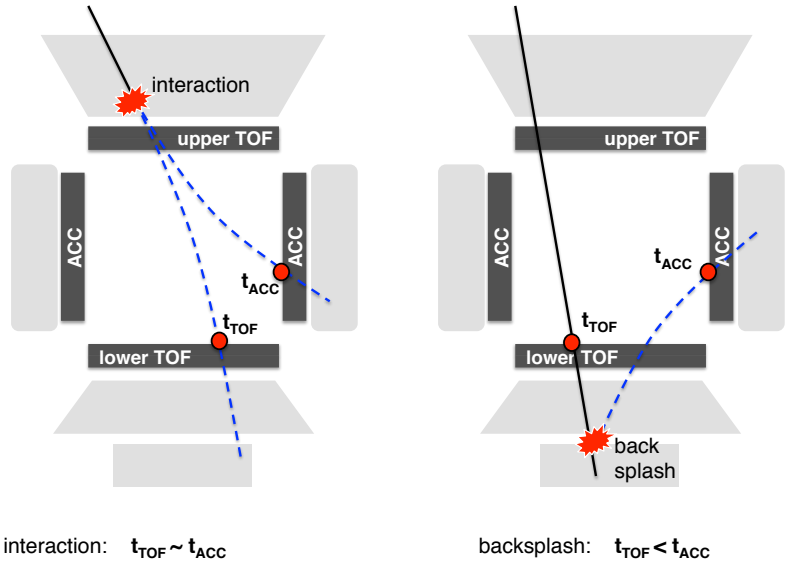

FIGURE 3.12: The time detection of ToF and ACC can be used in order to separate between the interaction events and back-splash ones.

with the AMS material. The interactions produce secondary particles which introduce an high level of activity in the sub-detector making hard the proper reconstruction of the information related to the primary particle. Moreover, the interactions can introduce unwanted correlations between the various sub-detectors: for example, high energy secondaries produced in the TRD can be clustered as primaries in the ECAL.
The interaction events can be identified by means of the energy deposits on ToF paddles looking if the deposited energy is greater than the one for the single particles. Using time information coming both from the ACC and from the ToF, it is possible to define the *number of interactions*. In general, a big number of interactions correspond to an high ACC value but this is true also in case of backsplash events. In order to distinguish between the two cases it is possible to use the time information coming from ToF and ACC as described in figure 3.12. Unfortunately a cut based on the number of ACC or on ToF energy deposits is not so efficient on an electrons sample and moreover the MC data are not able to satisfactorily simulate the ACC and ToF responses as show in figure 3.13.

However, the number of interactions seems to be related to the number of reconstructed tracks as shown in figure 3.14. Only the events with a number of reconstructed `Tracker Track` equal to one have been taken into account. This cut helps to remove the interacting events, has an efficiency of $\sim 90\%$ and its efficiency doesn't depend on the energy. Moreover this request helps to reduced the *irreducible background*. A typical event that constitutes this kind of background is shown in figure 3.15: the primary particle is a proton that interacts in the first part of the TRD

and produces a secondary high energetic electron. Both the signal in TRD and ECAL are associated to the secondary electron that will be reconstructed as the primary particle. The effect of this irreducible background has been studied over a MC protons sample and it is negligible especially over the single `Tracker Track` sample.

In order to reduce the charge confusion (CC), more requests have been applied on the `Tracker Track`. Only the events with a tracker pattern containing also layer 2 have been taken. As will be discussed in section 3.3.3, this cut helps in having a good Tracker reconstruction without the introduction of a significant systematic.

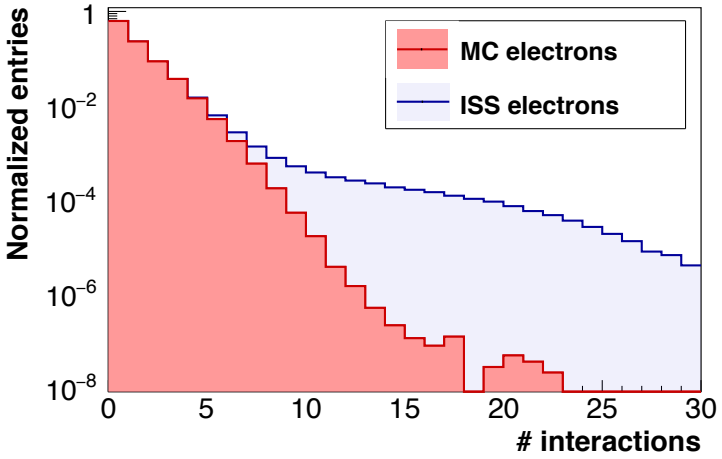

FIGURE 3.13: The distributions of the number of interactions (# interactions) between electrons selected from DATA and MC electrons are not in agreement.

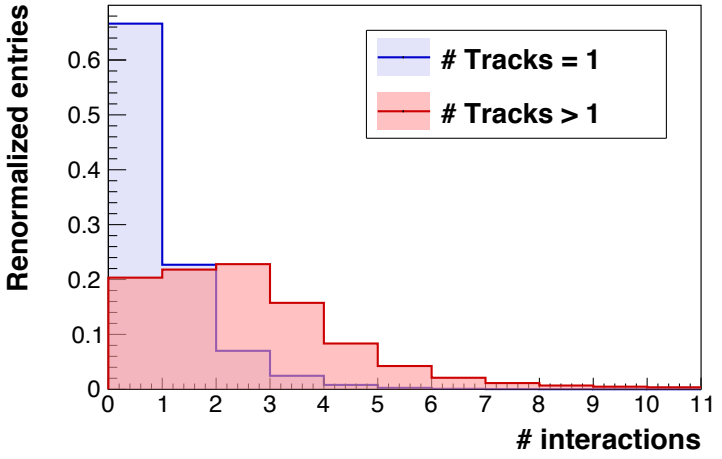

FIGURE 3.14: Number of interactions in a single track sample (# Tracks=1) and in a multi Tracks sample (# Tracks>1).

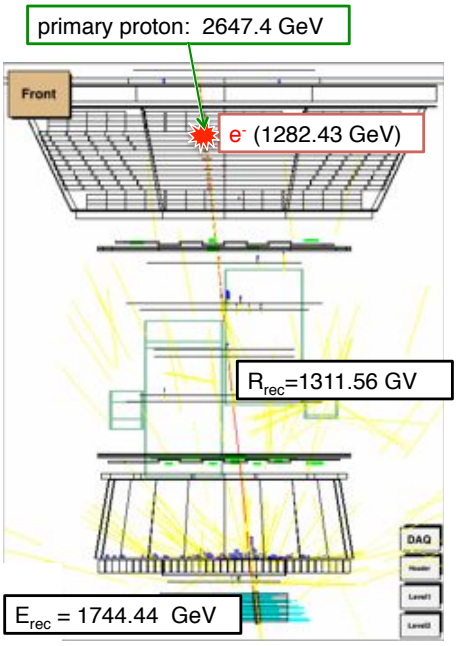

FIGURE 3.15: A typical event of proton (from MC) that constitutes an irreducible background.

3.2.4 Above geomagnetic cut-off

The last request that have been applied has the scope to select only primary particles. A fraction of the events that cross AMS are secondary particles trapped in the geomagnetic field. In order to reject those kind of particles, a cut over the energy of the particles compared with the value of the Støermer Rigidity Cutoff ($R^{\pm}_{\rm cutoff}(\theta,\phi)$). $R^{\pm}_{\rm cutoff}(\theta,\phi)$ has been computed both for positive and negative particles, using equation 1.19 where the geomagnetic altitude and azimuthal angles θ, ϕ have been evaluated in the AMS reference frame. For the cut, the Maximum Rigidity cutoff $R^{40^{\rm o}}_{\rm max}$, calculated as the maximum, between positive and negative, value of $R^{\pm}_{\rm cutoff}(\theta,\phi)$ for positive and negative particle in the whole AMS field of view and conservatively assumed to be $40^{\rm o}$, has been used:

$$R^{40^{\rm o}}_{\rm max} = max\{R^{+}_{\rm cutoff}(\theta,\phi), R^{-}_{\rm cutoff}(\theta,\phi)\}, \qquad \theta,\phi \in \Omega^{\rm AMS_{FoV}}_{40^{\rm o}} \tag{3.1}$$

Where $\Omega^{\rm AMS_{FoV}}_{40^{\rm o}}$ is the domain of θ and ϕ for the AMS filed of view.

The figure 3.16 shows the $R^{40^{\rm o}}_{\rm max}$ for the various latitudes and longitudes. The value of $R^{40^{\rm o}}_{\rm max}$ goes from few GV's (at the pole) up to $\sim 30\,$GV (at the equator). In order to select only primary particles, for each event belonging to the energy interval $[E_{\rm min}, E_{\rm max}]$, only the events with the $E_{\rm min} > 1.2 \cdot R^{40^{\rm o}}_{\rm max}$ have been selected. The requirement has been applied on the energy bin low edge to be consistent with the evaluation of the exposure time (see section 4.2). The factor 1.2 has been added

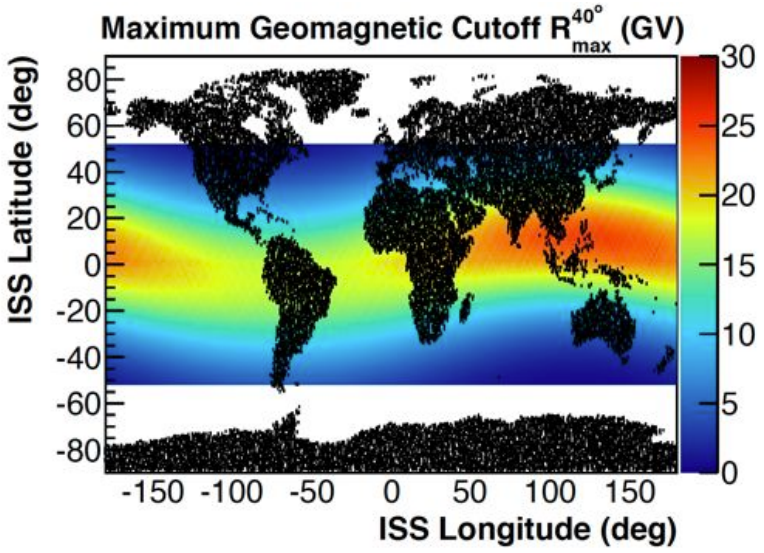

FIGURE 3.16: Maximum geomagnetic cutoff as a function of the ISS orbit position in geographical coordinates.

in order to have a conservative cut, since the value value of $R_{\rm max}^{40^\circ}$ has uncertainties due to Stoermer approximation used. As shown in figure 3.17, the this cut reduces the sample to the $\sim$ 10%. However the rejected events are almost composed by the protons component of the cosmic rays, since the energy used for the cut is the one measured by the ECAL and it is smaller than the true proton energy. . Above cutoff protons are rejected by the cut $E_{\rm min} > 1.2 \cdot R_{\rm max}^{40^\circ}$. For the $e^{\pm}$ component, the efficiency of the cutoff request is $\sim$ 100%.

3.2.5 Conclusions about preselection

The preselection has been applied over a total of 4.09×10^{10} events taken by AMS. The number of events that have been selected is 1.14×10^{8}, that correspond to the $\sim$ 0.3% of the initial sample, as shown in figure 3.17. The final sample consists in good reconstructed events of downward going, relativistic and unitary charge particles. All the cuts applied in the preselection have an high efficiency on $e^{\pm}$ particles.

3.3 $e^+ \setminus e^-$ measurement

The sample obtained at the end of the preselection is mainly constituted by protons, that compose the *background* that has to been removed, and contains a little

percentage of *signal*, constituted by e^+ and e^-. It also contains a negligible amount of anti-protons.

In order to extract the signal from the overwhelming protonbackground, ECAL and TRD detector responses have been used.
Using the knowledge of the different response released by the signal and by thebackground both in ECAL and TRD, it is possible to reach a very high e/p rejection power. Since ECAL and TRD are uncorrelated, it is possible to select a sample for the signal andbackground with ECAL in order to study the response in TRD and viceversa. Since the major part of the selected sample is constituted by protons, is quite simple to obtain abackground sample in order to study the response of the sub/detectors. The request to have positive charge sign is enough. Anyway it is possible to obtain a high purity even for the signal sample, by means of a strong cut on the ECAL variables (or TRD variables) and asking for negative charge sign (i.e. negative rigidity). This ensure a deep and accurate study of ECAL and TRD detectors, without using MC data which would introduce systematic errors to take into account.

In order to distinguish between e^+ and e^-, the sign of charge should be known with very high accuracy. The sign of the rigidity measured by the Tracker has been used to identify the charge. The effect due to the charge confusion has been taken into account as will be discussed in the section 3.3.3.

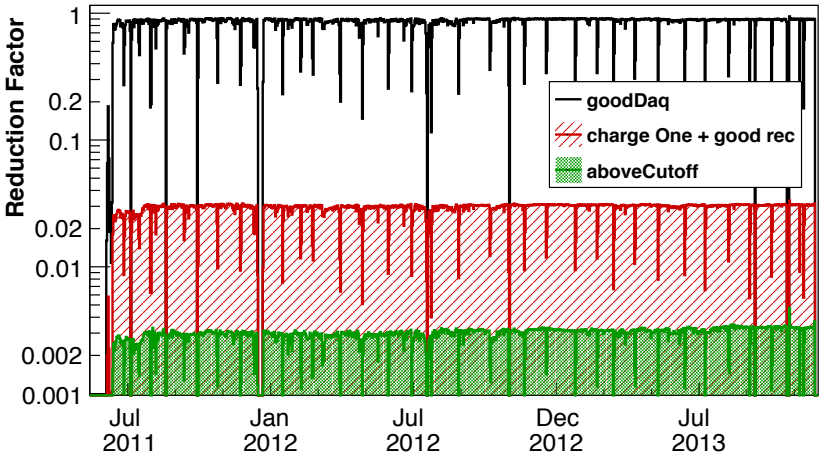

FIGURE 3.17: Reduction factor of the preselection at different levels: after the request to have good DAQ (black line), adding the request to have a sample of unitary charge and good reconstructed events (red line) and adding the request to have events above cutoff (green line).

3.3.1 e\p separation with ECAL

The signal released in a calorimeter is quite different for $e^{\pm}$ and protons [103]. When an electron (or a positron) reaches the first layer of ECAL, starts to emit photons due to the bremsstrahlung effect. Then the photon produces an electron-positron pair through the interaction with the atomic nuclei of the material. The secondary $e^{\pm}$ produced, again emit photons. These two processes (bremsstrahlung and pair-production) continue until photons fall below the pair production threshold, and energy losses of electrons due to ionization start to dominate over the losses due to bremsstrahlung. What has been produced it is the so called *electromagnetic shower*. The parametrization of the electromagnetic showers in a sampling calorimeter is well known as already discussed in section 2.1.7 and as reported in [104] When a proton reaches the calorimeter, the situation is quite different. Since the nuclear radiation length of ECAL is 0.6λ, the $\sim$55% of the protons go through the whole calorimeter losing their energy only trough the ionization process. These kind of protons arrived at ECAL as MIP ("minimum ionizing particles") and the energy that they depose in the calorimeter is very low ($\sim$200-400 MeV).

Remove thebackground constituted by MIP protons, is trivial. For example, a request on a minimum energy deposited in ECAL of $\sim$0.5 GeV or a minimum of 25 hits used for the Shower reconstruction are sufficient requests to remove proton MIP.

The problematicbackground is due by protons that give a shower in the calorimeter. The *hadronic shower* has very different characteristics with respect to the *electromagnetic* one. The hadronic showering process is dominated by a succession of inelastic hadronic interactions. At high energy, these are characterized by multiparticle production (mostly charged pions and nucleons) and particle emission originating from nuclear decay of excited nuclei. Due to the generation of π^0 that decay into $\gamma\gamma$, there is also an electromagnetic component present in hadronic showers.

Thank to the 3D reconstruction of the shower performed by ECAL, is it possible to exploit the different characteristic between electromagnetic and hadronic showers. The variables useful for distinguishing between signal andbackground (like the transverse and longitudinal shower development, the shower maximum, ecc...) are combined into a MultiVariate Approach (MVA), in particular, into a Boosted Decision Tree (BDT) [105], in order to maximize the rejection power of the calorimeter.

The BDT has been trained on electrons and proton samples selected from ISS data, without using MC. Thanks to a strong selection on TRD variables (as will be shown

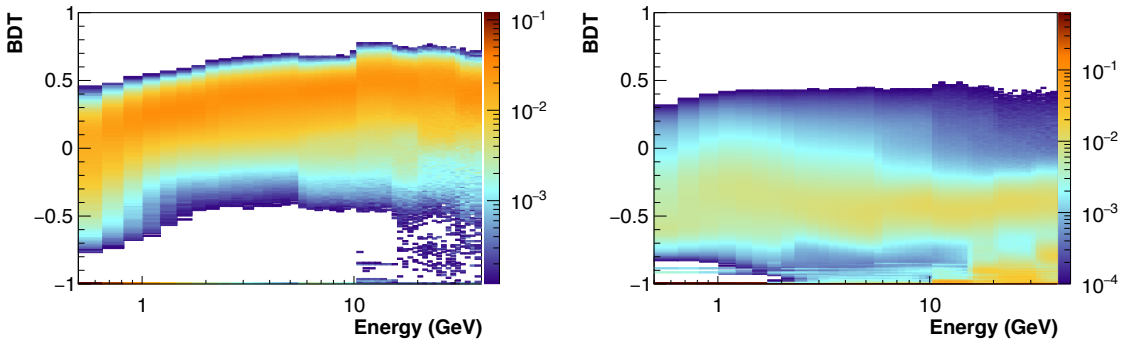

FIGURE 3.18: Distribution of BDT as a function of energy for an electron sample (left) and for a proton one (right).

in section 3.3.2) and to the selection of the charge sign reconstructed by Tracker, it is possible to have electrons and protons samples clean enough to tune the BDT.

The classification tool used in this analysis, $ECAL_{\mathrm{BDT}}$, relies on a total of 22 variables describing the longitudinal shower development and 39 variables describing the lateral shower development. The variables have been renormalized in order to remove their energy dependence, as described in [106]. The $ECAL_{\mathrm{BDT}}$ has been trained in 14 separate energy bins, the last one starting at ∼250 GeV, in order to locally maximize the e\p separation.

Figure 3.18 shows the distribution of BDT as a function of energy for an electron sample (left) and for a proton one (right) and figure 3.19 shows the BDT distribution in one energy bin (E=15.14–16.05 GeV). In the case of electrons, the BDT shows a major peak for value > 0. This is not true for the proton sample that show different populations according to the starting point of the shower. The most "dangerous" protons are the ones that start the shower quite early in ECAL since they have an high probability to be tagged as electrons by the BDT.

Figures 3.20 and 3.21 show the typical signal release in the AMS calorimeter by an electron, a MIP proton, a early showering proton and a deep showering proton.

3.3.2 e\p separation with TRD

The Transition Radiation (TR) is the process by which a charged particle emits soft x-rays in the crossing of a boundary between two media with different dielectric constants. The TR is emitted collinear to the primary particle's trajectory, and the amount of radiation emitted is proportional to the *Lorentz boost* γ and thus inversely proportional to the particle's rest mass. This dependence is the key for the e/p separation performed by the TRD: since the proton mass is ∼2000 times

the one for electron, a proton with kinetic energy 1TeV is like a 0.5 GeV electron in terms of transition radiation. Up to 300 GeV, electrons and positrons have as much higher probability of emitting transition radiation photons than protons, that the e\p rejection power is very high ($\sim 10^3$) before it starts to decrease. This difference in signal between protons and electrons is used to reach an high e/p rejection power through the TRD.

However, the signal of TRD has a strong dependence from the temperature gradients throughout the detector due to the environments conditions[107]. The gas contained in the straws tube (mixture of 90:10 of Xe and CO_2) continuously diffuses out of the pressurized proportional tubes with a consequent decrease in the gas pressure and change in the gas composition. This causes an increase in the gas gain and therefore an increase of the most probable value (MPV) of the energy deposited. For this reason, it is necessary to keep the gas mixture as stable as possible over time by means of two types of adjustments: high voltage adjustments (a decrease in high voltage will decrease the signal amplitudes) and gas refills (which increase the pressure and modify the gas composition).
In order to perform these adjustments a fast calibration is necessary. For this purpose a clean, single-track protons sample is used, since protons are the most abundant component ($\sim$ 90%) of the cosmic rays observed by AMS and they have a low probability to emit transition radiation, which allows in the calibration to use only the ionization signal. After applying the calibration, the detector response is stable for all tubes within 2%.

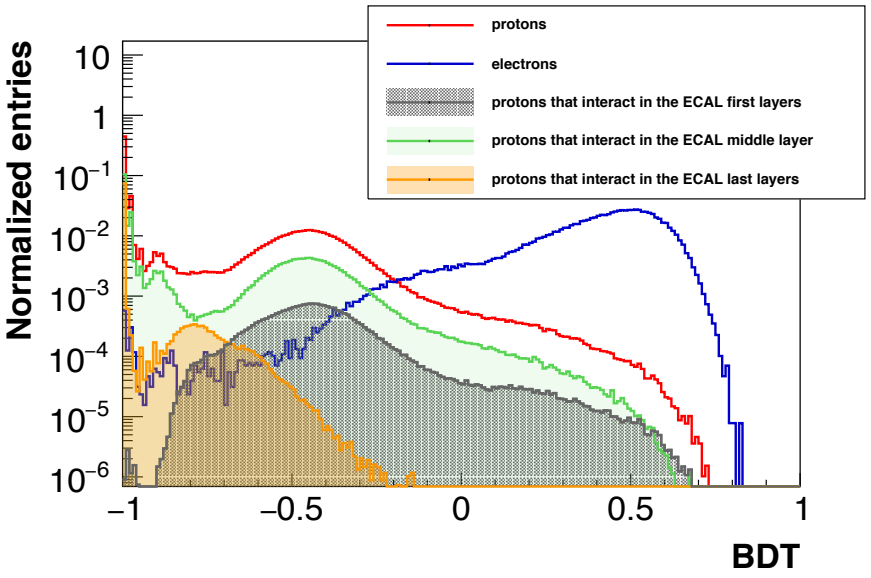

FIGURE 3.19: BDT distribution in one energy bin (E=15.14–16.05 GeV) for samples of electrons and protons interacting in different ECAL layers.

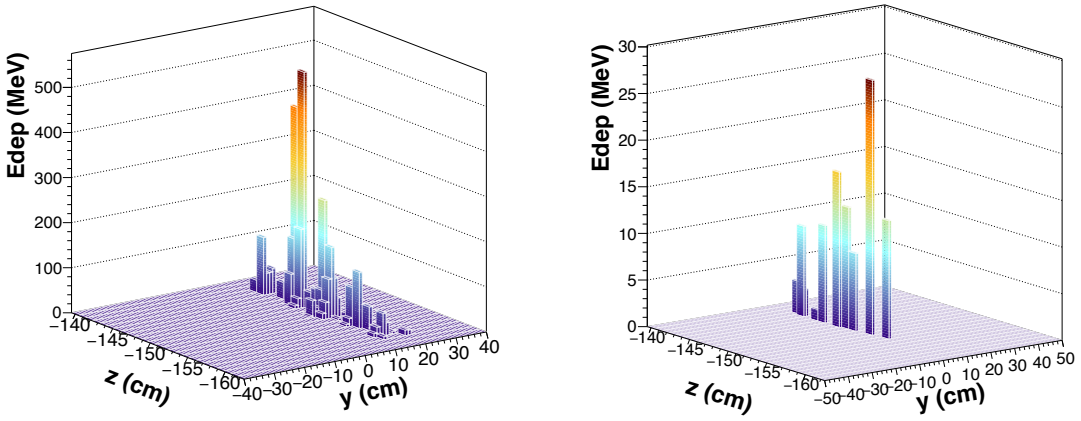

FIGURE 3.20: Left: energy deposit by an electron in the calorimeter. Right: energy deposit by a not interacting proton in the calorimeter.

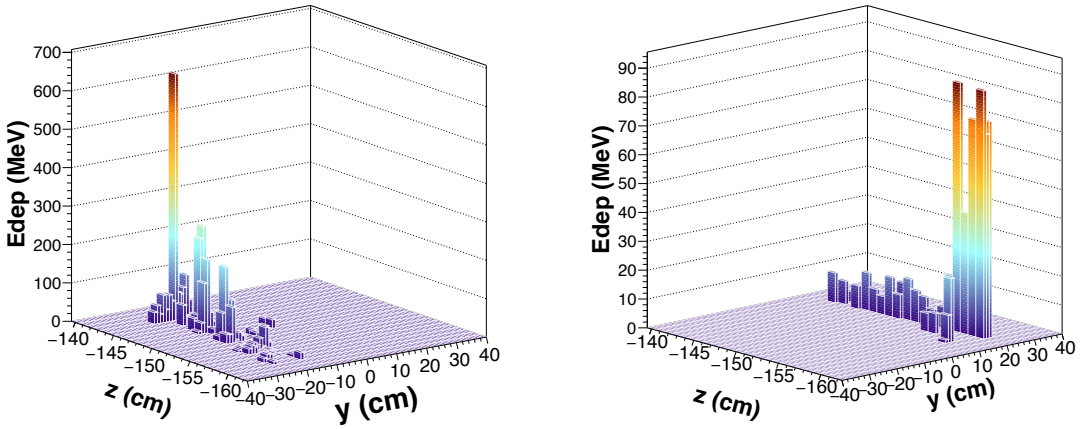

FIGURE 3.21: Energy deposit by a proton that interacts in the first layers of the calorimeter (left) and a proton that interacts in the last layers of the calorimeter (right).

Moreover, the temperature variations gradients affect also the physical positioning of the proportional tubes, which results in systematic errors in physics analysis. A standard alignment method is therefore present in the official AMS software. This method extrapolates the Tracker Track (the best known estimation of the particle track) to each TRD tube, where the track position is compared to the default position of the tube wire and the alignment correction is calculated. The alignment can then be accessed in the software to correctly calculate the path of each particle through the gas volume.

The straw tubes of the TRD are able to measure both the signal due to the ionization process, both the signal from the transition radiation. Figure 3.22 reports the signal in terms of ADC counts detected in the TRD by a proton sample and by electron

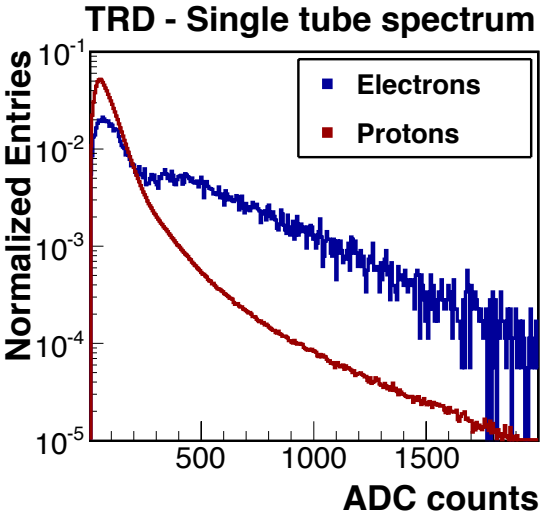

FIGURE 3.22: Signal in terms of ADC counts released in the TRD by a protons sample and by electrons sample.

sample (selected from ISS data by means of ECAL BDT and charge sign). In the proton sample is visible only the peak due to the dE/dx loss for ionization process. In the case of electrons there is the peak due to the ionization process plus a secondary peak due to the TR. The information from the energy deposited in all the 20 TRD layers has been combined in a classifier that is able to discriminate between electrons and protons. Since the ionization loss and transition radiation depends on various quantities like particle momentum p, path length in the tube l and Xe pressure $f_{\mathrm{X_e}}$, the classifier should take into account these dependencies. In order to build this classifier two clean samples of protons and electrons selected from ISS data by means of ECAL and Tracker have been used to define a parametrization of the *Probability Density Function* (PDF) $P_{\mathrm{i}}^{\mathrm{e,p}}(x|p,l,f_{\mathrm{X_e}})$ for the energy deposit in ADC deposit x in the i^{th} layer and for the electron e and proton p hypothesis.

The PDFs are used to define the *TRD likelihood* for the single event:

$$L^{\mathrm{e,p}} = \sqrt[n]{\prod_{\mathrm{i}=1}^{N} P_{\mathrm{i}}^{\mathrm{e,p}}(x_{\mathrm{i}}|p,l,f_{\mathrm{X_e}})} \tag{3.2}$$

where n is the number of TRD layers with energy deposit above threshold.

For the analysis a combination of L_{e} and L_{p} based on the *likelihood* algorithm (the same used in the published positron fraction analysis [65]) has been used in order to build a power classifier for e/p separation:

$$TRD_{\mathrm{lhr}}^{\mathrm{e/p}} = -\log\left(\frac{L^{\mathrm{e}}}{L^{\mathrm{e}}+L^{\mathrm{p}}}\right) \tag{3.3}$$

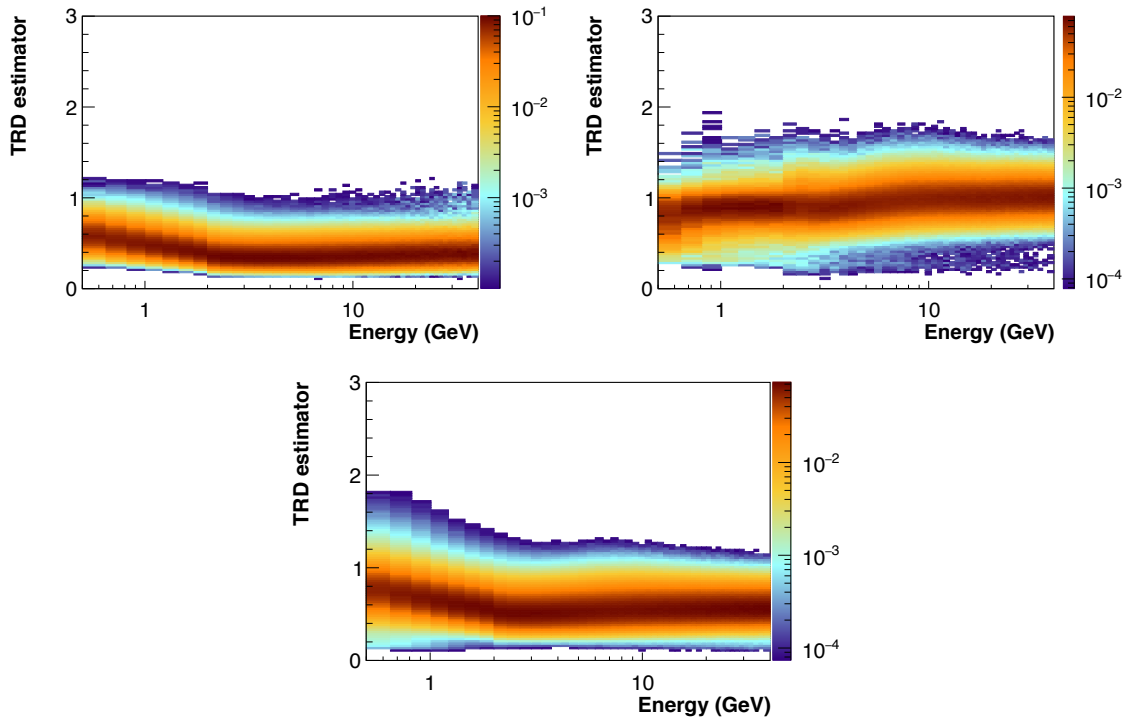

FIGURE 3.23: TRD e\p likelihood ratio distribution ($TRD^{e/p}_{lhr}$) as a function of energy for different samples: DATA electrons (top left), DATA protons (top right) and MC electrons (bottom).

In the figure 3.23 are shown the distributions of the likelihood ratio as a function of energy for electron and proton samples selected from ISS data and for MC electrons. Figure 3.24 shows the likelihood ratio distribution, for one energy bin 20.04–21.13 (GeV), for the electron sample compared both with protons and with MC electrons. As can be seen, the MC doesn't reproduce the DATA distribution, for this reason it can't be used for the definition of the templates that will be used to fit the signal (see section 3.4).

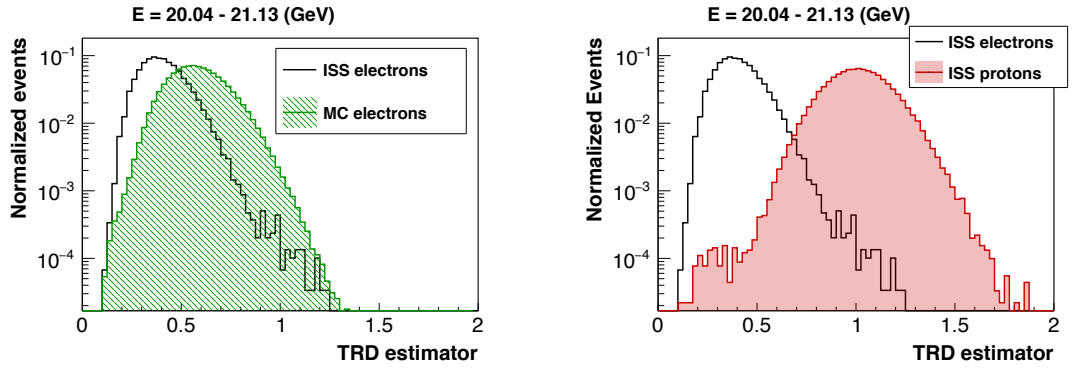

FIGURE 3.24: TRD e\p likelihood ratio distribution ($TRD^{e/p}_{lhr}$) for one energy bin (20.04–21.13 GeV) for DATA electrons (black line) compared with the same distribution for DATA protons (red filled line) and MC electrons (green filled line).

3.3.3 Tracker role in e^+, e^- measurement

The Tracker plays a fundamental role in the measurement of e^+ and e^-. The sign of the reconstructed rigidity together with the information coming from the ToF (*downward going* or *upward going* particle) give the sign of the charge and the possibility to distinguish between e^+ and e^-. However, the effect of the *charge confusion* (CC) should be taken into account in order to have the correct number of e^+ and e^-. Due to the CC, a negative electron can be reconstructed as a positron and viceversa. This means that even for background free e^+, e^- samples, the CC can spoil the electrons and positrons fluxes measurement.

The sources of CC are mainly two: the *spillover* and the *wrong hits* associated to the track [108].
The spillover is the dominant source of CC for high momentum particles: the curvature radius of the track inside the magnetic field increases as the particle momentum increases and, due to the finite measurement resolution of the trajectory, it becomes more and more probable to reconstruct the trajectory with a flipped curvature sign. At the MDR $\sim$ 16% of the particles are reconstructed with the wrong sign of the rigidity, due to this mechanism. This is a statistical effect and there's no way, except by the comparison to the absolute energy or momentum of the particle given by an independent detector, to reduce the resulting CC. However, since the analysis for the fluxes in time, is focused on the low energy part (up to $\sim$40 GeV), the spillover doesn't represent the main source of CC.

At lower energies, the largest source of CC is related to spurious hits, related to noise or interactions in the detector material, in the tracker, which are erroneously associated to the particle track in the pattern recognition. This hits are inducing a wrong reconstruction of its trajectory, hence, of its rigidity value and charge sign. This effect can be mitigated through the search for the effects of the interactions in the other sub detectors. Once their topology in the instrument is known they can be either rejected or statistically subtracted based on their characteristics distributions. As have been discussed in section 3.2.3, the request to have a hit in layer 2 has been included in the preselection to decrease the charge confusion. Figure 3.25, shows the CC as a function of energy evaluated from MC electrons and defined as the ratio between the events with the wrong reconstructed rigidity sign (R>0) and all electrons. The CC in this sample is $\sim$ 50% less with respect the one in a sample with all Tracker patterns.

The request on layer 2 helps in decreasing the charge confusion, but it is not enough. Up to $\sim$ 40 GeV, the effect of charge confusion can be negligible for the electrons but not for the positrons. If $\#e^{\pm}_{\text{observed}}$ is the number of observed electrons or positrons

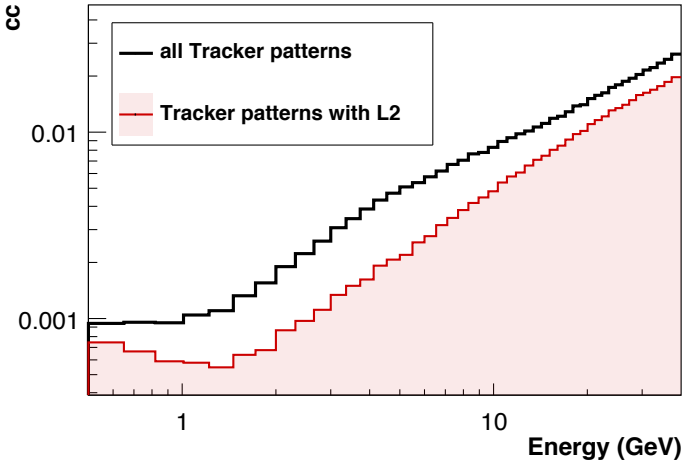

FIGURE 3.25: Charge confusion (CC) as a function of energy estimated from MC electrons, for a electron sample without any request on the Tracker pattern (black line) and for an electron sample which Tracker pattern has layer 2 (red and filled line). CC has been defined as the ratio between electrons with wrong reconstructed rigidity sign (R>0) and all electrons.

and $\#e^{\pm}_{\text{true}}$ is the real number of electrons or positrons, they are connected by the relations:

$$\begin{cases} \#e^{+}_{\text{obs}} = \#e^{+}_{\text{true}} \cdot (1 - cc) + \#e^{-}_{\text{true}} \cdot cc \\ \#e^{-}_{\text{obs}} = \#e^{-}_{\text{true}} \cdot (1 - cc) + \#e^{+}_{\text{true}} \cdot cc \end{cases} \tag{3.4}$$

The percentages of the wrong reconstructed number of $e^{\pm}$, $\delta^{\pm}$, can be defined as follow:

$$\begin{cases} \delta^{+} = \frac{\#e^{+}_{\text{true}} - \#e^{+}_{\text{obs}}}{\#e^{+}_{\text{true}}} \\ \delta^{-} = \frac{\#e^{-}_{\text{true}} - \#e^{-}_{\text{obs}}}{\#e^{-}_{\text{true}}} \end{cases} \rightarrow \begin{cases} \delta^{+} = cc \cdot (1 - \frac{\#e^{-}_{\text{true}}}{\#e^{+}_{\text{true}}}) \\ \delta^{-} = cc \cdot (1 - \frac{\#e^{+}_{\text{true}}}{\#e^{-}_{\text{true}}}) \end{cases} \tag{3.5}$$

At $\sim 10\,\text{GeV}$, the CC evaluated from electrons MC and defined as the ratio between the number of the electrons reconstructed with the wrong charge sign and the total number of electrons (see figure 3.25) is ~ 0.005. In the same energy interval, the value of the positron fraction is ~ 0.05 [65]. Substituting these value into the equation 3.6:

$$\begin{cases} \delta^{+} \sim 10\% \\ \delta^{-} \sim 0.5\% \end{cases} \tag{3.6}$$

In the case of positrons, the effect of charge confusion is not negligible and should be taken into account. The charge confusion is evaluated from MC electrons and the correct number of electrons and positrons are obtained from equation 3.4:

$$\begin{cases} \#e^{+}_{\text{true}} = \frac{\#e^{+}_{\text{obs}}(1-cc) - \#e^{-}_{\text{obs}} cc}{1-2cc} \\ \#e^{-}_{\text{true}} = \frac{\#e^{-}_{\text{obs}}(1-cc) - \#e^{+}_{\text{obs}} cc}{1-2cc} \end{cases} \tag{3.7}$$

The effect of the charge confusion correction can be appreciated in the case of positron fraction in figure 3.26. The errors on the fluxes due to charge confusion, can be derived from equation 3.7:

$$\begin{cases} \delta\#e^{+}_{\text{true}} = \frac{\#e^{+}_{\text{obs}} - \#e^{-}_{\text{obs}}}{(1-2cc)^2}\delta_{\text{CC}} \\ \delta\#e^{-}_{\text{true}} = \frac{\#e^{-}_{\text{obs}} - \#e^{+}_{\text{obs}}}{(1-2cc)^2}\delta_{\text{CC}} \end{cases} \tag{3.8}$$

Figure 3.27 shows the value of CC with its corresponding error, δ_{CC}, used for the fluxes evaluation, as a function of energy. The errors due to CC are shown in figure 3.27 (left plot), as a function of energy (GeV).

The errors on the CC, δ_{CC}, has been determined by the AMS collaboration [67] taking into account the DATA/MC discrepancies in the amount of CC itself. The CC can be extracted, directly form the DATA, using a dedicated estimator derived with a boosted decision tree technique which combines all the information from ToF, ACC and Tracker such as the track χ^2, the rigidity reconstructed using different sets of tracker layers, and the number of hits in the vicinity of the track. In each energy bin, two templates are defined, one for particles with correctly reconstructed charge sign and another for particles with the wrongly reconstructed one. The former is defined using the negative rigidity DATA sample. The latter is based on the Monte Carlo simulation.

Besides being the key instrument for the charge-sign reconstruction and, hence, for matter/anti-matter separation, the tracker can be also used for the e\p rejection. The ratio between the ECAL energy E and the Rigidity measured by the Tracker R can be used as a powerful discriminating variable to increase the e/p rejection capabilities of AMS. As explained in section 3.3.1 half part of protons arrived in the calorimeter as MIPs with the result that the measured energy is ∼0.4 GeV. The

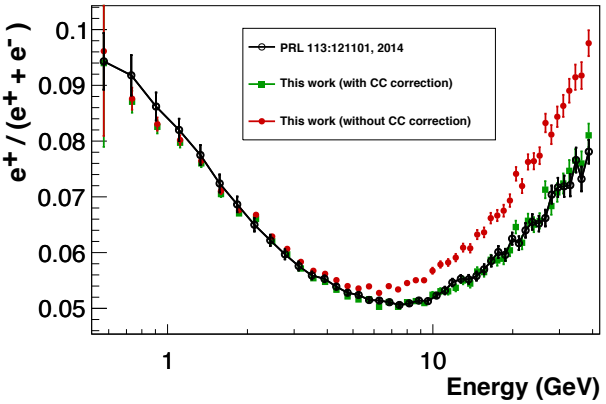

FIGURE 3.26: Result obtained with AMS positron fraction of positron fraction before.

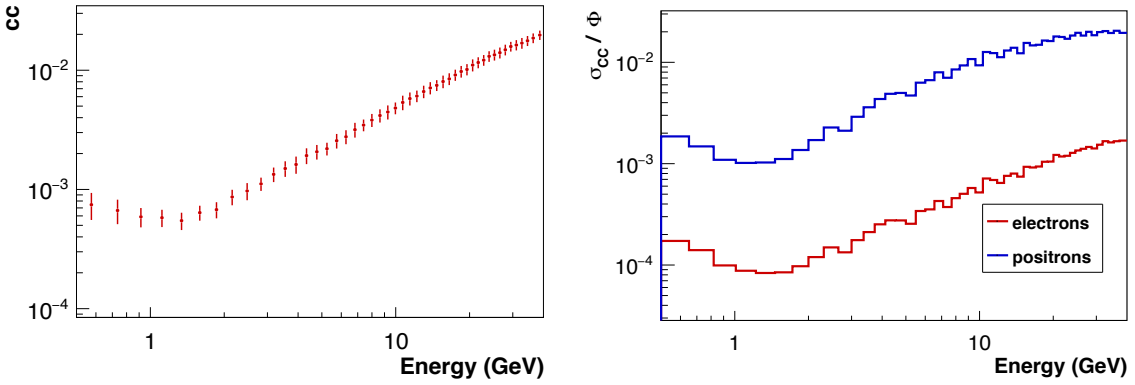

FIGURE 3.27: *cc* has a function of energy used for the fluxes evaluation (left) and relative errors on fluxes as a function of energy due to *cc* correction (rigth).

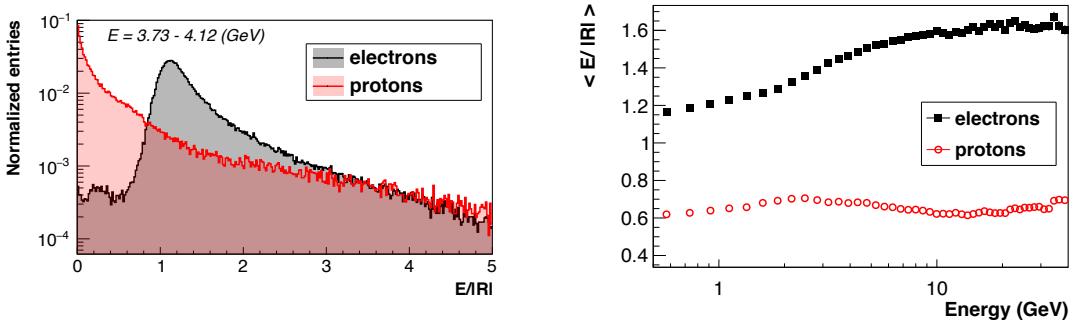

FIGURE 3.28: Distribution of E/R for an electron and a proton sample for one energy bin, E = 3.73–4.12 GeV, (left) and the E/R peak distribution for electrons and protons, as a function of energy (right).

remaining protons start an hadronic shower and the measured energy is, empirically, $E \sim 0.5R$. As result the major part of protons will have $E/R < 1$. Conversely, in case of the electrons, the energy measured by the ECAL is close to the rigidity measured by the Tracker and hence $E/R \sim 1$. Moreover, the electrons are subjected to the bremsstrahlung effect, as explained in section 3.2.3. Due to this phenomena, an electron can emit photons in the Tracker, loosing its energy. Consequently the rigidity measured by the Tracker will be less than the true electron energy. However the ECAL is able to measure both the remain energy of electron, both the energy of lost by the electron as emitted photons. The result is that the total energy measured by ECAL is near to the true value of the initial electrons energy. As result, the E/R ratio for electrons will be greater than 1.

Figure 3.28 (left) shows the distribution of E/R for an electron and a proton sample for one energy bin: the two peaks for $E/R < 1$ and $E/R \sim 1$ can be clearly observed.

Figure 3.28 (right) shows the peak of E/R as an indicator of the e/p separation

power of E/R. At least for the energy range considered in this work (0.5-40 GeV), E/R can be used to create control samples of electrons and protons.

3.4 Signal Extraction

In order to extract the signal constituted by e^- and e^+, the TRD likelihood ratio e/p ($TRD^{\mathrm{e/p}}_{\mathrm{lhr}}$), the Boosted Decision Tree build with the information coming from the ECAL ($ECAL_{\mathrm{BDT}}$), the E/R ratio and the Rigidity sign reconstructed by the Tracker have been used.

The analysis method used is the following:

- The signal has been extracted by means of a fit on the $TRD^{\mathrm{e/p}}_{\mathrm{lhr}}$, using the `RooFit` package [109, 110].
- The reference distributions (templates), used in the fit, have been extracted directly from DATA using the $ECAL_{\mathrm{BDT}}$, the E/R ratio and the sign of the charge.
- The electrons and the positrons have been separated using the information on the charge sign coming from the Tracker.

The method is similar to the one used for the *all electron* and separate $e^{\pm}$ measurements [67, 100] with mainly two differences. First, the $ECAL_{\mathrm{BDT}}$ is used only to define the templates and not for the suppression of the proton background in the sample to fit. With the increase of energy, the overlapping between electron and proton TRD templates increases making harder and harder the extraction of the signal (especially above 200 GeV). A cut on the $ECAL_{\mathrm{BDT}}$ with high efficiency on signal could be used to reduce the systematic uncertainty in the evaluation of the $e^{\pm}$ component [2]. However the energy range analyzed in this work is up to 40 GeV and a cut on the $ECAL_{\mathrm{BDT}}$ is not needed.

Another difference with the all electrons analysis is that the templates for signal and background are evaluated not only in each energy bin, but also as a function of time.

In this section will be described the whole signal extraction procedure. The assessment of the systematic uncertainties will be addressed in section 3.5.1.

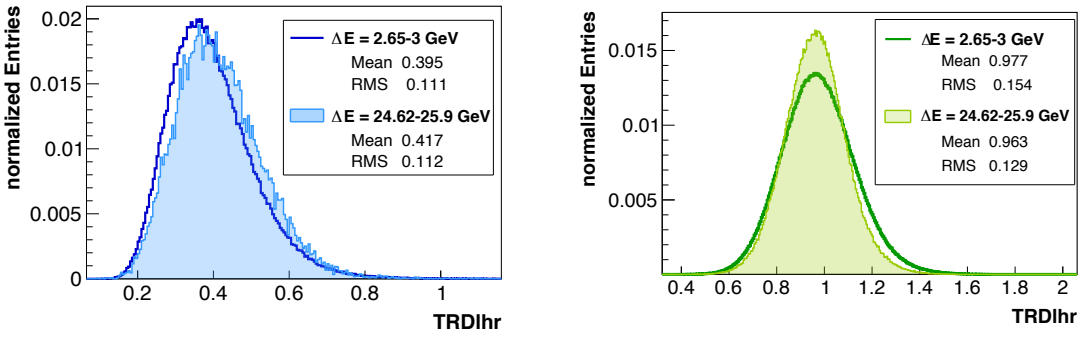

FIGURE 3.29: TRD_{lhr} distribution in two different energy bins for electron (left) and proton (right) samples selected on DATA.

3.4.1 Definition of TRD templates

As already discussed in section 3.3.2, the distributions of TRD_{lhr} for DATA and MC are not in agreement. For this reason, the reference distributions of TRD_{lhr} for signal and background have been extracted selected directly from DATA.

The templates have been defined cutting on the $ECAL_{\text{BDT}}$, E/R and the sign of the charge. These requirements ensure a high purity for the templates.

However the shape of the templates can depend from the selection applied. This dependence constitutes one of the major systematic uncertainties on the number of electron and positron counts obtained from the fit procedure as will be discussed in section 3.5.1.

Figure 3.29 shows electron and proton templates for two different energy bins. Is clear that there's a strong dependence from the energy. This is also clear from figure 3.30, that shows the median and the RMS of the templates, both for signal and protons as a function of the energy. For this reason, at least in the energy range in which the analysis has been performed (0.5-40 GeV), it is not possible use a *universal* reference distribution valid for the all energies as it has be done for the all electrons analysis, but the templates should be defined bin by bin.

The same kind of argument can be assessed for the time. Figure 3.31 shows the distributions for signal and background in two different time intervals of 27 days each, for a given energy bin. As in the case of the energy, the shape of the templates in two different time bin, is different. This is more clear in figure 3.32 that shows the median and the RMS of the templates as a function of time, in a given energy bin. The change in time in the TRD signal is expected and it is due either to the operation periodically performed on the TRD, and to the environmental conditions which have been explained in the section 3.3.2.

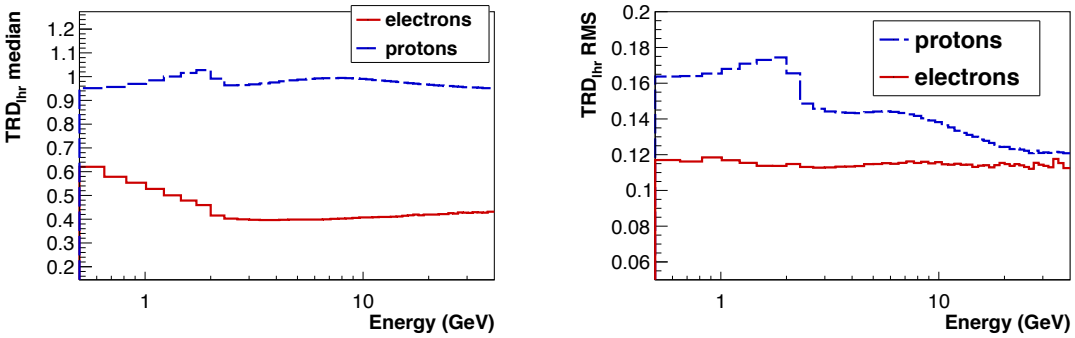

FIGURE 3.30: Median (left) and RMS (right) of TRD_{lhr} distribution as a function of energy for electrons and protons samples selected on DATA.

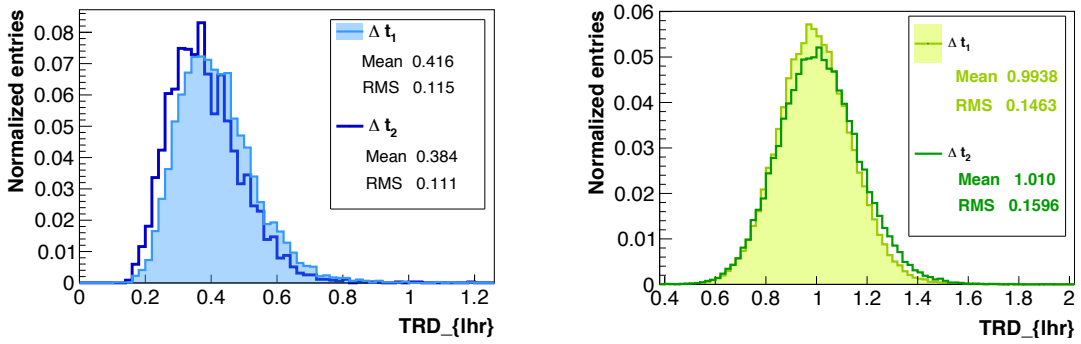

FIGURE 3.31: TRD_{lhr} distribution in two different time bins for electron (left) and proton (right) samples selected on DATA.

As an example, the median and the RMS of templates as a function of time appears more stable after 2011. This is due to the fact that TRD was first operated with weekly adjustments of the high voltage, so that the diffusion losses caused a gradual increase of the gas gain. This strategy was changed on October 26th, 2011, and daily adjustments of the high voltage are now being done, in order to keep the gas gain at a constant level. Whilst the sawtooth trend - more evident in the median and in the RMS of the proton template, due to less statistical fluctuations with respect to the electron one - is due to the refilling procedure performed $\sim$ every month.

Due to the time dependence of the TRD signal shown above, the reference distributions should be defined bin by bin not only in energy but also as a function of time .

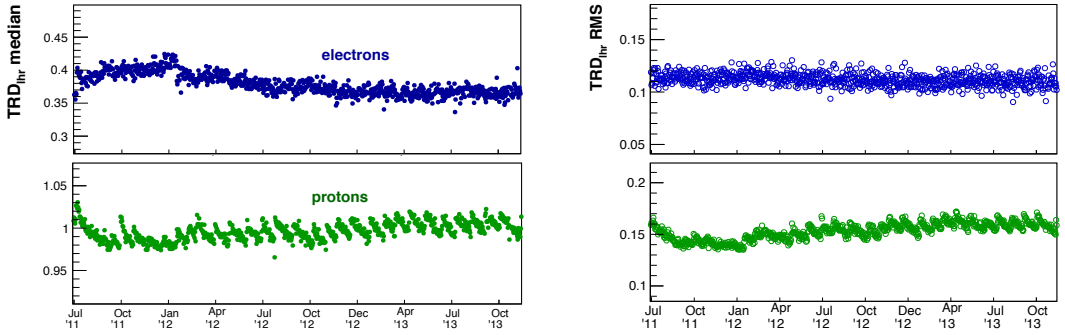

FIGURE 3.32: Median (left) and RMS (right) of the TRD_{lhr} distribution as a function of time for electron and proton samples selected on DATA.

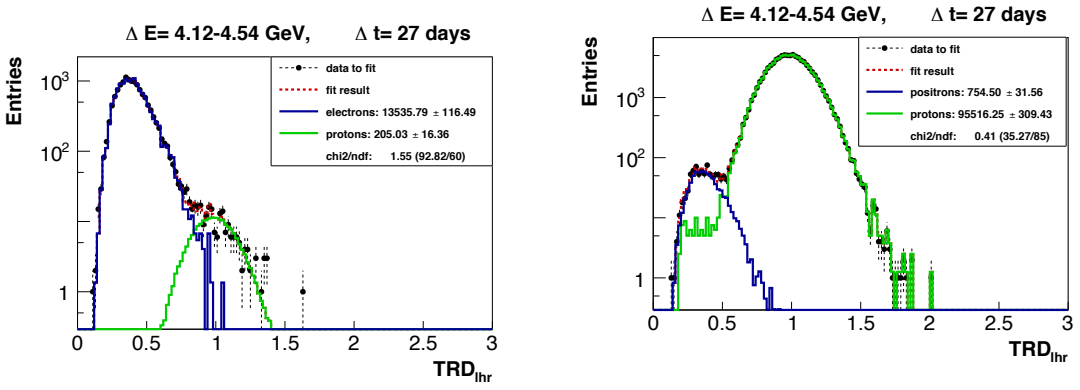

FIGURE 3.33: An example of the *template fit* procedure in one energy bin (ΔE=3.73-4.12 GeV) and in one time interval of 27 days for the extraction of e^- (left) and e^+ (right): the black point are the preselected DATA with positive charge sign, the red dashed line is the result of the fit that corresponds to the sum of signal (blue line) and background (green line).

3.5 Fitting procedure

The number of e^- and e^+ have been statistically extracted from the background of protons using a *template fit* procedure performed on the TRD_{lhr} distribution.

The sample to fit has been selected from DATA applying the preselection (see section 3.2) and the request on the charge sign (negative in case of electrons, positive in case of positrons). The resulting sample contains both signal and background.
For each energy bin and for each time bin, the TRD_{lhr} distribution of DATA is fitted as a sum of the signal and background single contributions using the TRD_{lhr} templates, using the `RooFit` package [109, 110]. As described in section 3.4.1 and as will be deeper discussed in section 3.4.1 the TRD_{lhr} templates have been defined directly from DATA applying request on $ECAL_{\mathrm{BDT}}$, E/R and the charge sign.

An example of the fitting procedure in one energy bin (ΔE=3.73-4.12 GeV) and in a time interval of 27 days is shown in figure 3.33, both for the extraction of the

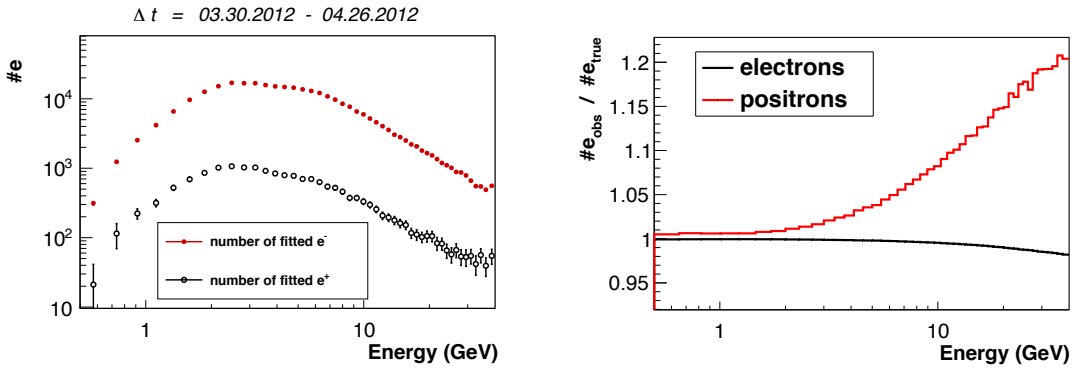

FIGURE 3.34: Left: Number of observed e^- and observed e^+, coming from the fitting procedure, in one time interval of 27 days. Right: Fraction of charge confused events ($\#e_{\rm obs}/\#e_{\rm true}$)) as a function of the energy.

number of e^- and e^+. The black points are the sample to fit, defined from DATA, the red dashed line is the result of the fit that corresponds to the sum of signal (blue line) and background (green line).

However, the shape of the templates depends on the selection applied to define them. Different templates give a different fit result. For this reason in each ΔE and Δt several fits have been performed with different signal and background templates. In particular, 436 different templates (i.e. 436 different fits) have been explored to fit the number of electrons and 144 different templates for the number of protons. More details will be given in section 3.5.1.

Each fit gives slightly different number of fitted electrons or positrons. As will be discussed in section 3.4, only the 45(15) results with the best χ^2's have been used for the electron(positron) measurement. The mean of distribution of fitted electrons or positrons has been taken as the number of observed e^- ($\#e^-_{\rm obs}$) or observed e^+ ($\#e^+_{\rm obs}$)

Figure 3.34 (left) shows $\#e^-_{\rm obs}$ and $\#e^+_{\rm obs}$, coming from the fitting procedure, in one time interval of 27 days as a function of the reconstructed energy.
However, in order to obtain the correct number of electrons and positrons ($\#e^\pm_{\rm true}$), the fraction of charge confused events has been taken into account in order to correct the number of electrons and positrons ($e^\pm_{\rm obs}$), according to the equation 3.4.
The figure 3.34 (right) shows the fraction of charge confused events ($\#e_{\rm obs}/\#e_{\rm true}$) as a function of the energy. As already discussed in section 3.3.3, the CC confusion affects more positrons than electrons and spoils the result of $\sim 20\%$ at 40 GeV.

3.5.1 Uncertainties

The number of electrons and positrons evaluated by the fitting procedure discussed above is affected both by an error that came from the statistical fluctuations, and by an error that came from the systematic uncertainties.

Statistical fluctuation uncertainties
The error returned by the fit procedure constitues the statistical error, δ_{stat}. This error is a combination of two different uncertainties:

- δ_{poisson}: **poissonian error** defined as $\delta_{\text{poisson}} = \sqrt{\#e^{\pm}}$ where $\#e^{\pm}$ is the number of fitted electrons or positrons;
- δ_{sep}: the *separation systematic* error related to the **finite TRD e/p separation capabilities**.

and they can be combained as follows:

$$\delta_{\text{stat}} = \delta_{\text{sep}} \oplus \delta_{\text{poisson}} \tag{3.9}$$

As figure 3.35 shows, the number of $\#e^{\pm}$, hence δ_{poisson}, depends on the energy. Another variable that affects δ_{poisson} is the width of the time interval in which the analysis is performed. As figure 3.35 shows, at low energies ($\Delta E = 3.73 - 4.12\,\text{GeV}$) the number of e^+ and e^- measured using DATA of 1 day presents a very low statistical power: $\delta_{\text{poisson}} \setminus \#e^- \sim 4\%$ in the case of electrons and in the case of positrons $\delta_{\text{poisson}} \setminus \#e^+ \sim 20\%$. At higher energies ($\Delta E = 27.25 - 28.68\,\text{GeV}$) the situation get worst: for electrons $\delta_{\text{poisson}}\#e^-$ increases up to $\sim 20\%$ and for positrons up to $\sim 70\%$. Using the DATA taken in one year, $\delta_{\text{poisson}}\#e^-(e^+)$ decreases up to $\sim 0.3\%\,(1\%)$ for low energies and up to $\sim 1\%\,(3\%)$ at higher energies.

Figure 3.36 shows, as a function of energy, the relative error $\delta_{\text{stat}}/\#e^{\pm}$ respectively for electrons and positrons divided in δ_{sep} and δ_{poisson}. For the electrons the major contribution to δ_{stat} is given by the instrinsic statistical error δ_{poisson} while the error coming from the separation capabilities of TRD can be neglected. This means that there is no need for an additional cut (for example over the ECAL variables) to suppress the proton background as instead needed for the high energy analysis [2]. For positrons δ_{sep} is almost negligible, with respect to δ_{poisson} only above $\sim$2 GeV. This indicates that below this energy the TRD is not able to clearly separate protons from positrons. However there is no way to reduce background below this energy applying other cuts without loosing a consistent part of the statistic.

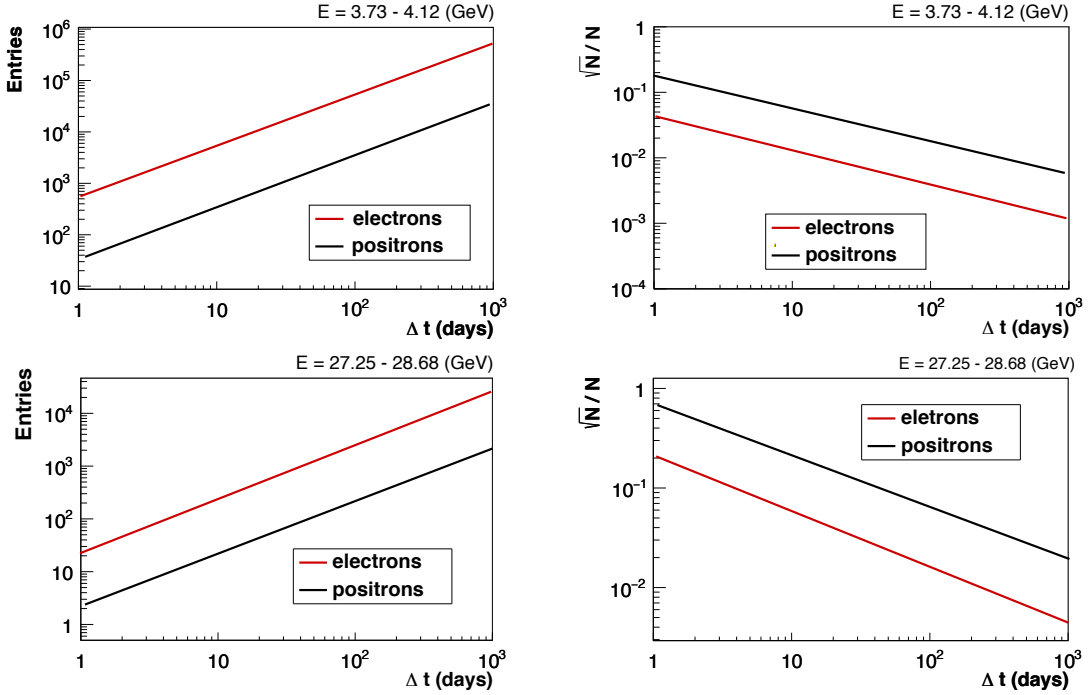

FIGURE 3.35: Number (left) and relative statistical error (right) on the fitted electrons (red points) and positrons (black points) as a function of the time bin used for the analysis, in two different energy bin.

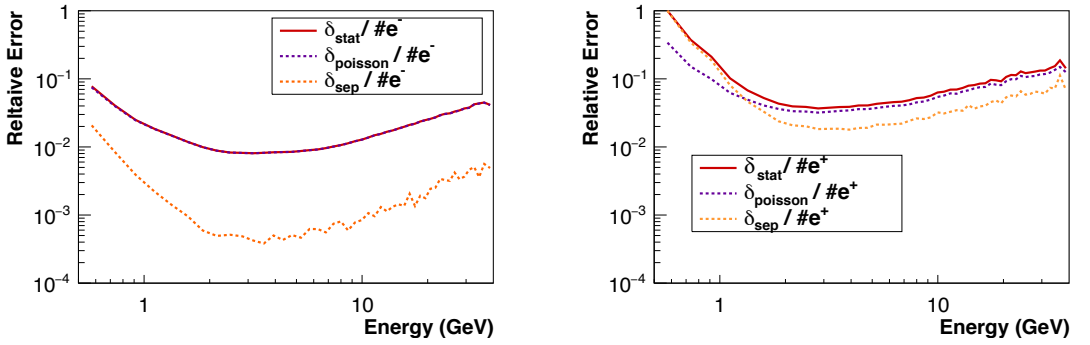

FIGURE 3.36: Relative error coming from the fit (red line) divided into the purely statistical one (violet dashed line) and into the one coming from the separation power of TRD_{lhr} variable (orange dashed line) for electrons (left) and positrons (right).

Systematic uncertainties

The systematics uncertainties are related to the template definition:

- uncertainty related to the selection used to obtain the templates ($\delta_{\mathrm{sel\_tmpl}}$);
- uncertainty and the one related to the finite statistics of them ($\delta_{\mathrm{stat\_tmpl}}$).

The $\delta_{\mathrm{sel\_tmpl}}$ uncertainty comes from the impossibility to achieve, after the very same selection used for the data to be fitted, the distribution of a pure sample of signal or background. In this analysis MC data are not used for the definition of the

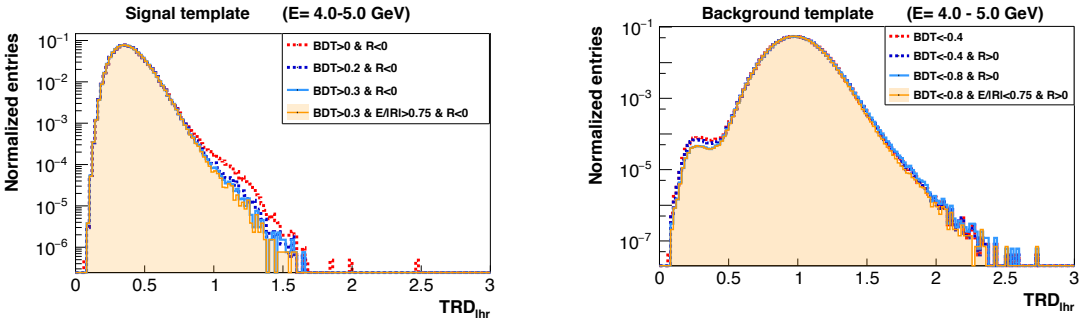

FIGURE 3.37: Templates distribution for signal (left) and background (right) obtained from different selections, in the energy interval E=4–5 GeV.

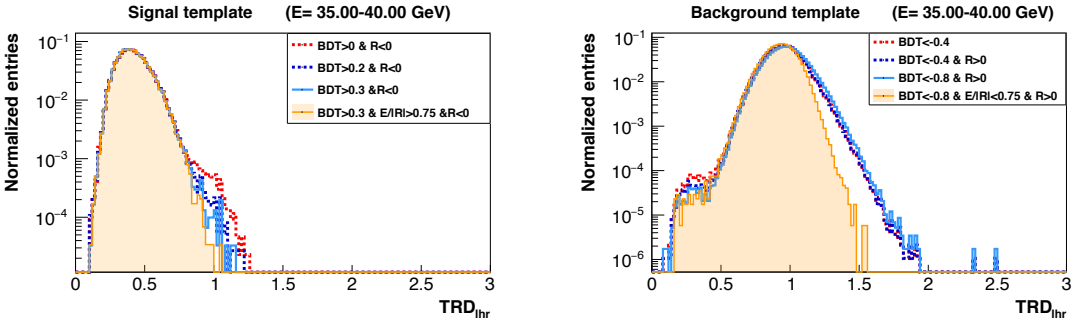

FIGURE 3.38: Templates distribution for signal (left) and background (right) obtained from different selections, in the energy interval E=35–40 GeV.

templates, since as explained in section 3.3.2 the TRD distributions between DATA and MC are not in agreement. For this reason the templates should be selected directly from DATA. In order to have a clean sample of electrons and protons to define respectively signal and background templates, a cut over BDT, sign of the Rigidity and E/R, has been applied. However, the templates distribution can be biased by the selection applied to obtain them as show in figures 3.37 and 3.38 for 2 different energy bins.

The second peak for low energy value of TRD_{lhr} that can be observed in the proton background template is due to Helium nuclei that fragment in the top of AMS and that are reconstructed as unitary charge particles by the inner tracker. This can be clearly seen in figure 3.39 that shows, for the proton sample used to define the template, TRD_{lhr} as a function of the charge measured using only the energy deposited on the first Tracker Layer. In order to select the protons template, the request to have a unitary charge measured by the inner tracker has been applied. However the figure shows a population with likelihood value less then 0.5 that has Z=2 according to the first tracker layer. Even after the unitary charge selection on the inner tracker charge value, a population detected as Helium by the first Tracker layer survived. This population have a typical likelihood value below 0.5,

close to the electron peak. Is important, hence, to keep this population in the template definition, avoiding any further selection that can reduce it, since this is a background population that has to be counted as background in the fitting procedure.

Several definitions of the same templates have been explored in order to estimate the systematics on the template definition ($\delta_{\text{sys\_tmpl}}$). For each template a fit has been performed in order to extract the signal.

For the estimation of $\delta_{\text{sys\_templ}}$, all the 30 months of data have been used. In this way the evaluation of the uncertainty is not spoiled by statistical effects.

For electrons, 12 different templates have been defined, combining 4 different cuts on BDT and 3 different cuts on E/R:

$$selection + R < 0 + \begin{bmatrix} ECAL_{\text{BDT}} > 0.1 \\ ECAL_{\text{BDT}} > 0.2 \\ ECAL_{\text{BDT}} > 0.25 \\ ECAL_{\text{BDT}} > 0.3 \end{bmatrix} + \begin{bmatrix} E/R > 0 \\ E/R > 0.5 \\ E/R > 0.75 \end{bmatrix} \tag{3.10}$$

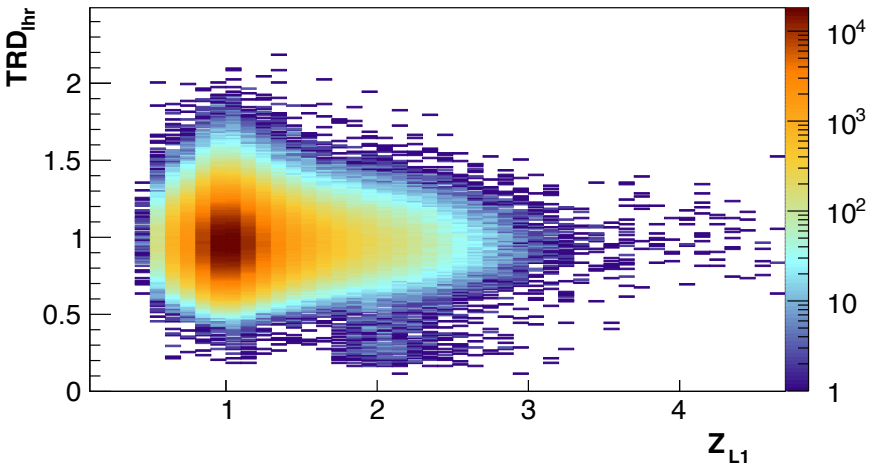

FIGURE 3.39: TRD_{lhr} vs the charge measured by the first layer of tracker (Z_{L1}) for the proton template sample. The second population with low value of TRD_{lhr} is, according to Z_{L1}, Helium.

For protons, 36 different templates have been defined, combining 4 different cuts on BDT, 3 different cuts on E/R and 3 different cuts on the Rigidity sign:

$$selection \begin{bmatrix} R>0 \\ R<0 \\ allR \end{bmatrix} + \begin{bmatrix} ECAL_{\mathrm{BDT}} > 0.1 \\ ECAL_{\mathrm{BDT}} > 0.2 \\ ECAL_{\mathrm{BDT}} > 0.25 \\ ECAL_{\mathrm{BDT}} > 0.3 \end{bmatrix} + \begin{bmatrix} E/R > 0 \\ E/R > 0.5 \\ E/R > 0.75 \end{bmatrix} \tag{3.11}$$

Even if the ones defined with R>0 constitute a genuine sample of protons, they do not are representative of the charge confused part of the proton background. In order to extract the signal for e^- all the electron and proton templates have been used, for a total of 432 combinations, hence 432 fits have been performed.

For the extraction of the signal for e^+, all the 12 electron templates have been used. For the proton template only the ones defined with R>0 have been used, since the other definitions can be rejected *a priori*. In order to extract the number of e^+ a total of 144 combinations of templates have been used.

Not all the combinations of templates give a result with a good χ^2. This means that not all the exploited templates are good to described the signal and background samples. For this reason, as anticipated in section section 3.4, between the different 432 (144) number of $e^-(e^+)$ obtained from the fitting procedure, only the 45 (15) results with the best χ^2, have been used for the flux measurment. An example of the distribution of the results with the best χ^2 is shown in figure 3.40 for positrons and electrons, as example in on energy bin ($\Delta E = 3.73 - 4.12\,\mathrm{GeV}$).

The MEAN and the RMS of the distribution of the results with the best χ^2 have been respectively taken as the number of observed events ($(e^{\pm}_{\mathrm{obs}})^{\mathrm{TOT}}$) and the systematic

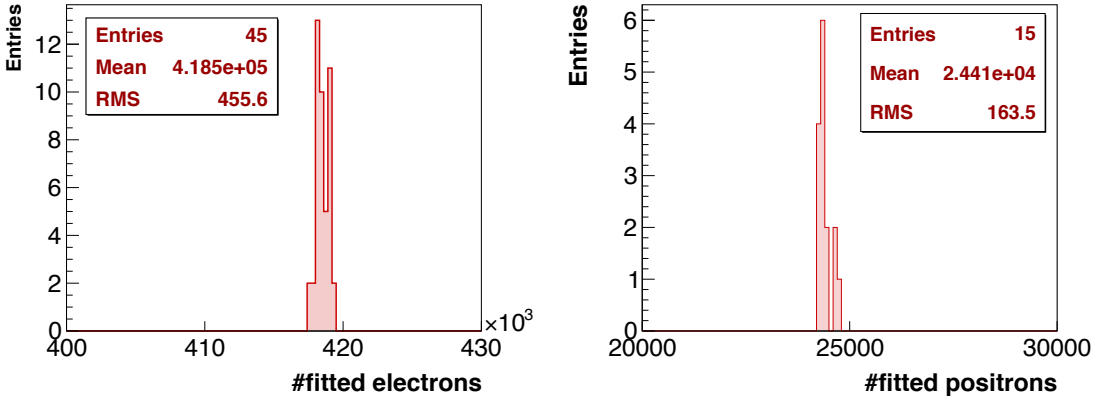

FIGURE 3.40: Distribution of the results with the best χ^2, for electrons (left) and positrons (right), in on energy bin ($\Delta E = 3.73 - 4.12\,\mathrm{GeV}$.

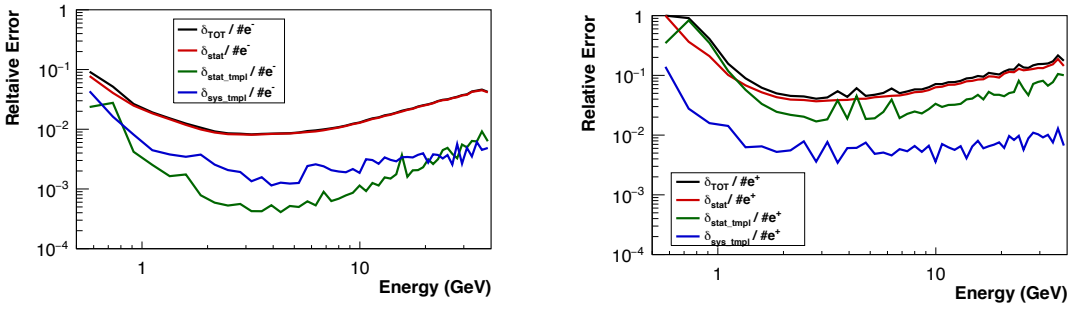

FIGURE 3.41: Total relative error on e^- (left) and e^+ (right) obtained from the fitting procedure and divided into $\delta_{\rm stat}$, $\delta_{\rm sys\_tmpl}$, $\delta_{\rm stat\_tmpl}$, as a function of energy.

error coming from the selection of template ($\delta^{\rm TOT}_{\rm sys\_templ}$). In order to obtaine the value of $\delta_{\rm sys\_templ}$ in one time interval ($\delta^{\Delta t}_{\rm sys\_templ}$) the following formula has been applied:

$$\frac{\delta^{\Delta t}_{\rm sys\_templ}}{(e^{\pm}_{\rm obs})^{\Delta t}} = \frac{\delta^{\rm TOT}_{\rm sys\_templ}}{(e^{\pm}_{\rm obs})^{\rm TOT}} \quad \rightarrow \quad \delta^{\Delta t}_{\rm sys\_templ} = \frac{\delta^{\rm TOT}_{\rm sys\_templ}}{(e^{\pm}_{\rm obs})^{\rm TOT}} \cdot (e^{\pm}_{\rm obs})^{\Delta t} \tag{3.12}$$

where $(e^{\pm}_{\rm obs})^{\Delta t}$ is the number of observed events in the time interval Δt.

Another systematic error comes from the finite statistic of the templates ($\delta_{\rm stat\_tmpl}$). For the estimation of $\delta_{\rm stat\_tmpl}$, in each energy bin and in one time interval[4] the following procedure has been applied:

1. Template distributions for electrons and protons are generated. Each $i^{\rm th}$ template bin has been filled with a random number from a poisson distribution with mean $\rm N_i$, where $\rm N_i$ is the number of the events in each $i^{\rm th}$ bin of the template really used for the the flux measurement.

2. The fit procedure is performed in order to extract the signal.

This procedure has been applied 1000 times in each energy bin. The RMS of the distribution of these 1000 results has been taken as δ_{sel_tmpl}.

In figure 3.41, as a function of energy, the total relative error on e^- and e^+ ($\delta_{\rm tot}/\#e^{\pm}$) obtained from the fitting procedure and divided into $\delta_{\rm stat}$, $\delta_{\rm sys\_tmpl}$, $\delta_{\rm stat\_tmpl}$, are shown. The major contribution to $\delta_{\rm tot}$ is given by the error coming from the fit $\delta_{\rm stat}$, hence from the statistical one (as already discuss for Figure 3.36).

The systematic uncertainty is anyhow negligible with respect to statistical one.

[4]Here there is the assumption that the error due to the finite statistic of the templates doesn't change in time. For this reason it is evaluated only in one time interval Δt.

Chapter 4

Flux normalization

In this section all the elements used in the experimental measurement of the flux will be discussed. The time and energy dependence of the efficiencies of all the cuts applied, discussed in section 3.2, will be reviewed.

4.1 Flux definition

The differential flux of a cosmic ray species (Φ), is defined as the number of particles, of that species, per unit of energy E, time t, area and solid angle. It is measured in units of ($\mathrm{GeV}^{-1}\,\mathrm{m}^{-2}\,\mathrm{s}^{-1}\,\mathrm{sr}^{-1}$) and in general is function of E, t, of the spatial coordinate $\overrightarrow{x}$ (i.e. the location of the detector) and of the arrival direction of the flux ω:

$$\Phi(E, t, \overrightarrow{x}, \omega) = \frac{\mathrm{d}N(E, t, \overrightarrow{x}, \omega)}{\mathrm{d}t\,\mathrm{d}E\,\mathrm{d}\sigma\,\mathrm{d}\omega} \quad (\mathrm{GeV}^{-1}\,\mathrm{m}^{-2}\,\mathrm{sr}^{-1}\,\mathrm{s}^{-1}) \tag{4.1}$$

where N is the number of particles, $\mathrm{d}\sigma$ and $\mathrm{d}\omega$ ($\mathrm{d}\phi\,\mathrm{d}\cos\theta$) are, respectively, the element of the area and the element of the solid angle traversed by the flux.
Given a detector, exposed to an isotropic flux, the number of counts experimentally detected will be [101]:

$$N(\Delta E, \Delta t) = \int_S \int_{\Delta E} \int_{\Delta t} \int_\Omega \Phi(E, t)\; F(E, t, \overrightarrow{x}, \omega)\; \hat{r} \cdot \mathrm{d}\overrightarrow{\sigma}\; \mathrm{d}E\; \mathrm{d}t\; \mathrm{d}\omega \tag{4.2}$$

where S is the area of the detector, Ω is the domain of ω and $\hat{r}$ is the unit vector in direction ω. The factor $F(E, t, \omega, \overrightarrow{x})$, that takes into account the detector properties, can be factorised as:

$$F(E, t, \omega, \overrightarrow{x}) = L(t)\, \epsilon_{\mathrm{cutoff}}(E, \omega, t)\, \epsilon(E, \omega, t, \overrightarrow{x}) \tag{4.3}$$

where:

- $L(t)$ is the livetime of the detector, defined as the fraction of time during which the instrument is ready to detect and record an event. It is related to the trigger rate the detector is undergoing, so ultimately only on time;
- $\epsilon_{\text{cutoff}}(E, \omega, t)$ takes into account the geomagnetic cutoff (see section 3.2.4). Given a particular position of the detector in the geomagnetic field, only a fraction of the flux spectrum is allowed. This, hence, has been treated as an efficiency function of the energy, of the arrival direction and of the detector position in the geomagnetic field (and so ultimately of the time);
- $\epsilon(E, \omega, t, \overrightarrow{x})$ is the detection efficiency of the instrument for that species.

Defining the *effective acceptance* of the detector as:

$$A_{\text{eff}}(E, t) = \int_S \int_\Omega \epsilon(E, \omega, t, \overrightarrow{x})\ \hat{r} \cdot \mathrm{d}\overrightarrow{\sigma}\ \mathrm{d}\omega \tag{4.4}$$

and grouping together the rest of $F(E, t, \omega, \overrightarrow{x})$:

$$\tau(E, \omega, t) = L(t)\, \epsilon_{\text{cutoff}}(E, \omega, t) \tag{4.5}$$

equation 4.2 can be rewritten as:

$$N(\Delta E, \Delta t) = \int_{\Delta t} \int_{\Delta E} \Phi(E, t)\, \tau(E, \omega, t)\, A_{\text{eff}}(E, t)\, \mathrm{d}E \tag{4.6}$$

and, under reasonable assumptions:

$$N(\Delta E, \Delta t) \approx \Phi(E, t)\, \Delta T_{\text{exp}}(\Delta E, \Delta t)\, A_{\text{eff}}(\Delta E, \Delta t)\, \Delta E \tag{4.7}$$

This gives the formula to determine the flux from the number of counts detected experimentally:

$$\Phi(E, t) = \frac{N(\Delta E, \Delta t)}{\Delta T_{\text{exp}}(\Delta E, \Delta t)\ A_{\text{eff}}(\Delta E, \Delta t)\ \Delta E} \tag{4.8}$$

According to equation 4.8, the factors that have to be evaluated experimentally for each energy and time bin $(\Delta E, \Delta t)$, in order to measure the electron and positron fluxes, are:

- $N_{e^\pm}(\Delta E, \Delta t)$: Number of identified electrons or positrons;

- $\Delta T_{\rm exp}(\Delta E, \Delta t)$: Exposure time of the measurement. This includes the live-time and the geomagnetic cutoff;
- $A_{\rm eff}(\Delta E, \Delta t)$: Effective Acceptance of the detector, calculated by using Monte Carlo simulation and including a factor that take into account the differences between DATA and Monte Carlo. This includes all the selection efficiencies and, hence, is function of the energy and could vary with time.

4.2 Exposure Time

The *exposure time* ($\Delta T_{\rm exp}$) for data recorded in the time interval Δt has been calculated removing the time during which the detector was not ready to receive new triggers. In addition to this, the data taking periods in not nominal conditions have been removed from the analysis sample (see section 3.2.1).

For each period Δt of data taking in which the analysis has been performed, livetime (Λ) weighted seconds, passing the selection described in Section 3.2.1, have been summed up. In addition, since at a certain geomagnetic coordinate, only the particles with rigidities above a certain threshold are primaries (see Section 1.2.2), this acts as an effective reduction of the exposure time. This effect, hence, introduces an energy dependence in the exposure time.

The exposure time has been set constant in each energy bin. For each energy bin and for each second of the DAQ the requirement on $R^{40^{\rm o}}_{\rm max}$ has been tested using the lower energy border of the bin. In the analysis, therefore, self-consistency has been achieved by selecting particles above $R^{40^{\rm o}}_{\rm max}$ not according to their rigidity/energy, but according to the lower edge of the bin in which they fall. The formula for the calculation of the exposure time $\Delta T_{\rm exp}([E_{\rm min}, E_{\rm max}]))$ for the energy E within the bin $[E_{\rm min}, E_{\rm max}]$ and for data taken in the time interval $\Delta t = t_{\rm max} - t_{\rm min}$, reads therefore:

$$\Delta T_{\rm exp}(E \in [E_{\rm min}, E_{\rm max}]) = \sum_{\rm t=t_{min}}^{\rm t=t_{max}} \Lambda(t)\theta(E_{\rm min} - R^{40^{\rm o}}_{\rm max}(t)) \tag{4.9}$$

where the sum runs over all the seconds of data taking and $\theta(E_{\rm min} - R^{40^{\rm o}}_{\rm max}(t))$ is the Heaviside step function. A typical exposure time, as a function of the energy, for $\Delta t = 27$ days is shown in figure 4.1.

This method, however, that has been used for the all-electron flux measurement [100], where the analysis has been performed over a Δt=30 months of data taking,

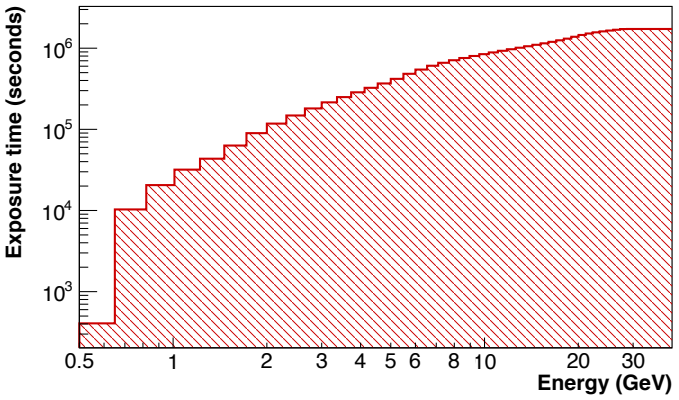

FIGURE 4.1: Typical exposure time, as a function of the energy, for $\Delta t = 27$ days.

presents some statistical problems with a smaller time interval, namely Δt=27 days. As shown in figure 4.2 the sample to be fit and the one used for the template definition (see 3.4) are so poor in terms of statistics that the extraction of any physical information is almost impossible.

In order to have more statistics the first bin has been split in 8 energy intervals[1]. In each one of the 8 different sub-intervals the exposure time has been evaluated according to Eq. 4.9. The exposure time for the "total" bin has been calculated as

[1]The first energy bin is [0.5–0.65] GeV and it has been split into 8 energy sub-intervals: [0.50–0.52],[0.52–0.54],[0.54–0.56],[0.56–0.58],[0.58–0.6],[0.6–0.62],[0.62–0.64],[0.64–0.65]

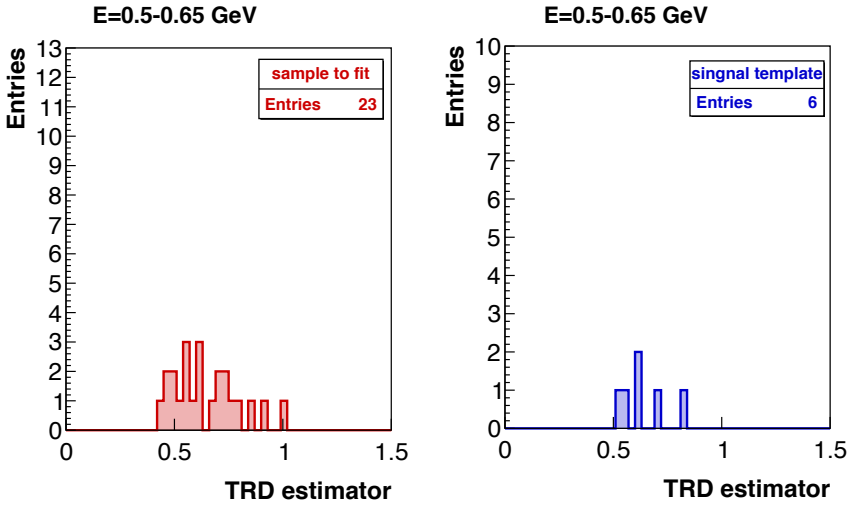

FIGURE 4.2: The sample to be fit (left) and the one used for the template definition (right) in the first energy bin (0.5–0.65 GeV) using a unique cutoff value for the whole bin.

the mean value of the integral[2] over the 8 sub-intervals (see figure 4.4).

The sample used for the template fit, instead, has been obtained summing all the events in the 8 sub-intervals.

Using this *fine binning* method, the DATA sample has been enriched by a factor ∼15 in this bin, as shown in figure 4.3.

A typical ΔT_{exp}, as a function of energy, obtained with the *fine binning* method, is shown in figure 4.5.

The mean *plateau* value of the exposure time above ∼30 GeV, where the effect of the geomagnetic field starts to be negligible, corresponds to an overall detector time efficiency of ∼ 80%.

[2] According to the *Mean Value Theorem for Integrals*, if a function f is continuous on the closed interval $[a, b]$, where$a < b$, and differentiable on the open interval (a, b), then there exist a point c in (a, b) such that:

$$f'(c) = \frac{f(b) - f(a)}{b - a}$$

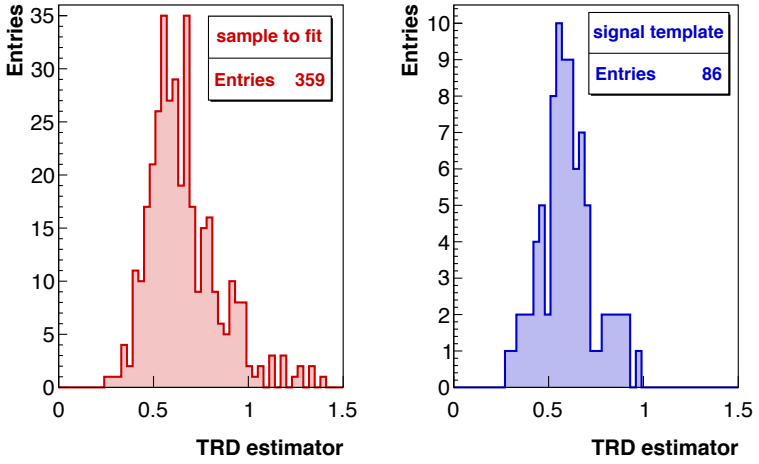

FIGURE 4.3: The sample to be fit (left) and the one used for the template definition (right) in the first energy bin (0.5–0.65 GeV) using the *fine binning* method.

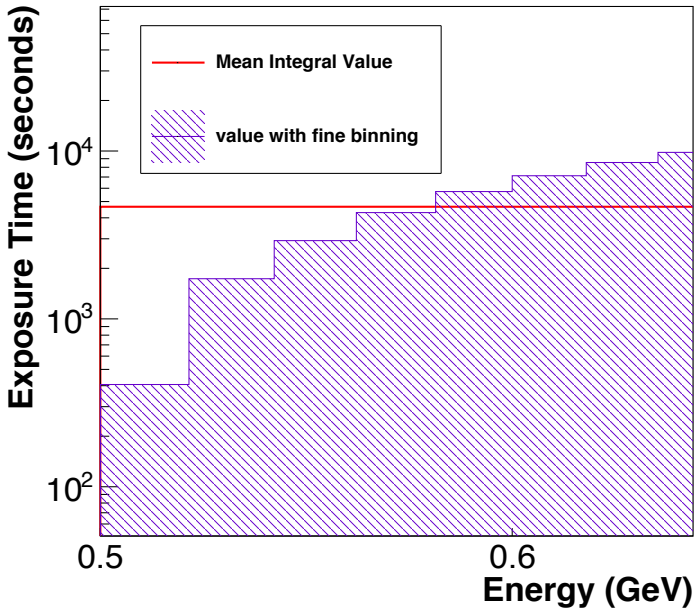

FIGURE 4.4: Exposure time for the 8 sub-intervals and their mean integral value.

4.3 Acceptance, $A_{\rm MC}$

The effective acceptance of the detector ($A_{\rm eff}$) that has been used for the flux definition in 4.8, can be written as follows:

$$A_{\rm eff} = \epsilon_{\rm trigg}(\Delta E, \Delta t) A_{\rm MC}(\Delta E) K(\Delta E, \Delta t) \tag{4.10}$$

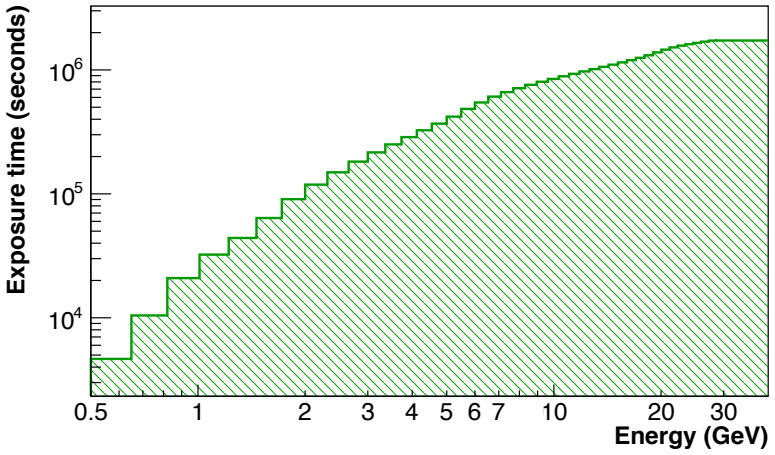

FIGURE 4.5: Typical exposure time, as a function of the energy, for $\Delta t = 27$ days, obtained with the *fine binning* method.

where:

- $\epsilon_{\text{trigg}}(\Delta E, \Delta t)$ is the trigger efficiency of the detector;
- $A_{\text{MC}}(\Delta E)$ is the acceptance of the detector evaluated using a Monte Carlo simulation. Includes both the geometrical factor and selection efficiencies;
- $K(\Delta E, \Delta t)$ is a correction factor for $A_{\text{MC}}(\Delta E)$ that takes into account the DATA/MC differences.

The A_{MC}, in a given energy interval ΔE, can be written as [101]:

$$A_{\text{MC}}(\Delta E) = \frac{N_{\text{sel}}(\Delta E)}{N_{\text{gen}}(\Delta E)} \cdot G \tag{4.11}$$

where:

- $N_{\text{sel}}(\Delta E)$ is the number of events, with energy within the interval ΔE, after the same selection applied on DATA;
- $N_{\text{gen}}(\Delta E)$ is the total number of generate events, with energy within the interval ΔE;
- G is the *generation surface acceptance*. For the MC used in this analysis, the generation plane is a square with side $l = 3.9\,\text{m}$, hence (see [101]):

$$G = \pi l^2 = 47.78\,\text{m}^2\,\text{sr} \tag{4.12}$$

In order to calculate A_{MC}, $N_{\text{sel}}(\Delta E)$ and $N_{\text{gen}}(\Delta E)$ have been evaluated as a function of the generated energy. Since in this case, the result is not affected by the energy spectrum of the generated sample, A_{MC} has been evaluated on a un-reweighted MC electrons sample.

A_{MC} as a function of E_{gen} has been obtained dividing the distribution of $N_{\text{sel}}(\Delta E)$ by $N_{\text{gen}}(\Delta E)$ and multiplying the result by the factor G. The procedure is schematically shown in figure 4.6. The number evaluation of $N_{\text{sel}}(\Delta E)$ and $N_{\text{gen}}(\Delta E)$ is described in detail in Appendix A, section A.2.1.

4.3.1 Evaluation of the Monte Carlo simulation acceptance, A_{MC}

The result for A_{MC} obtained with the procedure described above is shown in figure 4.7.

The deviation from an expected constant behavior at high energies is due to the increase of the selection requirements needed to reject the more abundant background. At low energies, the efficiency of the majority of selections decreases due to the multiple scattering undergone by the particle in the detector material, resulting in a unavoidable suppression of the acceptance for energies below 0.5 GeV. The energy dependence of A_{MC} has been parametrized using an analytical description and the value obtained from the fit is used for the evaluation of electrons and positrons fluxes, according to the equation 4.8.

The acceptance calculated in this work relies completely on the level of agreement to which the MC simulation is able to describe the DATA. This is, however, the only possible method to assess to absolute normalization of the detector acceptance. The MC simulation can, however, not be fully representative of the detector response. Therefore, a detailed comparison of DATA and MC is needed in order to asses the

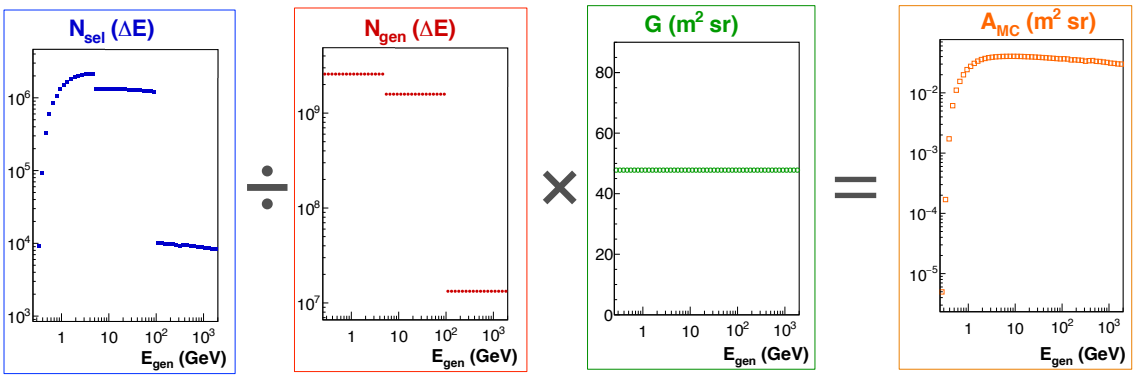

FIGURE 4.6: Schematically review of the procedure applied for the acceptance calculation.

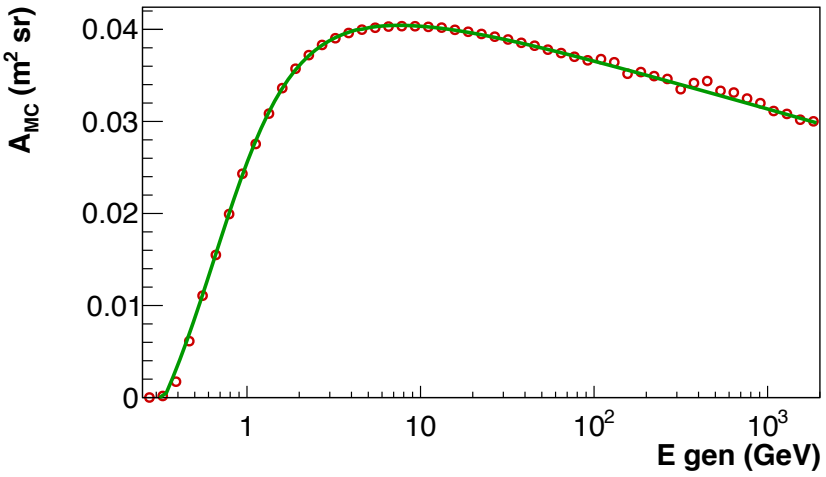

FIGURE 4.7: The obtained result for A_{MC} as a function of generated energy red point and its parametrization (green line).

correctness of the MC simulation and, in case, correct for such discrepancies. This problem will be described in detail in the in section 4.4.

4.4 Acceptance correction, $K(\Delta E, \Delta t)$

The detector acceptance $A_{\rm MC}$, evaluated as described in section 4.3, is completely based on MC informations. Only MC, in fact, can be used to asses the absolute acceptance normalization.

The preselection requirements (see section 3.2), except for the request of physics triggers, enter as a multiplicative factors with efficiency $\epsilon < 1$ in the definition of the acceptance $A_{\rm MC}(\Delta E)$ due to the finite level to which the MC simulation is able to describe the interactions with the detector materials and all other properties of the flight data.

The $A_{\rm MC}(\Delta E)$ has therefore to be corrected by a factor that take into account the differences between DATA e MC.

Since some selections, as will be discuss in section 4.8, are both energy and time dependent also the acceptance correction factor should be dependent both on energy and time ($K(\Delta E, \Delta t)$).

The method for the calculation of the *correction factor* has been already studied and applied for the (e^++e^-) flux measurement [100]. The procedure that has been used in this work is similar, with the major exception that $K(\Delta E, \Delta t)$ has been evaluated in each time interval.

In this section, the strategy used to evaluate the *correction factor* and its systematic uncertainties will be reviewed.

In principle, the correct procedure to calculate K should be the comparison of the efficiencies between an electron sample from DATA and an electron sample from MC, for each cut used in the evaluation of $A_{\rm MC}$. To avoid apparent discrepancies introduced by background component in the electron sample.

However, electrons are a rare species in the cosmic radiation. Therefore, a stronger selection than that applied during the analysis is needed to select a pure sample of electrons. On the other hand, the MC simulation has been run on the electron hypothesis only. This mainly introduces some additional difficulties. First, any unavoidable proton background will contaminate the DATA electron sample, and could potentially induce a bias when comparing MC and DATA detector response.

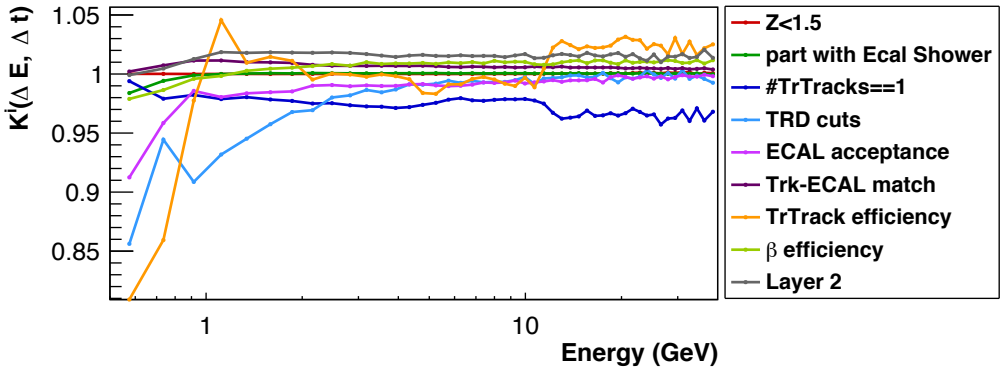

FIGURE 4.8: Single corrections $K(\Delta E, \Delta t)^i$ for all the selections used in the $A_{\rm MC}$ calculation as a function of reconstructed energy, in one time interval of 27 days.

Moreover, any additional electron selection could introduce unwanted biases in the selected DATA or MC sample and it may hide some different features between DATA and MC. The selection applied for the calculation of each efficiency will be discuss in section 4.6.

In this analysis the efficiencies in each ΔE and Δt intervals on electron DATA ($\epsilon^i_{\rm DATA}(\Delta E, \Delta t)$) and in each ΔE interval on MC electrons ($\epsilon^i_{\rm MC}(\Delta E)$) have been evaluated for each cut used in the $A_{\rm MC}$ calculation. The correction coming from the $i-th$ cut, that has to been applied to the acceptance for the time interval Δt and energy interval ΔE ($K(\Delta E, \Delta t)^i$), has been calculated as the ratio between the DATA and MC efficiencies:

$$K(\Delta E, \Delta t)^i = \frac{\epsilon^i_{\rm DATA}(\Delta E, \Delta t)}{\epsilon^i_{\rm MC}(\Delta E, \Delta t)} \tag{4.13}$$

The total correction being therefore:

$$\kappa(\Delta E, \Delta t) = \prod_{\rm i} K(\Delta E, \Delta t)^i \tag{4.14}$$

Figures 4.8 and 4.9 show, as a function of the reconstructed energy and for one time intervals of 27 days, respectively all the single corrections $K(\Delta E, \Delta t)^i$ for each cut applied in the $A_{\rm MC}$ calculation, and the result obtained for $\kappa(\Delta E, \Delta t)$.

In order to smooth out statistical fluctuations, $\kappa(\Delta E, \Delta t)$ has been parametrized using a log linear fit for energies above 2 GeV. Under 2 GeV, the correction has been evaluated point by point to best represent its non trivial energy dependence.

At low energies, the discrepancies between DATA and MC correction amount to 30–40% at 0.5 GeV. In the analysis only half correction has been applied, since there is no particular reason to privilege MC over DATA, or viceversa. The arbitrariness of

this choice is however covered by the systematic uncertainty given by the DATA/MC discrepancy that will be discuss in the next section.

4.4.1 Uncertainties on $K(\Delta E, \Delta t)$

Four kinds of effects have been taken into account to evaluate the uncertainties of $K(\Delta E, \Delta t)$ (σ_{K}).

- $\sigma_{\mathrm{K}}^{\mathrm{abs}}$: uncertainty introduced by the level of disagreement between DATA and MC;
- $\sigma_{\mathrm{K}}^{\mathrm{stab}}$: uncertainty introduced by the level of stability in time of K;
- $\sigma_{\mathrm{K}}^{\mathrm{par}}$: uncertainty introduced by the parametrization resulting from the fit performed above 2 GeV on $K(\Delta E, \Delta t)$;
- $\sigma_{\mathrm{K}}^{\mathrm{res}}$: uncertainty introduced by the the goodness of the fit performed above 2 GeV on $K(\Delta E, \Delta t)$.

The four uncertainties have been evaluated as a function of energy and combined assuming complete uncorrelation:

$$\sigma_{\mathrm{K}} = \sigma_{\mathrm{K}}^{\mathrm{abs}} \oplus \sigma_{\mathrm{K}}^{\mathrm{stab}} \oplus \sigma_{\mathrm{K}}^{\mathrm{par}} \oplus \sigma_{\mathrm{K}}^{\mathrm{res}} \tag{4.15}$$

Absolute systematic, $\sigma_{\mathrm{K}}^{\mathrm{abs}}$

Figure 4.10 shows the deviation of the ratio $\epsilon_{\mathrm{DATA}}/\epsilon_{\mathrm{MC}}$ from 1, δ, as a function of energy for all K_{i}. In this case the whole time interval has been considered.

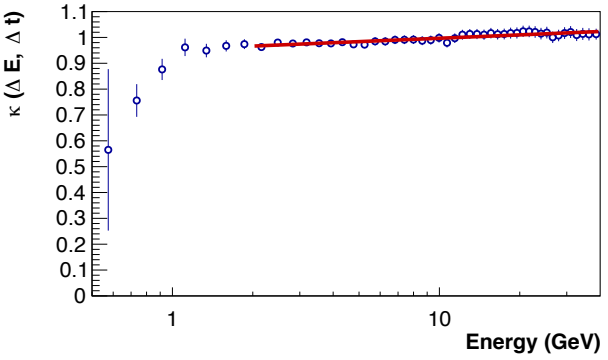

FIGURE 4.9: Total correction (κ) as a function of reconstructed energy obtained from the single corrections show in figure 4.8 according to the formula 4.13, in one time interval of 27 days, with, superimposed, a linear polynomial fit for energies 2 GeV.

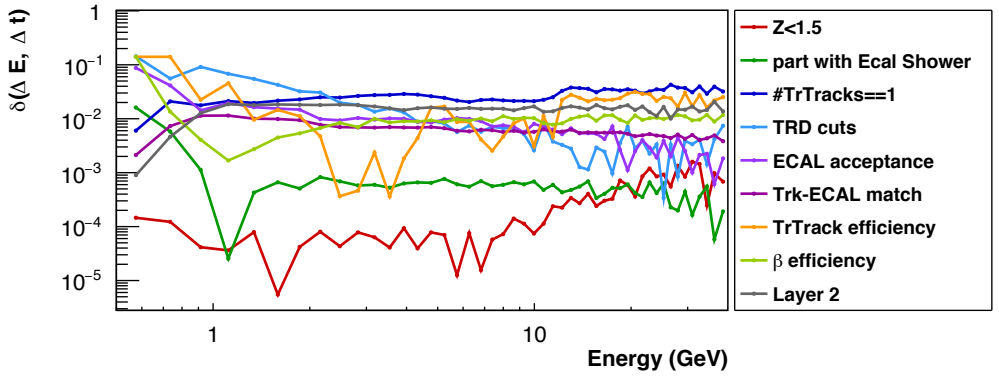

FIGURE 4.10: Deviation from 1, δ, as a function of energy for all K_i time integrated.

Some selections show a negligible deviation from 1, pointing to an optimal agreement between DATA and MC. Other selections, instead, show an appreciable deviation from 1. This deviation, which contributes to uncertainty on the knowledge of the acceptance, it is described in this analysis by the **absolute systematic** σ_K^{abs}. For each selection, the half difference of the point from the unity, $\delta^i_{1/2}$, is used as estimation of such uncertainty and the quadratic sum of every contribution defines the yield of the absolute systematic:

$$\sigma_K^{abs} = \left[\sum_i (\delta^i_{1/2})^2\right]^{1/2} \tag{4.16}$$

σ^{abs} has been evaluated in each energy interval and time integrated, since it depends on the uncertainties of the knowledge of A_{MC} (i.e. of the knowledge of MC sample) that doesn't depend on time.

K stability over time, σ_K^{stab}

The value of *acceptance correction factor* evaluated in each Δt ($K^{\Delta t}$) could be different from that evaluated over all the time ($K^{t_{TOT}}$), not only because the DATA efficiencies could change in time, but also for purely statistical effects. This effect is included with the error σ_K^{stab}.

For each energy interval, the differences between the acceptance correction evaluated in a time interval $K^{\Delta t}$ and its mean value in the same time interval $< K^{\Delta t} >$ has been evaluated. For example, the distribution of all the differences obtained in one energy bin is shown in figure 4.11. For each energy bin the spread of such distribution has been used to quantify σ_K^{stab}.

Particular care should be paid to the definition of the mean value of K. In order to have only the effect due to the statistical fluctuations, the mean value should be

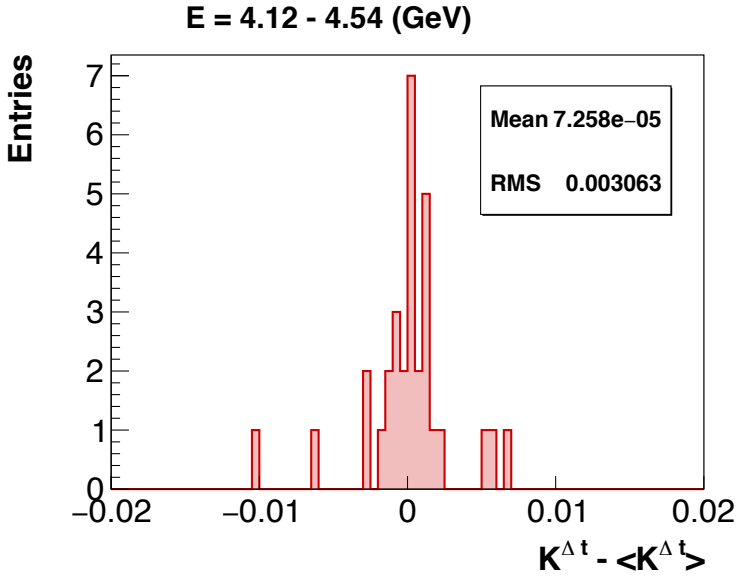

FIGURE 4.11: Distribution of the differences between K and its mean value integrated over time in one energy bin.

evaluated after the subtraction of the time dependencies effect of efficiencies. As will be show in section 4.8, not all the efficiencies used for the acceptance correction are time dependent. To the time dependence of K contribute:

- The **TRD efficiency** that has a time dependence with different behaviors in each energy bin;
- The **Tracker** related efficiencies (track reconstruction efficiency, single track and layer 2 efficiency) that show an energy independent time dependency.

An example of contribution to K from TRD efficiency in one energy bin is shown in figure 4.12. The TRD behavior as a function of time can be described by a linear parametrization, assumed to be different in each energy bin. In fact, for this particular selection, as will be shown in section 4.8, the time and energy dependences are correlated.

Figure 4.12 shows the contribution to K given by the track related efficiencies. The trend as a function of time shows discontinuities that, as will be shown in section 4.8, have the same effect over all the energies. The origin of the steps is well know (see section 4.8). For this reason the contribution shown has been evaluated over all the energies.

The mean value of K has been evaluated performing a fit on a *corrected* K as a function of time obtained from K after correcting for the discontinuities observed int the track efficiency as shown in figure 4.13. The fit has been performed using

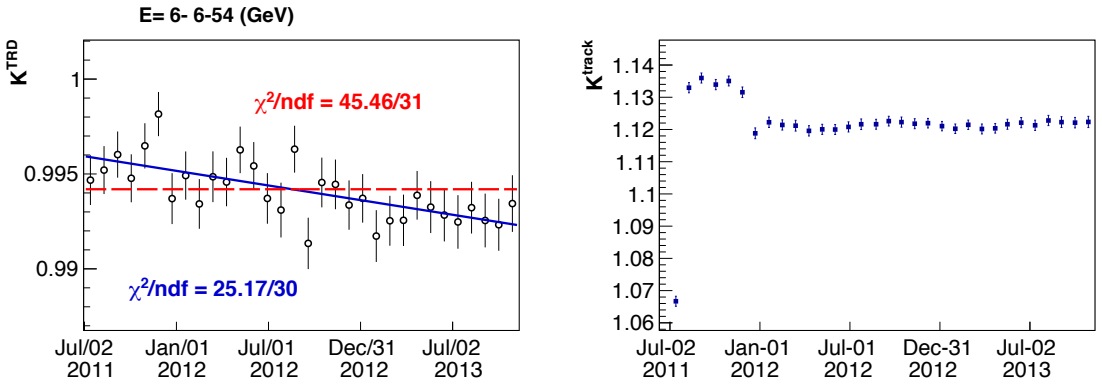

FIGURE 4.12: Contribution to K as a function of time given by the TRD efficiency (left) and Tracker (track + layer 2 + single track) efficiencies (right).

a linear parametrization to describe the time dependent effect given by TRD. An example of the fit is reported in figure 4.13.

The result obtained using this method is very conservative and represents an upper limit on the uncertainty of K due to its stability in time. The parametrization used to evaluate the mean value of K, removes the main time trend but it cannot be excluded that <K> still contains trends time dependent. However, as shown in figure 4.14 the $\sigma_{\mathrm{K}}^{\mathrm{abs}}$ contribution is very low so the fact that it represents an upper limit doesn't represent a problem.

Parametrization systematic, σ^{par}

Since the parametrization of K itself can introduce an additional systematic uncertainty also the error coming from the fit performed on K should be taken into account. Such uncertainty for a certain value of energy E has been evaluated

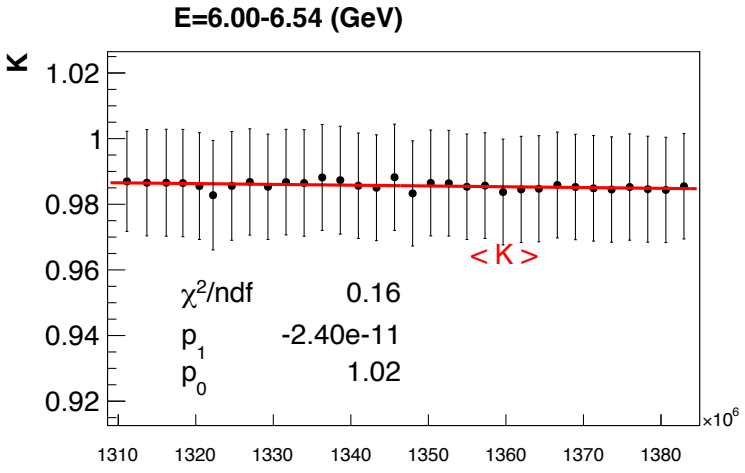

FIGURE 4.13: Fit performed on the corrected K as a function of time.

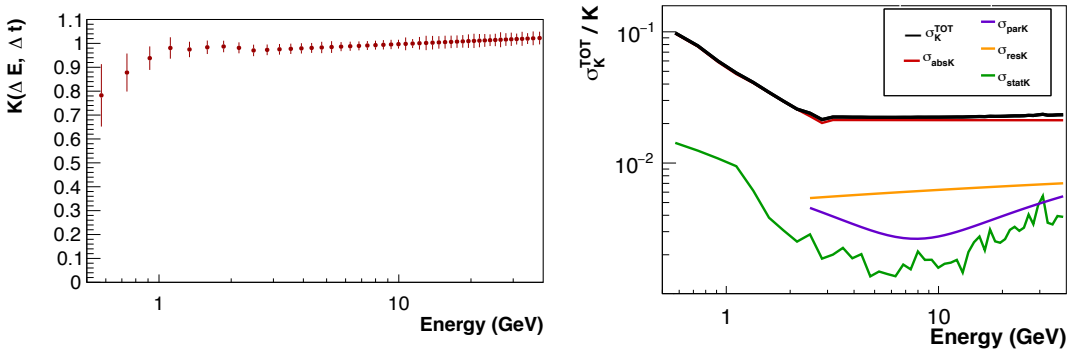

FIGURE 4.14: *Left: Acceptance correction factor* K evaluated in a time interval of 27 days and as a function of energy. Each point has $\sigma_{\mathrm{K}}^{\mathrm{TOT}}$ as error. Right: Total relative error $(\sigma_{\mathrm{K}}^{\mathrm{TOT}}/K)$ with the single contributions coming from the absolute, K differences, parametrization and residual systematic for the *acceptance correction factor* K evaluated in a time interval of 27 days and as a function of energy.

through the propagation of the uncertainties of the parameters p_0 and p_1 estimated during the fit procedure.

Residual systematic, σ^{res}

In the total uncertainty on K, the *goodness* of the fit has been taken into account considering the distance of the single fitted point respect to the value obtained from the fit:

$$\sigma^{\mathrm{res}} = |\kappa(E) - \kappa_{\mathrm{FIT}}(E)| \tag{4.17}$$

The obtained result has been fitted as shown in figure 4.13 and the result of the fit is used as value for σ^{res}.

Figure 4.14 shows the *acceptance correction factor* K and its total relative error (σ^{K}/K) with the single contributions coming from the absolute, K differences, parametrization and residual systematic. The last two contributions are considered only for E>2 GeV. The same procedure has been applied independently for each time interval.

At all energies, the dominating contribution to the uncertainty of the MC acceptance parametrization is given by the $\sigma_{\mathrm{K}}^{\mathrm{abs}}$, which describes the finite level to which the MC simulation is able to represent the features of flight data.
The additional uncertainties due to the time stability of the correlation are negligible.

4.5 Trigger efficiency

As has been explained in section 2.1.9 the AMS-02 trigger is based on *fast trigger* and *level 1 trigger signals (LV1)*.

The LVL1 triggers are seven:

LV1-0: *Unbiased charged* (FTC) presc.factor ∼100
= 3/4 TOF HT, gate 240 ns

LV1-1: *Single charged* (FTC + ANTI)
= 4/4 TOF HT, Nacc=0, gate 240 ns

LV1-2: *Normal Ions* (FTC + Z>1)
= 4/4 TOF SHT, Nacc<5, gate 240 ns

LV1-3: *Slow Ions* (FTZ)
= 4/4 TOF SHT, gate 640 ns

LV1-4: *Electrons* (FTC & FTE)
= 4/4 TOF HT, ECALF&, gate 240 ns

LV1-5: *Photons* (FTE & ECLVL1)
= ECALA&, gate 640 ns

LV1-6: *Unbiased EM* (FTE) presc.factor ∼1000
= ECALF||, gate 240 ns

The five triggers from LV1-1 to LV1-5, are the so called "*Physics triggers*", while the other two, LV1-0 and LV1-6, are addressed to as "*Unbiased triggers*". This last category has been meant to be used for trigger efficiency calculation from DATA. For this reason, they are determined with much more loose requests respect to the Physics triggers. Therefore, a fixed prescale factor is applied on board in order reduce the data size. The applied prescale factor is 1/100 for unbiased charge and 1/1000 for unbiased EM. This pre-scaling is not simulated on MC data.

For the calculation of Trigger efficiency, the additional category "*Not Physics Triggers*", defined by events triggered by at least one of unbiased trigger and by no Physics triggers, has been introduced. Using this category, the trigger efficiency is defined as follows:

$$\epsilon_{\text{trigger}} = \frac{(\text{Physics Triggers})}{(\text{not Physics Trigger}) + (\text{Physics Trigger})} \tag{4.18}$$

4.5.1 Trigger Efficiency on electrons

The formula 4.18 can be explicated in the term of LV1:

$$\epsilon_{\text{trigger}} = \frac{\text{LV1-(1 ||...|| 5)}}{[\text{w}_0*(\text{LV1-0})+\text{w}_6*(\text{LV1-6})+\text{w}_{06}*(\text{LV1-(0\&6)}]_{\text{notPhys}} + [\text{LV1-(1 ||...|| 5)}]} \tag{4.19}$$

The factors w_0, w_6 and w_{06} are the factors that should be know in order to take into account the pre-scaling of the unbiased triggers. After a deep study on the unbiased triggers (for more details see A.3 in appendix A), they have been set w_0=w_6=w_{06}=100.

Figure 4.15 shows the trigger efficiency evaluated over a sample of electron MC and electron DATA. The same selection that has been applied to select the electron and positron samples on DATA has been also applied to select MC electrons. This assumes to minimize any bias in the selection that could effect the evaluation of the trigger efficiency.

The cuts that have been applied on DATA in order to select an electrons sample, have been also applied on electrons MC with the purpose of remove any bias that can spoil the trigger efficiency distribution. Above 4 GeV the trigger efficiency is $\sim$ 100% both on DATA and MC. At lower energies the value is $<$ 100%. A big discrepancy between DATA and MC samples at the level of $\sim$ 5% at $\sim$1 GeV has been observed.

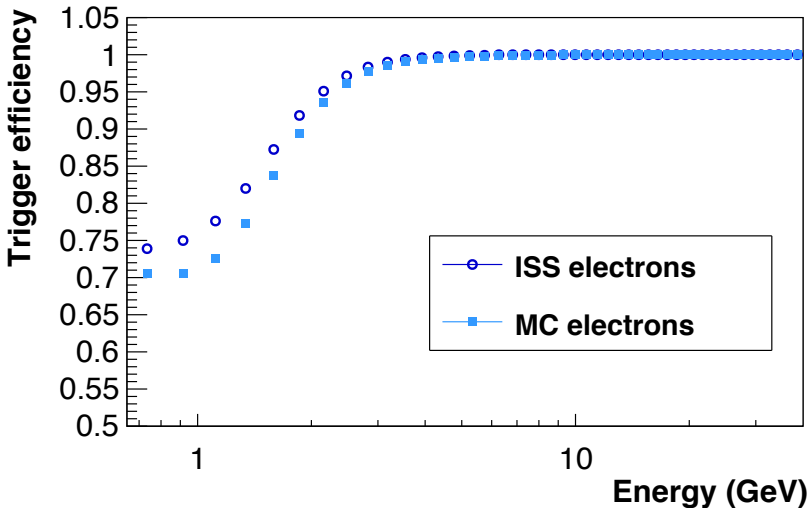

FIGURE 4.15: Trigger efficiency as a function of reconstructed energy, for MC electrons (red points) and DATA electrons (black points).

In order to avoid DATA/MC correction for this efficiency that would be introduce a big systematic (see section 4.4), the trigger efficiency has been evaluated directly from DATA as *last cut* according to the formula 4.19. The number of electrons with *physics trigger* and the number of electrons with *no physics triggers* has been evaluated through the fitting procedure explained in chapter 3 over a sample that satisfied the preselection 3.2[3].

The whole 30 months data taking period has been used to evaluate the trigger efficiency for $e^{\pm}$ since, as will be discussed later in this chapter in section 4.8, does not depend on time. The obtained result is shown in figure 4.16. In order to avoid statistic fluctuations, a fit has been performed on the distribution and the value obtained from the fit is used in the calculation of the flux.

4.6 Efficiency evaluation

As explained in chapter 3, a list of cuts, which constitutes the *preselection* (see section 3.2) has been applied on DATA in order to define the sample from which extract the signal of $e^{\pm}$.

The acceptance of this preselection has been evaluated from MC electrons and corrected for a factor K that take into account DATA/MC discrepancies (see 4.4).

[3]for the *no physics trigger* the request to have *physics triggers* contained in the preselection 3.2 has been changed in the request to have *no physics triggers*

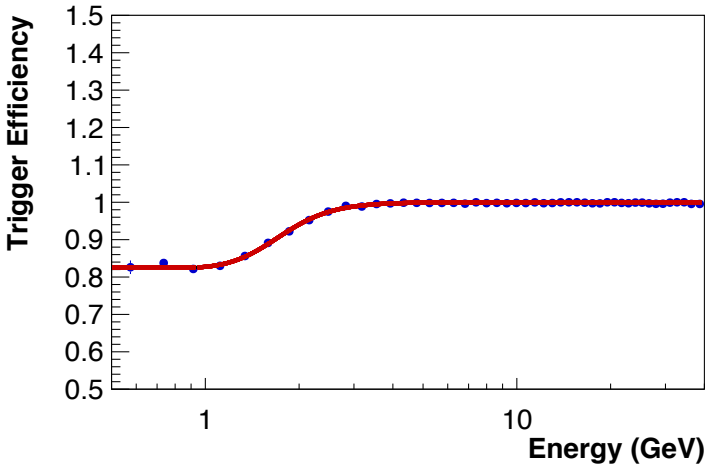

FIGURE 4.16: Trigger efficiency as a function of energy evaluated from DATA as *last cut*.

For the evaluation of K all the cuts contained in the preselection have been studied on DATA and MC electrons samples as a function of energy and, in case of DATA, also as a function of time.
However, while the MC electron sample has a purity of 100%, on DATA a strong selection has been applied to select a pure sample of electrons and to remove any background. The possible bias that a selection can introduce on a sample, should be taken into account and for this reason the same selection applied on DATA has been also applied on MC.

Moreover, a strong selection can introduce some bias on the result of the efficiencies. As example, this happens in the case of the reconstructed β by ToF and reconstructed $Track$ by Tracker. At first approach, the β efficiency can be evaluated over sample that has at least one reconstructed track by the Tracker and, viceversa, the $Track$ efficiency can be evaluated over a sample of particles that have a reconstructed β by the ToF.
However, the responses of ToF and Tracker are strongly correlated. This introduces a bias in the MC acceptance evaluation that should be avoid. Naively the sample on which evaluate the $Track$ efficiency can be defined with a selection that contains the cut on β and, viceversa, the β efficiency can be defined with a selection that contains the cut on $Track$. However following this procedure the obtained efficiencies will be both close to 100% that doesn't correspond to the true value. On the other hand if both efficiencies will be evaluated over an *unbiased* sample, without any request on $Track$ for the β efficiency evaluation and any request on β for the $Track$ efficiency evaluation, the obtained efficiencies will be too low respect to the true value. A fair choice can be the evaluation of one of two efficiencies on an*unbiased* sample and the other efficiency on an *biased* sample. Following this approach the obtained result for $Track{+}\beta$ efficiency is more similar to the true value.

The solution adopted is the following: the $Track$ efficiency has been evaluated using an *unbiased* sample, obtained without any request on β and the the β efficiency is evaluated over a *biased* sample defined cutting on $Track$. The viceversa, β efficiency evaluated on an *unbiased* sample and the $Track$ efficiency on a *biased* sample, brings at the same results. The choice of which procedure as to been followed is arbitrary.

The electrons samples used for the β and $Track$ efficiencies have been selected, both on DATA and MC, applying a selection based on ECAL and TRD variables. In addition, for the Tracker efficiency, the request to have a unitary charge and relativistic downgoing particle has been added using the information coming from the ToF. The obtained efficiencies as a function of the reconstructed energy both for DATA and MC are shown in figure 4.17 and the relative DATA/MC ratio as a function of energy in figure 4.18. In the case of Track efficiency there is a very good

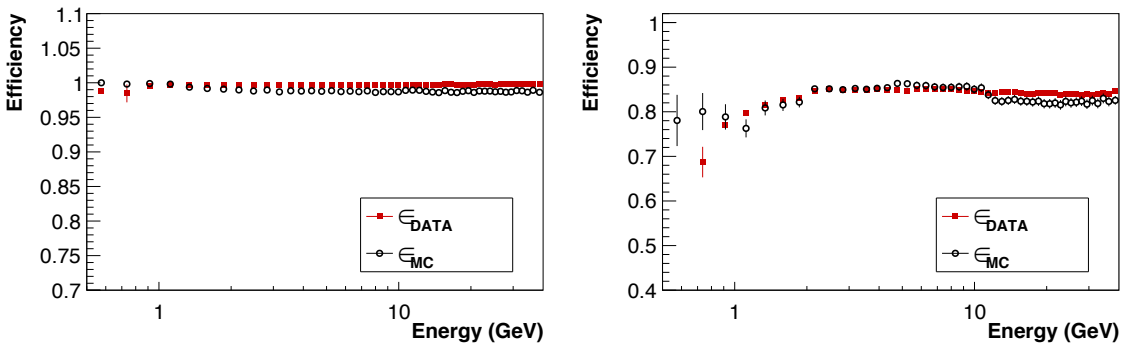

FIGURE 4.17: Efficiencies of β reconstruction (left) and Track reconstruction (right) as a function of the reconstructed energy both for DATA and MC.

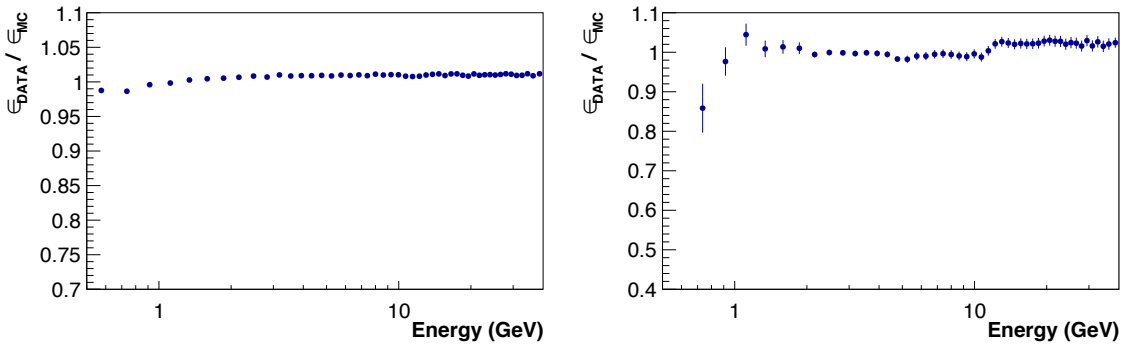

FIGURE 4.18: DATA/MC ratio of β reconstruction efficiency (left) and Track reconstruction efficiency (right) as a function of the reconstructed energy.

agreement between data and MC, for the β efficiency the agreement is at the level of $\sim 1-2\%$

The efficiency of the request to have at least one reconstructed shower has been evaluated over an electrons samples selected on DATA by means of a loose selection. Only cuts on the TRD and Tracker variables have been applied since a cut on ECAL variables could completely spoil the value of this efficiency. For the same reason this efficiency has been evaluated as a function of the reconstructed rigidity since any informations coming from ECAL , as the reconstructed energy, imply the presence of a shower and will give an efficiency of 100%. The result as a function of the reconstructed rigidity is shown in figure 4.19 both for DATA and MC on the left and the relative DATA/MC ratio that shows a very good agreement between DATA and MC on the right.

The other two efficiencies related to the ECAL, are checking that the track is inside the ECAL fiducial volume and checking the tTrack-ECAL matching. As in the case of β and $Track$, also these two efficiencies are strongly correlated and a special care is needed in order to not repress any feature with a strong selection.
The check of Track inside the ECAL fiducial volume, has been evaluated over an

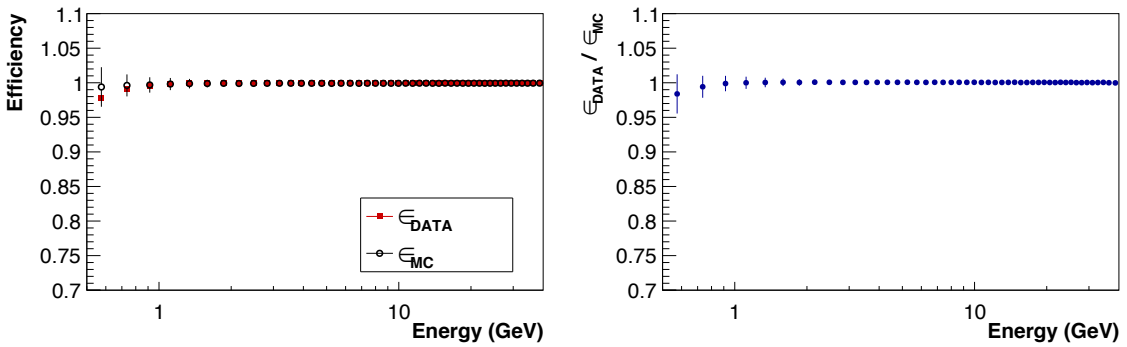

FIGURE 4.19: Efficiencies of the request of ECAL reconstruction as a function of the reconstructed rigidity both for DATA and MC (left) and the relative DATA/MC ratio as a function of the reconstructed rigidity (right).

electron sample selected using the informations coming from TRD, Tracker and also ECAL, excluding the request of Tracker-ECAL matching. The same sample, but adding the request to have the reconstructed track inside the ECAL fiducial volume, has been used for the evaluation of Tracker-ECAL match. The obtained results as a function of reconstructed energy and the relative DATA/MC ratio are shown in figure 4.20 and the relative DATA/MC ratio in figure 4.21. For both efficiencies there is a very good agreement between DATA and MC except for energies below 1 GeV in the case of Track in ECAL fiducial volume.

The efficiency of the requests on TRD has been evaluated over an electron sample selected using the ECAL variables and Tracker variables. No cuts on the TRD variables have been applied. The results for DATA and MC as a function of the reconstructed energy and the relative DATA/MC ratio are shown in figure 4.22. The requests on TRD include, as explained in section 3.2, three different cuts: a minimum number on the TRD hits used for the likelihood reconstruction, the presence of e/p likelihood ratio and a tight cut on e/He likelihood ratio used to remove residual helium. However the cuts on the likelihoods ratio have an efficiency of $\sim 100\%$ after the request on the number of TRD hits. So the trends as a function of the energy shown in figures 4.22 are due only to the request on the number of TRD hits. For this cut there is a good agreement between DATA and MC above 5 GeV but below this energy the comparison gets worst reaching a desagreement of $\sim 5\%$.

The efficiency of the requirement to have a unitary charge reconstructed by the inner Tracker (Z_{inn}) has been evaluated over an electrons sample selected using information coming from TRD, ECAL, ToF and Tracker. The obtained results for DATA and MC as a function of reconstructed energy are in good agreement as

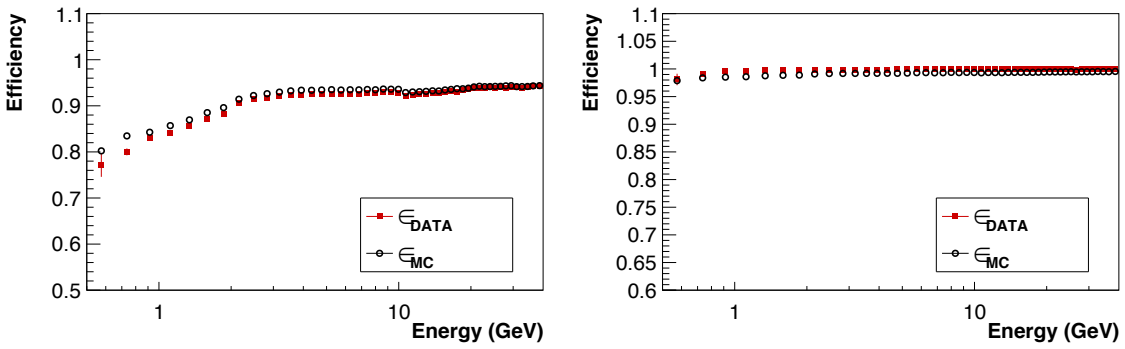

FIGURE 4.20: Efficiencies of the request to have Track inside the ECAL fiducial volume (left) and Track-ECAL matching (right) as a function of the reconstructed energy, both for DATA and MC.

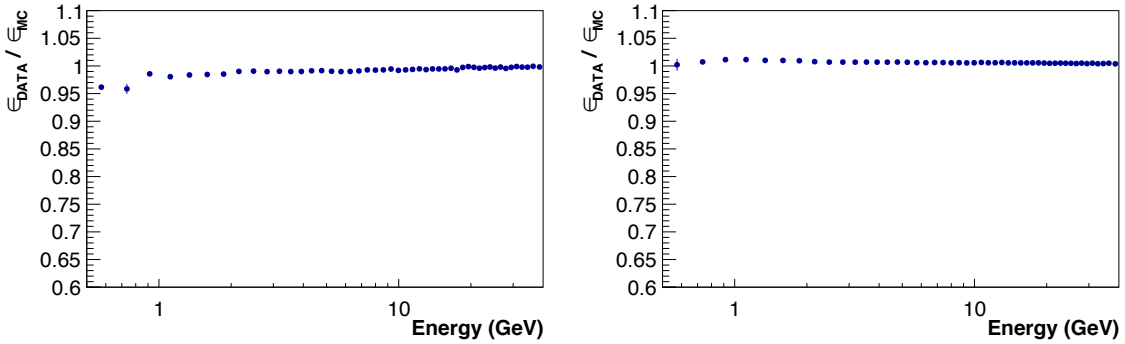

FIGURE 4.21: DATA/MC ratio of the request to have Track inside the ECAL fiducial volume (left) and Track-ECAL matching (right) as a function of the reconstructed energy, both for DATA and MC.

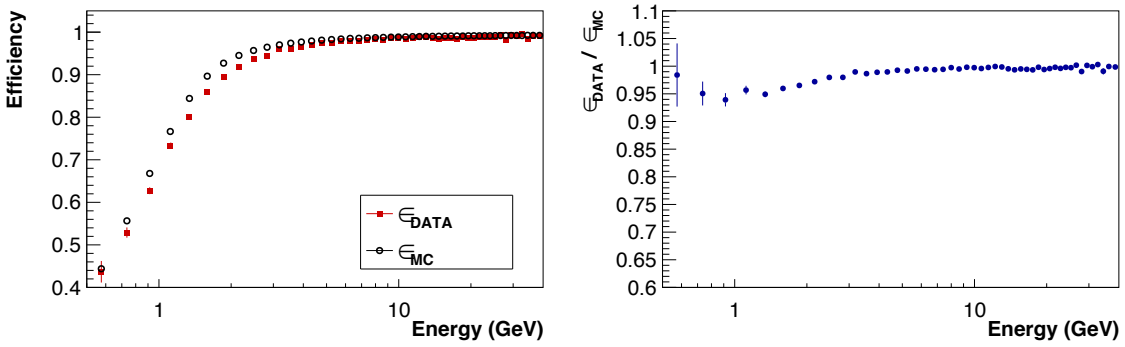

FIGURE 4.22: Efficiencies of the request on the minimum number of reconstructed hits on TRD used for the likelihood as a function of the reconstructed energy, both for DATA and MC (left) and the relative DATA/MC efficiencies ratio (right).

shown in figure 4.23. However this efficiency shows a slight decrease with the energy due to an asymmetric shape of Z_{inn} distribution for electrons sample where the energy starts to increase as explained in section 3.2.3. The asymmetric tail is due to secondary particles produced by the primary electron before the inner Tracker. This behavior is confirmed also by the MC simulation.

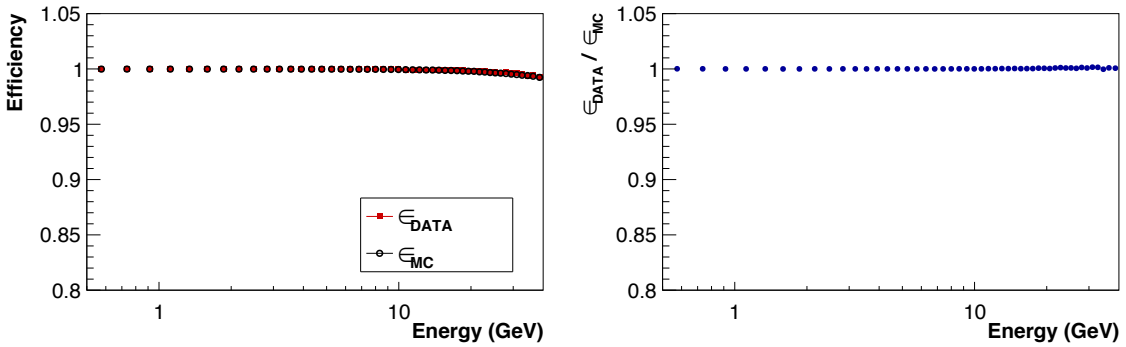

FIGURE 4.23: Efficiencies of the request of unitary charge as a function of the reconstructed energy both for DATA and MC (left) and the relative DATA/MC efficiencies ratio (right).

The efficiencies of the requests to have only one reconstructed track and layer 2 in the track pattern[4] have been evaluated on a clean sample of downgoing unitary charge particles selected using TRD, ECAL, ToF and Tracker. For the layer 2 efficiency is also required the single track. The results as a function of reconstructed energy both for DATA and MC are shown in figure 4.24 and the relative DATA/MC efficiencies ratio in figure 4.25. The single track efficiency is the one that presents the greater DATA/MC discrepancy. The DATA/MC discrepancy is up to $\sim 3\%$ in the considered energy range.

4.6.1 DATA efficiencies as a function of time

An quantitatively way has been used to study the DATA efficiencies dependences on time as will be explained in section 4.8. However, a first look of the efficiencies trend as a function of time and energy integrated, can show some important features.

Figure 4.26 shows the efficiencies evaluated on DATA as a function of time[5] for the request on charge, β, reconstructed shower, Track in ECAL acceptance and Track-ECAL matching. These efficiencies don't show particular trends as a function of time at least at the ‰ level.

In figure 4.27 the efficiencies that present some trend as a function of time are shown. The efficiencies related to the requests on Track reconstructed by the Tracker show two jumps: the first one between July and August 2011 and the second one between December 2011 and January 2012. These are due to well known events:

[4]The *track pattern* is a variable that contains the information on which Tracker layers have been used for the tracker reconstruction.

[5]All the efficiencies shown in subsection 4.6.1 are energies integrated.

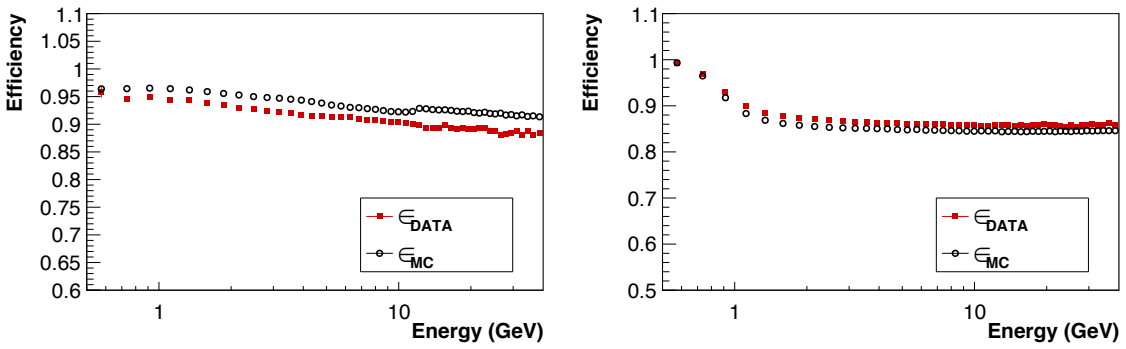

FIGURE 4.24: Efficiencies of the request to have one track (left) and layer 2 in tracker reconstruction (right) as a function of the reconstructed energy both for DATA and MC.

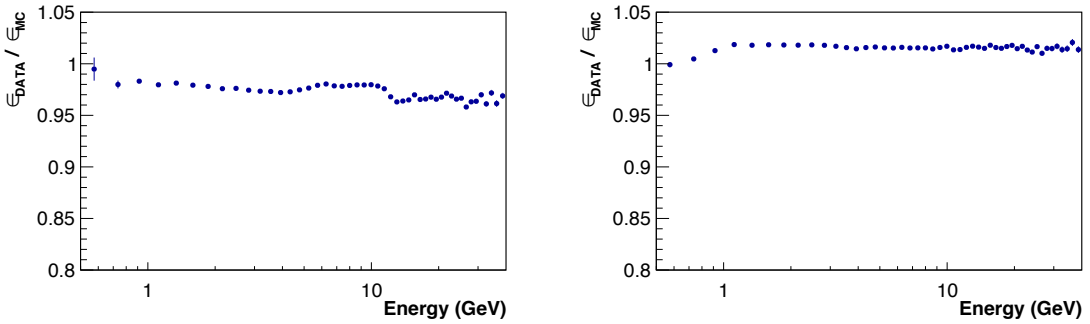

FIGURE 4.25: DATA/MC ratio of the request to have one track (left) and layer 2 in tracker reconstruction (right) as a function of the reconstructed energy both for DATA and MC.

- on 24th August 2011, the procedure for the Tracker calibration has been changed and this caused an increase in the tracker track reconstruction efficiency;
- on 1st December 2011, the loss of ∼1% of channels caused a decrease of the Tracker track reconstruction efficiency.

Following the method shown in section 4.8.2, has been observed that the time dependence of the requests related to the Track don't depend on energy.

The TRD efficiency clearly increase with time and the variation is ∼ 1.5%. Moreover, it has been found (with the method explained in section 4.8.2) that the time dependence of the TRD request changes with energy.

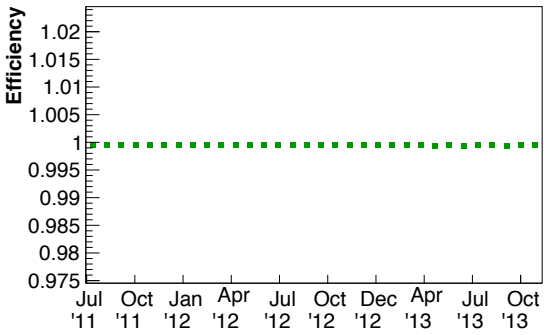

(A) Unitary charge request efficiency.

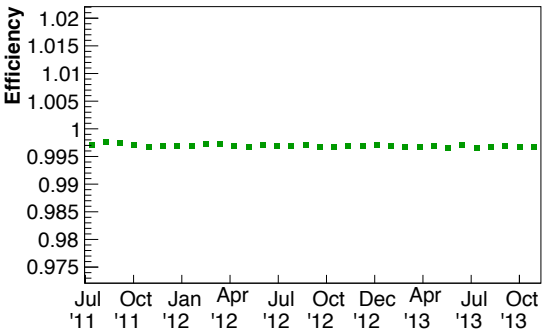

(B) β efficiency.

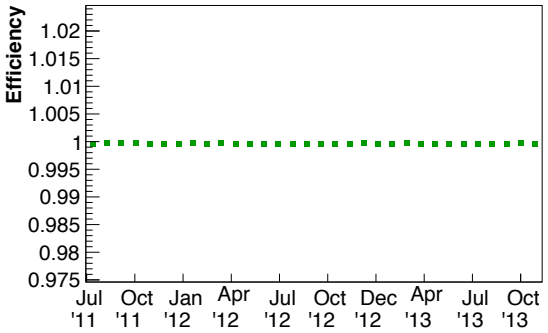

(C) Presence of a reconstructed shower efficiency.

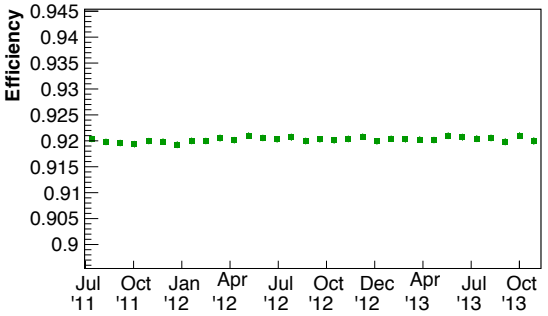

(D) Track in ECAL acceptance efficiency.

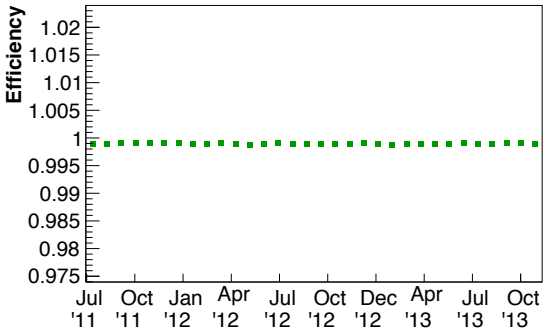

(E) Track-ECAL matching efficiency

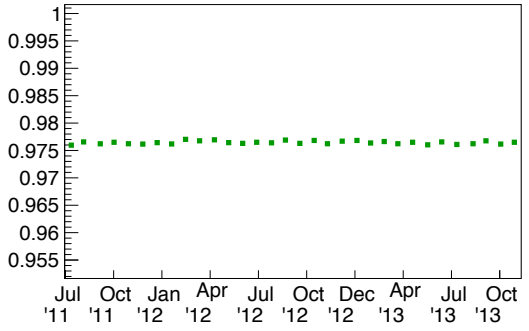

(F) Trigger efficiency.

FIGURE 4.26: Efficiencies on DATA as a function of time that don't show particular trend as a function of time at least at the level.

4.7 Evaluation of efficiencies used for the acceptance correction K

As explained in section 4.4 the acceptance correction factor for a list of cuts, have been evaluated following the equation 4.13:

$$\kappa(\Delta E, \Delta t) = \prod_{\mathrm{i}} K(\Delta E, \Delta t)^i$$

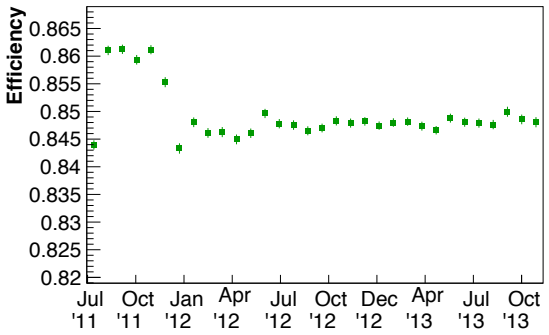

(A) Track reconstruction efficiency.

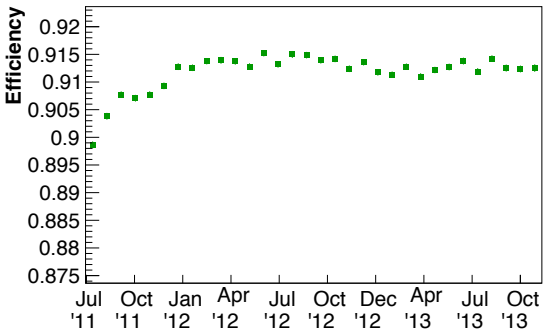

(B) Single track efficiency.

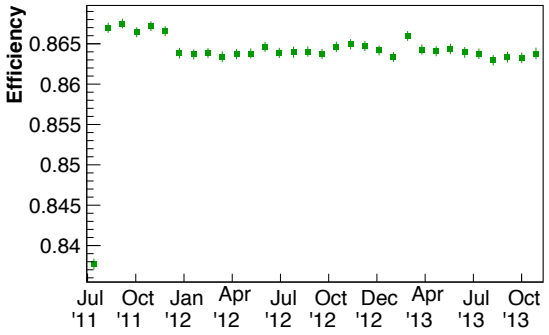

(C) Request of layer 2 efficiency.

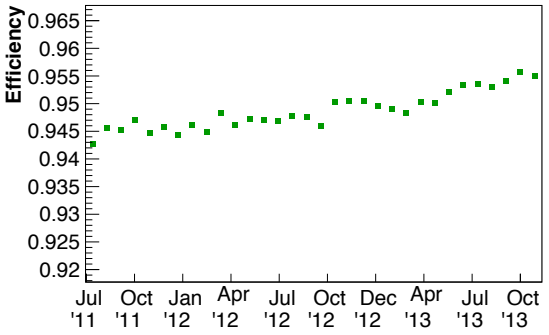

(D) TRD efficiency.

FIGURE 4.27: Efficiencies on DATA as a function of time that clearly show particular trends as a function of time.

where $K(\Delta E, \Delta t)^i$ is defined by the ratio between the efficiency for the i^{th} cut evaluated on DATA (ϵ_{DATA}) and the efficiency for the i^{th} cut evaluated on MC (ϵ_{MC}).

Both ϵ_{DATA} and ϵ_{MC} should be evaluated as a function of energy since all the efficiencies are energy dependent. In addition, only on DATA, the efficiencies should be evaluated as a function of time, in order to take into account possible time dependences.

This means that at each time interval and energy interval, will correspond a different $K(\Delta E, \Delta t)$.

According to the equation 4.13, naively can be followed, for the evaluation of $K(\Delta E, \Delta t)$, the following procedure: the efficiencies in each ΔE and Δt on electrons DATA ($\epsilon^i_{\text{DATA}}(\Delta E, \Delta t)$) for each cut applied in the preselection, have been evaluated using only the data taking during the time interval Δt.

As an example, the efficiency on electron DATA of the request to have only one reconstructed track evaluated in a time interval of 27 days is reported in figure 4.28 as a function of energy compared with the one obtained from MC electrons.

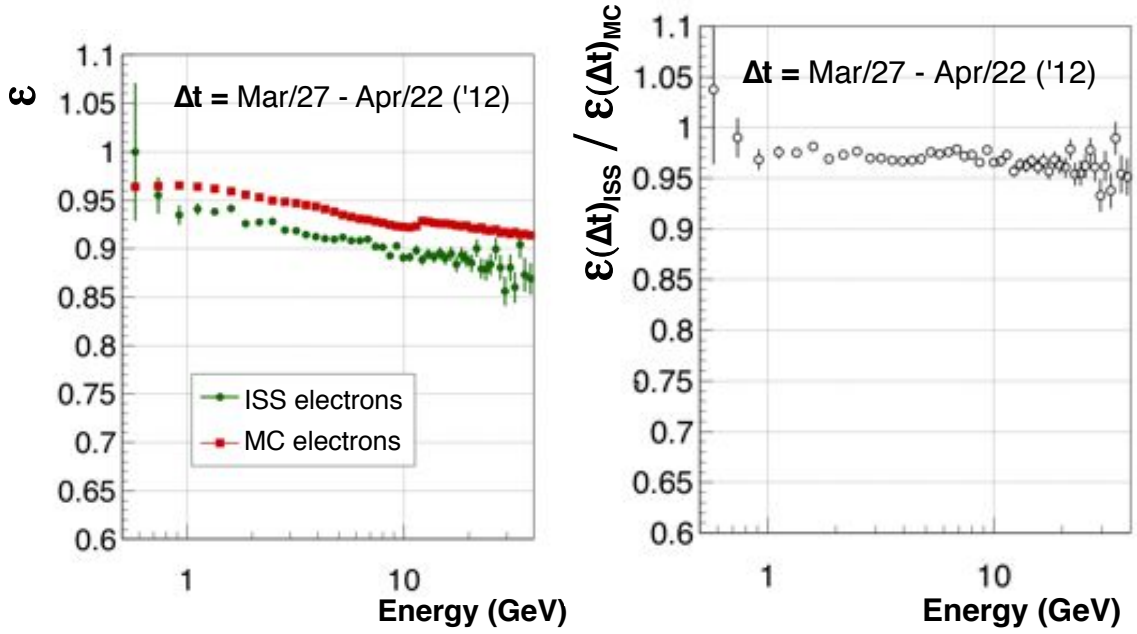

FIGURE 4.28: Contribution to the acceptance correction due to the request to have only one reconstructed track in the time interval Δt = Mar/27–Apr/22 ('12). Efficiency as a function of energy for MC electron (red squared point) and ISS electron DATA (green circle points) is shown on the left, and the relative ISS/MC efficiency ratio on the right. For the calculation of the ISS efficiency only the events taken during Δt = Mar/27–Apr/22 ('12) are taking into account.

The same figure shows the contribution (calculated as the ratio between DATA/MC efficiency) to the factor K coming from the single track efficiency.

By evaluating all the DATA/MC ratio for the others efficiencies and performing the product according to 4.13, it is possible to obtain the factor K for the considered time interval Δt. The result is shown in figure 4.29 as a function of energy and for the time interval Δt=Mar/27–Apr/22(2012).

However this naively method presents some statistical problems, since the efficiencies on DATA are evaluated using only the data taken in the considered time interval. As result, the evaluated K is subjected to quite large statistical fluctuations, especially above 10 GeV as shown in figure 4.29.

4.7.1 *Integrated approach* for $K(\Delta E, \Delta t)$ evaluation.

From the work already carried out for the all electrons flux [100] is well known that all the efficiencies that should be taken into account for the K evaluation are energy dependent. However, there are some efficiencies that don't change in time. For these efficiencies it is possible to use the whole statistic in order to decrease the

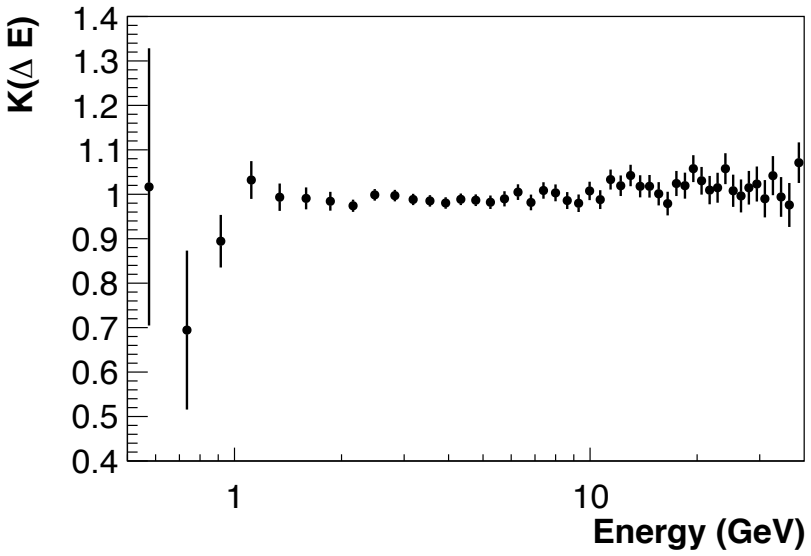

FIGURE 4.29: The obtained K as a function of energy for one time interval of 27 days with a *naively approach*, using only the data in each energy and time bin for ISS efficiencies evaluation.

statistical fluctuations on the final correction $K(\Delta E, \Delta t)$. For this purpose, a deep study of the variation in time and energy of each efficiency is needed.

According to the kind of time dependence, the efficiencies can be divided into the following classes:

a. **Only E dependent**
   Efficiencies that depend from energy (E), but not from time.

b. **E and t dependent, E and t uncorrelated**
   Efficiencies that depend both from energy (E) and time (t), with the energy and time dependences *uncorrelated*.

c. **E and t dependent, E and t correlated**
   Efficiencies that depend both from energy (E) and time (t), with the energy and time dependences *correlated*.

In order to use the highest possible statistic, each class of efficiency is treated in a different way that will be explained in details in this section. The method used to divide the efficiencies into the three classes shown above is explained in section 4.8.

The kind of time dependence can be described by a variable ρ defined as follow:

$$\rho(\Delta E, \Delta t) = \frac{\epsilon(\Delta E, \Delta t)}{< \epsilon(\Delta E) >} \tag{4.20}$$

where:

- $\epsilon(\Delta E, \Delta t)$ is the efficiency in the time interval Δt and in the energy interval ΔE;
- $< \epsilon(\Delta E) >$ is the mean efficiency time integrated for the energy interval ΔE;

The time variation, energy integrated, $(< \rho(\Delta t) >)$ will be:

$$< \rho(\Delta t) >= \frac{< \epsilon(\Delta t) >}{< \epsilon >} \tag{4.21}$$

where:

- $< \epsilon(\Delta t) >$ is the efficiency in the time interval Δt, energy integrated.
- $< \epsilon >$ is the mean efficiency time and energy integrated;

a. Efficiencies only energy dependent

The efficiencies that belong to this class are the following:

- trigger efficiency;
- TRD likelihood efficiencies;
- particle with shower;
- Track inside ECAL;
- Trk-ECAL match;
- β effciency;
- $Z_{\mathrm{TRK}} < 1.5$.

These efficiencies doesn't depend on time and from equations 4.20 and 4.21 for these kind of efficiencies:

$$\rho(\Delta E, \Delta t) =< \rho(\Delta t) >= 1 \quad \rightarrow \quad \epsilon(\Delta E, \Delta t) =< \epsilon(\Delta E) > \tag{4.22}$$

According to equation 4.22 for the calculation of $\epsilon^{i}_{\mathrm{DATA}}(\Delta E, \Delta t)$ which is applied in order to obtain $K(\Delta E, \Delta t)$, there is no reason to use only the data taken in the time

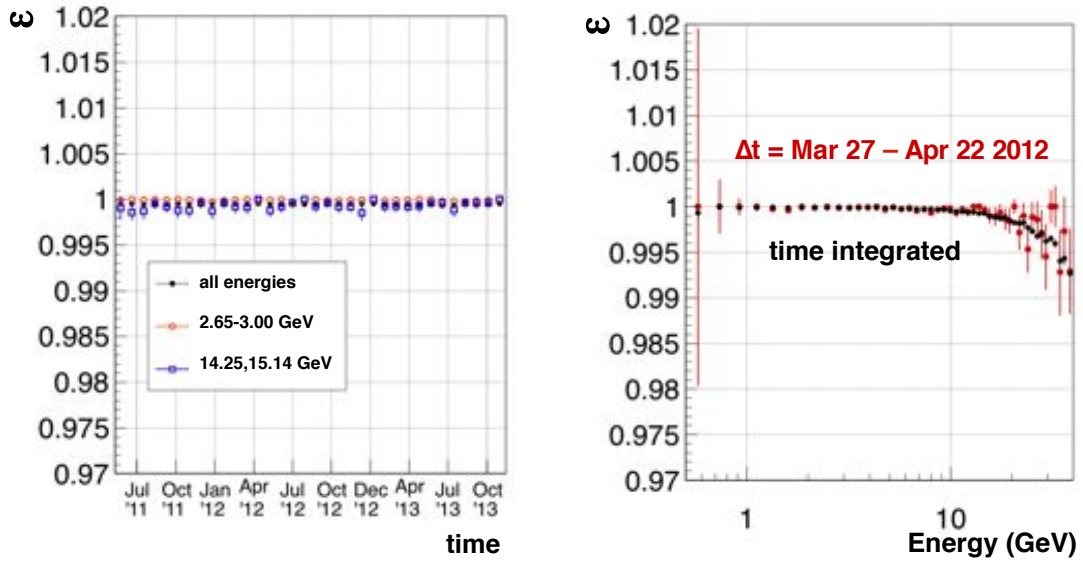

FIGURE 4.30: Left: Z_{TRK} <1.5 efficiency on DATA as a function of time, integrated over all energies (black circle filled markers), and for two different energy intervals, 2.65–3.00 GeV (black hollowed circle markers) and 14.25–15.14 GeV (blue hollowed square markers). There is no evidence of a time dependence at least at the level of 0.1%. Right: Z_{TRK} <1.5 efficiency on DATA as a function of energy. The red points are obtained using the DATA taken in 27 days, the black points are obtained using data taken over all the 30 months. Since there is no time dependence evidence for the $K(\Delta E, \Delta t)$ the time integrated efficiency can be used to improve the statistic.

interval Δt, but it can be evaluated as a function of energy and time integrated. In this way is possible to obtain a great improvement from the statistical point of view.

As an example, the efficiency on DATA of the request $Z_{\mathrm{TRK}} < 1.5$ as a function of time is shown in figure 4.30 (left), both integrated over all energies and for two different energy intervals (2.65–3.00 GeV and 14.25–15.14 GeV). The same figure (on the right) shows the DATA/MC ratio for the Z efficiency, evaluated using only data taken in a time interval of 27 days and using a time integrated method. With the second method the statistical fluctuation are clearly decreased.

b. Efficiencies energy and time dependent, energy and time uncorrelated

The efficiencies that belong to this class, are the following:

- nTrTracks>0;
- nTrTracks=1;
- Layer2;

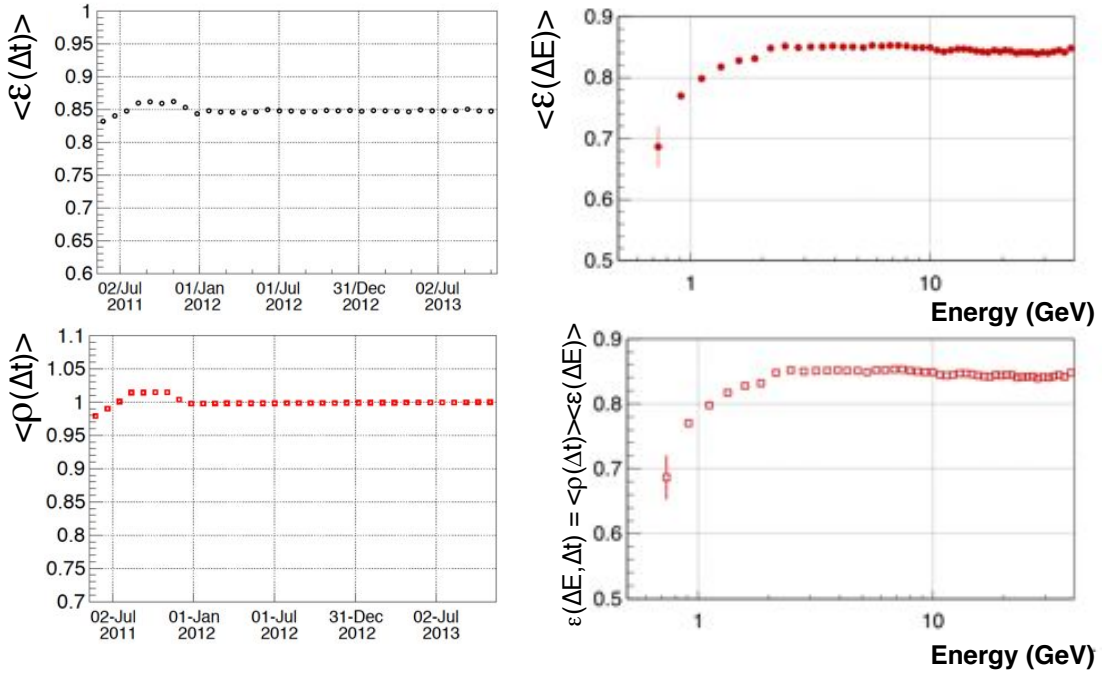

FIGURE 4.31: Method for the calculation of $\epsilon(\Delta E, \Delta t)$ applied in the case of the track efficiency (that belong to the class of efficiencies with time dependence and energy dependence uncorrelated).

These efficiencies are both energy and time dependent, but the time and energy variations are uncorrelated. From equations 4.20 and 4.21 this means that:

$$\rho(\Delta E, \Delta t) =< \rho(\Delta t) > \quad \rightarrow \quad \epsilon(\Delta E, \Delta t) =< \epsilon(\Delta E) >< \epsilon(\Delta t) > \tag{4.23}$$

This means that we can calculate $\epsilon(\Delta E, \Delta t)$ through $< \epsilon(\Delta E) >$ and $< \epsilon(\Delta t) >$ that are, respectively, energy and time integrated efficiencies.

As an example the figure 4.31, shows this method applied to the track efficiency.

c. Efficiencies energy and time dependent, energy and time correlated

The only efficiency that belong to this class is the request to have at least 9 hits on TRD for the likelihood reconstruction. Figure 4.32 (left) shows the TRD cuts efficiencies as a function of time, energy integrated (black filled markers) and for two different energy bins, 2.65–3.00 GeV (blue squared hollowed markers) and 14.25-15.14 GeV (orange circle hollowed markers). This efficiency depends both from energy and time, and the energy and time variations are *correlated*.
In this case, equations 4.20 and 4.21 give:

$$\rho(\Delta E, \Delta t) \neq< \rho(\Delta t) > \quad \rightarrow \quad \epsilon(\Delta E, \Delta t) = \epsilon(\Delta E, \Delta t) > \tag{4.24}$$

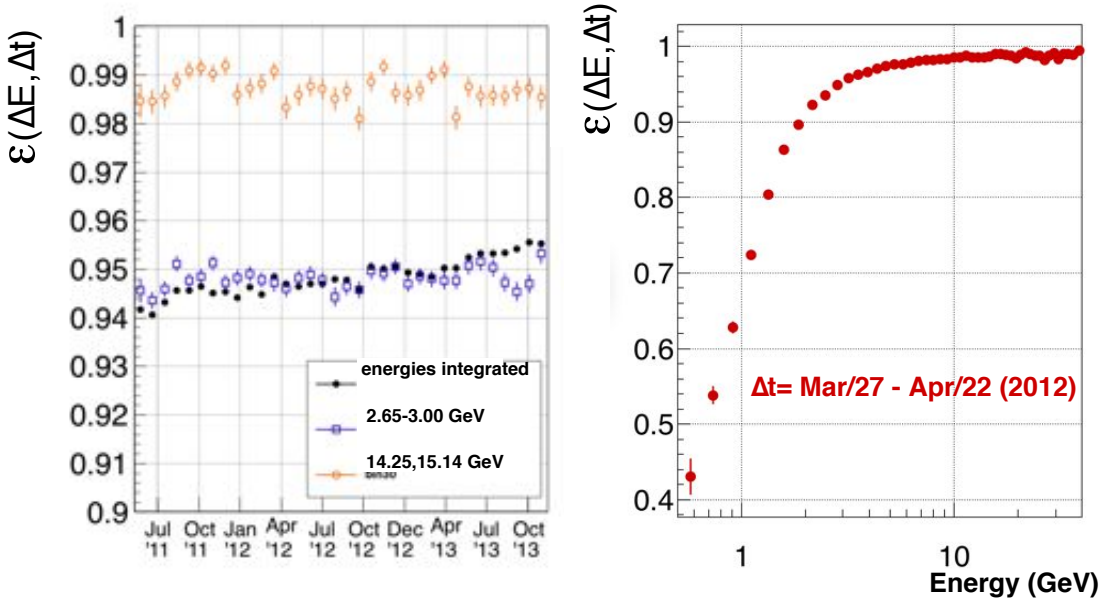

FIGURE 4.32: Left: TRD cut efficiency as a function of time energy integrated (black filled markers) and for two different energy bins, 2.65–3.00 GeV (blue squared hollowed markers) and 14.25-15.14 GeV (orange circle hollowed markers). Right: DATA/MC TRD cut efficiencies ratio as a function of energy calculate in a time interval of 27 days.

In this case, it is possible to calculate $\epsilon(\Delta E, \Delta t)$ only using the data taken in time interval Δt and which energy is in the interval ΔE. The obtained contribution to K (DATA/MC efficiencies ratio) is shown as a function of energy in Figure 4.32 (right). There is no way to increase the statistics and the TRD efficiency obtained in a time interval of 27 days is shows in figure 4.32.

Figure 4.33 shows the improvement reached with an *integrated approach* in the $K(\Delta E, \Delta t)$ calculation, respect to a *naively approach*.

4.8 Study of the time dependence

In order to divide the efficiencies on DATA into the three class described in section 4.7.1, first the efficiencies that are time dependent are individuate, then the efficiencies with time and energy dependences correlated are distinguished from the efficiencies with time and energy dependences uncorrelated.

In this section the method that has been applied in these two steps will be described.

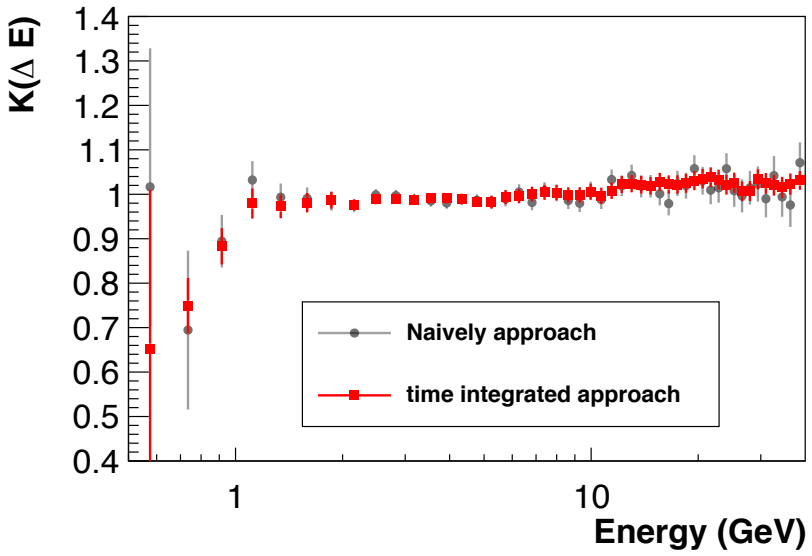

FIGURE 4.33: Comparison between K obtained with the *first approach* (gray points) and K obtained with the *integrated approach* (red points), in a time interval of 27 days.

4.8.1 Individuation of time dependent efficiencies

For each efficiency ϵ, the following variable has been defined:

$$t_{\rm var} = 1 - \frac{\epsilon(\Delta E, \Delta t_{\rm i})}{< \epsilon(\Delta E) >} = 1 - \rho(\Delta E, \Delta t_{\rm i}) \tag{4.25}$$

where $\epsilon(\Delta E, \Delta t_{\rm i})$ is the efficiency evaluated as a function of energy and in the time interval $\Delta t_{\rm i}$ and $< \epsilon(\Delta E) >$ the efficiency evaluated in the the energy bin ΔE and time integrated.

The distribution of $t_{\rm var}$ for all the time intervals and all energy intervals indicates how much is the deviation for an efficiency at time $\Delta t_{\rm i}$ from the time integrated efficiency. If there aren't time dependences $t_{\rm var}$, should be a symmetric distribution around 0 where the spread is given only by the statistical fluctuations.

Dividing $t_{\rm var}$ by the statistical errors of $\epsilon(\Delta E, \Delta t_{\rm i})$ $(\delta_{\rm S})$[6] a gaussian distribution is obtained and the σ of the gaussian gives the information about the time dependence of the efficiency:

- a gaussian with $\sigma = 1$ implies no time dependences
- a no-gaussian distribution or a gaussian with $\sigma \neq 1$ implie time dependences

[6]The statistical errors coming from $< \epsilon(\Delta E) >$ are negligible with respect to the ones coming from $\epsilon(\Delta E, \Delta t_{\rm i})$.

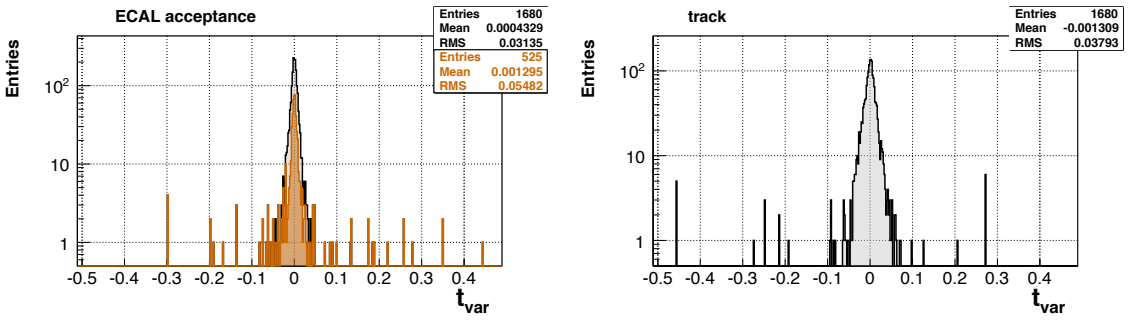

FIGURE 4.34: Distribution of t_{var} for the efficiency of the Track-ECAL (left) and for the track efficiency (right).

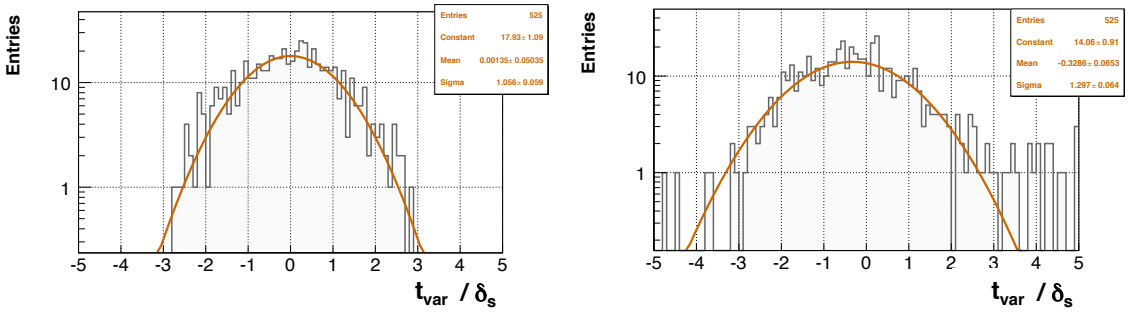

FIGURE 4.35: Distribution of t_{var} divided by the statistical error δ_{S} with, superimposed, a gaussian fit, for the Track-ECAL (left) and for the track efficiency (right).

As an example, the distribution of t_{var} for the efficiency of the Track-ECAL and for the track efficiency are shown in figure 4.34. Both the distribution are symmetric with respect to 0. Figure 4.35 shows the distribution of t_{var} divided by the statistical error δ_{S} with, superimposed, a gaussian fit. The sigma obtained in case of Track-ECAL matching efficiency is 1.056 ± 0.059 and indicates that there aren't time dependences. In the case of the Track efficiency the fitted sigma is $1.29 \pm 0.064 \neq 1$ within the error and this means that there are time dependences.

4.8.2 Individuation of correlation between time and energy dependences

With the method shown above is possible to distinguish between the efficiency time dependent and not time dependent. However, there are no information about possible correlations between energy and time dependences.

In order to study this correlation, for each efficiency the following quantity have been studied:

$$< \Delta\epsilon > = < \epsilon > - < \epsilon(\Delta E) > \tag{4.26}$$

and

$$\Delta\epsilon^{\Delta t} =< \epsilon(\Delta t) > -\epsilon(\Delta E, \Delta t) \tag{4.27}$$

where:

- $< \epsilon >$ is the efficiency energy and time integrated;
- $< \epsilon(\Delta E) >$ is the efficiency time integrated in a given energy bin ΔE
- $< \epsilon(\Delta t) >$ is the efficiency energy integrated in a given time bin Δt
- $\epsilon(\Delta E, \Delta t)$ is the efficiency evaluated in a energy binΔE and in a time bin Δt

The equation evaluated in each ΔE gives a distribution with a shape that depends on the energy dependence of the efficiency ϵ.

The quantity $\Delta\epsilon^{\Delta t}$ defined by the equation 4.27 is $< \Delta\epsilon >$ but evaluated in a given time interval Δt.

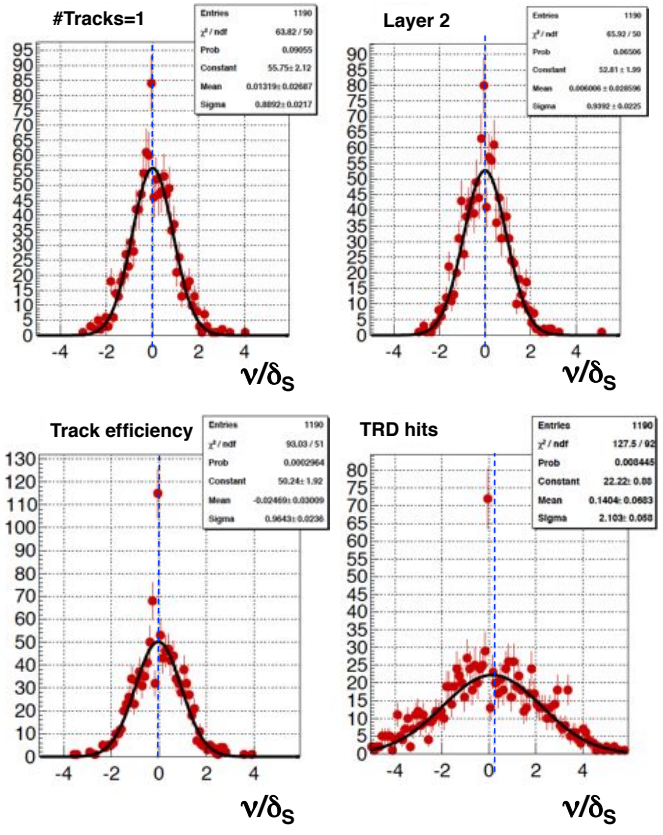

FIGURE 4.36: ν/δ_S distribution for the single track efficiency, layer 2 efficiency, track efficiency and TRD hits efficiency. A gaussian fit is performed over the distributions to evaluate the energy/time correlations according to the method described in this section.

If the energy dependence of ϵ doesn't depend on time, this means that $\Delta\epsilon(\Delta t) \sim < \Delta\epsilon >$. This feature can be described by the quantity:

$$\nu = < \Delta\epsilon > - \Delta\epsilon(\Delta t) \tag{4.28}$$

The distribution obtained for all the time intervals Δt and all energy intervals ΔE of ν and divided by the statistical errors of $\epsilon(\Delta E, \Delta t)$, δ_S[7], gives a gaussian distribution with a sigma that contains the information about the energy and time correlations:

- $\sigma = 1$: the differences between $< \Delta\epsilon >$ and $\Delta\epsilon(\Delta t)$ are due only to the statistical fluctuations. There are no energy/time correlations;
- $\sigma > 1$: the differences between $< \Delta\epsilon >$ and $\Delta\epsilon(\Delta t)$ are due to the statistical fluctuations and to the systematic component. This last one is a sign of an energy/time correlation.

The distributions of ν/δ_S for the 4 efficiencies that are time dependent are reported in figure 4.36 with, superimposed, a gaussian fit. As result the efficiencies related to the track (presence of track, single track and presence of layer 2) as $\sigma = 1$ so they are classified as efficiencies without energy/time correlations. The distribution for TRD hits efficiency shows a $\sigma > 1$ so it is classified as an efficiency with energy/time correlations.

[7]The statistical errors on $< \epsilon >$,$< \epsilon(\Delta E) >$ and $< \epsilon(\Delta t) >$ are negligible respect to the ones on $\epsilon(\Delta E, \Delta t)$.

Chapter 5

Time dependence of $e^{\pm}$ fluxes

In this chapter the obtained results for electron and positron fluxes in time are presented and their measurement uncertainties reviewed. A first interpretation of the observed time dependencies within the Force Field approximation will be then discussed, however, the unprecedented accuracy and fine time binning of our data will demonstrate some limits of this approach.

5.1 Electron and positron fluxes

Using the techniques previously described, the electron and positron fluxes have been measured using AMS data in the energy range 0.5–40. GeV and in 32 time intervals of 27 days, starting on July 1^{st} 2011.

Along this chapter, the fluxes will be often represented multiplied by a power of the energy to better appreciate spectral features. The representative value for the bin energy, $\tilde{E}$, has been evaluated according to the prescriptions from [111] with an input power law spectrum $\Phi \propto \mathrm{E}^{\gamma}$ as follows:

$$\widetilde{\mathrm{E}} = \left(\frac{\mathrm{E}_{\mathrm{max}}^{1-\gamma} - \mathrm{E}_{\mathrm{min}}^{1-\gamma}}{(1-\gamma)(\mathrm{E}_{\mathrm{max}} - \mathrm{E}_{\mathrm{min}})} \right)^{-\frac{1}{\gamma}} \tag{5.1}$$

where E_{min} and E_{max} represent the minimum and maximum energy of the bin and a spectral index γ=3, representative of the $e^{\pm}$ spectra has been assumed. In the following, even if not specified, the notation "E" will correspond to "$\widetilde{\mathrm{E}}$".

The electron fluxes multiplied by E^3 as a function of the energy, obtained in the 32 different time intervals, are shown in figure 5.1. Each color corresponds to a

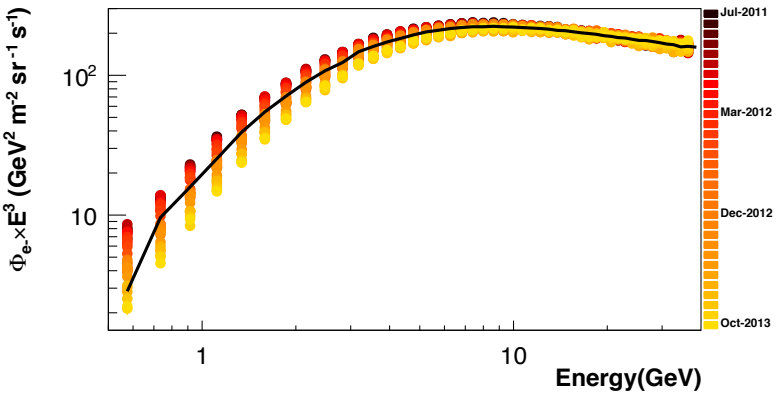

FIGURE 5.1: Electron fluxes multiplied by E^3 as a function of the energy, obtained in the 32 time intervals of our measurement. Each color corresponds to a different time interval of 27 days.

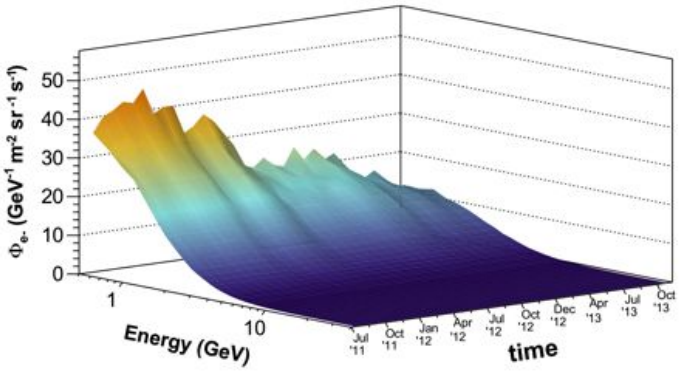

FIGURE 5.2: Electron flux as a function of energy and time. The decrease of the intensity at low energies as a function of time is clearly visible.

different time interval of 27 days and it is clear that the intensity of the flux in the low energy part decreases with time as also shown in figure 5.2.

The same features can be observed on the obtained results for positron fluxes, as shown in figures 5.3 and 5.4.

Figure 5.5 shows the normalized fluxes in each time interval with respect to the time integrated flux[1] both for electrons and positrons in one energy bin. Electrons and positrons follow the same trend (more evident at low energies) with the intensity that decreases as a function of time. The results are in agreement with the solar activity that occurred during the data taking period. The last solar cycle activity in time is represented in terms of sunspot number in figure 5.6. Each point represents

[1]The time integrated flux is the flux measured using the whole time period of the first 30 months of data taking by AMS-02.

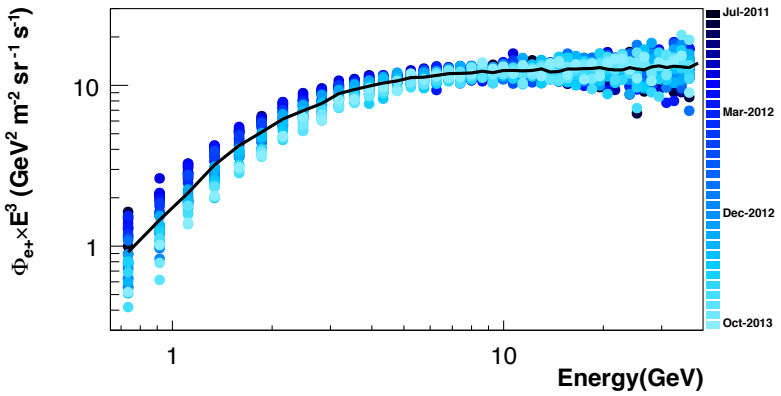

FIGURE 5.3: Positron fluxes multiplied by E^3 as a function of the energy, obtained in the 32 time intervals of our measurement. Each color corresponds to a different time interval of 27 days.

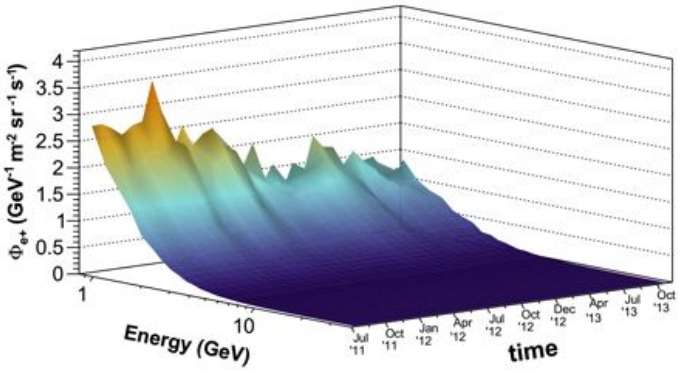

FIGURE 5.4: Positron flux as a function of energy and time. The decrease of the intensity at low energies as a function of time is clearly visible.

the monthly averaged sunspot number (from [112]) increased since Dec. 2008, when the current 24$^{\text{th}}$ solar cycle began, up to April 2014, when it reached its maximum. This implies, as already discussed in section 1.2.1, that the intensity of the CR fluxes observed in our analysis should decrease with time as indeed observed in figure 5.5. Together with the main decreasing trend as function of time due to the approaching of maximum solar activity, the evolution of the fluxes as a function of time is also affected by the *Forbush decreases* and by an annual modulation. A Forbush decrease is a rapid decrease in the galactic cosmic ray intensity following a solar flare. During the following days from the flare, the solar cosmic ray intensity returns to normal. The flare ejects clouds of plasma, constituted by electrons protons and Helium nuclei, through the corona of the sun into space. This plasma typically reaches the Earth a day or two after the event and its magnetic field is sweeping some of the galactic cosmic rays away from Earth. At the altitude of the ISS the reduction of

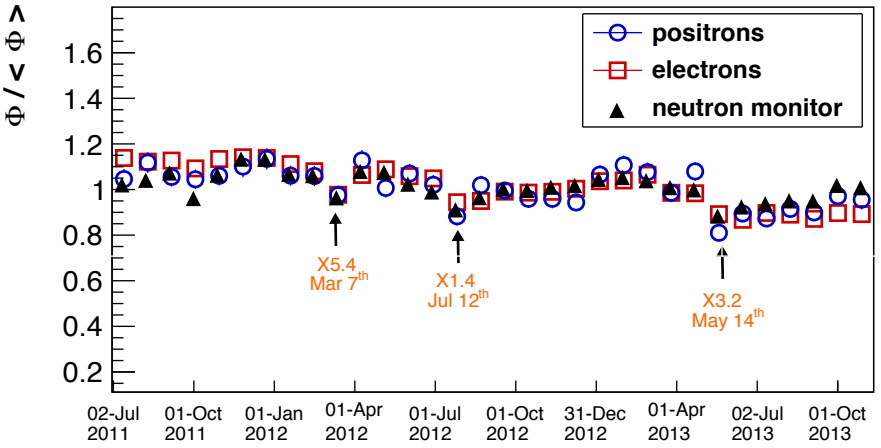

FIGURE 5.5: Normalized electron (red squared markers) and positron fluxes (blue circled markers) in each time interval with respect to the time integrated flux, in one energy bin (4.12–4.54 GeV). The black triangled markers are the normalized counts from the neutron monitors.

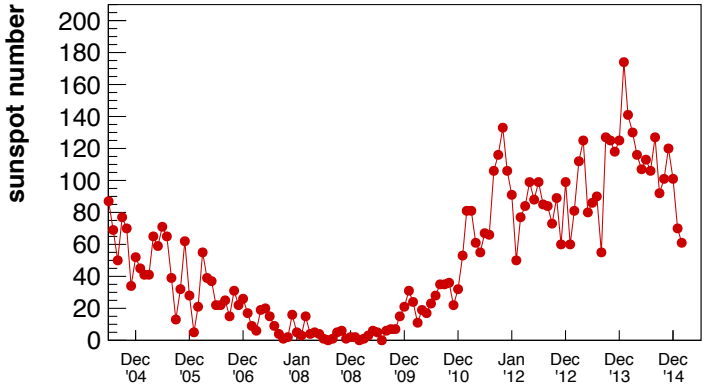

FIGURE 5.6: Sunspot number as a function of time. Each point represents the monthly averaged sunspots number. Data taken from [112].

comics rays intensity during a Forbush decrease can reach also 30%. The magnitude of the Forbush decrease depends on the intensity of the solar flare. The stronger solar flares that occurred during the data taking period used for the analysis are clearly visible as a strong flux intensity decrease on electrons and positrons, as reported in figure 5.5.

Figure 5.7 shows, both for electrons and positrons, the ratio between the fluxes evaluated in all the 32 time intervals and the time integrated flux. The differences that can be observed at low energies between the fluxes in each time interval and the time integrated one, is due to the solar modulation. The effect of the solar

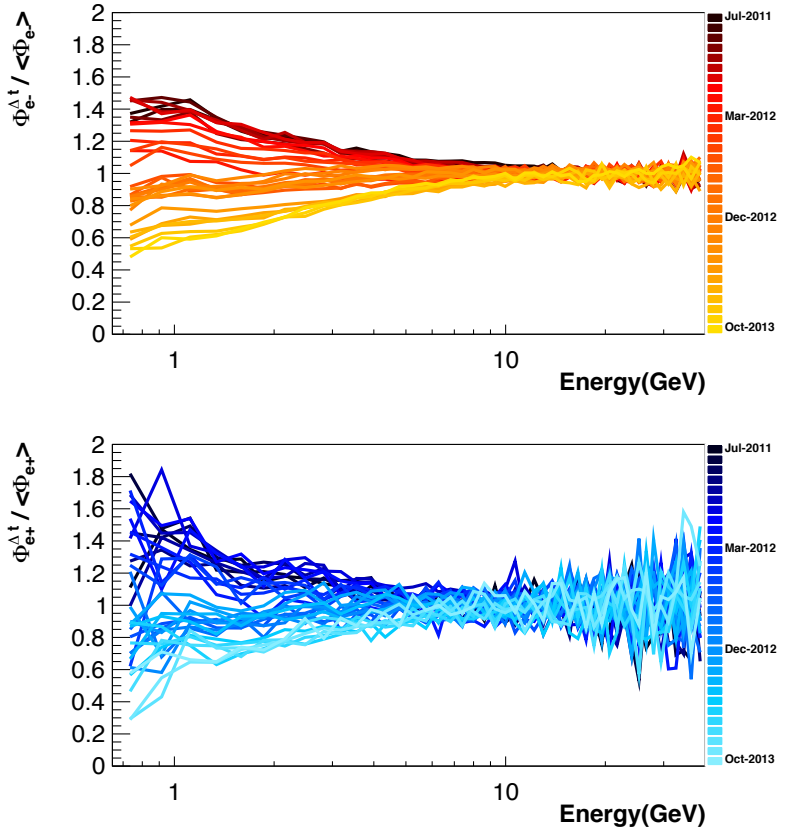

FIGURE 5.7: Ratio between the fluxes evaluated in all the 32 time intervals and the time integrated flux as a function of energy for electrons (top) and positrons (bottom).

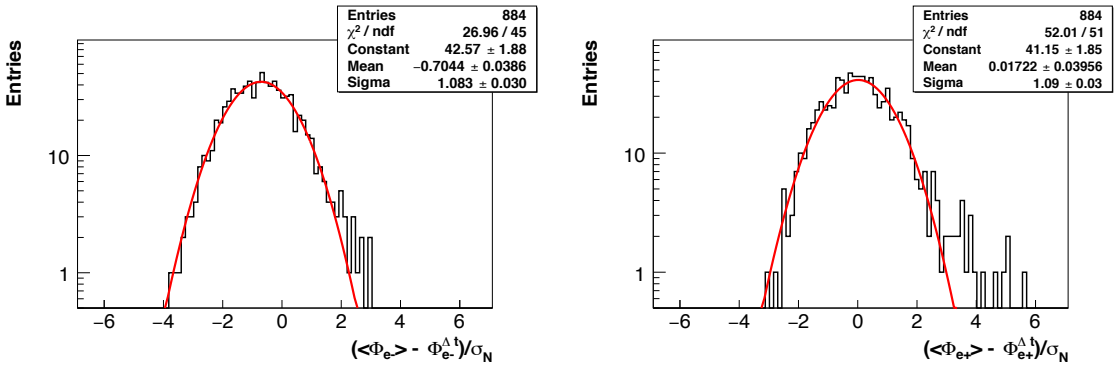

FIGURE 5.8: Difference between the time integrated flux and the fluxes in each time interval for energies >20 GeV, divided by the statistical errors. The obtained distribution is a gaussian with sigma =1 and this confirms that the fluctuations observed in figure 5.7 for energy >20 GeV are purely statistical.

modulation decreases with energy and disappears for energies >20 GeV where the discrepancy that can be observed is due to statistical fluctuations. This is confirmed in figure 5.8 where the difference between the time integrated flux and the fluxes in each time interval for energies >20 GeV, divided by the statistical errors, is reported. The obtained distribution is a gaussian with unitary width, i.e. $\sigma = 1$.

Figure 5.9 shows the flux as a function of time for electrons and positrons in one energy bin with, superimposed, a linear polynomial fit. The result of the fit shows that the annual variation ($d\Phi/dt$) for the electrons and for positrons with energy ∼4 GeV is respectively of 9.29±0.31% and 6.41±0.69%. The observed variation in time is larger than the systematic errors on the measurements (shown by the light-blue colored band around the fit). This confirms that the observed trend is caused by physical phenomena. The difference in the flux variation between electrons and positrons is due to charge-sign dependent effects of solar modulation as discussed in 1.2.1. This difference can be clearly seen also in figure 5.10 that shows the ratio between the positron and the electron fluxes as a function of time, in one energy bin. The annual variation observed for the flux ratio at ∼4 GeV is 3.76±1.01%.

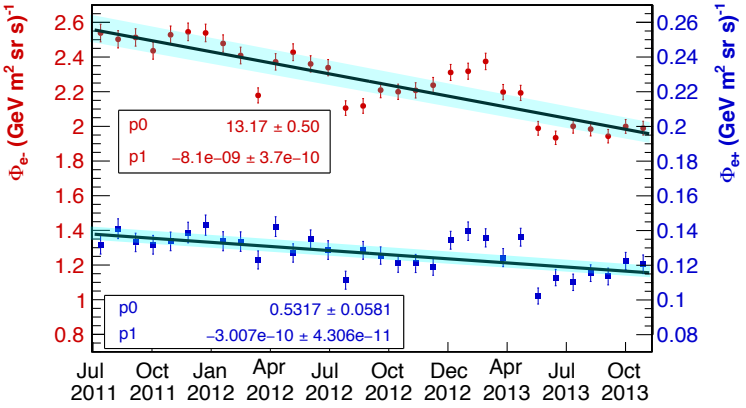

FIGURE 5.9: Flux in time for electrons (red markers) and positrons (blue markers) as a function of time in one energy bin (4.12–4.54 GeV) with, superimposed, a linear polynomial fit. The light blue colored band around the fit is obtained taking into account the systematic errors on the measurements.

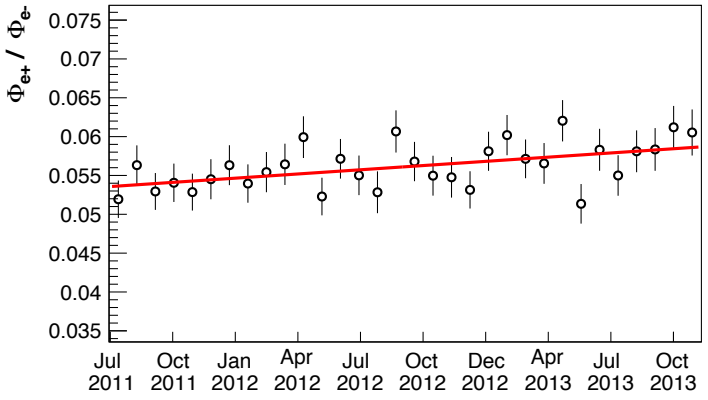

FIGURE 5.10: Ratio between the positron and electron fluxes as a function of time in one energy bin (4.12–4.54 GeV).

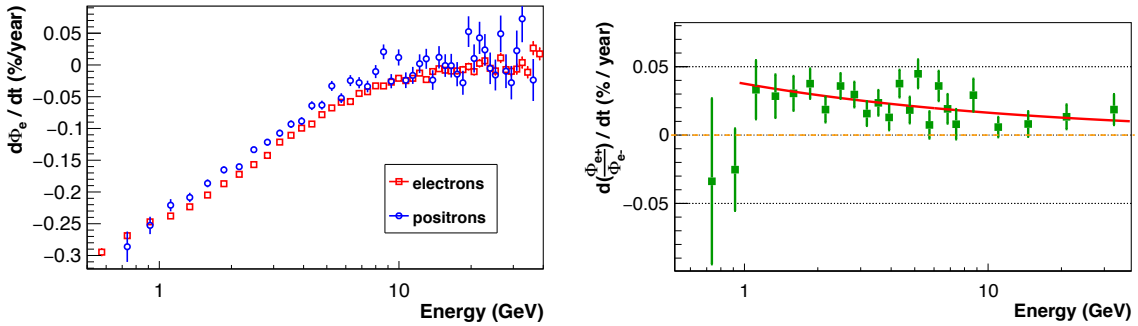

FIGURE 5.11: Annual variation of e^- and e^+ fluxes (left) and of e^+/e^- fluxes (right) as a function of energy.

The annual variation of the fluxes is reported in figure 5.11 (left). It is clear that the flux variation is greater at low energies and decreases with the energy, going from -30% at ∼0.5 GeV and vanishing at ∼20 GeV. In figure 5.11 (right) the annual variation as a function of energy of the ratio between positrons and electrons is reported. The ratio is systematically >0 for energies <20 GeV and excluding energies <1 GeV (where the statistic fluctuations for positrons are to large to draw a conclusion).

The values of the fluxes in all the energy and time bins with all the evaluated uncertainties can be found in tables B.2–B.33 both for electrons and positrons, in appendix B.

5.2 Flux uncertainties

All the possible sources of uncertainties that can affect both the energy and time dependence of the fluxes have been taken into account. The errors came from the identification of electrons and positrons events removing the background with the fit procedure explained in chapter 3 ($N_{e^{\pm}}$), from the acceptance knowledge uncertainty, from the accuracy of the ECAL energy measurement and from the knowledge of charge confusion correction (CC), and they are:

- statistical uncertainties (see section 3.5.1);
  - σ_{stat}: statistical error on the number of electrons and positrons;
- systematic uncertainties;
  - $\sigma_{\text{stat\_templ}}$: error coming from the finite statistic of the templates;
  - $\sigma_{\text{sel\_templ}}$: error coming from the template definition;

- $\sigma_{\mathrm{K}}^{\mathrm{abs}}$: error coming from the uncertainty on acceptance correction;
- $\sigma_{\mathrm{K}}^{\mathrm{stab}}$: error that takes into account the stability of the acceptance correction;
- $\sigma_{\mathrm{K}}^{\mathrm{par}}$ and $\sigma_{\mathrm{K}}^{\mathrm{res}}$: errors coming from the acceptance correction parametrization;
- σ_{CC}: error due to the uncertainty on the charge confusion estimated from Monte Carlo;
- $\sigma_{\mathrm{ECAL\_stab}}$: error related to the stability in time of the ECAL response;
- $\sigma_{\mathrm{ECAL\_abs}}$: error related to the ECAL absolute energy scale.

The uncertainties coming from the number of events and from charge confusion have been already discussed on 3 as well as the uncertainties coming from acceptance correction have been discussed in 4. In the next section the errors coming from the reconstructed energy by ECAL will be reviewed.

According to the kind of correlation bin-to-bin in time or energy, the errors can be divided into 4 different (but not disjoint) categories:

1. errors that do not correlate bin at different times;
2. errors that correlate bin at different times;
3. errors that do not correlate bin at different energies;
4. errors that correlate bin at different energies.

Some of the errors are not correlating bins neither in time, neither in energy (for example σ_{stat}), some of them are correlating bins both in energy and in time (for example $\sigma_{\mathrm{ECAL\_stab}}$).

The classification of errors according to the criteria shown above, is reported in table 5.1.

5.2.1 Uncertainties related to ECAL energy measurement

The best estimation for the energy of electrons and positrons is given by the energy measured by the ECAL. Three kind of uncertainties affect the energy meauserement:

- the ECAL resolution error $\delta^{\mathrm{ECAL\_res}}$;

		time bins		energy bins		coming from:
		corr	uncorr	corr	uncorr	
statistic	σ_{stat}	✗	✔	✗	✔	$N^{e^{\pm}}$
sistematic	$\sigma_{\text{stat\_tmpl}}$	✗	✔	✗	✔	$N^{e^{\pm}}$
	$\sigma_{\text{sel\_tmpl}}$	✔	✗	✗	✔	$N^{e^{\pm}}$
	$\sigma_{\text{K}}^{\text{abs}}$	✔	✗	70%[2]	30%[2]	K
	$\sigma_{\text{K}}^{\text{stab}}$	✗	✔	✗	✔	K
	$\sigma_{\text{K}}^{\text{par}}$	✔	✗	✗	✔	K
	$\sigma_{\text{K}}^{\text{res}}$	✔	✗	✗	✔	K
	σ_{CC}	✔	✗	✔	✗	CC
	$\sigma_{\text{ECAL\_stab}}$	✗	✔	✔	✗	Energy measurement
	$\sigma_{\text{ECAL\_abs}}$	✔	✗	✔	✗	Energy measurement

TABLE 5.1: Classification of errors according to the criteria discussed in section 5.2

- the ECAL absolute scale error $\delta^{\text{ECAL\_abs}}$;

- the ECAL stability in time $\delta^{\text{ECAL\_stab}}$.

The first one is due to the finite resolution of the ECAL detector that, recalling the formula 2.2, can be parametrized as follows:

$$\delta^{\text{ECAL\_res}}(E)/E = \frac{(10.4 \pm 0.2)\%}{\sqrt{E(GeV)}} \oplus (1.4 \pm 0.1)\% \tag{5.2}$$

The ECAL resolution error , $\delta^{\text{ECAL\_res}}$, is typically well contained inside the bin size used in our flux measurements. Bin-to-bin migration effects are therefore potentially relevant only to close to bin edges, however they are mitigated by the symmetric exchange between adjacent bins. For this reason $\delta^{\text{ECAL\_res}}$ is negligible at all energies.

The ECAL absolute scale error $\delta^{\text{ECAL\_abs}}$ represents the error related to any miscalibration of the absolute energy measurement. The ECAL energy calibration has been tuned using test beam data and using the MC simulation in the energy range not covered by the test beams. On flight data the energy scale is verified by using the ratio E/R. The comparison between the E/R peak position on flight data and on test beam data confirms that the ECAL calibration and the energy scale defined on ground can be safely applied on flight data. This comparison limits the uncertainty of the absolute energy scale to 2% in the range covered by the beam test results, 10–290 GeV. It increases to 5% at 1 GeV and to 3% at 500 GeV. These error represents a not-negligible contribution to the total systematic error, in particular

[2]The error $\sigma_{\text{K}}^{\text{abs}}$ is evaluated from the ratio of DATA/MC acceptances. A large part of this error (70%) is expected to be correlated in different energy bins since this quantity is described with a fitted smooth function over the full energy range.

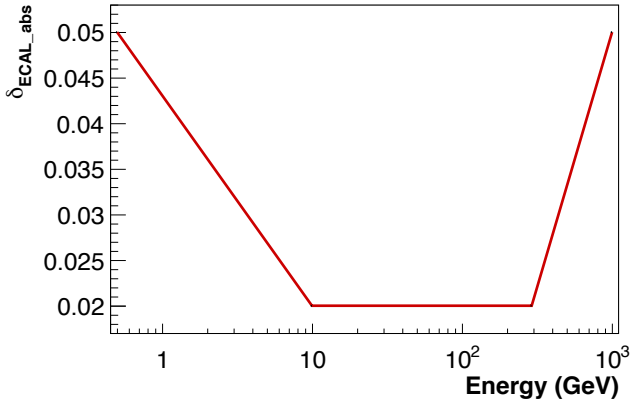

FIGURE 5.12: ECAL absolute scale error as a function of energy.

below 5 GeV, where it dominates. $\delta^{\text{ECAL\_abs}}$ as a function of energy is shown in figure 5.12. Unlike $\delta^{\text{ECAL\_res}}$ this uncertainty translates indirectly into a systematic effect on the flux measurement.

As for the published AMS $e^{\pm}$ flux measurements [65, 67, 100], in this work the uncertainty on the ECAL energy scale is treated as uncertainty on the energy bin borders. However, $\sigma_{\text{ECAL\_abs}}$ translates indirectly into a systematic effect on the flux measurement. This has to be carefully taken into account when the flux measurement is used to infer physics information through the comparison of physics models to the data points. The ECAL stability in time $\delta_{\text{ECAL\_stab}}$ takes into account any possible variation in time of ECAL response which stability is checked with the E/R for $e^{\pm}$ samples. Figure 5.13 shows the peak of E/R distribution as a function of time for an electron sample selected on data. The RMS of the distribution coming from the different values of E/R peaks has been taken as $\delta_{\text{ECAL\_stab}}$.

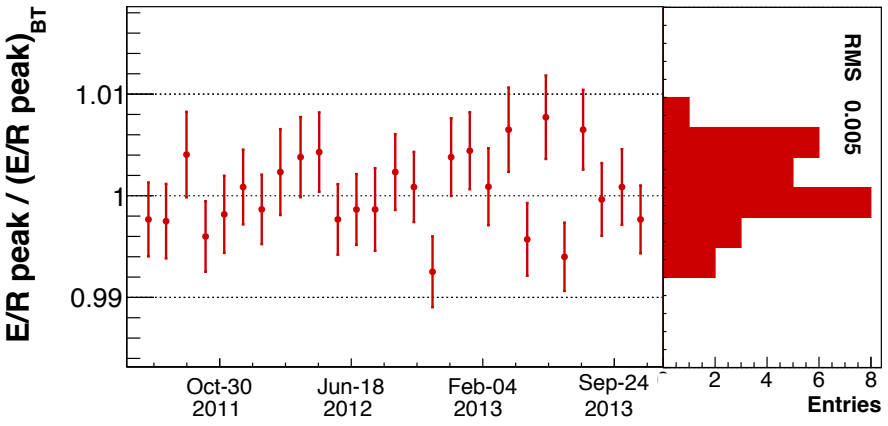

FIGURE 5.13: Peak of E/R distribution as a function of time for an electron sample selected on data. The RMS of the distribution has been taken as $\delta_{\text{ECAL\_stab}}$.

For the evaluation of the errors on fluxes due to $\delta_{\text{ECAL\_abs}}$ and $\delta_{\text{ECAL\_stab}}$ the same procedure has been applied and it is explained in the following. A solid shift of $\pm\delta_{\text{E}}$ (where δ_{E} represents $\delta_{\text{ECAL\_abs}}$ or $\delta_{\text{ECAL\_stab}}$) on the fluxes has been applied on value of δE term in equation 4.8. After this procedure, two new values for the fluxes are obtained, one for $+\delta_{\text{ECAL}}$ shift and one for $-\delta_{\text{ECAL}}$ shift:

$$\begin{aligned}
\text{shift} = -\delta_{\text{E}} \quad &\rightarrow \quad \Delta E = \Delta E - \delta E \Delta E \\
&\rightarrow \quad \Phi(E - \delta E \cdot E) = \Phi_{-\delta \text{E}} = \Phi(E)\frac{1}{1-\delta E} \\
\text{shift} = +\delta_{\text{E}} \quad &\rightarrow \quad \Delta E = \Delta E + \delta E \Delta E \\
&\rightarrow \quad \Phi(E + \delta E \cdot E) = \Phi_{+\delta \text{E}} = \Phi(E)\frac{1}{1+\delta E}
\end{aligned} \tag{5.3}$$

An example for the shifted electron fluxes considering $\delta_{\text{E}} = \delta_{\text{ECAL\_abs}}$ obtained with this method is shown in Figure 5.14. The systematic uncertainties $\sigma_{\text{ECAL\_abs}}$ and

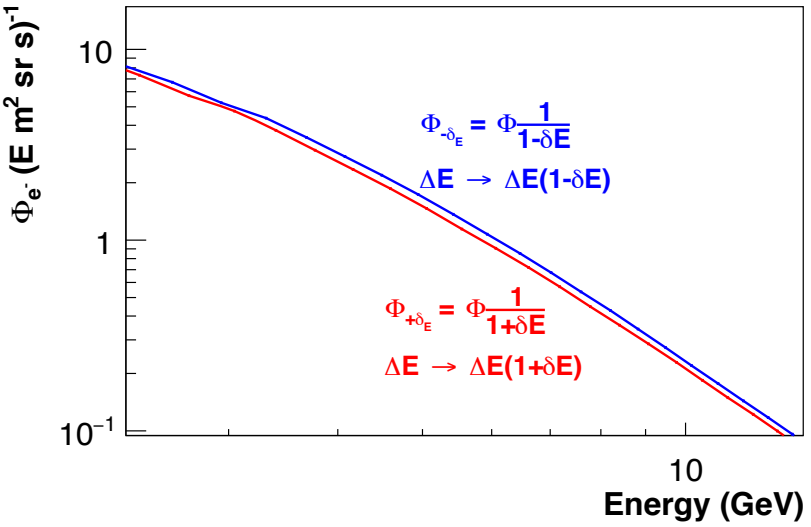

FIGURE 5.14: $\Phi_{-\delta \text{E}}$ and $\Phi_{+\delta \text{E}}$ obtained for electron flux in the case of $\delta_{\text{E}} = \delta_{\text{ECAL\_abs}}$.

$\sigma_{\text{ECAL\_stab}}$ are defined by the half difference between $\Phi_{-\delta \text{E}}$ and $\Phi_{+\delta \text{E}}$:

$$\begin{aligned}
\sigma_{\text{ECAL_abs}} &= \frac{|\Phi_{-\delta \text{E}} - \Phi_{+\delta \text{E}}|}{2} \quad \text{with } \delta_{\text{E}} = \delta_{\text{ECAL_abs}} \\
&\text{and} \\
\sigma_{\text{ECAL_stab}} &= \frac{|\Phi_{-\delta \text{E}} - \Phi_{+\delta \text{E}}|}{2} \quad \text{with } \delta_{\text{E}} = \delta_{\text{ECAL_stab}}
\end{aligned} \tag{5.4}$$

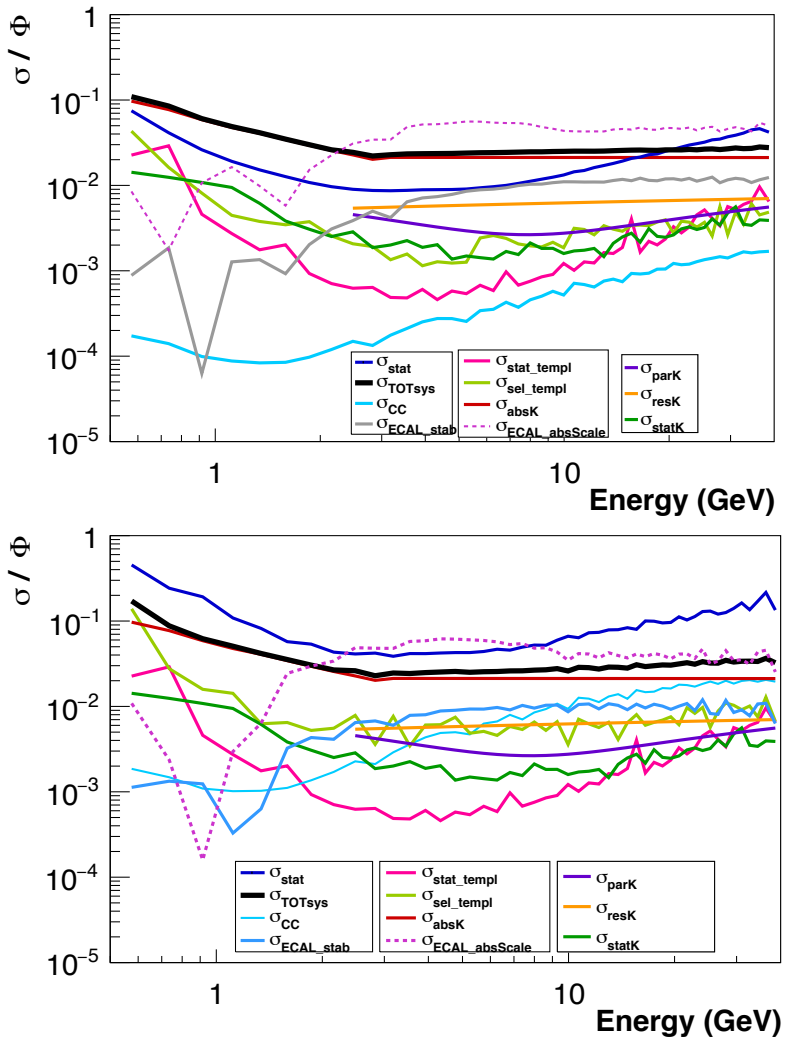

FIGURE 5.15: All the uncertainties on the flux measurement taken into account for this work as a function of energy in one time bin of 27 days, for electron flux (top) and positron flux (bottom).

5.2.2 Uncertainties summary

Measurement uncertainties as a function of the energy are summarised in Figure 5.15 for the electrons (top) and the positron (bottom) fluxes in one time bin of 27 days. Systematic errors are comparable for the two species and dominate the e^- measurement at energies below ∼10 GeV, whereas statistical uncertainties dominate the e^+ flux measurement.

The total systematic errors has been obtained by the sum in quadrature of all the single systematic errors excluding $\sigma_{\text{ECAL\_abs}}$ since, as explained above, the uncertainty on the ECAL energy scale is treated as uncertainty on the energy bin borders:

$$\sigma_{\text{TOTsys}} = \sigma_{\text{stat\_tmpl}} \oplus \sigma_{\text{sel\_tmpl}} \oplus \sigma_{\text{K}}^{\text{abs}} \oplus \sigma_{\text{K}}^{\text{stab}} \oplus \sigma_{\text{K}}^{\text{par}} \oplus \sigma_{\text{K}}^{\text{res}} \oplus \sigma_{\text{CC}} \oplus \sigma_{\text{ECAL\_stab}} \quad (5.5)$$

Moreover, the obtained systematic uncertainties $\sigma_{\mathrm{K}}^{\mathrm{abs}}$, $\sigma_{\mathrm{ECAL\_stab}}$ and $\sigma_{\mathrm{ECAL\_abs}}$ on the time integrated fluxes are coherent with those evaluated in [67],[100].

5.3 Phenomenological interpretation of results

A simple phenomenological interpretation of the obtained electron and positron fluxes as a function of time can be given using the *Force Field Approximation* model. As discussed in section 1.2.1.1, the Force Field Approximation is a very basic model that describes the CRs propagation in the Heliosphere. It doesn't take into account all the solar modulation effects, like the charge-sign dependent ones, however it can be used to draw basic physics conclusions.

According to this model the fluxes measured in the heliosphere ($\Phi_{\mathrm{e}^{\pm}}^{\mathrm{meas}}$), and hence affected by the solar modulation, is related to the *Local Interstellar fluxes* ($\Phi_{\mathrm{e}^{\pm}}^{\mathrm{LIS}}$), i.e. the fluxes outside the heliosphere and hence not affected by the solar modulation, by the formula:

$$\Phi_{\mathrm{e}^{\pm}}^{\mathrm{meas}}(E) = \frac{E^2 - m_{\mathrm{e}}^2}{(E+\phi)^2 - m_{\mathrm{e}}^2} \cdot \Phi_{\mathrm{e}^{\pm}}^{\mathrm{LIS}}(E+\phi) \tag{5.6}$$

where:

- E is the detected energy in the heliosphere(in GeV);
- ϕ is the effective solar modulation potential (in GV);
- m_{e} is the mass of electrons (in GeV/c^2).

For the parametrization of $\Phi_{\mathrm{e}^{\pm}}^{\mathrm{LIS}}$ has been decided to apply a procedure widely adopted in literature [113]. The flux of primary e^- produced and accelerated by SNR can be described by a broken power law and the flux of secondary e^+ produced by the interaction of primary CRs with the ISM can be described by a simple power law. Several trials have been done with or without the break in the electron energy spectrum and the best fit has been obtained in the case of the broken power law. The break in the energy spectrum for e^- can be explained by the existence of two injection processes at the source or by two different propagation mechanisms that dominate in different energy ranges.

Moreover a common primary source of $e^{\pm}$ should be invoked in order to correctly describe the observed excess in the e^+ flux [65, 67]. The common primary source can be parametrized by a power law spectrum with a cutoff energy E_{cutoff}. The cutoff energy parameter defines the energy at which the common source contribution to

the $e^{\pm}$ fluxes starts to drop. This is a first order modelization for the common source expected for primary $e^{\pm}$ produced by pulsars or DM annihilation.

According to the parametrization described above $\Phi^{\mathrm{LIS}}_{\mathrm{e}^{\pm}}$ in equation 5.6 can be written as follow:

$$\Phi^{\mathrm{LIS}}_{\mathrm{e}^-} = A_{\mathrm{e}-} E^{\gamma_{\mathrm{e}-}} \left(1 + \left(\frac{E}{E_{\mathrm{b}}}\right)^{\frac{\Delta\gamma}{s}}\right)^{s} + A_{\mathrm{comm}} E^{\gamma_{\mathrm{comm}}} \mathrm{e}^{-\frac{\mathrm{E}}{\mathrm{E_{cutoff}}}}$$
$$\Phi^{\mathrm{LIS}}_{\mathrm{e}^+} = A_{\mathrm{e}+} E^{\gamma_{\mathrm{e}+}} + A_{\mathrm{comm}} E^{\gamma_{\mathrm{comm}}} \mathrm{e}^{-\frac{\mathrm{E}}{\mathrm{E_{cutoff}}}} \tag{5.7}$$

where $A_{\mathrm{e}-}$, $A_{\mathrm{e}+}$ and A_{comm} represent the normalization for the single $e^{\pm}$ power laws and for the common source, γ_{e^+} and γ_{comm} are the spectral indices for the single e^+ power law and for the common source. The first term of $\Phi^{\mathrm{LIS}}_{\mathrm{e}^-}$ is a broken power law. γ is the value of the spectral index before the breaks and $\Delta\gamma$ the difference between the spectral index after and before the break. E_{b}, free parameter of the fit, is the energy at which the break occurs. s is an additional free parameter of the fit that allows the break to be smooth: a sharp break, indeed, would be completely unphysical. This parametrization represents an extended version of minimal model that has been used by the AMS collaboration in [65, 66].

The described parametrization has been used to fit the obtained $e^{\pm}$ fluxes with a minimal assumption for a time dependent analysis that however, as will be shown in section 5.3.2, allows to well described the obtained data. According to this assumption only the solar modulation potentials $\phi_{\mathrm{e}-}$ and $\phi_{\mathrm{e}+}$ are time dependent. In total the function used to perform the fit has 12 independent parameters with 10 of them time independent and 2 time dependent.

To have the best estimation of the time independent parameters the following procedure has been applied:

1. a combined fit on the time integrated all-electron flux and positron fraction has been performed using the parametrization described by the equations 5.6 and 5.7 imposing only one constrain on parameters: A_{comm}, γ_{comm} and E_{cutoff} should be the same for e^- and e^+;

2. The $\phi_{\mathrm{e}^{\pm}}$ fluxes are fitted in each time bin used in the analysis with the parametrization described by the equations 5.6 and 5.7. The time independent parameters have been fixed using the values obtained from the fits on time integrated all-electron flux and positron fraction. The only free parameters for each fit performed in the different time bins are $\phi_{\mathrm{e}-}$ and $\phi_{\mathrm{e}+}$.

In the next subsections the obtained results from the flux parametrization will be shown.

5.3.1 Time independent fit

In order to determine the set of time independent free parameters in equations 5.6 and 5.7 with the minimum error, a simultaneous fit on the time integrated all-electron flux and positron fraction has been performed. The correlations between the two datasets can be neglected, since the systematic uncertainties on all-electron flux and positron fraction are not correlated. An alternative approach is the use of the separate e^- and e^+ fluxes to perform the fit. In this case, the systematic uncertainties are correlated between the two dataset and should be taken into account. However, the separate fluxes present additional systematic uncertainties respect to the all-electron flux, and the combination of the e^- and e^+ fluxes has less constraining power on the fit parameters than the combination of the all-electron flux and positron fraction. Moreover the all-electron flux measurement extend up to 1 TeV and it increases the maximum energy to which the data parametrization can be tested.

The data on which the fit has been performed are those published in[65, 100].

All the energy intervals of dataset have been used (0.5–1 TeV for the all-electrons flux and 0.5–500 GeV for the positron fraction). This energy interval is larger than the one discussed below (see section 5.3.2). However, the fit at high energies is fundamental to have the best value for the parameters related to the common source since the high energy part of $e^{\pm}$ spectrum is the more sensitive to this source.

The bin-to-bin energy correlated systematic uncertainties (see table 5.1) have been removed from the data points used for the fit procedure. The results of the combined fit is shown in figure 5.16 and in table 5.2. Both the total χ^2 of the fit and the local χ^2 indicates that the data are well described by the parametrization described by the equations 5.6 and 5.7. The value of χ^2 <1 is due to the fact that the fit has been performed without take into account the correlation between the data errors.

The obtained values for $A_{\mathrm{e}-}$, $\gamma_{\mathrm{e}-}$, $\Delta\gamma_{\mathrm{e}-}$, $A_{\mathrm{e}+}$, $\gamma_{\mathrm{e}+}$, A_{comm}, γ_{comm}, $1/E_{\mathrm{cutoff}}$, E_{b} and s are assumed to be time independent and will be used as fixed parameters for the fit of the fluxes in time. The values found for the two time dependent parameters, $< \phi_{\mathrm{e}-} >$=1.50±0.05±0.01 (GV) and $< \phi_{\mathrm{e}+} >$=1.15±0.06±0.01 (GV) represent an effective value over the time interval July 2011 – November 2013.

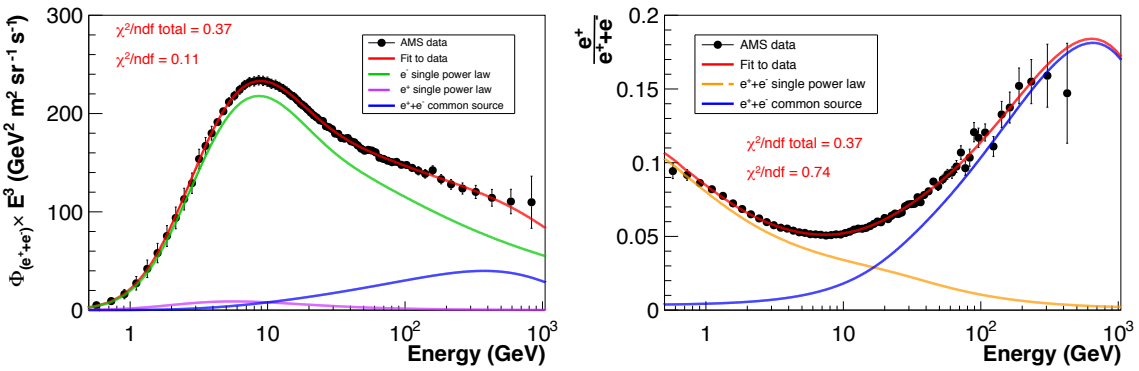

FIGURE 5.16: Result of the combined fit on all-electron flux (left) and positron fraction (right).

	value	$\sigma^{\mathrm{p}}_{\mathrm{fromFit}}$	$\sigma^{\mathrm{p}}_{\mathrm{sys}}$
$A_{\mathrm{e}-}$ (GeV^{-1} m^{-2} sr^{-1} s^{-1})	2676.97	165.52	39.54
$\gamma_{\mathrm{e}-}$	3.78	0.02	0.014
$\Delta\gamma_{\mathrm{e}-}$	0.45	0.045	0.01
$A_{\mathrm{e}+}$ (GeV^{-1} m^{-2} sr^{-1} s^{-1})	112.40	3.51	0.00
$\gamma_{\mathrm{e}+}$	3.90	0.01	0.01
A_{comm}	2.53	0.02	0.00
γ_{comm}	2.58	0.01	0.01
$1/E_{\mathrm{cutoff}}$ (TeV^{-1})	1.10	0.29	0.01
E_{b} (GeV)	31.72	1.93	2.43
s	0.151	0.015	0.025
$\phi_{\mathrm{e}-}$ (GV)	1.33	0.03	0.09
$\phi_{\mathrm{e}+}$ (GV)	1.02	0.02	0.08

TABLE 5.2: Parameter values obtained from the combined fit.

For the evaluation of the systematic uncertainties on the parameters obtained from the fit shown above, the effect of the energy bin-to-bin correlated errors reported in table 5.1 should be taken into account. Two solid shifts on the all-electron flux have been applied within the errors:

$$\begin{aligned} \Phi{+}\delta\Phi &= \Phi + \delta\Phi_{\mathrm{ene\_corr}} \\ \Phi{-}\delta\Phi &= \Phi - \delta\Phi_{\mathrm{ene\_corr}} \end{aligned} \tag{5.8}$$

where only the bin-to-bin correlated errors contribute to $\delta\Phi_{\mathrm{ene\_corr}}$:

$$\delta\Phi_{\mathrm{ene_corr}} = (0.7 * \sigma^{\mathrm{abs}}_{\mathrm{K}}) \oplus \sigma_{\mathrm{CC}} \oplus \sigma_{\mathrm{ECAL\_abs}} \tag{5.9}$$

A fit with the parametrization described by the equations 5.6 and 5.7 has been performed both on $\Phi{+}\delta\Phi$ and $\Phi{-}\delta\Phi$ obtaining two values for each parameter, $p^{+\delta\Phi}$ and

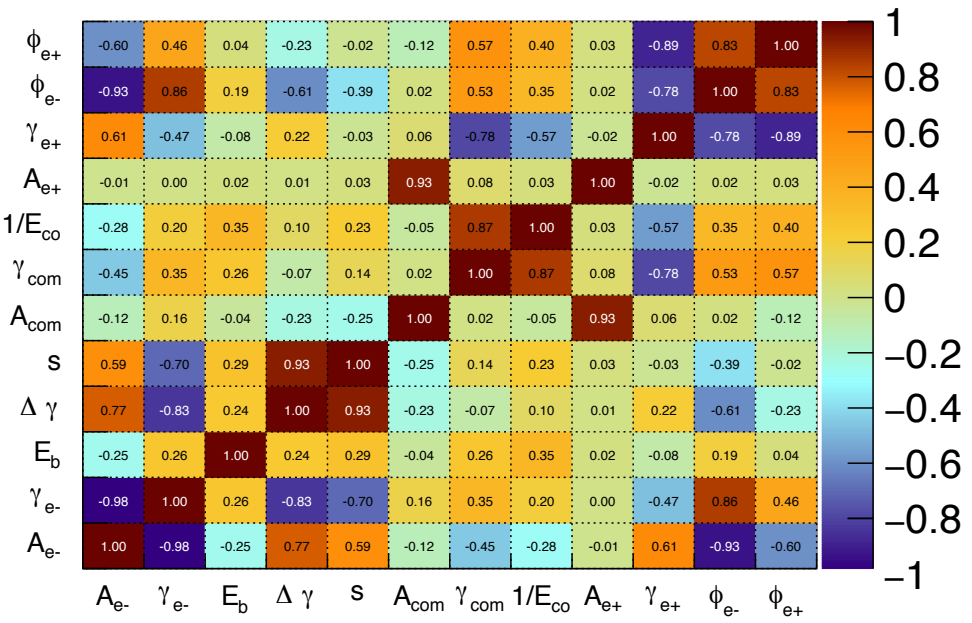

FIGURE 5.17: Correlation matrix returned by the fit procedure between the parameters.

$p^{-\delta\Phi}$. For each parameter p, the systematic uncertainties have been conservatively defined as the semi-dispersion of $p^{+\delta\Phi}$ and $p^{-\delta\Phi}$:

$$\sigma^{\mathrm{p}}_{\mathrm{sys}} = \frac{|p^{+\delta\Phi} - p^{-\delta\Phi}|}{2} \tag{5.10}$$

Actually the correlation between the parameters, shown in Figure 5.17, should be taken into account. The correlation is not negligible and the error returned from the fit for each parameter contains this correlation. In the next section this correlation will be taken into account in order to evaluate the systematic errors on the obtained value for $\phi_{e^{\pm}}$ in each time bin.

5.3.2 Fit to electron and positron fluxes in time

The electron and positron fluxes measured in each Δt have been fitted using the parametrization described by the equations 5.6 and 5.7 where only the parameters related to the solar potential ($\phi_{\mathrm{e}-}$ and $\phi_{\mathrm{e}+}$) are left free.

The bin-to-bin energy and time correlated systematic uncertainties (see table 5.1) have been removed from the data points on which the fit has been performed. The

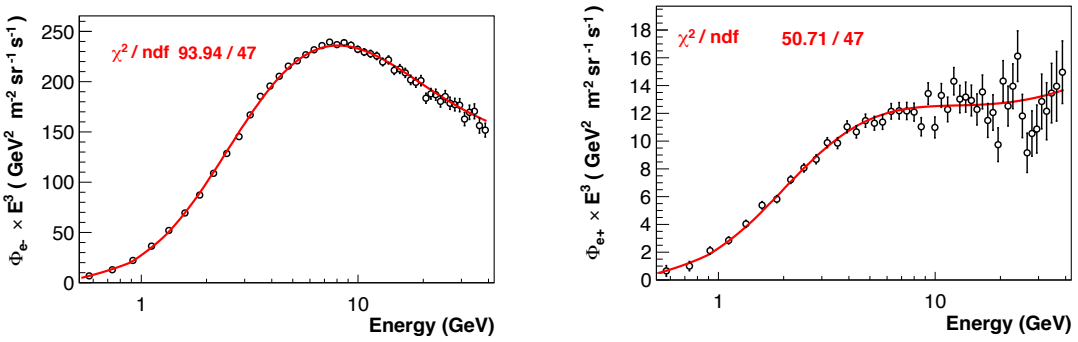

FIGURE 5.18: An example of the fit on electron flux (left) and positron flux (right) in one time bin (1 July 2011 – 27 July 2011).

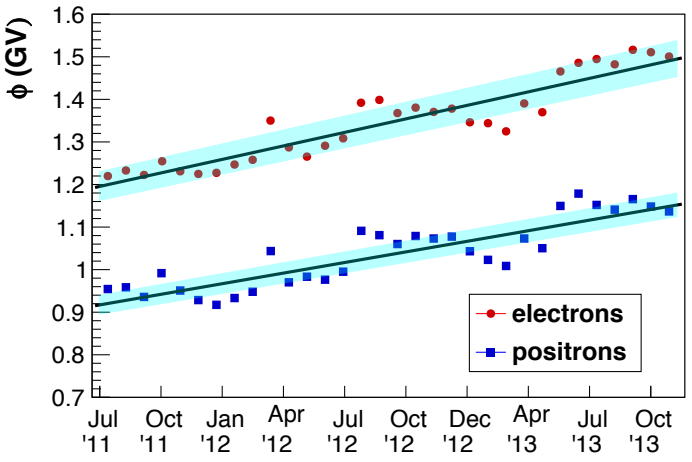

FIGURE 5.19: The obtained results for solar modulation potentials ϕ_{e+} and ϕ_{e-} in each Δt.

fitted points contains only the errors: σ_{stat}, $\sigma_{\text{stat\_tmpl}}$ and $\sigma_{\text{K}}^{\text{stab}}$. An example of the fit on the electron flux and positron flux in one time bin is shown in figure 5.18.

The obtained results for ϕ_{e+} and ϕ_{e-} in each Δt are shown in figure 5.19 and reported in appendix B in tables B.34 and B.35.

The points contain only the fit errors. The effect of systematic errors is shown as a light-blue band around a linear polynomial fit that gives an annual variation for ϕ_{e-} of 9.95±0.03% and for ϕ_{e+} of 9.87±0.18%.

The increase in time observed for both ϕ corresponds to a decrease in the flux intensity as already discussed in section 5.1. In this case the annual variation observed is the same both for electrons and positrons in contrast to the expected charge-sign dependent solar modulation effects. However, this could be due to the fact that the Force Field Approximation is a very basic model that doesn't take into account any charge-sign dependent effects. The trend of the obtained solar potential

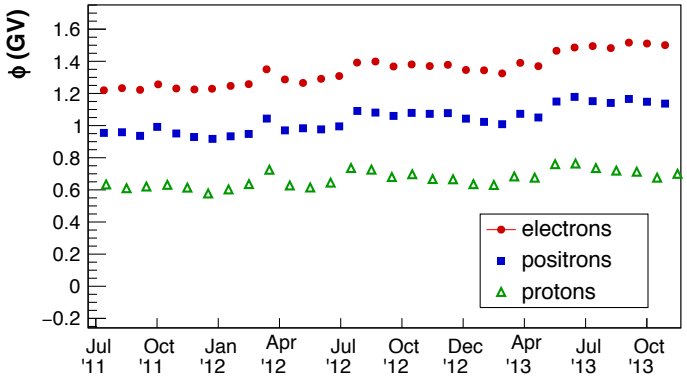

FIGURE 5.20: The obtained results for the solar modulation potentials ϕ_{e+} and ϕ_{e-} in each Δt.

($\phi^{\pm}$) as function of time (see Figure 5.19) is in agreement with the behavior of the solar cycle during which the data analyzed have been taken. As shown in figure 5.20 the trend as a function of time followed by $\phi^{\pm}$ is the same observed for protons, evaluated with an independent analysis on AMS data [114].

Figure 5.20 shows $\phi_{e^{\pm}}$ together with the ϕ evaluated on AMS protons. The solar potential ϕ has the same trend as function of time both for electrons, positrons and protons even though with different absolute values. However, its absolute scale is model dependent and doesn't represent any physical behavior unlike the trend in time.

In addition to the errors on ϕ coming from the fit procedure, systematic uncertainties should be taken into account. Two errors contribute to the systematic uncertainties on ϕ:

- the errors coming from the bin-to-bin correlated errors in energy or time (see table 5.1), $(\sigma_{\rm sys}^{\rm bin-to-bin\ corr})^{\Delta t}$;
- the errors coming from the correlation between $\phi_{e^{\pm}}$ and the time independent parameters, $(\sigma_{\rm sys}^{\rm par\_corr})^{\Delta t}$.

For $(\sigma_{\rm sys}^{\rm bin-to-bin\ corr}))^{\Delta t}$ the same procedure described in section 5.3.1 for $\sigma_{\rm sys}^{\rm p}$ has been followed. In this case only the energy or time bin-to-bin correlated errors contribute to $\delta\Phi$:

$$\delta\Phi = \delta\Phi_{\rm ene\_time\_corr} = \sigma_{\rm sel\_tmpl} \oplus \sigma_{\rm K}^{\rm abs} \oplus \sigma_{\rm K}^{\rm par} \oplus \sigma_{\rm K}^{\rm res} \oplus \sigma_{\rm CC} \oplus \sigma_{\rm ECAL\_stab} \oplus \sigma_{\rm ECAL\_abs} \quad (5.11)$$

The correlation between $\phi_{e^{\pm}}$ and the others parameters contribute to $\sigma_{\rm sys}^{\rm par\_corr}$. As shown in Figure 5.17, $\phi_{e^{\pm}}$ are strongly correlated (or anti-correlated) with the others

parameters and the errors coming from the fit procedure σ_{fromFit} ($\sim$ 2.42 % for $< \phi_{e-} >$ and $\sim$ 1.68 % for $< \phi_{e+} >$) performed on the all-electron flux and on the positrons fraction contain this correlation.

Performing again the combined fit on all-electron flux and positron fraction fixing all the time independent variables, the obtained errors from fit, $\sigma_{\text{fromFit}}^{\text{par\_uncorr}}$, is $\sim$ 0.49 % for $< \phi_{e-} >$ and $\sim$ 0.64 % for $< \phi_{e+} >$. This errors don't contain the correlation between the parameters that has been found according to the formula:

$$\sigma_{\text{sys}}^{\text{par\_corr}} = \sqrt{(\sigma_{\text{fromFit}})^2 - (\sigma_{\text{fromFit}}^{\text{par\_uncorr}})^2} \tag{5.12}$$

$\sigma_{\text{sys}}^{\text{par\_corr}}$ has been found to be $\sim$ 2.37 % for $< \phi_{e-} >$ and $\sim$ 1.55 % for $< \phi_{e+} >$.

The relative error due to the correlation is assumed to be time independent, hence:

$$\frac{\sigma_{\text{sys}}^{\text{par\_corr}}}{< \phi_{e^{\pm}} >} = \frac{(\sigma_{\text{sys}}^{\text{par\_corr}})^{\Delta t}}{\phi_{e^{\pm}}} \quad \rightarrow \quad (\sigma_{\text{sys}}^{\text{par\_corr}})^{\Delta t} = \frac{\sigma_{\text{sys}}^{\text{par\_corr}}}{< \phi_{e^{\pm}} >} \phi_{e^{\pm}} \tag{5.13}$$

5.4 Summary

In this chapter the obtained results for the electron and positron fluxes in 32 time intervals have been presented. An interpretation of these data based on the Force Field Approximation has been given in section 5.3. According to this interpretation the flux variation in time can be totally described by a single parameter: the solar potential ϕ. Figure 5.21 shows e^- (left) and e^+ (right) fluxes as a function of the energy in 3 time intervals of 27 days. The points represent the AMS data and they are well described by the superimposed curves obtained from the parametrization defined by the equations 5.6 and 5.7. The only parameter that is changing for the 3 curves is the solar potential ϕ.

Using the equation 5.6 and the values obtained from the fit procedure (see section 5.3.1 and table 5.2), the electron and positron Interstellar fluxes can be determined. Figure 5.22 shows the time integrated flux obtained in this work both for electrons (left) and positrons (right) with, superimposed, the parametrization represented by a continuous line. The dashed line represents an estimation of the interstellar flux (i.e. the flux not affected by the solar modulation) and it has been obtained from 5.6 by fixing $\phi_{e\pm}$=0, with all the other parameters fixed accordingly to the values reported in table 5.2.

A good knowledge of the solar modulation allows the comparison between data taken by different experiments during different periods. Figure 5.23 shows the

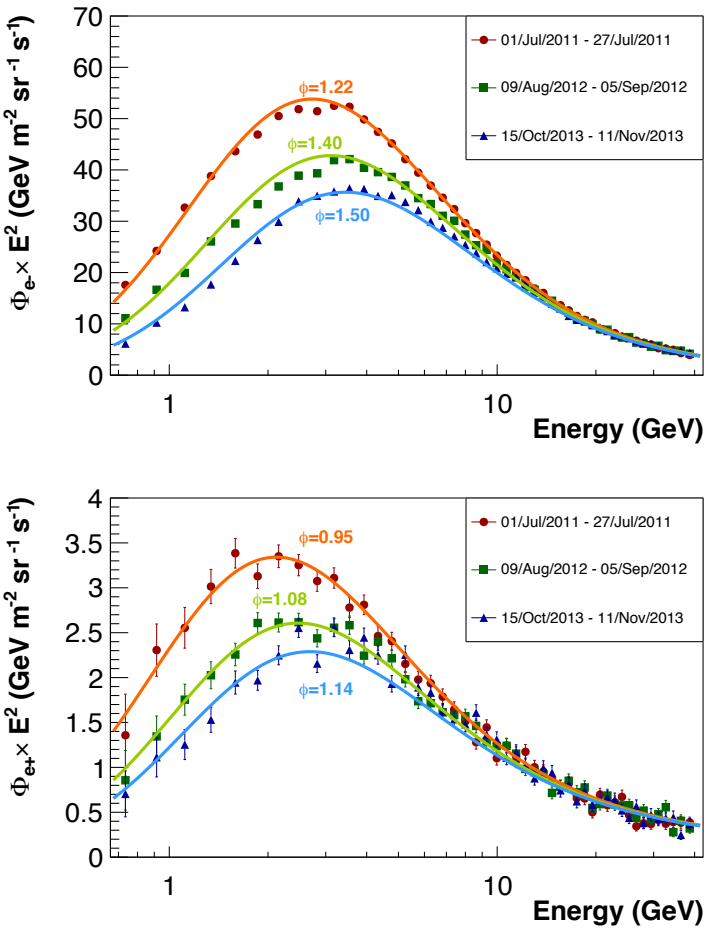

FIGURE 5.21: AMS data for 3 different time intervals of 27 days for e^- flux (top) and e^+ flux (bottom). The data are well described by the parametrization defined by equations 5.6 and 5.7, where all the parameters are fixed, but $\phi_{e^\pm}$ that have been free in each time interval.

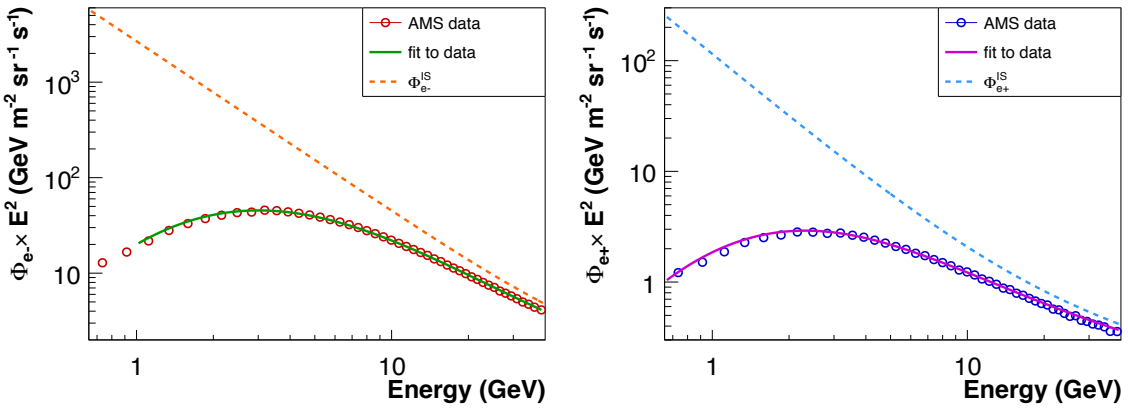

FIGURE 5.22: The points represent the time integrated flux as a function of energy both for electrons (left) and positrons (right) with, superimposed, the parametrization (solid line) performed as described in section 5.3.1. The dashed line represents an estimation of the Interstellar Flux.

time integrated electron flux obtained in this work compared with the electron flux measured by PAMELA multiplied by E^2, as a function of energy. There is a big discrepancy between the two dataset especially for energies <10 GeV. This disagreement is clearly due to the different data taking period (Jul 2011 – Nov 2013 for AMS and Jul 2006 – Jan 2010 for PAMELA) and, hence, the solar modulation effects are different.

The knowledge of ϕ in the various periods allows to correct the LIS spectrum including the solar modulation effects for a giving period. The AMS data are well described by a solar potential value of ϕ=1.33 GV. It is possible to found a value for ϕ according to which the AMS parametrization can be in agreement with the PAMELA data. This value corresponds to ϕ=1.16 GV. The AMS parametrization with this value of ϕ is reported with a light-blue dashed line and seems to be in agreement with PAMELA results for energies <4 GeV.

Above this energy AMS and PAMELA are still in disagreement. However this discrepancy can be simply due to the fact that the minimal model that has been used, together with the parametrization of the solar modulation described by the Force Field Approximation, is not adequate to describe the current data.

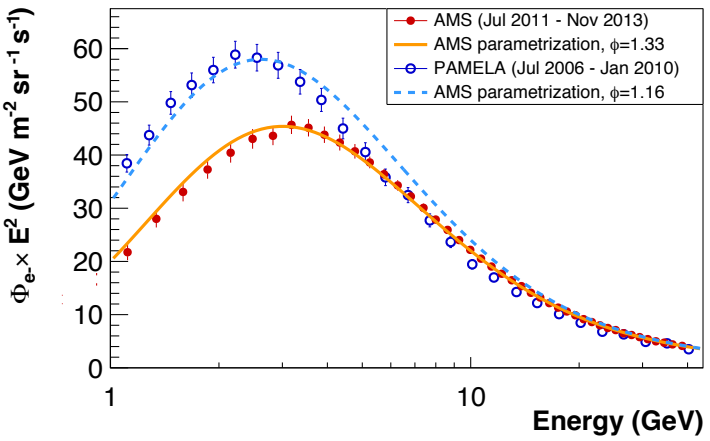

FIGURE 5.23: AMS (red points) and PAMELA (blue points) electron flux multiplied by E^2, as a function of energy. The solid and the dashed lines represent the parametrization of AMS data respectively during the AMS data taking period and PAMELA data taking period. The latter has been found performing a fit on PAMELA data with the AMS parameterization where only the ϕ parameter has been left free.

The results shown in this work represent the first direct measurement ever performed in the energy range 0.5–40. GeV with such a detailed time binning on e^- and on e^+. Up to now the only similar analysis for the electronic component of cosmic rays has been performed, only for e^-, by PAMELA experiment [115]. The results obtained by PAMELA are based on data collected between 2006 July and 2009 December

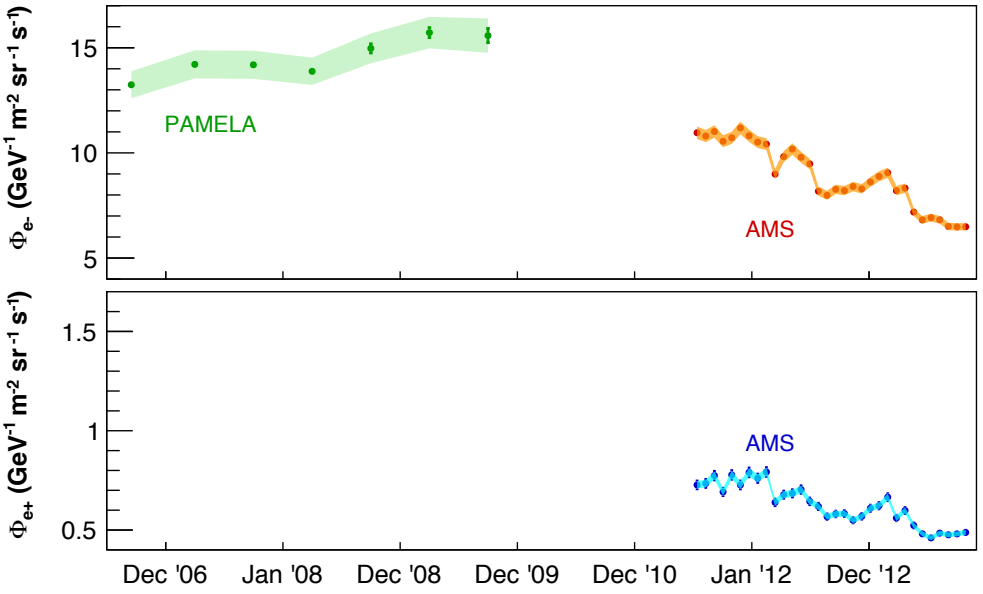

FIGURE 5.24: Electron flux measured by PAMELA and electron and positron fluxes obtained in this work as a function of time, in the energy bin E=2–2.30 GeV.

and the electron flux has been evaluated in six-month time periods. Figure 5.24 shows the electron flux measured by PAMELA and the electron and positron fluxes obtained in this work as a function of time, in one energy bin (E=2–2.30 GeV) as example. The points are reported with their statical errors and the colored band represents the systematic errors. The high accuracy reached with AMS is clearly visible. In the energy bin shown in the figure, the statistical error is ∼1% both for PAMELA and AMS, however, while the time interval for PAMELA data corresponds to 6 months of data taking, the time interval for AMS data corresponds to 27 days.

Conclusion

The measurement of energy spectra of galactic cosmic rays electrons and positrons provides fundamental information regarding the origin and propagation of cosmic rays. Moreover, the $e^{\pm}$ spectrum measured at Earth can potentially show indirect presence of Dark Matter. A correct understanding of galactic $e^{\pm}$ fluxes is fundamental for a correct interpretation of the measured data. Cosmic rays spectrum measured near Earth is significantly affected by the solar activity in the low energy part (E<20 GeV). The solar activity changes in time inducing a time dependence of the measured CR. A comprehensive description of the cosmic radiation must therefore include the transport and modulation of cosmic rays inside the heliosphere.

In this dissertation we presented a new precise measurement of the e^+ and e^- fluxes in the energy range 0.5–40 GeV based on the statistics collected during the first 30 months of AMS-02 operation in space. Starting from 1^{st} July 2011, the $e^{\pm}$ differential energy spectra have been measured in 48 energy bins following their evolution in time with a granularity of 27 days, for a total of 32 measurements. This is the first direct measurement ever performed at these energies with such a detailed time binning on e^- and on e^+.

A decrease of the $e^{\pm}$ fluxes with time has been observed which is consistent to solar activity in the period of our measurements. Indeed, the beginning of the 24th solar cycle was in January 2008, and our data were collected in 2011-2013 when approaching to the maximum of the solar cycle, which occurred in April 2014. A good agreement was also found with the time evolution of the neutron monitors counting rates on ground, which are related to total CR flux intensity reaching the Earth atmosphere.

The simultaneous measurement of e^- and e^+ has also allowed to study differences of the solar modulation effects which are related only to the charge-sign of the particles. For example in the energy bin 4.12–4.54 GeV the annual variation observe on electrons and positrons fluxes is respectively (9.29±0.31)% and (6.41±0.69)%.

These new accurate experimental data will be of great relevance to improve the current models of CR propagation in the heliosphere, therefore allowing a deeper understanding of the local interstellar spectrum of cosmic rays.

A deep understanding of detector related effects in the flux measurement was gained during this work and specific analysis techniques were developed to allow the prompt extension of this measurement as more data will be collected by the experiment. The analysis of the data set up to September 2014 is already on-going, showing even larger charge-sign dependent effects at the solar maximum. Since, AMS-02 is foreseen to operate for the entire ISS lifetime, up to 2024, it will be able to follow in detail the time evolution of the e^+ and e^- fluxes along a full solar cycle.

Appendix A

Technical issues

In this appendix some technical issues, related to the argument discussed in chapter 4, will be reviewed.

A.1 Reweight of MC

The generated MC energy spectrum, $\left(\frac{dN}{dE}\right)_{MC}$, doesn't present the same energy spectrum features of the real DATA spectrum, $\left(\frac{dN}{dE}\right)_{DATA}$. Moreover discontinuities in $\left(\frac{dN}{dE}\right)_{MC}$ spectrums arise on the borders of different generation intervals. This behaviors can be clearly see in Figure A.1 in which the energy spectrum for the electron MC sample and the AMS-02 electron DATA sample as a function of the generated energy (for MC) and reconstructed energy (for DATA) are compared.

This differences between the two spectra don't affect the calculation of the acceptance A_{MC} due to the method applied for its evaluation (see section 4.3). However, such differences could bias the evaluation of the efficiencies used in the calculation of $K(\Delta E, \Delta t)$ and the estimation of the proton irreducible background. To avoid this, the energy spectrum of generated MC events should be:

1. "reweighted", in order to correct the MC sample energy trend to best represent that observed in DATA;
2. normalized, in order to have a continuous behavior as a function of energy (no "jump" between two different intervals of generation).
3. normalized, in order to simulate the same statistical fluctuation due to the finite data sample used for the analysis.

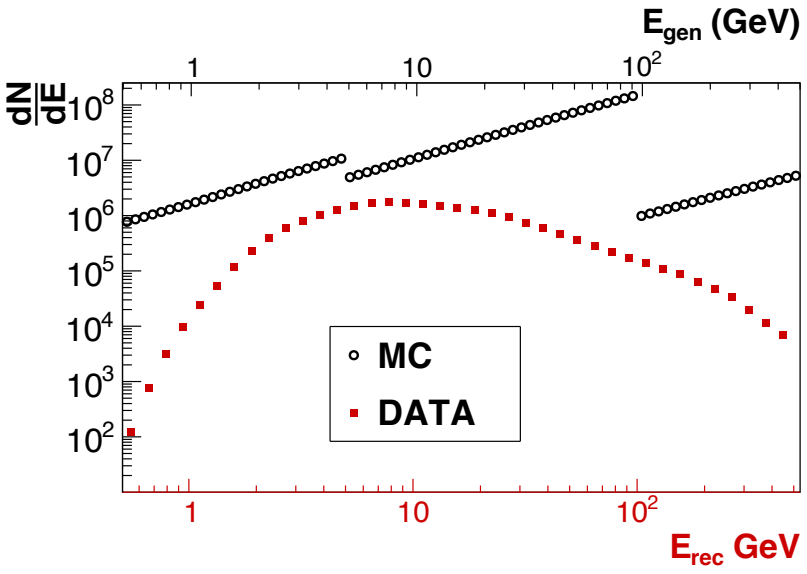

FIGURE A.1: The AMS-02 energy spectrum of electron DATA (red points) as function of the reconstructed energy and of electron MC (black points) as function of generated energy.

The first two items are mandatory to have a correct simulation of the DATA trends as a function of reconstructed variables. The third item is needed if, in addition to the trends, a correct simulation of the DATA statistics as a function of reconstructed variables is required[1].

As shown in Figure A.2 (left) the MC events have been generated in an energy interval $\Delta E_{\rm gen}$=$[E_{\rm min}, E_{\rm max}]$ according to the following distribution:

$$\left(\frac{\mathrm{d}N}{\mathrm{d}(lnE)}\right)_{\rm MC} = \left(\frac{\mathrm{d}N}{\frac{1}{E}\mathrm{d}(E)}\right)_{\rm MC} = k = constant \tag{A.1}$$

such that:

$$\begin{aligned} \rightarrow \quad & \int_0^{\mathrm{N}_{\rm gen}^{[\mathrm{E}_{\rm min},\mathrm{E}_{\rm max}]}} \mathrm{d}N = \int_{\mathrm{E}_{\rm min}}^{\mathrm{E}_{\rm max}} k\frac{1}{E}\mathrm{d}E \\ \rightarrow \quad & N_{\rm gen}^{[\mathrm{E}_{\rm min},\mathrm{E}_{\rm max}]} = k(lnE_{\rm max} - lnE_{\rm min}) \end{aligned} \tag{A.2}$$

Equation A.2 allows to evaluate k as:

$$k = \frac{N_{\rm gen}^{[\mathrm{E}_{\rm min},\mathrm{E}_{\rm max}]}}{lnE_{\rm max} - lnE_{\rm min}} \tag{A.3}$$

[1]This is the case for the study of the *irreducible background*

and finally express the MC energy spectrum as:

$$\left(\frac{dN}{dE}\right)_{\mathrm{MC}} = \frac{N_{\mathrm{gen}}^{[\mathrm{E_{min}},\mathrm{E_{max}}]}}{lnE_{\mathrm{max}} - lnE_{\mathrm{min}}} \tag{A.4}$$

Since all the quantities are evaluated in finite size intervals, equation A.4 becomes:

$$\left(\frac{\Delta N}{\Delta E}\right)_{\mathrm{MC}} = \frac{N_{\mathrm{gen}}^{[\mathrm{E_{min}},\mathrm{E_{max}}]}}{lnE_{\mathrm{max}} - lnE_{\mathrm{min}}} \tag{A.5}$$

In order to obtain a correct description of the data energy spectrum and statistical fluctuations, a weight factor w should be applied to MC data such that:

$$w \times \Phi_{\mathrm{MC}} = \Phi_{\mathrm{DATA}} \quad \rightarrow \quad w = \frac{\Phi_{\mathrm{DATA}}}{\Phi_{\mathrm{MC}}} \tag{A.6}$$

where, according to equation 4.8:

$$\Phi_{\mathrm{MC}} = \left(\frac{\Delta N}{\Delta E}\right)_{\mathrm{MC}} \frac{1}{A_{\mathrm{eff}} \Delta T_{\mathrm{exp}}} \tag{A.7}$$

In the case of generated flux, the acceptance is given only by a geometrical factor that depends on the surface used for the generation (see section 4.3). The MC events used in this work, have been generated from a single surface of a cube of side l, this means:

$$A_{\mathrm{eff}} = G = \pi l^2 \tag{A.8}$$

The exposure time, correspond to the one in which the Φ_{DATA} is measured. In this way the MC flux is normalized to the same statistic of DATA.

Combining equations A.5, A.7 and A.9 w can be expressed as:

$$w = \frac{\Phi_{\mathrm{DATA}}}{\left(\frac{\Delta N}{\Delta E}\right)_{\mathrm{MC}}} A_{\mathrm{eff}} \Delta T_{\mathrm{exp}} \tag{A.9}$$

w has been evaluated and applied as a function of energy. The spectrum after reweighing in the case of electron MC is shown in figure A.2. The same procedure can be applied on MC protons.

The results obtained from a parametrization of the published electron[67] and proton fluxes [76] have been used for the evaluation of Φ_{DATA} in equation A.9. The parametrization of the fluxes obtained from the fit are shown in figure A.3 for electron and proton fluxes.

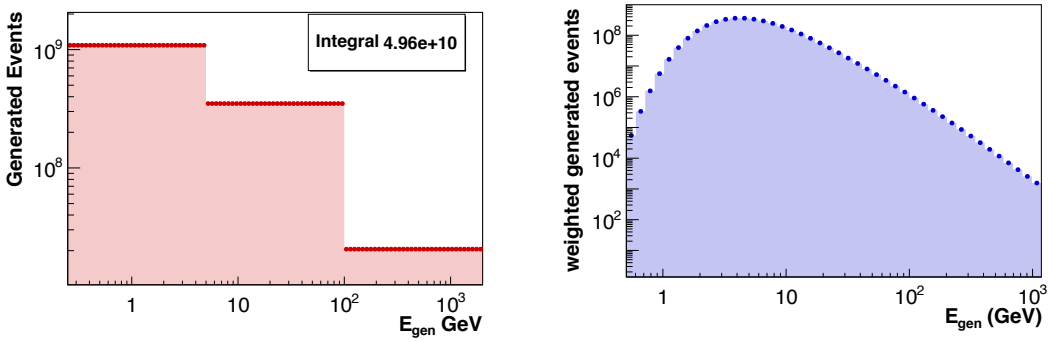

FIGURE A.2: Left: Number of generated events for MC electrons samples as a function of the generated energy ($E_{\rm gen}$). Right: Reweighed number of generated events in MC electrons samples as a function of the generated energy ($E_{\rm gen}$).

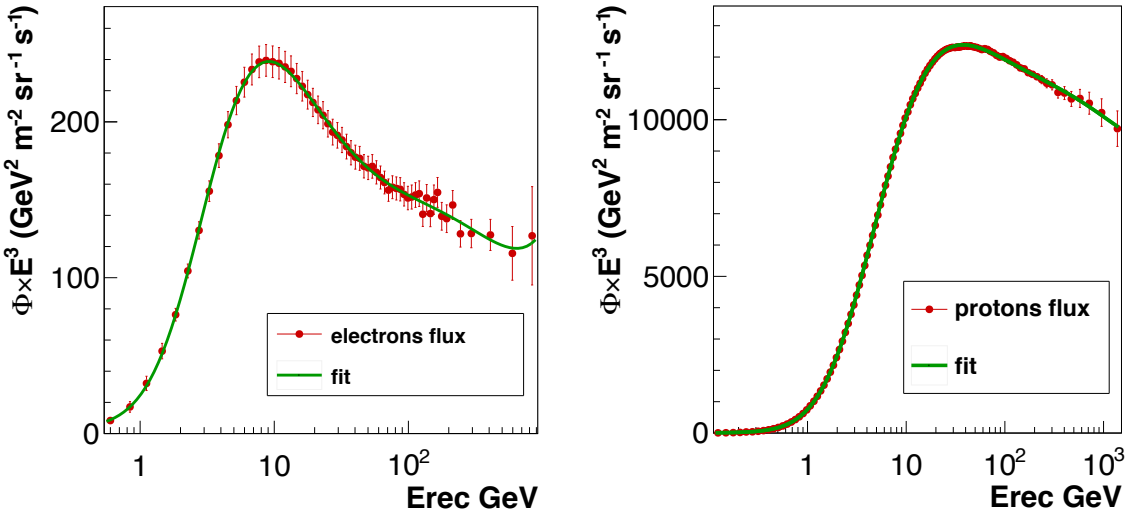

FIGURE A.3: Parametrization on the published electron (left) and proton (right) fluxes [76]. The result from the fit is used in the formula A.9 to evaluate the weight factor w for MC protons.

A.2 The binning for $A_{\rm MC}$ histogram

A correct choice of the binning for the histogram of the $N_{\rm sel}$, $N_{\rm gen}$, G and consequently $A_{\rm MC}$, is fundamental in order to avoid problems between two different energy intervals of generation.

MC electrons are generated in 3 different *nominal* energy intervals, $\Delta E_{\rm gen}^{\rm NOM}$.

Each $\Delta E_{\rm gen}^{\rm NOM}$ is delimited by a *nominal* minimum value of energy, $E_{\rm NOM}^{\rm min}$, and *nominal* maximum value of energy, $E_{\rm NOM}^{\rm max}$. The 3 different intervals of generation are:

- $(\Delta E_{\rm gen}^{\rm NOM})_1 = [E_{\rm NOM})^{\rm min} - E_{\rm NOM}^{\rm max}]_1$=[0.25–5.] GeV;

- $(\Delta E_{\rm gen}^{\rm NOM})_2 = [E_{\rm NOM}^{\rm min} - E_{\rm NOM}^{\rm max}]_2$=[5.–100.] GeV;
- $(\Delta E_{\rm gen}^{\rm NOM})_3 = [E_{\rm NOM}^{\rm min} - E_{\rm NOM}^{\rm max}]_3$=[100.–2000.] GeV;

However, in each energy $\Delta E_{\rm gen}^{\rm NOM}$, the events are generated with energies between a *real* energy interval, $\Delta E_{\rm gen}^{\rm REAL}$, that is longer then the *nominal* one.
An example of this is reported in table A.1 for two different `job`[2] used for the generation of MC electrons in the $\Delta E_{\rm gen}^{\rm NOM}$=5.–100. GeV.

	$E_{\rm NOM}^{\rm min}$	$E_{\rm NOM}^{\rm min}$	$N_{\rm gen}^{\rm NOM}$	$E_{\rm REAL}^{\rm min}$	$E_{\rm REAL}^{\rm min}$	$N_{\rm gen}^{\rm REAL}$
I `job`	5 GeV	100 GeV	425012	4.963 GeV	100.703 GeV	422974
II `job`	5 GeV	100 GeV	451521	4.921 GeV	100.593 GeV	448253

TABLE A.1: Example of the number of generated events in the nominal energy interval ($N_{\rm gen}^{\rm NOM}$) and the number of generated events in the real energy interval of generation ($N_{\rm gen}^{\rm REAL}$) for two different `jobs`.

The binning for $E_{\rm gen}$ has been choosen in order to have, for each $\Delta E_{\rm gen}^{\rm NOM}$, one bin which low edge correspond to $E_{\rm NOM}^{\rm min}$ and one bin which up edge correspond to $E_{\rm NOM}^{\rm max}$.

Moreover, for the analysis only the MC events which generated energy is within the *nominal* value, have been taken into account.

A.2.1 The number of selected and generated events, $N_{\rm sel}(\Delta E)$ and $N_{\rm gen}(\Delta E)$

The distribution of $N_{\rm sel}(\Delta E)$ for MC electrons as a function of $E_{\rm gen}$ has been obtained applying the same selection applied on DATA, described in section 3.2. The only cut that has not been applied is the physics trigger requirement. The efficiency of this cut, as will be explained in section 4.5, in fact has been evaluated directly from DATA as *last cut* and therefore it has not been included. For the calculation of $A_{\rm MC}$ only the number of generated events inside the *nominal* interval ($N_{\rm gen}^{\rm NOM}$) should be taken into account.

Unfortunately, as explained in section A.2, several job are used for one $\Delta E_{\rm gen}^{\rm NOM}$, each with its own $\Delta E_{\rm gen}^{\rm REAL}$. For each job is known the *real* energy interval of generation, and the number of events that are generated inside this interval ($N_{\rm gen}^{\rm REAL}$) that doesn't correspond to $N_{\rm gen}^{\rm NOM}$. However, exploiting the fact that the number of events in MC are generated flat as a function of the energy logarithm (see section

[2]for each ($\Delta E_{\rm gen}^{\rm NOM}$) several `job` are used for the MC electrons generation. Each `job` has its different ($\Delta E_{\rm gen}^{\rm REAL}$) and its different number of generated events.

A.1 in Appendix A), the number of generated events in the *nominal* interval can be obtained from the following formula:

$$\frac{N_{\rm gen}^{\rm NOM}}{\Delta E_{\rm gen}^{\rm NOM}} = \frac{N_{\rm gen}^{\rm REAL}}{\Delta E_{\rm gen}^{\rm REAL}} \quad \rightarrow \quad N_{\rm gen}^{\rm NOM} = \Delta E_{\rm gen}^{\rm NOM} \frac{N_{\rm gen}^{\rm REAL}}{\Delta E_{\rm gen}^{\rm REAL}} \tag{A.10}$$

A.3 Study of unbiased triggers

On DATA data sample, these factors have been chosen according to the following argument.
There are three different categories of *not physics triggers*:

1) events triggered only by *unbiased charge* ($[\text{LV1-0}]_{\rm notPhys}$)
this category is pre-scaled on DATA data by a factor 1/100, so $w_0^{\rm DATA}$=100;

2) events triggered only by unbiased ecal ($[\text{LV1-6}]_{\rm notPhys}$)
this category is pre-scaled on DATA data by a factor 1/1000, so $w_6^{\rm DATA}$=1000;

3) events triggered only by *unbiased charge* & *unbiased ecal* ($[\text{LV1-0 \& LV1-6}]_{\rm notPhys}$).
For this category, the chose of multiplicative factor is a little bit complicate. In principle should be:

$$w_{06} = 100 * (\text{LV1-0})_{\%} + 1000 * (\text{LV1-6})_{\%}$$

where $(\text{LV1-0})_{\%}$ are the percentages of di events triggered by unb charge and $(\text{LV1-6})_{\%}$ by unb ecal. However, due to a known malfunctioning of the trigger box on DATA data, it cannot be distinguished if an event was triggered because it was an *unbiased ecal* or an *unbiased charged*.

Differently from flight data, the trigger configuration for each MC event is know. In order to estimate $(\text{LV1-0})_{\%}$ and $(\text{LV1-6})_{\%}$ the same pre scale factors have been applied to the MC simulation. Figure A.4 shows the distributions of the three categories of *not Physics triggers* as a function of reconstructed energy, for the electrons MC sample,without pre-scale. In table A.2 the percentages of the three categories of unbiased trigger, in different low energy range are reported.

The distributions of the three categories obtained after the application of the pre-scaling on MC data, are shown in Figure A.5 on the left and for DATA on the right.

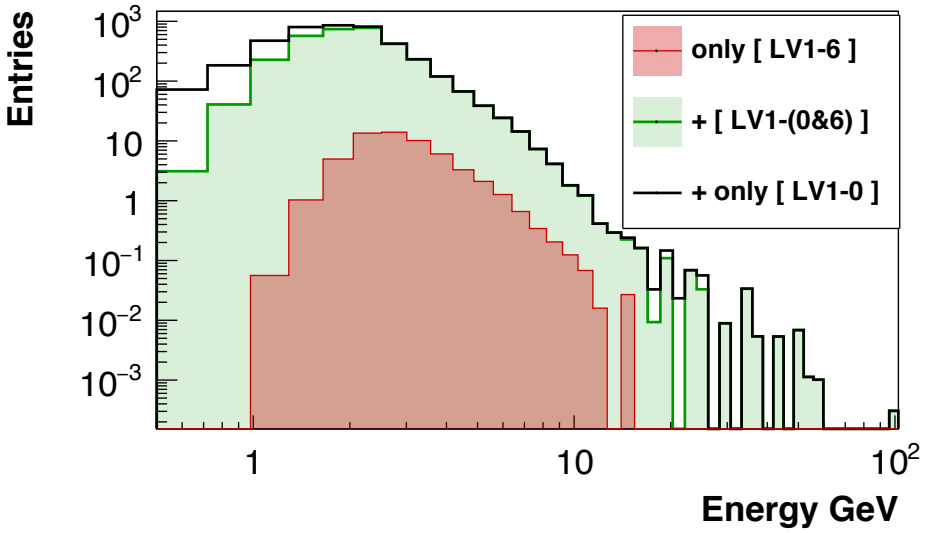

FIGURE A.4: MC electrons: distributions of the three category of not Physics triggers as a function of reconstructed energy, without pre-scaling.

		Energy (GeV)					
		0.5-1.	1.-1.7	1.7-2.5	2.5-3.6	3.6-4.9	4.9-6.4
Not Phys %	LV1-0	82.87	37.41	9.34	0.81	0.27	5.45
	LV1-6	0	8.51	1.10	3.68	5.00	5.34
	LV1-(0&6)	17.13	62.50	89.56	95.51	94.72	94.11

TABLE A.2: Percentages of the three categories of unbiased for all not Physics triggers, in different low energy range, for MC electrons (before pre scaling).

The percentages of the three categories of unbiased over all *not Physics triggers*, in different low energy range, both for DATA and MC electrons (after pre-scaling), are reported in tab A.3.

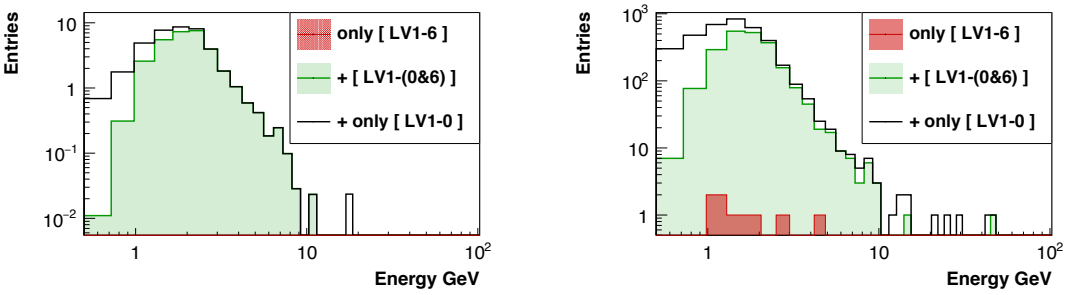

FIGURE A.5: Distributions of the three category of not Physics triggers as a function of reconstructed energy, after the pre scaling on MC (left) and on DATA electrons (right).

After applying the pre-scaling, all the not physics triggers events on MC electrons that have been triggered as unb charge and unb ecal, are recorded because they

			Energy					
			0.5-1.	1.-1.7	1.7-2.5	2.5-3.6	3.6-4.9	4.9-6.4
Not Phys (%)	LV1-0	MC	86.9	35.9	11.0	0.4	0.	0.
		DATA	84.1	40.9	12.5	3.2	6.8	0.
	LV1-6	MC	0	0	0	0	0	0
		DATA	0	0	0	0	0	0
	LV1-(0&6)	MC	13.1	64.1	88.9	99.7	1.0	1.0
		DATA	15.9	59.1	87.5	96.8	93.2	1.0

TABLE A.3: Percentages of the three categories of unbiased over all not Physics triggers, in different low energy range, both for DATA and MC electrons (after pre scaling).

were an *unbiased charged*, so $(\text{LV1-0})_{\%}$=100 and $(\text{LV1-6})_{\%}$=0.
According to that, w_{06} as been set =100.

Appendix B

Tables

In the following the tables with the values of the measured fluxes and the values of the solar potential parameters obtained from the fit procedure explained in 5.3 will be reported.
In table B.1 all the information about the used energy binning can be found:

- E_{min}: lower limit of the energy bin (in GeV);
- E_{max}: upper limit of the energy bin (in GeV);
- $\widetilde{E}$: the most representative energy point (in GeV) in the energy bin [E_{min},E_{max}] evaluted as described in section 5.1;

From table B.2 to table B.33 the measured electron and positron fluxes in each time interval are reported. Each table corresponds to a different time interval and contains:

- $\delta\widetilde{E}$: Error (in GeV) on energy value $\widetilde{E}$ coming from ECAL absolute scale (see 5.2.1);
- Φ_{e-}: value of the electron flux between E_{min} and E_{max} (in GeV^{-1} m^{-2} sr^{-1} s^{-1});
- Φ_{e+}: value of the positron flux between E_{min} and E_{max} (in GeV^{-1} m^{-2} sr^{-1} s^{-1});
- σ_{stat}: statistical error on flux (in GeV^{-1} m^{-2} sr^{-1} s^{-1});

- σ_{sys}: total systematic error on flux excluding the error coming from the uncertainty on the ECAL energy scale ($\sigma_{\text{ECAL\_abs}}$) since this last one is treated as uncertainty on the energy bin borders (in GeV^{-1} m^{-2} sr^{-1} s^{-1}).

$$\sigma_{\text{TOTsys}} = \sigma_{\text{stat\_tmpl}} \oplus \sigma_{\text{sel\_tmpl}} \oplus \sigma_{\text{K}}^{\text{abs}} \oplus \sigma_{\text{K}}^{\text{stab}} \oplus \sigma_{\text{K}}^{\text{par}} \oplus \sigma_{\text{K}}^{\text{res}} \oplus \sigma_{\text{CC}} \oplus \sigma_{\text{ECAL\_stab}} \quad \text{(B.1)}$$

- σ_{uc}^{t} (%): percentages of the total systematic error time bin-to-bin uncorrelated;
- σ_{uc}^{E}(%): percentages of the total systematic error energy bin-to-bin uncorrelated;

Finally, in tables B.34 and B.35 the solar modulation parameters $\phi_{\text{e}-}$ and $\phi_{\text{e}+}$ have been reported respectively for electrons and positrons. The tables contains:

- Δt: time interval;
- $\phi^{\pm}$: solar potential parameter for $e^{\pm}$ obtained from the fit procedure explained in 5.3 (in GV);
- σ_{fromFit}: error on $\phi^{\pm}$ returned from the fit (in GV);
- $\sigma_{\text{sys}}^{par\_corr}$: systematic error on $\phi^{\pm}$ coming from the correlation between the parameters contained in the equations used for the fit procedure (equations 5.6 and 5.7), in GV;
- $\sigma_{\text{sys}}^{bin-to-bin\ corr}$: systematic error on $\phi^{\pm}$ coming from the errors energy or time bin-to-bin correlated, evaluated with the method explained in 5.3.2 (in GV).

E_{min} (GeV)	E_{max} (GeV)	$\tilde{E} \pm \delta\tilde{E}$ (GeV)
0.50	0.65	0.57 ± 0.03
0.65	0.82	0.73 ± 0.04
0.82	1.01	0.91 ± 0.04
1.01	1.22	1.11 ± 0.05
1.22	1.46	1.33 ± 0.06
1.46	1.72	1.58 ± 0.07
1.72	2.00	1.85 ± 0.08
2.00	2.31	2.15 ± 0.10
2.31	2.65	2.47 ± 0.11
2.65	3.00	2.82 ± 0.12
3.00	3.36	3.17 ± 0.13
3.36	3.73	3.54 ± 0.14
3.73	4.12	3.92 ± 0.15
4.12	4.54	4.32 ± 0.16
4.54	5.00	4.76 ± 0.17
5.00	5.49	5.24 ± 0.18
5.49	6.00	5.74 ± 0.19
6.00	6.54	6.26 ± 0.20
6.54	7.10	6.81 ± 0.20
7.10	7.69	7.39 ± 0.21
7.69	8.30	7.99 ± 0.21
8.30	8.95	8.62 ± 0.21
8.95	9.62	9.28 ± 0.20
9.62	10.32	9.96 ± 0.20
10.32	11.04	10.67 ± 0.21
11.04	11.80	11.41 ± 0.23
11.80	12.59	12.19 ± 0.24
12.59	13.41	12.99 ± 0.26
13.41	14.25	13.82 ± 0.28
14.25	15.14	14.69 ± 0.29
15.14	16.05	15.59 ± 0.31
16.05	17.00	16.52 ± 0.33
17.00	17.98	17.48 ± 0.35
17.98	18.99	18.48 ± 0.37
18.99	20.04	19.51 ± 0.39
20.04	21.13	20.58 ± 0.41
21.13	22.25	21.68 ± 0.43
22.25	23.42	22.83 ± 0.46
23.42	24.62	24.01 ± 0.48
24.62	25.90	25.25 ± 0.51
25.90	27.25	26.56 ± 0.53
27.25	28.68	27.95 ± 0.56
28.68	30.21	29.43 ± 0.59
30.21	31.82	31.00 ± 0.62
31.82	33.53	32.66 ± 0.65
33.53	35.36	34.43 ± 0.69
35.36	37.31	36.32 ± 0.73
37.31	40.00	38.62 ± 0.77

TABLE B.1: Used energy binning.

Δt: **01/Jul/2011 - 27/Jul/2011**						
$\bar{E}$ (GeV)	$\Phi_{e-} \pm \sigma_{\text{stat}} \pm \sigma_{\text{sys}}$ ($\text{GeV}^{-1}\ \text{m}^{-2}\ \text{sr}^{-1}\ \text{s}^{-1}$)	$\sigma^{\text{t}}_{\text{uc}}$ (%)	σ^{E}_{uc} (%)	$\Phi_{e+} \pm \sigma_{\text{stat}} \pm \sigma_{\text{sys}}$ ($\text{GeV}^{-1}\ \text{m}^{-2}\ \text{sr}^{-1}\ \text{s}^{-1}$)	$\sigma^{\text{t}}_{\text{uc}}$ (%)	σ^{E}_{uc} (%)
0.57	$(3.67 \pm 0.25 \pm 0.40)\times10^{1}$	22	53	$(3.52 \pm 2.07 \pm 0.60)\times10^{0}$	14	84
0.73	$(3.32 \pm 0.12 \pm 0.27)\times10^{1}$	30	46	$(2.56 \pm 0.86 \pm 0.22)\times10^{0}$	29	51
0.91	$(2.94 \pm 0.06 \pm 0.18)\times10^{1}$	19	37	$(2.80 \pm 0.35 \pm 0.17)\times10^{0}$	19	43
1.11	$(2.66 \pm 0.04 \pm 0.13)\times10^{1}$	20	37	$(2.08 \pm 0.18 \pm 0.11)\times10^{0}$	19	44
1.33	$(2.19 \pm 0.03 \pm 0.09)\times10^{1}$	16	35	$(1.70 \pm 0.11 \pm 0.07)\times10^{0}$	15	36
1.58	$(1.74 \pm 0.02 \pm 0.06)\times10^{1}$	12	33	$(1.35 \pm 0.07 \pm 0.05)\times10^{0}$	15	36
1.85	$(1.37 \pm 0.01 \pm 0.04)\times10^{1}$	13	34	$(9.12 \pm 0.40 \pm 0.28)\times10^{-1}$	18	35
2.15	$(1.10 \pm 0.01 \pm 0.03)\times10^{1}$	16	33	$(7.27 \pm 0.27 \pm 0.19)\times10^{-1}$	18	37
2.47	$(8.49 \pm 0.07 \pm 0.20)\times10^{0}$	21	39	$(5.33 \pm 0.19 \pm 0.14)\times10^{-1}$	28	47
2.82	$(6.48 \pm 0.05 \pm 0.14)\times10^{0}$	25	39	$(3.88 \pm 0.14 \pm 0.09)\times10^{-1}$	31	40
3.17	$(5.22 \pm 0.04 \pm 0.12)\times10^{0}$	21	39	$(3.09 \pm 0.11 \pm 0.07)\times10^{-1}$	26	47
3.54	$(4.18 \pm 0.03 \pm 0.10)\times10^{0}$	30	38	$(2.22 \pm 0.09 \pm 0.05)\times10^{-1}$	34	39
3.92	$(3.25 \pm 0.03 \pm 0.08)\times10^{0}$	32	37	$(1.83 \pm 0.07 \pm 0.05)\times10^{-1}$	34	43
4.32	$(2.54 \pm 0.02 \pm 0.06)\times10^{0}$	33	38	$(1.32 \pm 0.06 \pm 0.03)\times10^{-1}$	36	42
4.76	$(1.99 \pm 0.02 \pm 0.05)\times10^{0}$	34	37	$(1.06 \pm 0.04 \pm 0.03)\times10^{-1}$	36	45
5.24	$(1.53 \pm 0.01 \pm 0.04)\times10^{0}$	37	37	$(7.85 \pm 0.35 \pm 0.20)\times10^{-2}$	38	40
5.74	$(1.20 \pm 0.01 \pm 0.03)\times10^{0}$	38	38	$(6.01 \pm 0.28 \pm 0.15)\times10^{-2}$	37	40
6.26	$(9.43 \pm 0.09 \pm 0.23)\times10^{-1}$	38	39	$(4.94 \pm 0.23 \pm 0.13)\times10^{-2}$	39	39
6.81	$(7.46 \pm 0.07 \pm 0.18)\times10^{-1}$	40	39	$(3.85 \pm 0.19 \pm 0.10)\times10^{-2}$	36	42
7.39	$(5.93 \pm 0.06 \pm 0.15)\times10^{-1}$	41	38	$(3.02 \pm 0.15 \pm 0.08)\times10^{-2}$	40	41
7.99	$(4.64 \pm 0.05 \pm 0.11)\times10^{-1}$	43	39	$(2.37 \pm 0.13 \pm 0.06)\times10^{-2}$	37	43
8.62	$(3.73 \pm 0.04 \pm 0.09)\times10^{-1}$	43	39	$(1.72 \pm 0.10 \pm 0.05)\times10^{-2}$	39	40
9.28	$(2.96 \pm 0.04 \pm 0.07)\times10^{-1}$	44	39	$(1.68 \pm 0.10 \pm 0.05)\times10^{-2}$	38	42
9.96	$(2.35 \pm 0.03 \pm 0.06)\times10^{-1}$	45	39	$(1.11 \pm 0.08 \pm 0.03)\times10^{-2}$	34	40
10.67	$(1.89 \pm 0.03 \pm 0.05)\times10^{-1}$	44	41	$(1.09 \pm 0.07 \pm 0.03)\times10^{-2}$	37	42
11.41	$(1.53 \pm 0.02 \pm 0.04)\times10^{-1}$	44	41	$(8.26 \pm 0.60 \pm 0.24)\times10^{-3}$	38	41
12.19	$(1.25 \pm 0.02 \pm 0.03)\times10^{-1}$	44	42	$(7.90 \pm 0.54 \pm 0.22)\times10^{-3}$	35	42
12.99	$(1.00 \pm 0.02 \pm 0.03)\times10^{-1}$	44	43	$(5.94 \pm 0.45 \pm 0.17)\times10^{-3}$	38	42
13.82	$(8.39 \pm 0.15 \pm 0.22)\times10^{-2}$	46	43	$(4.99 \pm 0.41 \pm 0.14)\times10^{-3}$	37	39
14.69	$(6.67 \pm 0.13 \pm 0.17)\times10^{-2}$	47	43	$(4.08 \pm 0.35 \pm 0.12)\times10^{-3}$	34	44
15.59	$(5.61 \pm 0.12 \pm 0.15)\times10^{-2}$	47	46	$(3.24 \pm 0.30 \pm 0.10)\times10^{-3}$	38	45
16.52	$(4.63 \pm 0.10 \pm 0.12)\times10^{-2}$	47	44	$(3.00 \pm 0.27 \pm 0.09)\times10^{-3}$	34	42
17.48	$(3.78 \pm 0.09 \pm 0.10)\times10^{-2}$	46	46	$(2.15 \pm 0.23 \pm 0.07)\times10^{-3}$	37	44
18.48	$(3.16 \pm 0.08 \pm 0.08)\times10^{-2}$	45	46	$(1.91 \pm 0.20 \pm 0.06)\times10^{-3}$	34	43
19.51	$(2.71 \pm 0.07 \pm 0.07)\times10^{-2}$	47	46	$(1.31 \pm 0.16 \pm 0.04)\times10^{-3}$	32	45
20.58	$(2.10 \pm 0.06 \pm 0.06)\times10^{-2}$	48	46	$(1.64 \pm 0.17 \pm 0.05)\times10^{-3}$	35	42
21.68	$(1.84 \pm 0.05 \pm 0.05)\times10^{-2}$	46	48	$(1.23 \pm 0.14 \pm 0.04)\times10^{-3}$	35	47
22.83	$(1.57 \pm 0.05 \pm 0.04)\times10^{-2}$	48	48	$(1.17 \pm 0.14 \pm 0.04)\times10^{-3}$	32	47
24.01	$(1.30 \pm 0.04 \pm 0.03)\times10^{-2}$	47	50	$(1.16 \pm 0.13 \pm 0.04)\times10^{-3}$	39	48
25.25	$(1.15 \pm 0.04 \pm 0.03)\times10^{-2}$	49	51	$(7.33 \pm 0.97 \pm 0.24)\times10^{-4}$	32	44
26.56	$(9.52 \pm 0.32 \pm 0.26)\times10^{-3}$	50	49	$(4.88 \pm 0.76 \pm 0.16)\times10^{-4}$	31	49
27.95	$(8.11 \pm 0.29 \pm 0.22)\times10^{-3}$	44	53	$(4.83 \pm 0.75 \pm 0.17)\times10^{-4}$	36	48
29.43	$(6.93 \pm 0.26 \pm 0.19)\times10^{-3}$	50	53	$(4.26 \pm 0.68 \pm 0.14)\times10^{-4}$	34	52
31.00	$(5.46 \pm 0.22 \pm 0.15)\times10^{-3}$	52	55	$(4.31 \pm 0.66 \pm 0.15)\times10^{-4}$	36	50
32.66	$(4.86 \pm 0.21 \pm 0.13)\times10^{-3}$	50	53	$(3.49 \pm 0.59 \pm 0.12)\times10^{-4}$	31	51
34.43	$(4.18 \pm 0.18 \pm 0.12)\times10^{-3}$	47	56	$(3.30 \pm 0.53 \pm 0.11)\times10^{-4}$	38	48
36.32	$(3.26 \pm 0.16 \pm 0.10)\times10^{-3}$	55	60	$(2.91 \pm 0.52 \pm 0.11)\times10^{-4}$	42	57
38.62	$(2.63 \pm 0.12 \pm 0.08)\times10^{-3}$	52	56	$(2.60 \pm 0.39 \pm 0.09)\times10^{-4}$	32	51

TABLE B.2: Results for electron and positron flux in time interval: 01/Jul/2011 - 27/Jul/2011

Δt: **28/Jul/2011 - 23/Aug/2011**						
$\tilde{E}$ (GeV)	$\Phi_{e-} \pm \sigma_{\text{stat}} \pm \sigma_{\text{sys}}$ (GeV^{-1} m^{-2} sr^{-1} s^{-1})	$\sigma^{\text{t}}_{\text{uc}}$ (%)	σ^{E}_{uc} (%)	$\Phi_{e+} \pm \sigma_{\text{stat}} \pm \sigma_{\text{sys}}$ (GeV^{-1} m^{-2} sr^{-1} s^{-1})	$\sigma^{\text{t}}_{\text{uc}}$ (%)	σ^{E}_{uc} (%)
0.57	$(4.05 \pm 0.27 \pm 0.44)\times10^{1}$	21	52	$(2.96 \pm 2.18 \pm 0.51)\times10^{0}$	13	84
0.73	$(3.19 \pm 0.12 \pm 0.27)\times10^{1}$	32	47	$(4.20 \pm 1.01 \pm 0.36)\times10^{0}$	31	52
0.91	$(2.90 \pm 0.07 \pm 0.18)\times10^{1}$	19	37	$(2.81 \pm 0.38 \pm 0.17)\times10^{0}$	19	42
1.11	$(2.55 \pm 0.04 \pm 0.12)\times10^{1}$	20	36	$(2.38 \pm 0.19 \pm 0.12)\times10^{0}$	19	44
1.33	$(2.17 \pm 0.03 \pm 0.09)\times10^{1}$	15	34	$(1.62 \pm 0.11 \pm 0.07)\times10^{0}$	15	36
1.58	$(1.72 \pm 0.02 \pm 0.06)\times10^{1}$	12	33	$(1.27 \pm 0.07 \pm 0.04)\times10^{0}$	15	36
1.85	$(1.35 \pm 0.01 \pm 0.04)\times10^{1}$	12	34	$(9.61 \pm 0.41 \pm 0.29)\times10^{-1}$	18	35
2.15	$(1.08 \pm 0.01 \pm 0.03)\times10^{1}$	15	33	$(7.35 \pm 0.28 \pm 0.20)\times10^{-1}$	18	37
2.47	$(8.45 \pm 0.07 \pm 0.20)\times10^{0}$	20	40	$(5.06 \pm 0.19 \pm 0.13)\times10^{-1}$	27	47
2.82	$(6.51 \pm 0.05 \pm 0.14)\times10^{0}$	25	40	$(4.00 \pm 0.15 \pm 0.09)\times10^{-1}$	31	41
3.17	$(5.17 \pm 0.04 \pm 0.12)\times10^{0}$	21	39	$(3.05 \pm 0.11 \pm 0.07)\times10^{-1}$	26	48
3.54	$(4.05 \pm 0.03 \pm 0.09)\times10^{0}$	30	39	$(2.17 \pm 0.09 \pm 0.05)\times10^{-1}$	34	39
3.92	$(3.13 \pm 0.03 \pm 0.07)\times10^{0}$	32	38	$(1.77 \pm 0.07 \pm 0.04)\times10^{-1}$	33	43
4.32	$(2.50 \pm 0.02 \pm 0.06)\times10^{0}$	33	38	$(1.41 \pm 0.06 \pm 0.04)\times10^{-1}$	36	43
4.76	$(1.95 \pm 0.02 \pm 0.05)\times10^{0}$	34	38	$(1.03 \pm 0.04 \pm 0.03)\times10^{-1}$	36	45
5.24	$(1.51 \pm 0.01 \pm 0.04)\times10^{0}$	37	38	$(7.94 \pm 0.35 \pm 0.20)\times10^{-2}$	38	40
5.74	$(1.16 \pm 0.01 \pm 0.03)\times10^{0}$	38	39	$(6.24 \pm 0.28 \pm 0.16)\times10^{-2}$	37	41
6.26	$(9.38 \pm 0.09 \pm 0.23)\times10^{-1}$	38	39	$(4.79 \pm 0.22 \pm 0.12)\times10^{-2}$	39	40
6.81	$(7.25 \pm 0.07 \pm 0.18)\times10^{-1}$	39	39	$(3.64 \pm 0.18 \pm 0.09)\times10^{-2}$	36	42
7.39	$(5.77 \pm 0.06 \pm 0.14)\times10^{-1}$	41	39	$(2.98 \pm 0.15 \pm 0.08)\times10^{-2}$	40	41
7.99	$(4.50 \pm 0.05 \pm 0.11)\times10^{-1}$	43	39	$(2.31 \pm 0.13 \pm 0.06)\times10^{-2}$	37	43
8.62	$(3.59 \pm 0.04 \pm 0.09)\times10^{-1}$	43	39	$(1.97 \pm 0.11 \pm 0.05)\times10^{-2}$	39	40
9.28	$(2.82 \pm 0.04 \pm 0.07)\times10^{-1}$	44	40	$(1.50 \pm 0.09 \pm 0.04)\times10^{-2}$	38	42
9.96	$(2.30 \pm 0.03 \pm 0.06)\times10^{-1}$	45	40	$(1.11 \pm 0.08 \pm 0.03)\times10^{-2}$	34	40
10.67	$(1.87 \pm 0.03 \pm 0.05)\times10^{-1}$	44	41	$(9.60 \pm 0.67 \pm 0.28)\times10^{-3}$	37	42
11.41	$(1.51 \pm 0.02 \pm 0.04)\times10^{-1}$	44	41	$(8.50 \pm 0.60 \pm 0.24)\times10^{-3}$	38	41
12.19	$(1.21 \pm 0.02 \pm 0.03)\times10^{-1}$	44	42	$(6.74 \pm 0.50 \pm 0.19)\times10^{-3}$	35	42
12.99	$(1.02 \pm 0.02 \pm 0.03)\times10^{-1}$	44	43	$(5.93 \pm 0.47 \pm 0.17)\times10^{-3}$	38	42
13.82	$(8.05 \pm 0.15 \pm 0.21)\times10^{-2}$	46	43	$(4.87 \pm 0.39 \pm 0.14)\times10^{-3}$	37	39
14.69	$(6.37 \pm 0.13 \pm 0.17)\times10^{-2}$	47	43	$(4.37 \pm 0.36 \pm 0.12)\times10^{-3}$	34	44
15.59	$(5.30 \pm 0.11 \pm 0.14)\times10^{-2}$	47	46	$(3.01 \pm 0.29 \pm 0.09)\times10^{-3}$	38	45
16.52	$(4.48 \pm 0.10 \pm 0.12)\times10^{-2}$	47	44	$(2.66 \pm 0.27 \pm 0.08)\times10^{-3}$	34	42
17.48	$(3.75 \pm 0.09 \pm 0.10)\times10^{-2}$	46	45	$(2.30 \pm 0.23 \pm 0.07)\times10^{-3}$	37	43
18.48	$(3.05 \pm 0.08 \pm 0.08)\times10^{-2}$	45	46	$(1.70 \pm 0.19 \pm 0.05)\times10^{-3}$	34	43
19.51	$(2.65 \pm 0.07 \pm 0.07)\times10^{-2}$	47	46	$(1.39 \pm 0.17 \pm 0.04)\times10^{-3}$	32	45
20.58	$(2.23 \pm 0.06 \pm 0.06)\times10^{-2}$	48	46	$(1.23 \pm 0.15 \pm 0.04)\times10^{-3}$	34	42
21.68	$(1.75 \pm 0.05 \pm 0.05)\times10^{-2}$	46	48	$(1.37 \pm 0.15 \pm 0.04)\times10^{-3}$	35	47
22.83	$(1.46 \pm 0.04 \pm 0.04)\times10^{-2}$	48	48	$(9.99 \pm 1.26 \pm 0.32)\times10^{-4}$	32	47
24.01	$(1.37 \pm 0.04 \pm 0.04)\times10^{-2}$	47	49	$(7.09 \pm 0.97 \pm 0.24)\times10^{-4}$	39	47
25.25	$(1.09 \pm 0.04 \pm 0.03)\times10^{-2}$	49	51	$(4.16 \pm 0.71 \pm 0.14)\times10^{-4}$	32	44
26.56	$(8.72 \pm 0.31 \pm 0.24)\times10^{-3}$	51	49	$(7.07 \pm 0.90 \pm 0.23)\times10^{-4}$	31	49
27.95	$(8.01 \pm 0.29 \pm 0.22)\times10^{-3}$	44	52	$(5.57 \pm 0.81 \pm 0.20)\times10^{-4}$	36	48
29.43	$(6.59 \pm 0.25 \pm 0.18)\times10^{-3}$	51	53	$(5.09 \pm 0.74 \pm 0.17)\times10^{-4}$	34	52
31.00	$(5.40 \pm 0.22 \pm 0.15)\times10^{-3}$	52	55	$(4.92 \pm 0.71 \pm 0.17)\times10^{-4}$	36	50
32.66	$(4.85 \pm 0.21 \pm 0.13)\times10^{-3}$	50	53	$(2.60 \pm 0.47 \pm 0.09)\times10^{-4}$	31	51
34.43	$(4.11 \pm 0.18 \pm 0.11)\times10^{-3}$	47	56	$(2.29 \pm 0.46 \pm 0.08)\times10^{-4}$	38	48
36.32	$(3.06 \pm 0.15 \pm 0.09)\times10^{-3}$	57	61	$(1.76 \pm 0.41 \pm 0.07)\times10^{-4}$	43	58
38.62	$(2.65 \pm 0.12 \pm 0.08)\times10^{-3}$	53	56	$(2.58 \pm 0.38 \pm 0.09)\times10^{-4}$	32	50

TABLE B.3: Results for electron and positron flux in time interval: 28/Jul/2011 - 23/Aug/2011

Δt: **24/Aug/2011 - 19/Sep/2011**						
$\tilde{E}$ (GeV)	$\Phi_{e-} \pm \sigma_{\rm stat} \pm \sigma_{\rm sys}$ (GeV^{-1} m^{-2} sr^{-1} s^{-1})	$\sigma^{\rm t}_{\rm uc}$ (%)	$\sigma^{E}_{\rm uc}$ (%)	$\Phi_{e+} \pm \sigma_{\rm stat} \pm \sigma_{\rm sys}$ (GeV^{-1} m^{-2} sr^{-1} s^{-1})	$\sigma^{\rm t}_{\rm uc}$ (%)	$\sigma^{E}_{\rm uc}$ (%)
0.57	$(4.18 \pm 0.25 \pm 0.45)\times10^{1}$	19	52	$(4.42 \pm 2.26 \pm 0.76)\times10^{0}$	12	84
0.73	$(3.51 \pm 0.12 \pm 0.29)\times10^{1}$	28	44	$(3.35 \pm 0.93 \pm 0.29)\times10^{0}$	27	50
0.91	$(3.05 \pm 0.06 \pm 0.18)\times10^{1}$	18	37	$(2.70 \pm 0.34 \pm 0.17)\times10^{0}$	18	42
1.11	$(2.64 \pm 0.04 \pm 0.13)\times10^{1}$	20	36	$(2.31 \pm 0.18 \pm 0.12)\times10^{0}$	19	44
1.33	$(2.20 \pm 0.03 \pm 0.09)\times10^{1}$	15	34	$(1.73 \pm 0.11 \pm 0.07)\times10^{0}$	15	36
1.58	$(1.74 \pm 0.02 \pm 0.06)\times10^{1}$	12	33	$(1.31 \pm 0.06 \pm 0.05)\times10^{0}$	15	36
1.85	$(1.39 \pm 0.01 \pm 0.04)\times10^{1}$	12	34	$(1.01 \pm 0.04 \pm 0.03)\times10^{0}$	17	35
2.15	$(1.10 \pm 0.01 \pm 0.03)\times10^{1}$	15	33	$(7.74 \pm 0.28 \pm 0.21)\times10^{-1}$	18	37
2.47	$(8.58 \pm 0.07 \pm 0.21)\times10^{0}$	20	40	$(5.31 \pm 0.19 \pm 0.14)\times10^{-1}$	27	47
2.82	$(6.55 \pm 0.05 \pm 0.14)\times10^{0}$	25	40	$(3.97 \pm 0.14 \pm 0.09)\times10^{-1}$	31	41
3.17	$(5.20 \pm 0.04 \pm 0.12)\times10^{0}$	21	39	$(3.19 \pm 0.11 \pm 0.08)\times10^{-1}$	26	47
3.54	$(4.12 \pm 0.03 \pm 0.10)\times10^{0}$	30	38	$(2.45 \pm 0.09 \pm 0.06)\times10^{-1}$	34	39
3.92	$(3.21 \pm 0.03 \pm 0.07)\times10^{0}$	32	37	$(1.92 \pm 0.07 \pm 0.05)\times10^{-1}$	33	43
4.32	$(2.51 \pm 0.02 \pm 0.06)\times10^{0}$	33	37	$(1.33 \pm 0.05 \pm 0.03)\times10^{-1}$	36	42
4.76	$(1.95 \pm 0.02 \pm 0.05)\times10^{0}$	34	37	$(1.04 \pm 0.04 \pm 0.03)\times10^{-1}$	36	45
5.24	$(1.51 \pm 0.01 \pm 0.04)\times10^{0}$	37	37	$(7.85 \pm 0.33 \pm 0.19)\times10^{-2}$	38	40
5.74	$(1.18 \pm 0.01 \pm 0.03)\times10^{0}$	38	37	$(6.53 \pm 0.27 \pm 0.16)\times10^{-2}$	37	40
6.26	$(9.24 \pm 0.09 \pm 0.22)\times10^{-1}$	38	38	$(4.90 \pm 0.22 \pm 0.12)\times10^{-2}$	39	39
6.81	$(7.39 \pm 0.07 \pm 0.18)\times10^{-1}$	40	38	$(3.63 \pm 0.18 \pm 0.09)\times10^{-2}$	36	41
7.39	$(5.77 \pm 0.06 \pm 0.14)\times10^{-1}$	41	37	$(3.03 \pm 0.15 \pm 0.08)\times10^{-2}$	40	40
7.99	$(4.49 \pm 0.05 \pm 0.11)\times10^{-1}$	43	38	$(2.39 \pm 0.12 \pm 0.06)\times10^{-2}$	37	42
8.62	$(3.64 \pm 0.04 \pm 0.09)\times10^{-1}$	43	38	$(1.82 \pm 0.10 \pm 0.05)\times10^{-2}$	39	39
9.28	$(2.90 \pm 0.04 \pm 0.07)\times10^{-1}$	44	38	$(1.47 \pm 0.09 \pm 0.04)\times10^{-2}$	38	41
9.96	$(2.32 \pm 0.03 \pm 0.06)\times10^{-1}$	45	38	$(1.18 \pm 0.08 \pm 0.03)\times10^{-2}$	34	38
10.67	$(1.82 \pm 0.03 \pm 0.05)\times10^{-1}$	45	39	$(1.07 \pm 0.07 \pm 0.03)\times10^{-2}$	37	41
11.41	$(1.49 \pm 0.02 \pm 0.04)\times10^{-1}$	44	40	$(8.37 \pm 0.58 \pm 0.24)\times10^{-3}$	38	40
12.19	$(1.23 \pm 0.02 \pm 0.03)\times10^{-1}$	45	40	$(6.37 \pm 0.49 \pm 0.17)\times10^{-3}$	35	41
12.99	$(1.02 \pm 0.02 \pm 0.03)\times10^{-1}$	44	41	$(5.83 \pm 0.44 \pm 0.17)\times10^{-3}$	38	40
13.82	$(7.96 \pm 0.15 \pm 0.20)\times10^{-2}$	46	41	$(4.82 \pm 0.39 \pm 0.14)\times10^{-3}$	37	37
14.69	$(6.67 \pm 0.13 \pm 0.17)\times10^{-2}$	47	41	$(3.81 \pm 0.34 \pm 0.11)\times10^{-3}$	34	43
15.59	$(5.46 \pm 0.11 \pm 0.14)\times10^{-2}$	48	44	$(3.56 \pm 0.31 \pm 0.11)\times10^{-3}$	38	44
16.52	$(4.48 \pm 0.10 \pm 0.12)\times10^{-2}$	48	42	$(2.53 \pm 0.25 \pm 0.07)\times10^{-3}$	34	40
17.48	$(3.60 \pm 0.08 \pm 0.09)\times10^{-2}$	47	43	$(2.30 \pm 0.23 \pm 0.07)\times10^{-3}$	38	42
18.48	$(3.23 \pm 0.08 \pm 0.08)\times10^{-2}$	46	43	$(2.03 \pm 0.20 \pm 0.06)\times10^{-3}$	35	41
19.51	$(2.61 \pm 0.07 \pm 0.07)\times10^{-2}$	47	44	$(1.58 \pm 0.17 \pm 0.05)\times10^{-3}$	32	43
20.58	$(2.21 \pm 0.06 \pm 0.06)\times10^{-2}$	48	44	$(1.48 \pm 0.16 \pm 0.05)\times10^{-3}$	34	40
21.68	$(1.83 \pm 0.05 \pm 0.05)\times10^{-2}$	47	45	$(1.07 \pm 0.13 \pm 0.03)\times10^{-3}$	35	45
22.83	$(1.50 \pm 0.04 \pm 0.04)\times10^{-2}$	49	45	$(9.23 \pm 1.20 \pm 0.29)\times10^{-4}$	32	45
24.01	$(1.27 \pm 0.04 \pm 0.03)\times10^{-2}$	48	47	$(1.09 \pm 0.12 \pm 0.04)\times10^{-3}$	39	46
25.25	$(1.12 \pm 0.04 \pm 0.03)\times10^{-2}$	49	48	$(9.42 \pm 1.07 \pm 0.30)\times10^{-4}$	32	42
26.56	$(8.81 \pm 0.30 \pm 0.24)\times10^{-3}$	51	47	$(5.72 \pm 0.82 \pm 0.18)\times10^{-4}$	31	47
27.95	$(8.06 \pm 0.28 \pm 0.21)\times10^{-3}$	44	50	$(5.42 \pm 0.79 \pm 0.19)\times10^{-4}$	37	47
29.43	$(6.64 \pm 0.25 \pm 0.18)\times10^{-3}$	51	50	$(5.67 \pm 0.78 \pm 0.19)\times10^{-4}$	34	51
31.00	$(5.36 \pm 0.22 \pm 0.15)\times10^{-3}$	52	52	$(5.04 \pm 0.70 \pm 0.17)\times10^{-4}$	35	48
32.66	$(4.22 \pm 0.19 \pm 0.12)\times10^{-3}$	52	52	$(3.44 \pm 0.56 \pm 0.12)\times10^{-4}$	32	50
34.43	$(3.83 \pm 0.17 \pm 0.10)\times10^{-3}$	48	54	$(3.09 \pm 0.50 \pm 0.10)\times10^{-4}$	38	46
36.32	$(3.23 \pm 0.15 \pm 0.09)\times10^{-3}$	56	58	$(3.49 \pm 0.55 \pm 0.13)\times10^{-4}$	42	55
38.62	$(2.68 \pm 0.12 \pm 0.08)\times10^{-3}$	53	53	$(2.22 \pm 0.36 \pm 0.07)\times10^{-4}$	31	48

TABLE B.4: Results for electron and positron flux in time interval: 24/Aug/2011 - 19/Sep/2011

Δt: **20/Sep/2011 - 16/Oct/2011**						
$\tilde{E}$ (GeV)	$\Phi_{e-} \pm \sigma_{\rm stat} \pm \sigma_{\rm sys}$ (GeV^{-1} m^{-2} sr^{-1} s^{-1})	$\sigma^{\rm t}_{\rm uc}$ (%)	$\sigma^{E}_{\rm uc}$ (%)	$\Phi_{e+} \pm \sigma_{\rm stat} \pm \sigma_{\rm sys}$ (GeV^{-1} m^{-2} sr^{-1} s^{-1})	$\sigma^{\rm t}_{\rm uc}$ (%)	$\sigma^{E}_{\rm uc}$ (%)
0.57	$(4.37 \pm 0.26 \pm 0.47)\times10^{1}$	18	52	$(2.01 \pm 2.32 \pm 0.34)\times10^{0}$	12	84
0.73	$(3.27 \pm 0.11 \pm 0.27)\times10^{1}$	29	45	$(2.94 \pm 0.81 \pm 0.25)\times10^{0}$	28	51
0.91	$(2.76 \pm 0.06 \pm 0.17)\times10^{1}$	19	37	$(2.56 \pm 0.35 \pm 0.16)\times10^{0}$	18	42
1.11	$(2.52 \pm 0.04 \pm 0.12)\times10^{1}$	20	36	$(1.92 \pm 0.19 \pm 0.10)\times10^{0}$	19	44
1.33	$(2.03 \pm 0.03 \pm 0.08)\times10^{1}$	15	34	$(1.67 \pm 0.11 \pm 0.07)\times10^{0}$	15	36
1.58	$(1.65 \pm 0.02 \pm 0.06)\times10^{1}$	12	33	$(1.18 \pm 0.06 \pm 0.04)\times10^{0}$	15	36
1.85	$(1.32 \pm 0.01 \pm 0.04)\times10^{1}$	12	34	$(8.80 \pm 0.38 \pm 0.27)\times10^{-1}$	17	35
2.15	$(1.06 \pm 0.01 \pm 0.03)\times10^{1}$	15	33	$(6.92 \pm 0.26 \pm 0.19)\times10^{-1}$	18	37
2.47	$(8.15 \pm 0.06 \pm 0.20)\times10^{0}$	20	40	$(4.88 \pm 0.18 \pm 0.13)\times10^{-1}$	27	47
2.82	$(6.17 \pm 0.05 \pm 0.13)\times10^{0}$	25	40	$(3.52 \pm 0.13 \pm 0.08)\times10^{-1}$	31	41
3.17	$(4.99 \pm 0.04 \pm 0.11)\times10^{0}$	21	39	$(3.10 \pm 0.11 \pm 0.08)\times10^{-1}$	26	48
3.54	$(3.94 \pm 0.03 \pm 0.09)\times10^{0}$	30	38	$(2.21 \pm 0.09 \pm 0.05)\times10^{-1}$	34	39
3.92	$(3.09 \pm 0.03 \pm 0.07)\times10^{0}$	32	38	$(1.68 \pm 0.07 \pm 0.04)\times10^{-1}$	33	43
4.32	$(2.44 \pm 0.02 \pm 0.06)\times10^{0}$	33	38	$(1.32 \pm 0.05 \pm 0.03)\times10^{-1}$	36	42
4.76	$(1.90 \pm 0.02 \pm 0.04)\times10^{0}$	34	37	$(9.96 \pm 0.41 \pm 0.25)\times10^{-2}$	36	45
5.24	$(1.48 \pm 0.01 \pm 0.04)\times10^{0}$	37	37	$(7.21 \pm 0.32 \pm 0.18)\times10^{-2}$	38	40
5.74	$(1.14 \pm 0.01 \pm 0.03)\times10^{0}$	38	38	$(6.24 \pm 0.27 \pm 0.16)\times10^{-2}$	37	40
6.26	$(9.09 \pm 0.09 \pm 0.22)\times10^{-1}$	38	38	$(4.71 \pm 0.22 \pm 0.12)\times10^{-2}$	39	39
6.81	$(7.13 \pm 0.07 \pm 0.17)\times10^{-1}$	40	38	$(3.91 \pm 0.18 \pm 0.10)\times10^{-2}$	36	41
7.39	$(5.59 \pm 0.06 \pm 0.14)\times10^{-1}$	41	38	$(2.72 \pm 0.14 \pm 0.07)\times10^{-2}$	40	40
7.99	$(4.41 \pm 0.05 \pm 0.11)\times10^{-1}$	43	38	$(2.26 \pm 0.12 \pm 0.06)\times10^{-2}$	37	43
8.62	$(3.54 \pm 0.04 \pm 0.09)\times10^{-1}$	43	38	$(1.89 \pm 0.10 \pm 0.05)\times10^{-2}$	39	40
9.28	$(2.80 \pm 0.03 \pm 0.07)\times10^{-1}$	44	39	$(1.44 \pm 0.09 \pm 0.04)\times10^{-2}$	38	42
9.96	$(2.21 \pm 0.03 \pm 0.06)\times10^{-1}$	45	39	$(1.20 \pm 0.08 \pm 0.03)\times10^{-2}$	34	39
10.67	$(1.79 \pm 0.03 \pm 0.05)\times10^{-1}$	44	40	$(8.92 \pm 0.63 \pm 0.26)\times10^{-3}$	37	42
11.41	$(1.43 \pm 0.02 \pm 0.04)\times10^{-1}$	44	40	$(8.12 \pm 0.57 \pm 0.23)\times10^{-3}$	38	41
12.19	$(1.20 \pm 0.02 \pm 0.03)\times10^{-1}$	44	40	$(6.84 \pm 0.50 \pm 0.19)\times10^{-3}$	35	41
12.99	$(9.70 \pm 0.17 \pm 0.25)\times10^{-2}$	44	42	$(5.08 \pm 0.41 \pm 0.15)\times10^{-3}$	38	41
13.82	$(7.90 \pm 0.14 \pm 0.20)\times10^{-2}$	46	42	$(4.98 \pm 0.38 \pm 0.14)\times10^{-3}$	37	38
14.69	$(6.58 \pm 0.13 \pm 0.17)\times10^{-2}$	47	42	$(3.75 \pm 0.33 \pm 0.11)\times10^{-3}$	34	43
15.59	$(5.28 \pm 0.11 \pm 0.14)\times10^{-2}$	48	45	$(2.70 \pm 0.27 \pm 0.08)\times10^{-3}$	38	45
16.52	$(4.29 \pm 0.09 \pm 0.11)\times10^{-2}$	48	43	$(3.24 \pm 0.28 \pm 0.10)\times10^{-3}$	34	41
17.48	$(3.61 \pm 0.08 \pm 0.09)\times10^{-2}$	47	44	$(2.48 \pm 0.23 \pm 0.07)\times10^{-3}$	37	42
18.48	$(2.92 \pm 0.07 \pm 0.08)\times10^{-2}$	46	45	$(2.00 \pm 0.20 \pm 0.06)\times10^{-3}$	35	42
19.51	$(2.58 \pm 0.07 \pm 0.07)\times10^{-2}$	47	45	$(1.82 \pm 0.18 \pm 0.06)\times10^{-3}$	32	44
20.58	$(2.12 \pm 0.06 \pm 0.06)\times10^{-2}$	48	45	$(1.45 \pm 0.16 \pm 0.05)\times10^{-3}$	34	41
21.68	$(1.79 \pm 0.05 \pm 0.05)\times10^{-2}$	47	46	$(1.02 \pm 0.12 \pm 0.03)\times10^{-3}$	35	46
22.83	$(1.62 \pm 0.05 \pm 0.04)\times10^{-2}$	48	46	$(1.05 \pm 0.12 \pm 0.03)\times10^{-3}$	32	46
24.01	$(1.29 \pm 0.04 \pm 0.03)\times10^{-2}$	47	48	$(9.86 \pm 1.15 \pm 0.33)\times10^{-4}$	39	46
25.25	$(1.07 \pm 0.03 \pm 0.03)\times10^{-2}$	49	49	$(8.94 \pm 1.10 \pm 0.29)\times10^{-4}$	32	43
26.56	$(8.77 \pm 0.31 \pm 0.24)\times10^{-3}$	51	48	$(6.95 \pm 0.89 \pm 0.23)\times10^{-4}$	31	48
27.95	$(7.55 \pm 0.27 \pm 0.20)\times10^{-3}$	44	51	$(4.95 \pm 0.75 \pm 0.17)\times10^{-4}$	37	47
29.43	$(6.55 \pm 0.24 \pm 0.18)\times10^{-3}$	51	51	$(5.49 \pm 0.73 \pm 0.18)\times10^{-4}$	34	51
31.00	$(5.92 \pm 0.23 \pm 0.16)\times10^{-3}$	51	53	$(3.31 \pm 0.56 \pm 0.11)\times10^{-4}$	35	49
32.66	$(4.71 \pm 0.20 \pm 0.13)\times10^{-3}$	50	52	$(2.90 \pm 0.50 \pm 0.10)\times10^{-4}$	31	50
34.43	$(3.90 \pm 0.17 \pm 0.11)\times10^{-3}$	47	55	$(2.22 \pm 0.42 \pm 0.08)\times10^{-4}$	38	47
36.32	$(3.23 \pm 0.15 \pm 0.09)\times10^{-3}$	55	58	$(3.47 \pm 0.52 \pm 0.13)\times10^{-4}$	42	56
38.62	$(2.51 \pm 0.12 \pm 0.07)\times10^{-3}$	53	55	$(1.55 \pm 0.29 \pm 0.05)\times10^{-4}$	32	49

TABLE B.5: Results for electron and positron flux in time interval: 20/Sep/2011 - 16/Oct/2011

Δt: **17/Oct/2011 - 12/Nov/2011**						
$\tilde{E}$ (GeV)	$\Phi_{e-} \pm \sigma_{\rm stat} \pm \sigma_{\rm sys}$ (GeV^{-1} m^{-2} sr^{-1} s^{-1})	$\sigma^{\rm t}_{\rm uc}$ (%)	$\sigma^{E}_{\rm uc}$ (%)	$\Phi_{e+} \pm \sigma_{\rm stat} \pm \sigma_{\rm sys}$ (GeV^{-1} m^{-2} sr^{-1} s^{-1})	$\sigma^{\rm t}_{\rm uc}$ (%)	$\sigma^{E}_{\rm uc}$ (%)
0.57	$(4.30 \pm 0.24 \pm 0.46)\times10^{1}$	18	51	$(5.23 \pm 2.38 \pm 0.89)\times10^{0}$	11	84
0.73	$(3.52 \pm 0.11 \pm 0.29)\times10^{1}$	26	43	$(2.30 \pm 0.74 \pm 0.20)\times10^{0}$	25	50
0.91	$(2.99 \pm 0.06 \pm 0.18)\times10^{1}$	18	37	$(2.70 \pm 0.35 \pm 0.17)\times10^{0}$	18	42
1.11	$(2.54 \pm 0.04 \pm 0.12)\times10^{1}$	20	36	$(2.07 \pm 0.18 \pm 0.10)\times10^{0}$	19	44
1.33	$(2.14 \pm 0.03 \pm 0.09)\times10^{1}$	15	34	$(1.68 \pm 0.11 \pm 0.07)\times10^{0}$	15	36
1.58	$(1.75 \pm 0.02 \pm 0.06)\times10^{1}$	12	33	$(1.27 \pm 0.06 \pm 0.04)\times10^{0}$	15	36
1.85	$(1.36 \pm 0.01 \pm 0.04)\times10^{1}$	12	34	$(9.27 \pm 0.38 \pm 0.28)\times10^{-1}$	17	35
2.15	$(1.07 \pm 0.01 \pm 0.03)\times10^{1}$	15	33	$(7.78 \pm 0.27 \pm 0.21)\times10^{-1}$	18	37
2.47	$(8.36 \pm 0.06 \pm 0.20)\times10^{0}$	20	39	$(5.41 \pm 0.19 \pm 0.14)\times10^{-1}$	27	47
2.82	$(6.48 \pm 0.05 \pm 0.14)\times10^{0}$	25	39	$(4.21 \pm 0.14 \pm 0.09)\times10^{-1}$	31	40
3.17	$(5.15 \pm 0.04 \pm 0.12)\times10^{0}$	21	38	$(3.03 \pm 0.11 \pm 0.07)\times10^{-1}$	26	47
3.54	$(4.08 \pm 0.03 \pm 0.09)\times10^{0}$	30	38	$(2.30 \pm 0.09 \pm 0.06)\times10^{-1}$	34	39
3.92	$(3.16 \pm 0.03 \pm 0.07)\times10^{0}$	32	37	$(1.78 \pm 0.07 \pm 0.04)\times10^{-1}$	33	42
4.32	$(2.53 \pm 0.02 \pm 0.06)\times10^{0}$	33	37	$(1.34 \pm 0.05 \pm 0.03)\times10^{-1}$	36	42
4.76	$(1.94 \pm 0.02 \pm 0.05)\times10^{0}$	34	37	$(1.04 \pm 0.04 \pm 0.03)\times10^{-1}$	36	44
5.24	$(1.51 \pm 0.01 \pm 0.04)\times10^{0}$	37	36	$(7.94 \pm 0.33 \pm 0.20)\times10^{-2}$	38	39
5.74	$(1.19 \pm 0.01 \pm 0.03)\times10^{0}$	38	37	$(6.28 \pm 0.27 \pm 0.16)\times10^{-2}$	37	39
6.26	$(9.25 \pm 0.08 \pm 0.22)\times10^{-1}$	38	38	$(4.67 \pm 0.21 \pm 0.12)\times10^{-2}$	39	38
6.81	$(7.34 \pm 0.07 \pm 0.18)\times10^{-1}$	40	38	$(3.67 \pm 0.17 \pm 0.09)\times10^{-2}$	36	41
7.39	$(5.59 \pm 0.06 \pm 0.14)\times10^{-1}$	42	37	$(2.96 \pm 0.15 \pm 0.08)\times10^{-2}$	40	40
7.99	$(4.58 \pm 0.05 \pm 0.11)\times10^{-1}$	43	38	$(2.40 \pm 0.12 \pm 0.06)\times10^{-2}$	37	42
8.62	$(3.65 \pm 0.04 \pm 0.09)\times10^{-1}$	43	38	$(1.78 \pm 0.10 \pm 0.05)\times10^{-2}$	39	39
9.28	$(2.90 \pm 0.04 \pm 0.07)\times10^{-1}$	44	38	$(1.45 \pm 0.09 \pm 0.04)\times10^{-2}$	38	41
9.96	$(2.26 \pm 0.03 \pm 0.06)\times10^{-1}$	45	38	$(1.18 \pm 0.08 \pm 0.03)\times10^{-2}$	34	38
10.67	$(1.87 \pm 0.03 \pm 0.05)\times10^{-1}$	45	39	$(1.12 \pm 0.07 \pm 0.03)\times10^{-2}$	37	41
11.41	$(1.46 \pm 0.02 \pm 0.04)\times10^{-1}$	44	40	$(7.88 \pm 0.56 \pm 0.22)\times10^{-3}$	38	40
12.19	$(1.20 \pm 0.02 \pm 0.03)\times10^{-1}$	45	40	$(6.62 \pm 0.49 \pm 0.18)\times10^{-3}$	35	41
12.99	$(1.01 \pm 0.02 \pm 0.03)\times10^{-1}$	44	41	$(5.48 \pm 0.42 \pm 0.16)\times10^{-3}$	38	40
13.82	$(8.02 \pm 0.14 \pm 0.20)\times10^{-2}$	46	41	$(4.15 \pm 0.36 \pm 0.12)\times10^{-3}$	37	37
14.69	$(6.56 \pm 0.12 \pm 0.17)\times10^{-2}$	47	41	$(3.74 \pm 0.33 \pm 0.11)\times10^{-3}$	34	43
15.59	$(5.43 \pm 0.11 \pm 0.14)\times10^{-2}$	48	44	$(3.55 \pm 0.30 \pm 0.11)\times10^{-3}$	38	44
16.52	$(4.53 \pm 0.10 \pm 0.12)\times10^{-2}$	48	42	$(2.76 \pm 0.26 \pm 0.08)\times10^{-3}$	34	41
17.48	$(3.70 \pm 0.08 \pm 0.10)\times10^{-2}$	47	43	$(2.76 \pm 0.24 \pm 0.08)\times10^{-3}$	37	42
18.48	$(3.07 \pm 0.07 \pm 0.08)\times10^{-2}$	46	44	$(2.04 \pm 0.20 \pm 0.06)\times10^{-3}$	35	41
19.51	$(2.60 \pm 0.06 \pm 0.07)\times10^{-2}$	47	44	$(1.49 \pm 0.17 \pm 0.05)\times10^{-3}$	32	43
20.58	$(2.06 \pm 0.06 \pm 0.05)\times10^{-2}$	48	44	$(1.21 \pm 0.15 \pm 0.04)\times10^{-3}$	35	40
21.68	$(1.78 \pm 0.05 \pm 0.05)\times10^{-2}$	47	45	$(9.19 \pm 1.18 \pm 0.30)\times10^{-4}$	35	45
22.83	$(1.54 \pm 0.04 \pm 0.04)\times10^{-2}$	49	46	$(9.89 \pm 1.20 \pm 0.31)\times10^{-4}$	32	45
24.01	$(1.29 \pm 0.04 \pm 0.03)\times10^{-2}$	47	47	$(6.34 \pm 0.99 \pm 0.21)\times10^{-4}$	39	46
25.25	$(1.13 \pm 0.04 \pm 0.03)\times10^{-2}$	49	48	$(7.97 \pm 1.01 \pm 0.26)\times10^{-4}$	31	42
26.56	$(9.03 \pm 0.31 \pm 0.24)\times10^{-3}$	51	47	$(6.53 \pm 0.81 \pm 0.21)\times10^{-4}$	31	47
27.95	$(7.61 \pm 0.27 \pm 0.20)\times10^{-3}$	44	50	$(5.93 \pm 0.82 \pm 0.21)\times10^{-4}$	37	47
29.43	$(7.04 \pm 0.25 \pm 0.19)\times10^{-3}$	50	50	$(5.62 \pm 0.72 \pm 0.19)\times10^{-4}$	33	50
31.00	$(5.78 \pm 0.22 \pm 0.16)\times10^{-3}$	52	52	$(3.91 \pm 0.62 \pm 0.13)\times10^{-4}$	35	48
32.66	$(4.65 \pm 0.19 \pm 0.13)\times10^{-3}$	50	51	$(4.68 \pm 0.62 \pm 0.16)\times10^{-4}$	31	49
34.43	$(3.91 \pm 0.17 \pm 0.11)\times10^{-3}$	47	54	$(2.78 \pm 0.47 \pm 0.09)\times10^{-4}$	38	46
36.32	$(3.04 \pm 0.15 \pm 0.09)\times10^{-3}$	56	59	$(2.32 \pm 0.45 \pm 0.09)\times10^{-4}$	42	56
38.62	$(2.57 \pm 0.12 \pm 0.07)\times10^{-3}$	53	54	$(2.50 \pm 0.38 \pm 0.08)\times10^{-4}$	32	48

TABLE B.6: Results for electron and positron flux in time interval: 17/Oct/2011 - 12/Nov/2011

Δt: **13/Nov/2011 - 09/Dec/2011**						
$\bar{E}$ (GeV)	$\Phi_{e-} \pm \sigma_{\text{stat}} \pm \sigma_{\text{sys}}$ (GeV^{-1} m^{-2} sr^{-1} s^{-1})	$\sigma^{\text{t}}_{\text{uc}}$ (%)	σ^{E}_{uc} (%)	$\Phi_{e+} \pm \sigma_{\text{stat}} \pm \sigma_{\text{sys}}$ (GeV^{-1} m^{-2} sr^{-1} s^{-1})	$\sigma^{\text{t}}_{\text{uc}}$ (%)	σ^{E}_{uc} (%)
0.57	$(4.64 \pm 0.29 \pm 0.50)\times10^{1}$	19	52	$(5.13 \pm 3.34 \pm 0.88)\times10^{0}$	12	84
0.73	$(3.53 \pm 0.13 \pm 0.29)\times10^{1}$	30	46	$(3.89 \pm 0.94 \pm 0.33)\times10^{0}$	29	51
0.91	$(2.87 \pm 0.07 \pm 0.17)\times10^{1}$	19	37	$(2.75 \pm 0.37 \pm 0.17)\times10^{0}$	18	42
1.11	$(2.53 \pm 0.04 \pm 0.12)\times10^{1}$	20	36	$(2.24 \pm 0.21 \pm 0.11)\times10^{0}$	19	44
1.33	$(2.17 \pm 0.03 \pm 0.09)\times10^{1}$	16	34	$(1.78 \pm 0.12 \pm 0.07)\times10^{0}$	15	36
1.58	$(1.73 \pm 0.02 \pm 0.06)\times10^{1}$	12	33	$(1.30 \pm 0.07 \pm 0.05)\times10^{0}$	15	36
1.85	$(1.34 \pm 0.01 \pm 0.04)\times10^{1}$	13	34	$(9.27 \pm 0.42 \pm 0.28)\times10^{-1}$	18	35
2.15	$(1.12 \pm 0.01 \pm 0.03)\times10^{1}$	15	33	$(7.27 \pm 0.29 \pm 0.19)\times10^{-1}$	18	37
2.47	$(8.41 \pm 0.07 \pm 0.20)\times10^{0}$	20	40	$(5.74 \pm 0.21 \pm 0.15)\times10^{-1}$	27	48
2.82	$(6.52 \pm 0.05 \pm 0.14)\times10^{0}$	25	41	$(4.27 \pm 0.16 \pm 0.10)\times10^{-1}$	31	41
3.17	$(5.24 \pm 0.04 \pm 0.12)\times10^{0}$	21	40	$(3.00 \pm 0.12 \pm 0.07)\times10^{-1}$	26	48
3.54	$(4.09 \pm 0.04 \pm 0.09)\times10^{0}$	29	39	$(2.47 \pm 0.10 \pm 0.06)\times10^{-1}$	34	40
3.92	$(3.25 \pm 0.03 \pm 0.08)\times10^{0}$	32	38	$(1.90 \pm 0.08 \pm 0.05)\times10^{-1}$	33	43
4.32	$(2.55 \pm 0.02 \pm 0.06)\times10^{0}$	33	38	$(1.39 \pm 0.06 \pm 0.03)\times10^{-1}$	36	43
4.76	$(1.96 \pm 0.02 \pm 0.05)\times10^{0}$	34	38	$(1.08 \pm 0.05 \pm 0.03)\times10^{-1}$	36	45
5.24	$(1.52 \pm 0.01 \pm 0.04)\times10^{0}$	37	38	$(8.62 \pm 0.37 \pm 0.22)\times10^{-2}$	38	41
5.74	$(1.19 \pm 0.01 \pm 0.03)\times10^{0}$	38	39	$(6.72 \pm 0.30 \pm 0.17)\times10^{-2}$	37	41
6.26	$(9.39 \pm 0.09 \pm 0.23)\times10^{-1}$	38	39	$(5.06 \pm 0.24 \pm 0.13)\times10^{-2}$	39	40
6.81	$(7.42 \pm 0.08 \pm 0.18)\times10^{-1}$	40	39	$(4.10 \pm 0.20 \pm 0.11)\times10^{-2}$	36	42
7.39	$(5.88 \pm 0.06 \pm 0.14)\times10^{-1}$	41	39	$(3.19 \pm 0.17 \pm 0.08)\times10^{-2}$	40	41
7.99	$(4.58 \pm 0.05 \pm 0.11)\times10^{-1}$	43	39	$(2.35 \pm 0.13 \pm 0.06)\times10^{-2}$	37	43
8.62	$(3.58 \pm 0.04 \pm 0.09)\times10^{-1}$	43	39	$(1.87 \pm 0.11 \pm 0.05)\times10^{-2}$	39	40
9.28	$(2.87 \pm 0.04 \pm 0.07)\times10^{-1}$	44	39	$(1.58 \pm 0.10 \pm 0.04)\times10^{-2}$	38	42
9.96	$(2.29 \pm 0.03 \pm 0.06)\times10^{-1}$	45	39	$(1.29 \pm 0.09 \pm 0.03)\times10^{-2}$	34	40
10.67	$(1.86 \pm 0.03 \pm 0.05)\times10^{-1}$	44	41	$(1.02 \pm 0.07 \pm 0.03)\times10^{-2}$	37	42
11.41	$(1.48 \pm 0.02 \pm 0.04)\times10^{-1}$	44	41	$(9.24 \pm 0.65 \pm 0.26)\times10^{-3}$	38	41
12.19	$(1.22 \pm 0.02 \pm 0.03)\times10^{-1}$	44	41	$(6.97 \pm 0.55 \pm 0.19)\times10^{-3}$	35	42
12.99	$(9.89 \pm 0.18 \pm 0.25)\times10^{-2}$	44	42	$(4.71 \pm 0.42 \pm 0.14)\times10^{-3}$	38	42
13.82	$(8.05 \pm 0.16 \pm 0.21)\times10^{-2}$	46	42	$(4.33 \pm 0.40 \pm 0.13)\times10^{-3}$	37	39
14.69	$(6.66 \pm 0.13 \pm 0.17)\times10^{-2}$	47	43	$(4.17 \pm 0.36 \pm 0.12)\times10^{-3}$	34	44
15.59	$(5.63 \pm 0.12 \pm 0.15)\times10^{-2}$	48	46	$(3.41 \pm 0.32 \pm 0.11)\times10^{-3}$	38	45
16.52	$(4.63 \pm 0.10 \pm 0.12)\times10^{-2}$	48	43	$(2.97 \pm 0.29 \pm 0.09)\times10^{-3}$	34	42
17.48	$(3.71 \pm 0.09 \pm 0.10)\times10^{-2}$	46	45	$(2.62 \pm 0.26 \pm 0.08)\times10^{-3}$	37	43
18.48	$(3.26 \pm 0.08 \pm 0.08)\times10^{-2}$	45	45	$(2.14 \pm 0.23 \pm 0.07)\times10^{-3}$	34	43
19.51	$(2.51 \pm 0.07 \pm 0.07)\times10^{-2}$	47	46	$(1.59 \pm 0.19 \pm 0.05)\times10^{-3}$	32	45
20.58	$(2.28 \pm 0.06 \pm 0.06)\times10^{-2}$	48	46	$(1.34 \pm 0.16 \pm 0.04)\times10^{-3}$	35	42
21.68	$(1.83 \pm 0.05 \pm 0.05)\times10^{-2}$	47	47	$(1.43 \pm 0.16 \pm 0.05)\times10^{-3}$	36	47
22.83	$(1.50 \pm 0.05 \pm 0.04)\times10^{-2}$	49	47	$(9.19 \pm 1.23 \pm 0.29)\times10^{-4}$	32	47
24.01	$(1.28 \pm 0.04 \pm 0.03)\times10^{-2}$	48	49	$(7.72 \pm 1.14 \pm 0.26)\times10^{-4}$	40	47
25.25	$(1.17 \pm 0.04 \pm 0.03)\times10^{-2}$	49	50	$(8.39 \pm 1.07 \pm 0.27)\times10^{-4}$	32	44
26.56	$(9.30 \pm 0.33 \pm 0.25)\times10^{-3}$	51	49	$(7.60 \pm 0.95 \pm 0.25)\times10^{-4}$	31	48
27.95	$(7.86 \pm 0.30 \pm 0.21)\times10^{-3}$	44	52	$(5.56 \pm 0.86 \pm 0.20)\times10^{-4}$	37	48
29.43	$(6.51 \pm 0.26 \pm 0.18)\times10^{-3}$	51	53	$(3.67 \pm 0.64 \pm 0.12)\times10^{-4}$	35	52
31.00	$(5.74 \pm 0.24 \pm 0.16)\times10^{-3}$	52	54	$(4.12 \pm 0.66 \pm 0.14)\times10^{-4}$	36	50
32.66	$(4.62 \pm 0.21 \pm 0.13)\times10^{-3}$	51	53	$(4.01 \pm 0.63 \pm 0.14)\times10^{-4}$	32	51
34.43	$(4.38 \pm 0.20 \pm 0.12)\times10^{-3}$	47	56	$(3.18 \pm 0.54 \pm 0.11)\times10^{-4}$	38	47
36.32	$(3.39 \pm 0.17 \pm 0.10)\times10^{-3}$	56	60	$(2.62 \pm 0.48 \pm 0.10)\times10^{-4}$	43	57
38.62	$(2.82 \pm 0.13 \pm 0.08)\times10^{-3}$	53	56	$(2.31 \pm 0.38 \pm 0.08)\times10^{-4}$	32	50

TABLE B.7: Results for electron and positron flux in time interval: 13/Nov/2011 - 09/Dec/2011

Δt: **10/Dec/2011 - 05/Jan/2012**						
$\bar{E}$ (GeV)	$\Phi_{e-} \pm \sigma_{\rm stat} \pm \sigma_{\rm sys}$ (GeV^{-1} m^{-2} sr^{-1} s^{-1})	$\sigma^{\rm t}_{\rm uc}$ (%)	$\sigma^{E}_{\rm uc}$ (%)	$\Phi_{e+} \pm \sigma_{\rm stat} \pm \sigma_{\rm sys}$ (GeV^{-1} m^{-2} sr^{-1} s^{-1})	$\sigma^{\rm t}_{\rm uc}$ (%)	$\sigma^{E}_{\rm uc}$ (%)
0.57	$(3.94 \pm 0.25 \pm 0.43)\times10^{1}$	20	52	$(4.05 \pm 2.01 \pm 0.69)\times10^{0}$	13	84
0.73	$(3.57 \pm 0.12 \pm 0.29)\times10^{1}$	28	44	$(3.27 \pm 0.86 \pm 0.28)\times10^{0}$	27	50
0.91	$(2.84 \pm 0.06 \pm 0.17)\times10^{1}$	19	37	$(3.50 \pm 0.38 \pm 0.22)\times10^{0}$	18	42
1.11	$(2.55 \pm 0.04 \pm 0.12)\times10^{1}$	20	36	$(2.11 \pm 0.20 \pm 0.11)\times10^{0}$	19	44
1.33	$(2.14 \pm 0.03 \pm 0.09)\times10^{1}$	16	34	$(1.76 \pm 0.12 \pm 0.07)\times10^{0}$	15	36
1.58	$(1.78 \pm 0.02 \pm 0.06)\times10^{1}$	12	33	$(1.30 \pm 0.07 \pm 0.05)\times10^{0}$	15	36
1.85	$(1.38 \pm 0.01 \pm 0.04)\times10^{1}$	13	34	$(9.84 \pm 0.43 \pm 0.30)\times10^{-1}$	18	35
2.15	$(1.08 \pm 0.01 \pm 0.03)\times10^{1}$	15	33	$(7.90 \pm 0.30 \pm 0.21)\times10^{-1}$	18	37
2.47	$(8.40 \pm 0.07 \pm 0.20)\times10^{0}$	20	40	$(5.91 \pm 0.21 \pm 0.15)\times10^{-1}$	27	47
2.82	$(6.53 \pm 0.05 \pm 0.14)\times10^{0}$	25	40	$(4.15 \pm 0.15 \pm 0.09)\times10^{-1}$	31	41
3.17	$(5.21 \pm 0.04 \pm 0.12)\times10^{0}$	21	39	$(3.34 \pm 0.12 \pm 0.08)\times10^{-1}$	26	48
3.54	$(4.05 \pm 0.03 \pm 0.09)\times10^{0}$	30	38	$(2.41 \pm 0.09 \pm 0.06)\times10^{-1}$	34	39
3.92	$(3.20 \pm 0.03 \pm 0.07)\times10^{0}$	32	37	$(1.87 \pm 0.08 \pm 0.05)\times10^{-1}$	33	43
4.32	$(2.54 \pm 0.02 \pm 0.06)\times10^{0}$	33	38	$(1.43 \pm 0.06 \pm 0.04)\times10^{-1}$	36	42
4.76	$(1.96 \pm 0.02 \pm 0.05)\times10^{0}$	34	37	$(1.09 \pm 0.05 \pm 0.03)\times10^{-1}$	36	45
5.24	$(1.53 \pm 0.01 \pm 0.04)\times10^{0}$	37	37	$(7.93 \pm 0.36 \pm 0.20)\times10^{-2}$	38	40
5.74	$(1.17 \pm 0.01 \pm 0.03)\times10^{0}$	38	38	$(6.49 \pm 0.29 \pm 0.16)\times10^{-2}$	37	40
6.26	$(9.27 \pm 0.09 \pm 0.22)\times10^{-1}$	38	38	$(4.55 \pm 0.22 \pm 0.12)\times10^{-2}$	39	39
6.81	$(7.16 \pm 0.07 \pm 0.17)\times10^{-1}$	40	38	$(3.85 \pm 0.19 \pm 0.10)\times10^{-2}$	36	41
7.39	$(5.77 \pm 0.06 \pm 0.14)\times10^{-1}$	41	38	$(3.21 \pm 0.16 \pm 0.08)\times10^{-2}$	40	40
7.99	$(4.53 \pm 0.05 \pm 0.11)\times10^{-1}$	43	38	$(2.42 \pm 0.14 \pm 0.06)\times10^{-2}$	37	43
8.62	$(3.56 \pm 0.04 \pm 0.09)\times10^{-1}$	43	38	$(2.08 \pm 0.11 \pm 0.06)\times10^{-2}$	39	40
9.28	$(2.90 \pm 0.04 \pm 0.07)\times10^{-1}$	44	39	$(1.58 \pm 0.10 \pm 0.04)\times10^{-2}$	38	41
9.96	$(2.27 \pm 0.03 \pm 0.06)\times10^{-1}$	45	39	$(1.37 \pm 0.08 \pm 0.04)\times10^{-2}$	34	39
10.67	$(1.83 \pm 0.03 \pm 0.05)\times10^{-1}$	44	40	$(1.30 \pm 0.08 \pm 0.04)\times10^{-2}$	37	42
11.41	$(1.50 \pm 0.02 \pm 0.04)\times10^{-1}$	44	40	$(7.95 \pm 0.59 \pm 0.23)\times10^{-3}$	38	41
12.19	$(1.22 \pm 0.02 \pm 0.03)\times10^{-1}$	44	40	$(6.88 \pm 0.53 \pm 0.19)\times10^{-3}$	35	41
12.99	$(9.89 \pm 0.17 \pm 0.25)\times10^{-2}$	44	42	$(5.60 \pm 0.44 \pm 0.16)\times10^{-3}$	38	41
13.82	$(8.20 \pm 0.15 \pm 0.21)\times10^{-2}$	46	42	$(4.65 \pm 0.39 \pm 0.13)\times10^{-3}$	37	38
14.69	$(6.62 \pm 0.13 \pm 0.17)\times10^{-2}$	47	42	$(3.83 \pm 0.34 \pm 0.11)\times10^{-3}$	34	44
15.59	$(5.62 \pm 0.12 \pm 0.15)\times10^{-2}$	48	45	$(2.93 \pm 0.29 \pm 0.09)\times10^{-3}$	38	45
16.52	$(4.51 \pm 0.10 \pm 0.12)\times10^{-2}$	48	43	$(2.47 \pm 0.26 \pm 0.07)\times10^{-3}$	34	41
17.48	$(3.77 \pm 0.09 \pm 0.10)\times10^{-2}$	47	44	$(2.50 \pm 0.25 \pm 0.08)\times10^{-3}$	37	43
18.48	$(3.14 \pm 0.08 \pm 0.08)\times10^{-2}$	46	45	$(2.03 \pm 0.22 \pm 0.06)\times10^{-3}$	35	42
19.51	$(2.51 \pm 0.07 \pm 0.07)\times10^{-2}$	47	45	$(1.59 \pm 0.18 \pm 0.05)\times10^{-3}$	32	44
20.58	$(2.25 \pm 0.06 \pm 0.06)\times10^{-2}$	48	45	$(1.84 \pm 0.18 \pm 0.06)\times10^{-3}$	34	41
21.68	$(1.75 \pm 0.05 \pm 0.05)\times10^{-2}$	47	47	$(1.02 \pm 0.14 \pm 0.03)\times10^{-3}$	36	46
22.83	$(1.59 \pm 0.05 \pm 0.04)\times10^{-2}$	48	47	$(1.25 \pm 0.14 \pm 0.04)\times10^{-3}$	32	46
24.01	$(1.29 \pm 0.04 \pm 0.03)\times10^{-2}$	48	49	$(8.51 \pm 1.16 \pm 0.29)\times10^{-4}$	39	47
25.25	$(1.11 \pm 0.04 \pm 0.03)\times10^{-2}$	50	50	$(8.91 \pm 1.12 \pm 0.29)\times10^{-4}$	32	43
26.56	$(9.01 \pm 0.32 \pm 0.24)\times10^{-3}$	51	48	$(7.73 \pm 0.95 \pm 0.25)\times10^{-4}$	31	48
27.95	$(7.95 \pm 0.29 \pm 0.21)\times10^{-3}$	44	51	$(6.38 \pm 0.89 \pm 0.22)\times10^{-4}$	37	48
29.43	$(6.87 \pm 0.26 \pm 0.19)\times10^{-3}$	51	52	$(5.87 \pm 0.83 \pm 0.20)\times10^{-4}$	34	51
31.00	$(5.64 \pm 0.23 \pm 0.16)\times10^{-3}$	52	54	$(5.17 \pm 0.73 \pm 0.18)\times10^{-4}$	35	49
32.66	$(4.94 \pm 0.21 \pm 0.14)\times10^{-3}$	50	52	$(4.29 \pm 0.62 \pm 0.15)\times10^{-4}$	31	50
34.43	$(3.93 \pm 0.18 \pm 0.11)\times10^{-3}$	48	56	$(4.12 \pm 0.61 \pm 0.14)\times10^{-4}$	39	47
36.32	$(3.01 \pm 0.15 \pm 0.09)\times10^{-3}$	58	61	$(3.55 \pm 0.57 \pm 0.13)\times10^{-4}$	44	57
38.62	$(2.83 \pm 0.13 \pm 0.08)\times10^{-3}$	52	55	$(2.34 \pm 0.38 \pm 0.08)\times10^{-4}$	31	49

TABLE B.8: Results for electron and positron flux in time interval: 10/Dec/2011 - 05/Jan/2012

Δt: **06/Jan/2012 - 01/Feb/2012**						
$\bar{E}$ (GeV)	$\Phi_{e-} \pm \sigma_{\rm stat} \pm \sigma_{\rm sys}$ (GeV^{-1} m^{-2} sr^{-1} s^{-1})	$\sigma^{\rm t}_{\rm uc}$ (%)	$\sigma^{E}_{\rm uc}$ (%)	$\Phi_{e+} \pm \sigma_{\rm stat} \pm \sigma_{\rm sys}$ (GeV^{-1} m^{-2} sr^{-1} s^{-1})	$\sigma^{\rm t}_{\rm uc}$ (%)	$\sigma^{E}_{\rm uc}$ (%)
0.57	$(4.09 \pm 0.27 \pm 0.44)\times10^{1}$	20	52	$(5.61 \pm 2.40 \pm 0.96)\times10^{0}$	13	84
0.73	$(3.18 \pm 0.12 \pm 0.26)\times10^{1}$	31	46	$(3.80 \pm 0.88 \pm 0.33)\times10^{0}$	30	52
0.91	$(2.74 \pm 0.06 \pm 0.17)\times10^{1}$	19	37	$(2.84 \pm 0.38 \pm 0.18)\times10^{0}$	18	42
1.11	$(2.49 \pm 0.04 \pm 0.12)\times10^{1}$	20	36	$(2.38 \pm 0.19 \pm 0.12)\times10^{0}$	19	44
1.33	$(2.05 \pm 0.03 \pm 0.09)\times10^{1}$	16	34	$(1.69 \pm 0.11 \pm 0.07)\times10^{0}$	15	36
1.58	$(1.66 \pm 0.02 \pm 0.06)\times10^{1}$	12	33	$(1.38 \pm 0.07 \pm 0.05)\times10^{0}$	15	36
1.85	$(1.32 \pm 0.01 \pm 0.04)\times10^{1}$	12	34	$(9.51 \pm 0.41 \pm 0.29)\times10^{-1}$	18	35
2.15	$(1.05 \pm 0.01 \pm 0.03)\times10^{1}$	15	33	$(7.61 \pm 0.28 \pm 0.20)\times10^{-1}$	18	37
2.47	$(8.28 \pm 0.07 \pm 0.20)\times10^{0}$	20	39	$(5.56 \pm 0.20 \pm 0.14)\times10^{-1}$	28	47
2.82	$(6.35 \pm 0.05 \pm 0.14)\times10^{0}$	25	39	$(4.12 \pm 0.15 \pm 0.09)\times10^{-1}$	31	40
3.17	$(5.03 \pm 0.04 \pm 0.11)\times10^{0}$	21	38	$(2.93 \pm 0.11 \pm 0.07)\times10^{-1}$	26	47
3.54	$(4.01 \pm 0.03 \pm 0.09)\times10^{0}$	30	38	$(2.40 \pm 0.09 \pm 0.06)\times10^{-1}$	34	38
3.92	$(3.14 \pm 0.03 \pm 0.07)\times10^{0}$	32	37	$(1.86 \pm 0.07 \pm 0.05)\times10^{-1}$	34	42
4.32	$(2.48 \pm 0.02 \pm 0.06)\times10^{0}$	33	37	$(1.34 \pm 0.06 \pm 0.03)\times10^{-1}$	36	42
4.76	$(1.94 \pm 0.02 \pm 0.05)\times10^{0}$	34	36	$(1.05 \pm 0.04 \pm 0.03)\times10^{-1}$	36	44
5.24	$(1.48 \pm 0.01 \pm 0.04)\times10^{0}$	37	36	$(8.29 \pm 0.35 \pm 0.21)\times10^{-2}$	38	39
5.74	$(1.17 \pm 0.01 \pm 0.03)\times10^{0}$	38	37	$(6.13 \pm 0.28 \pm 0.15)\times10^{-2}$	37	39
6.26	$(9.16 \pm 0.09 \pm 0.22)\times10^{-1}$	38	37	$(5.28 \pm 0.23 \pm 0.13)\times10^{-2}$	39	38
6.81	$(7.19 \pm 0.07 \pm 0.17)\times10^{-1}$	40	38	$(4.01 \pm 0.19 \pm 0.10)\times10^{-2}$	36	41
7.39	$(5.64 \pm 0.06 \pm 0.14)\times10^{-1}$	42	37	$(3.20 \pm 0.16 \pm 0.08)\times10^{-2}$	40	40
7.99	$(4.44 \pm 0.05 \pm 0.11)\times10^{-1}$	43	38	$(2.49 \pm 0.13 \pm 0.07)\times10^{-2}$	37	42
8.62	$(3.58 \pm 0.04 \pm 0.09)\times10^{-1}$	43	38	$(1.77 \pm 0.10 \pm 0.05)\times10^{-2}$	39	39
9.28	$(2.77 \pm 0.04 \pm 0.07)\times10^{-1}$	44	38	$(1.57 \pm 0.09 \pm 0.04)\times10^{-2}$	38	41
9.96	$(2.32 \pm 0.03 \pm 0.06)\times10^{-1}$	45	38	$(1.24 \pm 0.08 \pm 0.03)\times10^{-2}$	34	38
10.67	$(1.79 \pm 0.03 \pm 0.04)\times10^{-1}$	45	39	$(9.71 \pm 0.67 \pm 0.28)\times10^{-3}$	37	41
11.41	$(1.52 \pm 0.02 \pm 0.04)\times10^{-1}$	44	40	$(8.55 \pm 0.60 \pm 0.24)\times10^{-3}$	38	40
12.19	$(1.17 \pm 0.02 \pm 0.03)\times10^{-1}$	45	40	$(7.31 \pm 0.52 \pm 0.20)\times10^{-3}$	35	41
12.99	$(9.99 \pm 0.17 \pm 0.25)\times10^{-2}$	44	41	$(5.49 \pm 0.43 \pm 0.16)\times10^{-3}$	38	41
13.82	$(7.83 \pm 0.15 \pm 0.20)\times10^{-2}$	46	41	$(4.37 \pm 0.37 \pm 0.13)\times10^{-3}$	37	38
14.69	$(6.63 \pm 0.13 \pm 0.17)\times10^{-2}$	47	41	$(3.77 \pm 0.33 \pm 0.11)\times10^{-3}$	34	43
15.59	$(5.51 \pm 0.11 \pm 0.14)\times10^{-2}$	48	44	$(3.28 \pm 0.30 \pm 0.10)\times10^{-3}$	38	44
16.52	$(4.20 \pm 0.09 \pm 0.11)\times10^{-2}$	48	42	$(2.57 \pm 0.25 \pm 0.08)\times10^{-3}$	34	41
17.48	$(3.89 \pm 0.09 \pm 0.10)\times10^{-2}$	47	44	$(2.47 \pm 0.25 \pm 0.07)\times10^{-3}$	37	42
18.48	$(3.20 \pm 0.08 \pm 0.08)\times10^{-2}$	46	44	$(2.11 \pm 0.21 \pm 0.06)\times10^{-3}$	35	42
19.51	$(2.66 \pm 0.07 \pm 0.07)\times10^{-2}$	47	44	$(1.89 \pm 0.19 \pm 0.06)\times10^{-3}$	32	43
20.58	$(2.13 \pm 0.06 \pm 0.06)\times10^{-2}$	48	44	$(1.46 \pm 0.16 \pm 0.05)\times10^{-3}$	35	41
21.68	$(1.93 \pm 0.05 \pm 0.05)\times10^{-2}$	47	46	$(1.38 \pm 0.14 \pm 0.04)\times10^{-3}$	35	46
22.83	$(1.50 \pm 0.04 \pm 0.04)\times10^{-2}$	49	46	$(1.00 \pm 0.12 \pm 0.03)\times10^{-3}$	32	46
24.01	$(1.28 \pm 0.04 \pm 0.03)\times10^{-2}$	47	48	$(8.71 \pm 1.15 \pm 0.29)\times10^{-4}$	39	46
25.25	$(1.09 \pm 0.04 \pm 0.03)\times10^{-2}$	50	49	$(7.02 \pm 1.02 \pm 0.23)\times10^{-4}$	32	43
26.56	$(8.94 \pm 0.31 \pm 0.24)\times10^{-3}$	51	47	$(6.51 \pm 0.91 \pm 0.21)\times10^{-4}$	31	47
27.95	$(7.32 \pm 0.27 \pm 0.20)\times10^{-3}$	45	51	$(7.23 \pm 0.91 \pm 0.25)\times10^{-4}$	37	47
29.43	$(6.48 \pm 0.25 \pm 0.18)\times10^{-3}$	51	51	$(5.66 \pm 0.75 \pm 0.19)\times10^{-4}$	34	51
31.00	$(5.71 \pm 0.23 \pm 0.16)\times10^{-3}$	52	53	$(4.99 \pm 0.71 \pm 0.17)\times10^{-4}$	35	49
32.66	$(4.52 \pm 0.19 \pm 0.12)\times10^{-3}$	51	52	$(3.80 \pm 0.56 \pm 0.13)\times10^{-4}$	31	50
34.43	$(4.04 \pm 0.18 \pm 0.11)\times10^{-3}$	47	55	$(3.77 \pm 0.57 \pm 0.13)\times10^{-4}$	38	46
36.32	$(3.34 \pm 0.16 \pm 0.10)\times10^{-3}$	55	58	$(2.77 \pm 0.45 \pm 0.10)\times10^{-4}$	41	56
38.62	$(2.77 \pm 0.12 \pm 0.08)\times10^{-3}$	52	54	$(1.90 \pm 0.32 \pm 0.06)\times10^{-4}$	31	49

TABLE B.9: Results for electron and positron flux in time interval: 06/Jan/2012 - 01/Feb/2012

Δt: **02/Feb/2012 - 28/Feb/2012**						
$\bar{E}$ (GeV)	$\Phi_{e-} \pm \sigma_{\rm stat} \pm \sigma_{\rm sys}$ (GeV^{-1} m^{-2} sr^{-1} s^{-1})	$\sigma^{\rm t}_{\rm uc}$ (%)	$\sigma^{E}_{\rm uc}$ (%)	$\Phi_{e+} \pm \sigma_{\rm stat} \pm \sigma_{\rm sys}$ (GeV^{-1} m^{-2} sr^{-1} s^{-1})	$\sigma^{\rm t}_{\rm uc}$ (%)	$\sigma^{E}_{\rm uc}$ (%)
0.57	$(4.08 \pm 0.25 \pm 0.44)\times10^{1}$	19	52	$(6.36 \pm 2.53 \pm 1.09)\times10^{0}$	12	84
0.73	$(3.16 \pm 0.11 \pm 0.26)\times10^{1}$	31	46	$(3.55 \pm 0.74 \pm 0.30)\times10^{0}$	29	51
0.91	$(2.73 \pm 0.06 \pm 0.17)\times10^{1}$	19	37	$(2.09 \pm 0.34 \pm 0.13)\times10^{0}$	18	42
1.11	$(2.38 \pm 0.04 \pm 0.12)\times10^{1}$	20	36	$(2.27 \pm 0.19 \pm 0.12)\times10^{0}$	19	44
1.33	$(2.04 \pm 0.03 \pm 0.08)\times10^{1}$	16	34	$(1.76 \pm 0.11 \pm 0.07)\times10^{0}$	15	36
1.58	$(1.67 \pm 0.02 \pm 0.06)\times10^{1}$	12	33	$(1.31 \pm 0.07 \pm 0.05)\times10^{0}$	15	36
1.85	$(1.28 \pm 0.01 \pm 0.04)\times10^{1}$	13	34	$(8.88 \pm 0.41 \pm 0.27)\times10^{-1}$	18	35
2.15	$(1.04 \pm 0.01 \pm 0.03)\times10^{1}$	15	33	$(7.92 \pm 0.29 \pm 0.21)\times10^{-1}$	18	37
2.47	$(8.04 \pm 0.07 \pm 0.19)\times10^{0}$	20	41	$(5.32 \pm 0.20 \pm 0.14)\times10^{-1}$	27	48
2.82	$(6.07 \pm 0.05 \pm 0.13)\times10^{0}$	24	42	$(4.14 \pm 0.15 \pm 0.09)\times10^{-1}$	31	42
3.17	$(5.08 \pm 0.04 \pm 0.12)\times10^{0}$	21	40	$(3.18 \pm 0.12 \pm 0.08)\times10^{-1}$	26	49
3.54	$(3.95 \pm 0.03 \pm 0.09)\times10^{0}$	29	40	$(2.40 \pm 0.09 \pm 0.06)\times10^{-1}$	34	40
3.92	$(3.09 \pm 0.03 \pm 0.07)\times10^{0}$	32	39	$(1.69 \pm 0.07 \pm 0.04)\times10^{-1}$	33	44
4.32	$(2.41 \pm 0.02 \pm 0.06)\times10^{0}$	33	39	$(1.34 \pm 0.06 \pm 0.03)\times10^{-1}$	36	43
4.76	$(1.92 \pm 0.02 \pm 0.05)\times10^{0}$	34	38	$(1.02 \pm 0.04 \pm 0.03)\times10^{-1}$	36	45
5.24	$(1.47 \pm 0.01 \pm 0.03)\times10^{0}$	37	38	$(8.00 \pm 0.36 \pm 0.20)\times10^{-2}$	38	41
5.74	$(1.17 \pm 0.01 \pm 0.03)\times10^{0}$	38	39	$(5.77 \pm 0.27 \pm 0.15)\times10^{-2}$	37	41
6.26	$(9.03 \pm 0.09 \pm 0.22)\times10^{-1}$	38	39	$(4.53 \pm 0.22 \pm 0.12)\times10^{-2}$	39	39
6.81	$(7.13 \pm 0.07 \pm 0.17)\times10^{-1}$	40	39	$(3.90 \pm 0.19 \pm 0.10)\times10^{-2}$	36	42
7.39	$(5.63 \pm 0.06 \pm 0.14)\times10^{-1}$	41	38	$(3.10 \pm 0.15 \pm 0.08)\times10^{-2}$	40	41
7.99	$(4.45 \pm 0.05 \pm 0.11)\times10^{-1}$	43	38	$(2.42 \pm 0.13 \pm 0.06)\times10^{-2}$	37	43
8.62	$(3.59 \pm 0.04 \pm 0.09)\times10^{-1}$	43	38	$(1.93 \pm 0.11 \pm 0.05)\times10^{-2}$	39	40
9.28	$(2.80 \pm 0.04 \pm 0.07)\times10^{-1}$	44	39	$(1.58 \pm 0.10 \pm 0.04)\times10^{-2}$	38	41
9.96	$(2.21 \pm 0.03 \pm 0.06)\times10^{-1}$	45	38	$(1.41 \pm 0.08 \pm 0.04)\times10^{-2}$	34	39
10.67	$(1.81 \pm 0.03 \pm 0.05)\times10^{-1}$	45	40	$(1.05 \pm 0.07 \pm 0.03)\times10^{-2}$	37	41
11.41	$(1.47 \pm 0.02 \pm 0.04)\times10^{-1}$	44	40	$(7.50 \pm 0.57 \pm 0.21)\times10^{-3}$	38	40
12.19	$(1.20 \pm 0.02 \pm 0.03)\times10^{-1}$	45	40	$(6.13 \pm 0.50 \pm 0.17)\times10^{-3}$	35	41
12.99	$(9.84 \pm 0.17 \pm 0.25)\times10^{-2}$	44	41	$(5.70 \pm 0.45 \pm 0.16)\times10^{-3}$	38	41
13.82	$(8.27 \pm 0.15 \pm 0.21)\times10^{-2}$	46	41	$(4.25 \pm 0.37 \pm 0.12)\times10^{-3}$	37	37
14.69	$(6.48 \pm 0.13 \pm 0.17)\times10^{-2}$	47	41	$(3.61 \pm 0.34 \pm 0.10)\times10^{-3}$	35	43
15.59	$(5.35 \pm 0.11 \pm 0.14)\times10^{-2}$	48	44	$(3.10 \pm 0.30 \pm 0.10)\times10^{-3}$	38	44
16.52	$(4.39 \pm 0.10 \pm 0.11)\times10^{-2}$	48	41	$(3.06 \pm 0.28 \pm 0.09)\times10^{-3}$	34	40
17.48	$(3.62 \pm 0.09 \pm 0.09)\times10^{-2}$	47	43	$(2.34 \pm 0.23 \pm 0.07)\times10^{-3}$	38	42
18.48	$(2.95 \pm 0.08 \pm 0.08)\times10^{-2}$	46	43	$(1.64 \pm 0.19 \pm 0.05)\times10^{-3}$	35	41
19.51	$(2.57 \pm 0.07 \pm 0.07)\times10^{-2}$	48	44	$(1.60 \pm 0.19 \pm 0.05)\times10^{-3}$	32	43
20.58	$(2.17 \pm 0.06 \pm 0.06)\times10^{-2}$	49	44	$(1.06 \pm 0.14 \pm 0.03)\times10^{-3}$	35	40
21.68	$(1.78 \pm 0.05 \pm 0.05)\times10^{-2}$	47	45	$(1.33 \pm 0.15 \pm 0.04)\times10^{-3}$	36	45
22.83	$(1.46 \pm 0.05 \pm 0.04)\times10^{-2}$	49	45	$(1.25 \pm 0.14 \pm 0.04)\times10^{-3}$	32	45
24.01	$(1.31 \pm 0.04 \pm 0.03)\times10^{-2}$	48	47	$(1.01 \pm 0.13 \pm 0.03)\times10^{-3}$	40	46
25.25	$(1.13 \pm 0.04 \pm 0.03)\times10^{-2}$	50	48	$(8.90 \pm 1.09 \pm 0.29)\times10^{-4}$	32	42
26.56	$(9.35 \pm 0.33 \pm 0.25)\times10^{-3}$	51	46	$(7.20 \pm 0.96 \pm 0.23)\times10^{-4}$	31	47
27.95	$(8.33 \pm 0.30 \pm 0.22)\times10^{-3}$	45	49	$(5.29 \pm 0.79 \pm 0.18)\times10^{-4}$	37	46
29.43	$(6.85 \pm 0.26 \pm 0.18)\times10^{-3}$	51	50	$(6.55 \pm 0.85 \pm 0.22)\times10^{-4}$	34	50
31.00	$(5.55 \pm 0.23 \pm 0.15)\times10^{-3}$	53	52	$(3.71 \pm 0.62 \pm 0.13)\times10^{-4}$	36	48
32.66	$(4.49 \pm 0.20 \pm 0.12)\times10^{-3}$	52	51	$(5.33 \pm 0.73 \pm 0.18)\times10^{-4}$	32	49
34.43	$(4.26 \pm 0.19 \pm 0.12)\times10^{-3}$	48	54	$(2.67 \pm 0.50 \pm 0.09)\times10^{-4}$	38	45
36.32	$(3.16 \pm 0.16 \pm 0.09)\times10^{-3}$	58	59	$(2.30 \pm 0.44 \pm 0.09)\times10^{-4}$	44	56
38.62	$(2.82 \pm 0.13 \pm 0.08)\times10^{-3}$	53	53	$(2.60 \pm 0.42 \pm 0.08)\times10^{-4}$	32	47

TABLE B.10: Results for electron and positron flux in time interval: 02/Feb/2012 - 28/Feb/2012

Δt: **29/Feb/2012 - 26/Mar/2012**						
$\bar{E}$ (GeV)	$\Phi_{e-} \pm \sigma_{\text{stat}} \pm \sigma_{\text{sys}}$ ($\text{GeV}^{-1}\ \text{m}^{-2}\ \text{sr}^{-1}\ \text{s}^{-1}$)	$\sigma^{\text{t}}_{\text{uc}}$ (%)	σ^{E}_{uc} (%)	$\Phi_{e+} \pm \sigma_{\text{stat}} \pm \sigma_{\text{sys}}$ ($\text{GeV}^{-1}\ \text{m}^{-2}\ \text{sr}^{-1}\ \text{s}^{-1}$)	$\sigma^{\text{t}}_{\text{uc}}$ (%)	σ^{E}_{uc} (%)
0.57	$(3.33 \pm 0.23 \pm 0.36)\times10^{1}$	22	53	$(4.63 \pm 15.39 \pm 0.79)\times10^{-1}$	14	84
0.73	$(2.76 \pm 0.11 \pm 0.23)\times10^{1}$	34	48	$(3.36 \pm 0.79 \pm 0.29)\times10^{0}$	32	53
0.91	$(2.36 \pm 0.06 \pm 0.14)\times10^{1}$	19	37	$(2.58 \pm 0.34 \pm 0.16)\times10^{0}$	19	43
1.11	$(1.96 \pm 0.04 \pm 0.10)\times10^{1}$	20	36	$(1.96 \pm 0.17 \pm 0.10)\times10^{0}$	19	44
1.33	$(1.75 \pm 0.03 \pm 0.07)\times10^{1}$	16	34	$(1.42 \pm 0.10 \pm 0.06)\times10^{0}$	15	36
1.58	$(1.39 \pm 0.02 \pm 0.05)\times10^{1}$	13	34	$(1.08 \pm 0.06 \pm 0.04)\times10^{0}$	15	36
1.85	$(1.09 \pm 0.01 \pm 0.03)\times10^{1}$	13	34	$(7.32 \pm 0.37 \pm 0.22)\times10^{-1}$	18	35
2.15	$(8.99 \pm 0.08 \pm 0.23)\times10^{0}$	16	33	$(6.39 \pm 0.26 \pm 0.17)\times10^{-1}$	18	37
2.47	$(6.98 \pm 0.06 \pm 0.17)\times10^{0}$	20	40	$(4.64 \pm 0.18 \pm 0.12)\times10^{-1}$	27	47
2.82	$(5.52 \pm 0.05 \pm 0.12)\times10^{0}$	25	40	$(3.39 \pm 0.14 \pm 0.08)\times10^{-1}$	31	41
3.17	$(4.45 \pm 0.04 \pm 0.10)\times10^{0}$	21	39	$(2.59 \pm 0.11 \pm 0.06)\times10^{-1}$	26	48
3.54	$(3.46 \pm 0.03 \pm 0.08)\times10^{0}$	30	39	$(2.11 \pm 0.09 \pm 0.05)\times10^{-1}$	34	39
3.92	$(2.76 \pm 0.02 \pm 0.06)\times10^{0}$	32	38	$(1.61 \pm 0.07 \pm 0.04)\times10^{-1}$	33	43
4.32	$(2.18 \pm 0.02 \pm 0.05)\times10^{0}$	33	38	$(1.23 \pm 0.05 \pm 0.03)\times10^{-1}$	36	43
4.76	$(1.71 \pm 0.02 \pm 0.04)\times10^{0}$	34	38	$(9.65 \pm 0.41 \pm 0.25)\times10^{-2}$	36	45
5.24	$(1.36 \pm 0.01 \pm 0.03)\times10^{0}$	37	37	$(7.10 \pm 0.33 \pm 0.18)\times10^{-2}$	38	40
5.74	$(1.04 \pm 0.01 \pm 0.02)\times10^{0}$	38	38	$(5.94 \pm 0.27 \pm 0.15)\times10^{-2}$	37	40
6.26	$(8.42 \pm 0.08 \pm 0.20)\times10^{-1}$	38	39	$(3.80 \pm 0.20 \pm 0.10)\times10^{-2}$	39	39
6.81	$(6.69 \pm 0.07 \pm 0.16)\times10^{-1}$	40	39	$(4.02 \pm 0.18 \pm 0.10)\times10^{-2}$	36	42
7.39	$(5.31 \pm 0.06 \pm 0.13)\times10^{-1}$	41	38	$(2.61 \pm 0.14 \pm 0.07)\times10^{-2}$	40	41
7.99	$(4.18 \pm 0.05 \pm 0.10)\times10^{-1}$	43	39	$(2.12 \pm 0.12 \pm 0.06)\times10^{-2}$	37	43
8.62	$(3.37 \pm 0.04 \pm 0.08)\times10^{-1}$	43	39	$(1.65 \pm 0.10 \pm 0.04)\times10^{-2}$	39	40
9.28	$(2.68 \pm 0.03 \pm 0.07)\times10^{-1}$	44	39	$(1.43 \pm 0.09 \pm 0.04)\times10^{-2}$	38	42
9.96	$(2.13 \pm 0.03 \pm 0.05)\times10^{-1}$	45	39	$(1.23 \pm 0.08 \pm 0.03)\times10^{-2}$	34	39
10.67	$(1.74 \pm 0.03 \pm 0.04)\times10^{-1}$	44	40	$(9.29 \pm 0.64 \pm 0.27)\times10^{-3}$	37	42
11.41	$(1.40 \pm 0.02 \pm 0.04)\times10^{-1}$	44	41	$(8.65 \pm 0.58 \pm 0.25)\times10^{-3}$	38	41
12.19	$(1.14 \pm 0.02 \pm 0.03)\times10^{-1}$	44	41	$(6.33 \pm 0.48 \pm 0.17)\times10^{-3}$	35	42
12.99	$(9.42 \pm 0.16 \pm 0.24)\times10^{-2}$	44	42	$(6.13 \pm 0.45 \pm 0.18)\times10^{-3}$	38	41
13.82	$(7.69 \pm 0.14 \pm 0.20)\times10^{-2}$	46	42	$(4.92 \pm 0.39 \pm 0.14)\times10^{-3}$	37	38
14.69	$(6.22 \pm 0.12 \pm 0.16)\times10^{-2}$	47	42	$(4.51 \pm 0.36 \pm 0.13)\times10^{-3}$	34	44
15.59	$(5.27 \pm 0.11 \pm 0.14)\times10^{-2}$	47	45	$(2.98 \pm 0.28 \pm 0.09)\times10^{-3}$	38	45
16.52	$(4.47 \pm 0.10 \pm 0.12)\times10^{-2}$	48	43	$(2.71 \pm 0.26 \pm 0.08)\times10^{-3}$	34	41
17.48	$(3.58 \pm 0.08 \pm 0.09)\times10^{-2}$	46	44	$(1.86 \pm 0.20 \pm 0.06)\times10^{-3}$	37	43
18.48	$(2.92 \pm 0.07 \pm 0.08)\times10^{-2}$	46	45	$(2.26 \pm 0.21 \pm 0.07)\times10^{-3}$	35	42
19.51	$(2.54 \pm 0.06 \pm 0.07)\times10^{-2}$	47	45	$(1.72 \pm 0.18 \pm 0.05)\times10^{-3}$	32	44
20.58	$(2.08 \pm 0.06 \pm 0.05)\times10^{-2}$	48	45	$(1.71 \pm 0.17 \pm 0.05)\times10^{-3}$	34	41
21.68	$(1.80 \pm 0.05 \pm 0.05)\times10^{-2}$	47	46	$(1.05 \pm 0.12 \pm 0.03)\times10^{-3}$	35	46
22.83	$(1.48 \pm 0.04 \pm 0.04)\times10^{-2}$	48	46	$(1.15 \pm 0.13 \pm 0.04)\times10^{-3}$	32	46
24.01	$(1.24 \pm 0.04 \pm 0.03)\times10^{-2}$	47	48	$(9.77 \pm 1.17 \pm 0.33)\times10^{-4}$	39	47
25.25	$(1.11 \pm 0.04 \pm 0.03)\times10^{-2}$	49	49	$(7.37 \pm 0.91 \pm 0.24)\times10^{-4}$	31	43
26.56	$(9.46 \pm 0.31 \pm 0.26)\times10^{-3}$	51	47	$(8.41 \pm 1.01 \pm 0.27)\times10^{-4}$	30	47
27.95	$(8.12 \pm 0.28 \pm 0.22)\times10^{-3}$	44	51	$(6.94 \pm 0.88 \pm 0.24)\times10^{-4}$	36	47
29.43	$(6.35 \pm 0.24 \pm 0.17)\times10^{-3}$	51	51	$(5.07 \pm 0.70 \pm 0.17)\times10^{-4}$	34	51
31.00	$(5.48 \pm 0.22 \pm 0.15)\times10^{-3}$	52	53	$(2.61 \pm 0.46 \pm 0.09)\times10^{-4}$	35	49
32.66	$(4.80 \pm 0.20 \pm 0.13)\times10^{-3}$	50	51	$(2.30 \pm 0.44 \pm 0.08)\times10^{-4}$	30	50
34.43	$(3.91 \pm 0.17 \pm 0.11)\times10^{-3}$	47	55	$(3.39 \pm 0.51 \pm 0.11)\times10^{-4}$	38	46
36.32	$(3.24 \pm 0.15 \pm 0.09)\times10^{-3}$	55	58	$(2.44 \pm 0.44 \pm 0.09)\times10^{-4}$	41	56
38.62	$(2.68 \pm 0.12 \pm 0.08)\times10^{-3}$	52	54	$(2.18 \pm 0.36 \pm 0.07)\times10^{-4}$	31	49

TABLE B.11: Results for electron and positron flux in time interval: 29/Feb/2012 - 26/Mar/2012

Δt: **27/Mar/2012 - 22/Apr/2012**						
$\tilde{E}$ (GeV)	$\Phi_{e-} \pm \sigma_{\rm stat} \pm \sigma_{\rm sys}$ (GeV^{-1} m^{-2} sr^{-1} s^{-1})	$\sigma^{\rm t}_{\rm uc}$ (%)	$\sigma^{E}_{\rm uc}$ (%)	$\Phi_{e+} \pm \sigma_{\rm stat} \pm \sigma_{\rm sys}$ (GeV^{-1} m^{-2} sr^{-1} s^{-1})	$\sigma^{\rm t}_{\rm uc}$ (%)	$\sigma^{E}_{\rm uc}$ (%)
0.57	$(3.48 \pm 0.23 \pm 0.38)\times10^{1}$	21	52	$(8.33 \pm 24.64 \pm 1.42)\times10^{-1}$	13	84
0.73	$(2.92 \pm 0.11 \pm 0.24)\times10^{1}$	32	46	$(3.96 \pm 0.81 \pm 0.34)\times10^{0}$	30	52
0.91	$(2.47 \pm 0.06 \pm 0.15)\times10^{1}$	19	37	$(2.17 \pm 0.33 \pm 0.13)\times10^{0}$	18	42
1.11	$(2.17 \pm 0.04 \pm 0.11)\times10^{1}$	20	36	$(2.03 \pm 0.18 \pm 0.10)\times10^{0}$	19	44
1.33	$(1.83 \pm 0.03 \pm 0.08)\times10^{1}$	16	34	$(1.51 \pm 0.10 \pm 0.06)\times10^{0}$	15	36
1.58	$(1.51 \pm 0.02 \pm 0.05)\times10^{1}$	12	33	$(1.17 \pm 0.06 \pm 0.04)\times10^{0}$	15	36
1.85	$(1.20 \pm 0.01 \pm 0.04)\times10^{1}$	13	34	$(9.32 \pm 0.41 \pm 0.28)\times10^{-1}$	18	35
2.15	$(9.82 \pm 0.09 \pm 0.26)\times10^{0}$	15	33	$(6.78 \pm 0.27 \pm 0.18)\times10^{-1}$	18	37
2.47	$(7.73 \pm 0.06 \pm 0.19)\times10^{0}$	20	41	$(5.28 \pm 0.19 \pm 0.14)\times10^{-1}$	27	48
2.82	$(5.89 \pm 0.05 \pm 0.13)\times10^{0}$	24	41	$(3.55 \pm 0.14 \pm 0.08)\times10^{-1}$	31	42
3.17	$(4.98 \pm 0.04 \pm 0.11)\times10^{0}$	21	40	$(2.97 \pm 0.11 \pm 0.07)\times10^{-1}$	26	48
3.54	$(3.80 \pm 0.03 \pm 0.09)\times10^{0}$	29	40	$(2.37 \pm 0.09 \pm 0.06)\times10^{-1}$	34	40
3.92	$(3.03 \pm 0.03 \pm 0.07)\times10^{0}$	32	39	$(1.79 \pm 0.07 \pm 0.04)\times10^{-1}$	33	44
4.32	$(2.37 \pm 0.02 \pm 0.06)\times10^{0}$	33	39	$(1.42 \pm 0.06 \pm 0.04)\times10^{-1}$	36	43
4.76	$(1.87 \pm 0.02 \pm 0.04)\times10^{0}$	34	38	$(1.06 \pm 0.04 \pm 0.03)\times10^{-1}$	36	45
5.24	$(1.47 \pm 0.01 \pm 0.03)\times10^{0}$	37	38	$(8.24 \pm 0.35 \pm 0.21)\times10^{-2}$	38	40
5.74	$(1.15 \pm 0.01 \pm 0.03)\times10^{0}$	38	38	$(6.24 \pm 0.28 \pm 0.16)\times10^{-2}$	37	40
6.26	$(9.00 \pm 0.09 \pm 0.22)\times10^{-1}$	38	38	$(5.34 \pm 0.23 \pm 0.14)\times10^{-2}$	39	39
6.81	$(7.03 \pm 0.07 \pm 0.17)\times10^{-1}$	40	39	$(3.78 \pm 0.18 \pm 0.10)\times10^{-2}$	36	41
7.39	$(5.54 \pm 0.06 \pm 0.14)\times10^{-1}$	41	38	$(3.26 \pm 0.16 \pm 0.08)\times10^{-2}$	40	40
7.99	$(4.38 \pm 0.05 \pm 0.11)\times10^{-1}$	43	38	$(2.38 \pm 0.13 \pm 0.06)\times10^{-2}$	37	43
8.62	$(3.55 \pm 0.04 \pm 0.09)\times10^{-1}$	43	38	$(1.92 \pm 0.11 \pm 0.05)\times10^{-2}$	39	39
9.28	$(2.77 \pm 0.04 \pm 0.07)\times10^{-1}$	44	38	$(1.29 \pm 0.08 \pm 0.04)\times10^{-2}$	38	41
9.96	$(2.19 \pm 0.03 \pm 0.05)\times10^{-1}$	45	38	$(1.15 \pm 0.08 \pm 0.03)\times10^{-2}$	34	38
10.67	$(1.81 \pm 0.03 \pm 0.05)\times10^{-1}$	45	39	$(9.56 \pm 0.68 \pm 0.27)\times10^{-3}$	37	41
11.41	$(1.48 \pm 0.02 \pm 0.04)\times10^{-1}$	44	40	$(8.31 \pm 0.60 \pm 0.24)\times10^{-3}$	38	40
12.19	$(1.18 \pm 0.02 \pm 0.03)\times10^{-1}$	45	40	$(7.08 \pm 0.52 \pm 0.19)\times10^{-3}$	35	41
12.99	$(9.63 \pm 0.17 \pm 0.24)\times10^{-2}$	44	41	$(5.45 \pm 0.44 \pm 0.16)\times10^{-3}$	38	40
13.82	$(8.05 \pm 0.15 \pm 0.20)\times10^{-2}$	46	40	$(4.73 \pm 0.39 \pm 0.14)\times10^{-3}$	37	37
14.69	$(6.37 \pm 0.13 \pm 0.16)\times10^{-2}$	48	41	$(3.88 \pm 0.34 \pm 0.11)\times10^{-3}$	35	43
15.59	$(5.48 \pm 0.11 \pm 0.14)\times10^{-2}$	48	44	$(3.67 \pm 0.31 \pm 0.11)\times10^{-3}$	38	44
16.52	$(4.38 \pm 0.10 \pm 0.11)\times10^{-2}$	48	41	$(2.78 \pm 0.26 \pm 0.08)\times10^{-3}$	34	40
17.48	$(3.89 \pm 0.09 \pm 0.10)\times10^{-2}$	47	43	$(2.68 \pm 0.25 \pm 0.08)\times10^{-3}$	38	41
18.48	$(3.18 \pm 0.08 \pm 0.08)\times10^{-2}$	46	43	$(2.22 \pm 0.22 \pm 0.07)\times10^{-3}$	35	41
19.51	$(2.59 \pm 0.07 \pm 0.07)\times10^{-2}$	48	43	$(1.55 \pm 0.18 \pm 0.05)\times10^{-3}$	32	43
20.58	$(2.20 \pm 0.06 \pm 0.06)\times10^{-2}$	49	43	$(1.51 \pm 0.17 \pm 0.05)\times10^{-3}$	35	40
21.68	$(1.86 \pm 0.05 \pm 0.05)\times10^{-2}$	47	44	$(1.11 \pm 0.14 \pm 0.04)\times10^{-3}$	36	45
22.83	$(1.58 \pm 0.05 \pm 0.04)\times10^{-2}$	49	45	$(1.05 \pm 0.13 \pm 0.03)\times10^{-3}$	32	45
24.01	$(1.34 \pm 0.04 \pm 0.03)\times10^{-2}$	48	46	$(1.11 \pm 0.12 \pm 0.04)\times10^{-3}$	39	45
25.25	$(1.07 \pm 0.04 \pm 0.03)\times10^{-2}$	50	48	$(5.85 \pm 0.87 \pm 0.19)\times10^{-4}$	32	42
26.56	$(9.31 \pm 0.32 \pm 0.25)\times10^{-3}$	51	46	$(7.67 \pm 0.97 \pm 0.25)\times10^{-4}$	31	46
27.95	$(7.63 \pm 0.28 \pm 0.20)\times10^{-3}$	45	49	$(4.61 \pm 0.68 \pm 0.16)\times10^{-4}$	37	46
29.43	$(6.80 \pm 0.26 \pm 0.18)\times10^{-3}$	51	49	$(4.62 \pm 0.71 \pm 0.15)\times10^{-4}$	34	50
31.00	$(5.74 \pm 0.23 \pm 0.16)\times10^{-3}$	52	51	$(4.93 \pm 0.71 \pm 0.17)\times10^{-4}$	36	48
32.66	$(4.70 \pm 0.20 \pm 0.13)\times10^{-3}$	51	50	$(3.58 \pm 0.58 \pm 0.12)\times10^{-4}$	32	49
34.43	$(3.98 \pm 0.18 \pm 0.11)\times10^{-3}$	48	54	$(3.22 \pm 0.53 \pm 0.11)\times10^{-4}$	39	45
36.32	$(3.50 \pm 0.16 \pm 0.10)\times10^{-3}$	56	56	$(3.54 \pm 0.54 \pm 0.13)\times10^{-4}$	41	55
38.62	$(2.83 \pm 0.13 \pm 0.08)\times10^{-3}$	53	52	$(1.89 \pm 0.35 \pm 0.06)\times10^{-4}$	31	47

TABLE B.12: Results for electron and positron flux in time interval: 27/Mar/2012 - 22/Apr/2012

Δt: **23/Apr/2012 - 19/May/2012**						
$\bar{E}$ (GeV)	$\Phi_{e-} \pm \sigma_{\text{stat}} \pm \sigma_{\text{sys}}$ (GeV^{-1} m^{-2} sr^{-1} s^{-1})	$\sigma^{\text{t}}_{\text{uc}}$ (%)	σ^{E}_{uc} (%)	$\Phi_{e+} \pm \sigma_{\text{stat}} \pm \sigma_{\text{sys}}$ (GeV^{-1} m^{-2} sr^{-1} s^{-1})	$\sigma^{\text{t}}_{\text{uc}}$ (%)	σ^{E}_{uc} (%)
0.57	$(3.76 \pm 0.25 \pm 0.41)\times10^{1}$	21	52	$(2.41 \pm 1.65 \pm 0.41)\times10^{0}$	14	84
0.73	$(3.06 \pm 0.11 \pm 0.26)\times10^{1}$	32	47	$(3.04 \pm 0.89 \pm 0.26)\times10^{0}$	31	52
0.91	$(2.62 \pm 0.06 \pm 0.16)\times10^{1}$	19	37	$(2.36 \pm 0.32 \pm 0.15)\times10^{0}$	18	42
1.11	$(2.32 \pm 0.04 \pm 0.11)\times10^{1}$	20	37	$(1.81 \pm 0.18 \pm 0.09)\times10^{0}$	19	44
1.33	$(1.95 \pm 0.03 \pm 0.08)\times10^{1}$	16	34	$(1.55 \pm 0.10 \pm 0.06)\times10^{0}$	15	36
1.58	$(1.57 \pm 0.02 \pm 0.05)\times10^{1}$	12	33	$(1.12 \pm 0.06 \pm 0.04)\times10^{0}$	15	36
1.85	$(1.27 \pm 0.01 \pm 0.04)\times10^{1}$	13	34	$(8.56 \pm 0.38 \pm 0.26)\times10^{-1}$	18	35
2.15	$(1.02 \pm 0.01 \pm 0.03)\times10^{1}$	15	33	$(6.85 \pm 0.27 \pm 0.18)\times10^{-1}$	18	37
2.47	$(7.95 \pm 0.07 \pm 0.19)\times10^{0}$	20	39	$(4.95 \pm 0.19 \pm 0.13)\times10^{-1}$	28	47
2.82	$(6.17 \pm 0.05 \pm 0.13)\times10^{0}$	25	39	$(3.65 \pm 0.14 \pm 0.08)\times10^{-1}$	31	40
3.17	$(4.99 \pm 0.04 \pm 0.11)\times10^{0}$	21	38	$(3.10 \pm 0.11 \pm 0.08)\times10^{-1}$	26	47
3.54	$(3.86 \pm 0.03 \pm 0.09)\times10^{0}$	30	38	$(2.34 \pm 0.09 \pm 0.06)\times10^{-1}$	34	38
3.92	$(3.06 \pm 0.03 \pm 0.07)\times10^{0}$	32	37	$(1.74 \pm 0.07 \pm 0.04)\times10^{-1}$	34	42
4.32	$(2.43 \pm 0.02 \pm 0.06)\times10^{0}$	33	37	$(1.27 \pm 0.05 \pm 0.03)\times10^{-1}$	36	42
4.76	$(1.90 \pm 0.02 \pm 0.04)\times10^{0}$	34	37	$(1.07 \pm 0.04 \pm 0.03)\times10^{-1}$	36	45
5.24	$(1.47 \pm 0.01 \pm 0.03)\times10^{0}$	37	37	$(7.76 \pm 0.34 \pm 0.19)\times10^{-2}$	38	40
5.74	$(1.17 \pm 0.01 \pm 0.03)\times10^{0}$	38	38	$(6.55 \pm 0.28 \pm 0.17)\times10^{-2}$	37	40
6.26	$(9.17 \pm 0.09 \pm 0.22)\times10^{-1}$	38	38	$(4.56 \pm 0.21 \pm 0.12)\times10^{-2}$	39	39
6.81	$(7.16 \pm 0.07 \pm 0.17)\times10^{-1}$	40	38	$(3.68 \pm 0.18 \pm 0.10)\times10^{-2}$	36	41
7.39	$(5.69 \pm 0.06 \pm 0.14)\times10^{-1}$	41	38	$(3.13 \pm 0.15 \pm 0.08)\times10^{-2}$	40	40
7.99	$(4.46 \pm 0.05 \pm 0.11)\times10^{-1}$	43	38	$(2.58 \pm 0.13 \pm 0.07)\times10^{-2}$	37	43
8.62	$(3.58 \pm 0.04 \pm 0.09)\times10^{-1}$	43	39	$(1.87 \pm 0.10 \pm 0.05)\times10^{-2}$	39	40
9.28	$(2.79 \pm 0.04 \pm 0.07)\times10^{-1}$	44	39	$(1.58 \pm 0.09 \pm 0.04)\times10^{-2}$	38	42
9.96	$(2.30 \pm 0.03 \pm 0.06)\times10^{-1}$	45	39	$(1.30 \pm 0.08 \pm 0.03)\times10^{-2}$	34	39
10.67	$(1.88 \pm 0.03 \pm 0.05)\times10^{-1}$	44	41	$(1.11 \pm 0.07 \pm 0.03)\times10^{-2}$	37	42
11.41	$(1.48 \pm 0.02 \pm 0.04)\times10^{-1}$	44	41	$(8.50 \pm 0.59 \pm 0.24)\times10^{-3}$	38	41
12.19	$(1.21 \pm 0.02 \pm 0.03)\times10^{-1}$	44	41	$(6.46 \pm 0.49 \pm 0.18)\times10^{-3}$	35	42
12.99	$(9.86 \pm 0.17 \pm 0.25)\times10^{-2}$	44	42	$(5.20 \pm 0.42 \pm 0.15)\times10^{-3}$	38	42
13.82	$(7.87 \pm 0.15 \pm 0.20)\times10^{-2}$	46	42	$(4.86 \pm 0.40 \pm 0.14)\times10^{-3}$	37	39
14.69	$(6.70 \pm 0.13 \pm 0.17)\times10^{-2}$	47	43	$(4.04 \pm 0.34 \pm 0.11)\times10^{-3}$	34	44
15.59	$(5.50 \pm 0.11 \pm 0.14)\times10^{-2}$	47	46	$(3.51 \pm 0.31 \pm 0.11)\times10^{-3}$	38	45
16.52	$(4.53 \pm 0.10 \pm 0.12)\times10^{-2}$	47	43	$(2.40 \pm 0.24 \pm 0.07)\times10^{-3}$	34	42
17.48	$(3.83 \pm 0.09 \pm 0.10)\times10^{-2}$	46	45	$(2.31 \pm 0.23 \pm 0.07)\times10^{-3}$	37	43
18.48	$(3.14 \pm 0.08 \pm 0.08)\times10^{-2}$	45	46	$(1.80 \pm 0.19 \pm 0.06)\times10^{-3}$	34	43
19.51	$(2.59 \pm 0.07 \pm 0.07)\times10^{-2}$	47	46	$(1.62 \pm 0.18 \pm 0.05)\times10^{-3}$	32	45
20.58	$(2.24 \pm 0.06 \pm 0.06)\times10^{-2}$	48	46	$(1.68 \pm 0.17 \pm 0.05)\times10^{-3}$	34	42
21.68	$(1.85 \pm 0.05 \pm 0.05)\times10^{-2}$	46	47	$(1.15 \pm 0.14 \pm 0.04)\times10^{-3}$	35	47
22.83	$(1.49 \pm 0.04 \pm 0.04)\times10^{-2}$	48	48	$(1.09 \pm 0.13 \pm 0.03)\times10^{-3}$	32	47
24.01	$(1.33 \pm 0.04 \pm 0.04)\times10^{-2}$	47	49	$(7.12 \pm 1.04 \pm 0.24)\times10^{-4}$	39	47
25.25	$(1.10 \pm 0.04 \pm 0.03)\times10^{-2}$	49	50	$(7.59 \pm 1.00 \pm 0.25)\times10^{-4}$	32	44
26.56	$(9.33 \pm 0.32 \pm 0.25)\times10^{-3}$	50	49	$(6.46 \pm 0.88 \pm 0.21)\times10^{-4}$	30	49
27.95	$(8.24 \pm 0.29 \pm 0.22)\times10^{-3}$	44	52	$(4.94 \pm 0.72 \pm 0.17)\times10^{-4}$	36	48
29.43	$(7.21 \pm 0.26 \pm 0.20)\times10^{-3}$	50	52	$(6.06 \pm 0.79 \pm 0.20)\times10^{-4}$	33	52
31.00	$(5.55 \pm 0.22 \pm 0.16)\times10^{-3}$	51	54	$(4.96 \pm 0.69 \pm 0.17)\times10^{-4}$	35	50
32.66	$(4.39 \pm 0.19 \pm 0.12)\times10^{-3}$	51	54	$(4.23 \pm 0.65 \pm 0.15)\times10^{-4}$	32	51
34.43	$(4.16 \pm 0.18 \pm 0.12)\times10^{-3}$	46	56	$(3.96 \pm 0.58 \pm 0.14)\times10^{-4}$	38	48
36.32	$(3.44 \pm 0.16 \pm 0.10)\times10^{-3}$	54	59	$(2.79 \pm 0.47 \pm 0.10)\times10^{-4}$	41	56
38.62	$(2.81 \pm 0.12 \pm 0.08)\times10^{-3}$	52	56	$(2.66 \pm 0.40 \pm 0.09)\times10^{-4}$	31	50

TABLE B.13: Results for electron and positron flux in time interval: 23/Apr/2012 - 19/May/2012

Δt: **20/May/2012 - 15/Jun/2012**						
$\tilde{E}$ (GeV)	$\Phi_{e-} \pm \sigma_{\rm stat} \pm \sigma_{\rm sys}$ (GeV^{-1} m^{-2} sr^{-1} s^{-1})	$\sigma^{\rm t}_{\rm uc}$ (%)	$\sigma^{E}_{\rm uc}$ (%)	$\Phi_{e+} \pm \sigma_{\rm stat} \pm \sigma_{\rm sys}$ (GeV^{-1} m^{-2} sr^{-1} s^{-1})	$\sigma^{\rm t}_{\rm uc}$ (%)	$\sigma^{E}_{\rm uc}$ (%)
0.57	$(3.54 \pm 0.23 \pm 0.38)\times10^{1}$	21	52	$(3.48 \pm 1.71 \pm 0.60)\times10^{0}$	13	84
0.73	$(2.76 \pm 0.10 \pm 0.23)\times10^{1}$	32	47	$(1.43 \pm 0.77 \pm 0.12)\times10^{0}$	31	52
0.91	$(2.48 \pm 0.06 \pm 0.15)\times10^{1}$	19	37	$(2.45 \pm 0.32 \pm 0.15)\times10^{0}$	18	42
1.11	$(2.15 \pm 0.04 \pm 0.11)\times10^{1}$	20	36	$(2.00 \pm 0.17 \pm 0.10)\times10^{0}$	19	44
1.33	$(1.88 \pm 0.03 \pm 0.08)\times10^{1}$	16	34	$(1.50 \pm 0.10 \pm 0.06)\times10^{0}$	15	36
1.58	$(1.51 \pm 0.02 \pm 0.05)\times10^{1}$	12	33	$(1.23 \pm 0.06 \pm 0.04)\times10^{0}$	15	36
1.85	$(1.20 \pm 0.01 \pm 0.04)\times10^{1}$	13	34	$(9.02 \pm 0.39 \pm 0.27)\times10^{-1}$	18	35
2.15	$(9.79 \pm 0.06 \pm 0.26)\times10^{0}$	15	33	$(7.04 \pm 0.26 \pm 0.19)\times10^{-1}$	18	37
2.47	$(7.59 \pm 0.06 \pm 0.18)\times10^{0}$	20	40	$(5.12 \pm 0.19 \pm 0.13)\times10^{-1}$	27	48
2.82	$(5.86 \pm 0.05 \pm 0.13)\times10^{0}$	25	41	$(3.54 \pm 0.13 \pm 0.08)\times10^{-1}$	31	41
3.17	$(4.88 \pm 0.04 \pm 0.11)\times10^{0}$	21	40	$(3.12 \pm 0.11 \pm 0.08)\times10^{-1}$	26	48
3.54	$(3.83 \pm 0.03 \pm 0.09)\times10^{0}$	30	39	$(2.16 \pm 0.08 \pm 0.05)\times10^{-1}$	34	40
3.92	$(3.00 \pm 0.03 \pm 0.07)\times10^{0}$	32	38	$(1.68 \pm 0.07 \pm 0.04)\times10^{-1}$	33	43
4.32	$(2.36 \pm 0.02 \pm 0.06)\times10^{0}$	33	38	$(1.35 \pm 0.05 \pm 0.03)\times10^{-1}$	36	43
4.76	$(1.86 \pm 0.02 \pm 0.04)\times10^{0}$	34	37	$(9.85 \pm 0.41 \pm 0.25)\times10^{-2}$	36	45
5.24	$(1.43 \pm 0.01 \pm 0.03)\times10^{0}$	37	37	$(8.21 \pm 0.34 \pm 0.20)\times10^{-2}$	38	40
5.74	$(1.13 \pm 0.01 \pm 0.03)\times10^{0}$	38	38	$(6.13 \pm 0.27 \pm 0.16)\times10^{-2}$	37	40
6.26	$(8.86 \pm 0.08 \pm 0.21)\times10^{-1}$	38	38	$(4.97 \pm 0.22 \pm 0.13)\times10^{-2}$	39	39
6.81	$(7.01 \pm 0.07 \pm 0.17)\times10^{-1}$	40	38	$(4.06 \pm 0.18 \pm 0.11)\times10^{-2}$	36	41
7.39	$(5.58 \pm 0.06 \pm 0.14)\times10^{-1}$	41	38	$(2.81 \pm 0.14 \pm 0.07)\times10^{-2}$	40	40
7.99	$(4.44 \pm 0.05 \pm 0.11)\times10^{-1}$	43	38	$(2.41 \pm 0.13 \pm 0.06)\times10^{-2}$	37	43
8.62	$(3.56 \pm 0.04 \pm 0.09)\times10^{-1}$	43	38	$(1.88 \pm 0.10 \pm 0.05)\times10^{-2}$	39	40
9.28	$(2.80 \pm 0.03 \pm 0.07)\times10^{-1}$	44	38	$(1.52 \pm 0.09 \pm 0.04)\times10^{-2}$	38	41
9.96	$(2.21 \pm 0.03 \pm 0.06)\times10^{-1}$	45	38	$(1.31 \pm 0.08 \pm 0.03)\times10^{-2}$	34	39
10.67	$(1.82 \pm 0.03 \pm 0.05)\times10^{-1}$	44	40	$(1.17 \pm 0.07 \pm 0.03)\times10^{-2}$	37	41
11.41	$(1.53 \pm 0.02 \pm 0.04)\times10^{-1}$	44	40	$(7.83 \pm 0.56 \pm 0.22)\times10^{-3}$	38	40
12.19	$(1.19 \pm 0.02 \pm 0.03)\times10^{-1}$	44	40	$(6.79 \pm 0.51 \pm 0.19)\times10^{-3}$	35	41
12.99	$(9.79 \pm 0.17 \pm 0.25)\times10^{-2}$	44	41	$(6.35 \pm 0.46 \pm 0.18)\times10^{-3}$	38	41
13.82	$(8.26 \pm 0.15 \pm 0.21)\times10^{-2}$	46	41	$(5.16 \pm 0.40 \pm 0.15)\times10^{-3}$	37	38
14.69	$(6.51 \pm 0.13 \pm 0.17)\times10^{-2}$	47	41	$(3.88 \pm 0.34 \pm 0.11)\times10^{-3}$	34	43
15.59	$(5.53 \pm 0.11 \pm 0.14)\times10^{-2}$	47	44	$(3.49 \pm 0.30 \pm 0.11)\times10^{-3}$	38	44
16.52	$(4.47 \pm 0.10 \pm 0.12)\times10^{-2}$	48	42	$(2.90 \pm 0.27 \pm 0.09)\times10^{-3}$	34	41
17.48	$(3.73 \pm 0.09 \pm 0.10)\times10^{-2}$	47	44	$(2.54 \pm 0.24 \pm 0.08)\times10^{-3}$	38	42
18.48	$(3.11 \pm 0.07 \pm 0.08)\times10^{-2}$	46	44	$(2.24 \pm 0.22 \pm 0.07)\times10^{-3}$	35	42
19.51	$(2.68 \pm 0.07 \pm 0.07)\times10^{-2}$	47	44	$(1.76 \pm 0.19 \pm 0.05)\times10^{-3}$	32	43
20.58	$(2.16 \pm 0.06 \pm 0.06)\times10^{-2}$	48	44	$(1.44 \pm 0.16 \pm 0.05)\times10^{-3}$	35	40
21.68	$(1.91 \pm 0.05 \pm 0.05)\times10^{-2}$	47	45	$(1.23 \pm 0.14 \pm 0.04)\times10^{-3}$	35	46
22.83	$(1.60 \pm 0.05 \pm 0.04)\times10^{-2}$	49	46	$(1.13 \pm 0.13 \pm 0.04)\times10^{-3}$	32	45
24.01	$(1.37 \pm 0.04 \pm 0.04)\times10^{-2}$	47	47	$(1.08 \pm 0.12 \pm 0.04)\times10^{-3}$	39	46
25.25	$(1.12 \pm 0.04 \pm 0.03)\times10^{-2}$	49	48	$(9.56 \pm 1.10 \pm 0.31)\times10^{-4}$	32	42
26.56	$(9.58 \pm 0.32 \pm 0.26)\times10^{-3}$	51	47	$(7.62 \pm 0.97 \pm 0.25)\times10^{-4}$	31	47
27.95	$(7.90 \pm 0.28 \pm 0.21)\times10^{-3}$	44	50	$(5.49 \pm 0.76 \pm 0.19)\times10^{-4}$	37	47
29.43	$(6.84 \pm 0.25 \pm 0.18)\times10^{-3}$	51	50	$(5.15 \pm 0.75 \pm 0.17)\times10^{-4}$	34	51
31.00	$(5.64 \pm 0.22 \pm 0.16)\times10^{-3}$	52	52	$(5.08 \pm 0.69 \pm 0.17)\times10^{-4}$	35	48
32.66	$(4.65 \pm 0.20 \pm 0.13)\times10^{-3}$	51	51	$(3.26 \pm 0.54 \pm 0.11)\times10^{-4}$	31	49
34.43	$(3.76 \pm 0.17 \pm 0.10)\times10^{-3}$	48	55	$(3.34 \pm 0.53 \pm 0.11)\times10^{-4}$	39	46
36.32	$(3.50 \pm 0.16 \pm 0.10)\times10^{-3}$	55	57	$(3.05 \pm 0.50 \pm 0.11)\times10^{-4}$	41	55
38.62	$(2.90 \pm 0.12 \pm 0.08)\times10^{-3}$	52	53	$(2.42 \pm 0.37 \pm 0.08)\times10^{-4}$	30	48

TABLE B.14: Results for electron and positron flux in time interval: 20/May/2012 - 15/Jun/2012

Δt: **16/Jun/2012 - 12/Jul/2012**						
$\bar{E}$ (GeV)	$\Phi_{e-} \pm \sigma_{\text{stat}} \pm \sigma_{\text{sys}}$ (GeV^{-1} m^{-2} sr^{-1} s^{-1})	$\sigma^{\text{t}}_{\text{uc}}$ (%)	σ^{E}_{uc} (%)	$\Phi_{e+} \pm \sigma_{\text{stat}} \pm \sigma_{\text{sys}}$ (GeV^{-1} m^{-2} sr^{-1} s^{-1})	$\sigma^{\text{t}}_{\text{uc}}$ (%)	σ^{E}_{uc} (%)
0.57	$(3.20 \pm 0.21 \pm 0.35)\times10^{1}$	21	52	$(2.05 \pm 1.52 \pm 0.35)\times10^{0}$	13	84
0.73	$(2.54 \pm 0.10 \pm 0.21)\times10^{1}$	33	47	$(2.88 \pm 0.72 \pm 0.25)\times10^{0}$	32	52
0.91	$(2.41 \pm 0.05 \pm 0.15)\times10^{1}$	19	37	$(2.14 \pm 0.30 \pm 0.13)\times10^{0}$	18	42
1.11	$(2.05 \pm 0.04 \pm 0.10)\times10^{1}$	20	36	$(2.03 \pm 0.17 \pm 0.10)\times10^{0}$	19	44
1.33	$(1.77 \pm 0.02 \pm 0.07)\times10^{1}$	16	34	$(1.65 \pm 0.10 \pm 0.07)\times10^{0}$	15	36
1.58	$(1.45 \pm 0.02 \pm 0.05)\times10^{1}$	12	33	$(1.06 \pm 0.06 \pm 0.04)\times10^{0}$	15	36
1.85	$(1.17 \pm 0.01 \pm 0.04)\times10^{1}$	13	34	$(9.13 \pm 0.39 \pm 0.28)\times10^{-1}$	18	35
2.15	$(9.48 \pm 0.08 \pm 0.25)\times10^{0}$	15	33	$(6.44 \pm 0.25 \pm 0.17)\times10^{-1}$	18	37
2.47	$(7.43 \pm 0.06 \pm 0.18)\times10^{0}$	20	41	$(4.89 \pm 0.18 \pm 0.13)\times10^{-1}$	27	48
2.82	$(5.67 \pm 0.05 \pm 0.12)\times10^{0}$	24	42	$(3.36 \pm 0.13 \pm 0.08)\times10^{-1}$	31	43
3.17	$(4.68 \pm 0.04 \pm 0.11)\times10^{0}$	21	41	$(2.91 \pm 0.11 \pm 0.07)\times10^{-1}$	26	49
3.54	$(3.70 \pm 0.03 \pm 0.09)\times10^{0}$	29	40	$(2.29 \pm 0.09 \pm 0.06)\times10^{-1}$	34	41
3.92	$(2.96 \pm 0.03 \pm 0.07)\times10^{0}$	32	39	$(1.68 \pm 0.07 \pm 0.04)\times10^{-1}$	33	44
4.32	$(2.34 \pm 0.02 \pm 0.05)\times10^{0}$	33	39	$(1.29 \pm 0.05 \pm 0.03)\times10^{-1}$	36	44
4.76	$(1.84 \pm 0.02 \pm 0.04)\times10^{0}$	34	39	$(1.01 \pm 0.04 \pm 0.03)\times10^{-1}$	36	46
5.24	$(1.41 \pm 0.01 \pm 0.03)\times10^{0}$	36	38	$(7.65 \pm 0.34 \pm 0.19)\times10^{-2}$	38	41
5.74	$(1.12 \pm 0.01 \pm 0.03)\times10^{0}$	37	39	$(6.59 \pm 0.28 \pm 0.17)\times10^{-2}$	37	41
6.26	$(8.78 \pm 0.08 \pm 0.21)\times10^{-1}$	38	39	$(4.63 \pm 0.22 \pm 0.12)\times10^{-2}$	38	40
6.81	$(7.04 \pm 0.07 \pm 0.17)\times10^{-1}$	39	39	$(4.05 \pm 0.18 \pm 0.11)\times10^{-2}$	36	42
7.39	$(5.56 \pm 0.06 \pm 0.14)\times10^{-1}$	41	39	$(2.90 \pm 0.15 \pm 0.08)\times10^{-2}$	40	41
7.99	$(4.41 \pm 0.05 \pm 0.11)\times10^{-1}$	43	39	$(2.14 \pm 0.12 \pm 0.06)\times10^{-2}$	37	43
8.62	$(3.47 \pm 0.04 \pm 0.09)\times10^{-1}$	43	39	$(1.85 \pm 0.11 \pm 0.05)\times10^{-2}$	39	40
9.28	$(2.83 \pm 0.04 \pm 0.07)\times10^{-1}$	44	39	$(1.62 \pm 0.09 \pm 0.04)\times10^{-2}$	38	42
9.96	$(2.25 \pm 0.03 \pm 0.06)\times10^{-1}$	45	39	$(1.34 \pm 0.08 \pm 0.03)\times10^{-2}$	34	39
10.67	$(1.81 \pm 0.03 \pm 0.05)\times10^{-1}$	44	40	$(9.93 \pm 0.68 \pm 0.28)\times10^{-3}$	37	42
11.41	$(1.47 \pm 0.02 \pm 0.04)\times10^{-1}$	44	41	$(7.59 \pm 0.56 \pm 0.22)\times10^{-3}$	38	41
12.19	$(1.19 \pm 0.02 \pm 0.03)\times10^{-1}$	44	40	$(7.42 \pm 0.54 \pm 0.20)\times10^{-3}$	35	41
12.99	$(9.93 \pm 0.17 \pm 0.25)\times10^{-2}$	44	41	$(6.21 \pm 0.46 \pm 0.18)\times10^{-3}$	38	41
13.82	$(8.22 \pm 0.15 \pm 0.21)\times10^{-2}$	46	41	$(5.27 \pm 0.41 \pm 0.15)\times10^{-3}$	37	38
14.69	$(6.51 \pm 0.13 \pm 0.17)\times10^{-2}$	47	42	$(3.98 \pm 0.33 \pm 0.11)\times10^{-3}$	34	43
15.59	$(5.51 \pm 0.11 \pm 0.14)\times10^{-2}$	48	45	$(4.10 \pm 0.34 \pm 0.13)\times10^{-3}$	38	44
16.52	$(4.48 \pm 0.10 \pm 0.12)\times10^{-2}$	48	42	$(2.95 \pm 0.27 \pm 0.09)\times10^{-3}$	34	41
17.48	$(3.60 \pm 0.09 \pm 0.09)\times10^{-2}$	47	44	$(2.28 \pm 0.23 \pm 0.07)\times10^{-3}$	38	42
18.48	$(3.16 \pm 0.08 \pm 0.08)\times10^{-2}$	46	44	$(2.05 \pm 0.21 \pm 0.06)\times10^{-3}$	35	42
19.51	$(2.50 \pm 0.07 \pm 0.07)\times10^{-2}$	47	44	$(1.74 \pm 0.19 \pm 0.05)\times10^{-3}$	32	43
20.58	$(2.30 \pm 0.06 \pm 0.06)\times10^{-2}$	48	44	$(1.74 \pm 0.17 \pm 0.05)\times10^{-3}$	34	40
21.68	$(1.85 \pm 0.05 \pm 0.05)\times10^{-2}$	47	45	$(1.12 \pm 0.13 \pm 0.04)\times10^{-3}$	36	45
22.83	$(1.50 \pm 0.05 \pm 0.04)\times10^{-2}$	49	46	$(1.13 \pm 0.13 \pm 0.04)\times10^{-3}$	32	45
24.01	$(1.29 \pm 0.04 \pm 0.03)\times10^{-2}$	48	47	$(9.07 \pm 1.14 \pm 0.30)\times10^{-4}$	39	46
25.25	$(1.07 \pm 0.04 \pm 0.03)\times10^{-2}$	50	48	$(7.87 \pm 0.98 \pm 0.25)\times10^{-4}$	32	42
26.56	$(9.20 \pm 0.32 \pm 0.25)\times10^{-3}$	51	47	$(7.27 \pm 0.96 \pm 0.23)\times10^{-4}$	31	47
27.95	$(7.89 \pm 0.28 \pm 0.21)\times10^{-3}$	45	50	$(7.44 \pm 0.94 \pm 0.26)\times10^{-4}$	37	47
29.43	$(6.86 \pm 0.26 \pm 0.19)\times10^{-3}$	51	50	$(4.59 \pm 0.72 \pm 0.15)\times10^{-4}$	34	51
31.00	$(5.74 \pm 0.23 \pm 0.16)\times10^{-3}$	52	52	$(4.17 \pm 0.64 \pm 0.14)\times10^{-4}$	35	48
32.66	$(4.74 \pm 0.20 \pm 0.13)\times10^{-3}$	51	51	$(4.71 \pm 0.67 \pm 0.16)\times10^{-4}$	31	49
34.43	$(3.91 \pm 0.18 \pm 0.11)\times10^{-3}$	48	54	$(4.49 \pm 0.63 \pm 0.15)\times10^{-4}$	39	46
36.32	$(3.18 \pm 0.16 \pm 0.09)\times10^{-3}$	57	58	$(2.66 \pm 0.49 \pm 0.10)\times10^{-4}$	43	56
38.62	$(2.76 \pm 0.12 \pm 0.08)\times10^{-3}$	53	53	$(2.86 \pm 0.42 \pm 0.09)\times10^{-4}$	32	48

TABLE B.15: Results for electron and positron flux in time interval: 16/Jun/2012 - 12/Jul/2012

Δt: **13/Jul/2012 - 08/Aug/2012**						
$\tilde{E}$ (GeV)	$\Phi_{e-} \pm \sigma_{\rm stat} \pm \sigma_{\rm sys}$ (GeV^{-1} m^{-2} sr^{-1} s^{-1})	$\sigma^{\rm t}_{\rm uc}$ (%)	$\sigma^{E}_{\rm uc}$ (%)	$\Phi_{e+} \pm \sigma_{\rm stat} \pm \sigma_{\rm sys}$ (GeV^{-1} m^{-2} sr^{-1} s^{-1})	$\sigma^{\rm t}_{\rm uc}$ (%)	$\sigma^{E}_{\rm uc}$ (%)
0.57	$(2.86 \pm 0.21 \pm 0.31)\times10^{1}$	23	53	$(1.84 \pm 2.06 \pm 0.31)\times10^{0}$	15	84
0.73	$(2.22 \pm 0.09 \pm 0.19)\times10^{1}$	38	50	$(1.85 \pm 0.71 \pm 0.16)\times10^{0}$	36	55
0.91	$(2.04 \pm 0.05 \pm 0.12)\times10^{1}$	19	37	$(1.68 \pm 0.27 \pm 0.10)\times10^{0}$	19	43
1.11	$(1.81 \pm 0.03 \pm 0.09)\times10^{1}$	20	37	$(1.41 \pm 0.15 \pm 0.07)\times10^{0}$	19	44
1.33	$(1.54 \pm 0.02 \pm 0.06)\times10^{1}$	16	35	$(1.18 \pm 0.09 \pm 0.05)\times10^{0}$	15	36
1.58	$(1.27 \pm 0.02 \pm 0.04)\times10^{1}$	13	34	$(9.50 \pm 0.57 \pm 0.34)\times10^{-1}$	15	37
1.85	$(9.95 \pm 0.11 \pm 0.30)\times10^{0}$	13	34	$(6.94 \pm 0.36 \pm 0.21)\times10^{-1}$	18	35
2.15	$(8.18 \pm 0.08 \pm 0.21)\times10^{0}$	16	33	$(6.19 \pm 0.27 \pm 0.17)\times10^{-1}$	18	37
2.47	$(6.48 \pm 0.06 \pm 0.16)\times10^{0}$	20	39	$(4.14 \pm 0.18 \pm 0.11)\times10^{-1}$	28	47
2.82	$(5.12 \pm 0.05 \pm 0.11)\times10^{0}$	25	39	$(3.49 \pm 0.14 \pm 0.08)\times10^{-1}$	31	40
3.17	$(4.15 \pm 0.04 \pm 0.09)\times10^{0}$	21	38	$(2.33 \pm 0.10 \pm 0.06)\times10^{-1}$	26	47
3.54	$(3.39 \pm 0.03 \pm 0.08)\times10^{0}$	30	38	$(2.00 \pm 0.09 \pm 0.05)\times10^{-1}$	34	38
3.92	$(2.62 \pm 0.02 \pm 0.06)\times10^{0}$	32	37	$(1.54 \pm 0.07 \pm 0.04)\times10^{-1}$	34	42
4.32	$(2.11 \pm 0.02 \pm 0.05)\times10^{0}$	33	37	$(1.11 \pm 0.05 \pm 0.03)\times10^{-1}$	36	42
4.76	$(1.68 \pm 0.02 \pm 0.04)\times10^{0}$	34	36	$(9.63 \pm 0.42 \pm 0.24)\times10^{-2}$	36	44
5.24	$(1.33 \pm 0.01 \pm 0.03)\times10^{0}$	37	36	$(7.12 \pm 0.33 \pm 0.18)\times10^{-2}$	38	39
5.74	$(1.04 \pm 0.01 \pm 0.02)\times10^{0}$	38	37	$(5.56 \pm 0.27 \pm 0.14)\times10^{-2}$	37	39
6.26	$(8.31 \pm 0.09 \pm 0.20)\times10^{-1}$	38	37	$(4.21 \pm 0.22 \pm 0.11)\times10^{-2}$	39	38
6.81	$(6.39 \pm 0.07 \pm 0.15)\times10^{-1}$	40	37	$(3.41 \pm 0.18 \pm 0.09)\times10^{-2}$	36	40
7.39	$(5.24 \pm 0.06 \pm 0.13)\times10^{-1}$	42	37	$(2.66 \pm 0.14 \pm 0.07)\times10^{-2}$	40	39
7.99	$(4.11 \pm 0.05 \pm 0.10)\times10^{-1}$	43	37	$(2.10 \pm 0.12 \pm 0.06)\times10^{-2}$	37	42
8.62	$(3.33 \pm 0.04 \pm 0.08)\times10^{-1}$	43	37	$(1.88 \pm 0.11 \pm 0.05)\times10^{-2}$	39	39
9.28	$(2.75 \pm 0.04 \pm 0.07)\times10^{-1}$	44	38	$(1.36 \pm 0.09 \pm 0.04)\times10^{-2}$	38	41
9.96	$(2.13 \pm 0.03 \pm 0.05)\times10^{-1}$	45	37	$(1.25 \pm 0.08 \pm 0.03)\times10^{-2}$	34	38
10.67	$(1.82 \pm 0.03 \pm 0.05)\times10^{-1}$	45	39	$(8.43 \pm 0.65 \pm 0.24)\times10^{-3}$	38	41
11.41	$(1.45 \pm 0.02 \pm 0.04)\times10^{-1}$	45	39	$(7.61 \pm 0.58 \pm 0.22)\times10^{-3}$	39	40
12.19	$(1.16 \pm 0.02 \pm 0.03)\times10^{-1}$	45	39	$(5.76 \pm 0.48 \pm 0.16)\times10^{-3}$	35	40
12.99	$(9.66 \pm 0.17 \pm 0.24)\times10^{-2}$	44	40	$(5.39 \pm 0.45 \pm 0.16)\times10^{-3}$	38	40
13.82	$(8.00 \pm 0.15 \pm 0.20)\times10^{-2}$	46	40	$(4.33 \pm 0.39 \pm 0.12)\times10^{-3}$	37	37
14.69	$(6.26 \pm 0.13 \pm 0.16)\times10^{-2}$	48	41	$(3.68 \pm 0.35 \pm 0.10)\times10^{-3}$	35	43
15.59	$(5.56 \pm 0.12 \pm 0.14)\times10^{-2}$	48	44	$(3.21 \pm 0.30 \pm 0.10)\times10^{-3}$	38	44
16.52	$(4.31 \pm 0.10 \pm 0.11)\times10^{-2}$	48	41	$(2.96 \pm 0.28 \pm 0.09)\times10^{-3}$	34	40
17.48	$(3.60 \pm 0.09 \pm 0.09)\times10^{-2}$	47	43	$(2.08 \pm 0.23 \pm 0.06)\times10^{-3}$	38	42
18.48	$(3.04 \pm 0.08 \pm 0.08)\times10^{-2}$	46	43	$(1.90 \pm 0.21 \pm 0.06)\times10^{-3}$	35	41
19.51	$(2.57 \pm 0.07 \pm 0.07)\times10^{-2}$	48	44	$(1.52 \pm 0.17 \pm 0.05)\times10^{-3}$	33	43
20.58	$(2.14 \pm 0.06 \pm 0.06)\times10^{-2}$	49	44	$(1.32 \pm 0.16 \pm 0.04)\times10^{-3}$	35	40
21.68	$(1.85 \pm 0.05 \pm 0.05)\times10^{-2}$	47	45	$(1.12 \pm 0.14 \pm 0.04)\times10^{-3}$	36	45
22.83	$(1.58 \pm 0.05 \pm 0.04)\times10^{-2}$	49	45	$(9.96 \pm 1.21 \pm 0.31)\times10^{-4}$	32	45
24.01	$(1.29 \pm 0.04 \pm 0.03)\times10^{-2}$	48	47	$(8.85 \pm 1.15 \pm 0.30)\times10^{-4}$	40	46
25.25	$(1.17 \pm 0.04 \pm 0.03)\times10^{-2}$	50	48	$(8.87 \pm 1.06 \pm 0.29)\times10^{-4}$	32	42
26.56	$(8.99 \pm 0.32 \pm 0.24)\times10^{-3}$	52	47	$(8.42 \pm 1.05 \pm 0.27)\times10^{-4}$	31	47
27.95	$(8.10 \pm 0.30 \pm 0.21)\times10^{-3}$	45	50	$(4.53 \pm 0.73 \pm 0.16)\times10^{-4}$	37	47
29.43	$(6.54 \pm 0.26 \pm 0.18)\times10^{-3}$	52	51	$(5.16 \pm 0.78 \pm 0.17)\times10^{-4}$	35	51
31.00	$(5.47 \pm 0.23 \pm 0.15)\times10^{-3}$	53	53	$(4.66 \pm 0.67 \pm 0.16)\times10^{-4}$	36	49
32.66	$(4.54 \pm 0.20 \pm 0.12)\times10^{-3}$	52	52	$(4.13 \pm 0.66 \pm 0.14)\times10^{-4}$	32	50
34.43	$(3.89 \pm 0.18 \pm 0.11)\times10^{-3}$	49	55	$(3.03 \pm 0.56 \pm 0.10)\times10^{-4}$	39	47
36.32	$(3.22 \pm 0.16 \pm 0.09)\times10^{-3}$	58	59	$(2.64 \pm 0.45 \pm 0.10)\times10^{-4}$	44	56
38.62	$(2.69 \pm 0.13 \pm 0.08)\times10^{-3}$	54	54	$(2.07 \pm 0.36 \pm 0.07)\times10^{-4}$	33	49

TABLE B.16: Results for electron and positron flux in time interval: 13/Jul/2012 - 08/Aug/2012

Δt: **09/Aug/2012 - 04/Sep/2012**						
$\bar{E}$ (GeV)	$\Phi_{e-} \pm \sigma_{\text{stat}} \pm \sigma_{\text{sys}}$ (GeV^{-1} m^{-2} sr^{-1} s^{-1})	$\sigma^{\text{t}}_{\text{uc}}$ (%)	σ^{E}_{uc} (%)	$\Phi_{e+} \pm \sigma_{\text{stat}} \pm \sigma_{\text{sys}}$ (GeV^{-1} m^{-2} sr^{-1} s^{-1})	$\sigma^{\text{t}}_{\text{uc}}$ (%)	σ^{E}_{uc} (%)
0.57	$(2.28 \pm 0.17 \pm 0.25)\times10^{1}$	25	54	$(1.57 \pm 1.27 \pm 0.27)\times10^{0}$	16	84
0.73	$(2.10 \pm 0.09 \pm 0.18)\times10^{1}$	36	49	$(1.62 \pm 0.63 \pm 0.14)\times10^{0}$	35	54
0.91	$(2.02 \pm 0.05 \pm 0.12)\times10^{1}$	19	37	$(1.63 \pm 0.28 \pm 0.10)\times10^{0}$	18	42
1.11	$(1.62 \pm 0.03 \pm 0.08)\times10^{1}$	20	37	$(1.43 \pm 0.14 \pm 0.07)\times10^{0}$	19	44
1.33	$(1.47 \pm 0.02 \pm 0.06)\times10^{1}$	16	34	$(1.14 \pm 0.08 \pm 0.05)\times10^{0}$	15	36
1.58	$(1.18 \pm 0.01 \pm 0.04)\times10^{1}$	12	34	$(9.02 \pm 0.50 \pm 0.32)\times10^{-1}$	15	36
1.85	$(9.71 \pm 0.10 \pm 0.29)\times10^{0}$	13	34	$(7.60 \pm 0.34 \pm 0.23)\times10^{-1}$	18	35
2.15	$(7.98 \pm 0.07 \pm 0.21)\times10^{0}$	15	33	$(5.67 \pm 0.23 \pm 0.15)\times10^{-1}$	18	37
2.47	$(6.37 \pm 0.05 \pm 0.15)\times10^{0}$	20	39	$(4.28 \pm 0.16 \pm 0.11)\times10^{-1}$	28	47
2.82	$(4.96 \pm 0.04 \pm 0.11)\times10^{0}$	25	39	$(3.07 \pm 0.12 \pm 0.07)\times10^{-1}$	31	40
3.17	$(4.16 \pm 0.04 \pm 0.09)\times10^{0}$	21	38	$(2.54 \pm 0.10 \pm 0.06)\times10^{-1}$	26	47
3.54	$(3.36 \pm 0.03 \pm 0.08)\times10^{0}$	30	37	$(2.06 \pm 0.08 \pm 0.05)\times10^{-1}$	34	38
3.92	$(2.63 \pm 0.02 \pm 0.06)\times10^{0}$	32	36	$(1.46 \pm 0.06 \pm 0.04)\times10^{-1}$	34	42
4.32	$(2.12 \pm 0.02 \pm 0.05)\times10^{0}$	33	36	$(1.28 \pm 0.05 \pm 0.03)\times10^{-1}$	36	42
4.76	$(1.70 \pm 0.02 \pm 0.04)\times10^{0}$	34	36	$(9.77 \pm 0.40 \pm 0.25)\times10^{-2}$	36	44
5.24	$(1.35 \pm 0.01 \pm 0.03)\times10^{0}$	37	36	$(7.23 \pm 0.31 \pm 0.18)\times10^{-2}$	38	39
5.74	$(1.05 \pm 0.01 \pm 0.02)\times10^{0}$	38	37	$(5.28 \pm 0.25 \pm 0.13)\times10^{-2}$	37	39
6.26	$(8.51 \pm 0.08 \pm 0.20)\times10^{-1}$	38	37	$(4.37 \pm 0.20 \pm 0.11)\times10^{-2}$	39	38
6.81	$(6.69 \pm 0.07 \pm 0.16)\times10^{-1}$	40	37	$(3.48 \pm 0.17 \pm 0.09)\times10^{-2}$	36	41
7.39	$(5.52 \pm 0.06 \pm 0.13)\times10^{-1}$	42	37	$(2.90 \pm 0.15 \pm 0.08)\times10^{-2}$	40	40
7.99	$(4.30 \pm 0.05 \pm 0.11)\times10^{-1}$	43	37	$(2.46 \pm 0.12 \pm 0.07)\times10^{-2}$	37	42
8.62	$(3.41 \pm 0.04 \pm 0.08)\times10^{-1}$	43	38	$(1.97 \pm 0.10 \pm 0.05)\times10^{-2}$	39	39
9.28	$(2.84 \pm 0.03 \pm 0.07)\times10^{-1}$	44	38	$(1.49 \pm 0.09 \pm 0.04)\times10^{-2}$	38	41
9.96	$(2.20 \pm 0.03 \pm 0.05)\times10^{-1}$	45	38	$(1.25 \pm 0.08 \pm 0.03)\times10^{-2}$	34	38
10.67	$(1.81 \pm 0.03 \pm 0.05)\times10^{-1}$	45	39	$(1.09 \pm 0.07 \pm 0.03)\times10^{-2}$	37	41
11.41	$(1.47 \pm 0.02 \pm 0.04)\times10^{-1}$	44	40	$(8.85 \pm 0.59 \pm 0.25)\times10^{-3}$	38	40
12.19	$(1.16 \pm 0.02 \pm 0.03)\times10^{-1}$	44	40	$(6.62 \pm 0.49 \pm 0.18)\times10^{-3}$	35	41
12.99	$(9.85 \pm 0.17 \pm 0.25)\times10^{-2}$	44	41	$(5.60 \pm 0.44 \pm 0.16)\times10^{-3}$	38	41
13.82	$(7.95 \pm 0.14 \pm 0.20)\times10^{-2}$	46	41	$(4.83 \pm 0.38 \pm 0.14)\times10^{-3}$	37	38
14.69	$(6.73 \pm 0.13 \pm 0.17)\times10^{-2}$	47	42	$(3.32 \pm 0.31 \pm 0.09)\times10^{-3}$	34	43
15.59	$(5.37 \pm 0.11 \pm 0.14)\times10^{-2}$	47	45	$(3.22 \pm 0.30 \pm 0.10)\times10^{-3}$	38	44
16.52	$(4.46 \pm 0.10 \pm 0.12)\times10^{-2}$	48	42	$(3.12 \pm 0.28 \pm 0.09)\times10^{-3}$	34	41
17.48	$(3.62 \pm 0.08 \pm 0.09)\times10^{-2}$	47	44	$(2.37 \pm 0.24 \pm 0.07)\times10^{-3}$	37	42
18.48	$(3.10 \pm 0.07 \pm 0.08)\times10^{-2}$	46	44	$(2.27 \pm 0.22 \pm 0.07)\times10^{-3}$	34	42
19.51	$(2.61 \pm 0.07 \pm 0.07)\times10^{-2}$	47	45	$(1.44 \pm 0.16 \pm 0.04)\times10^{-3}$	32	44
20.58	$(2.11 \pm 0.06 \pm 0.06)\times10^{-2}$	48	45	$(1.40 \pm 0.15 \pm 0.04)\times10^{-3}$	34	41
21.68	$(1.89 \pm 0.05 \pm 0.05)\times10^{-2}$	47	46	$(1.46 \pm 0.15 \pm 0.05)\times10^{-3}$	35	46
22.83	$(1.48 \pm 0.04 \pm 0.04)\times10^{-2}$	48	47	$(1.13 \pm 0.12 \pm 0.04)\times10^{-3}$	32	46
24.01	$(1.27 \pm 0.04 \pm 0.03)\times10^{-2}$	47	48	$(1.00 \pm 0.12 \pm 0.03)\times10^{-3}$	39	47
25.25	$(1.16 \pm 0.04 \pm 0.03)\times10^{-2}$	49	49	$(9.07 \pm 1.06 \pm 0.29)\times10^{-4}$	31	43
26.56	$(8.99 \pm 0.31 \pm 0.24)\times10^{-3}$	51	48	$(6.22 \pm 0.85 \pm 0.20)\times10^{-4}$	31	48
27.95	$(7.84 \pm 0.28 \pm 0.21)\times10^{-3}$	44	51	$(6.64 \pm 0.86 \pm 0.23)\times10^{-4}$	36	47
29.43	$(6.39 \pm 0.24 \pm 0.17)\times10^{-3}$	51	52	$(4.89 \pm 0.72 \pm 0.16)\times10^{-4}$	34	52
31.00	$(5.97 \pm 0.23 \pm 0.17)\times10^{-3}$	51	53	$(4.98 \pm 0.66 \pm 0.17)\times10^{-4}$	35	49
32.66	$(4.56 \pm 0.19 \pm 0.13)\times10^{-3}$	50	52	$(5.22 \pm 0.71 \pm 0.18)\times10^{-4}$	31	50
34.43	$(3.98 \pm 0.18 \pm 0.11)\times10^{-3}$	47	55	$(2.35 \pm 0.43 \pm 0.08)\times10^{-4}$	38	47
36.32	$(3.62 \pm 0.16 \pm 0.10)\times10^{-3}$	54	57	$(3.07 \pm 0.50 \pm 0.11)\times10^{-4}$	40	55
38.62	$(2.79 \pm 0.12 \pm 0.08)\times10^{-3}$	52	55	$(2.14 \pm 0.35 \pm 0.07)\times10^{-4}$	31	49

TABLE B.17: Results for electron and positron flux in time interval: 09/Aug/2012 - 04/Sep/2012

Δt: **05/Sep/2012 - 01/Oct/2012**						
$\bar{E}$ (GeV)	$\Phi_{e-} \pm \sigma_{\rm stat} \pm \sigma_{\rm sys}$ (GeV^{-1} m^{-2} sr^{-1} s^{-1})	$\sigma^{\rm t}_{\rm uc}$ (%)	$\sigma^{E}_{\rm uc}$ (%)	$\Phi_{e+} \pm \sigma_{\rm stat} \pm \sigma_{\rm sys}$ (GeV^{-1} m^{-2} sr^{-1} s^{-1})	$\sigma^{\rm t}_{\rm uc}$ (%)	$\sigma^{E}_{\rm uc}$ (%)
0.57	$(2.20 \pm 0.17 \pm 0.24)\times10^{1}$	25	54	$(3.04 \pm 1.51 \pm 0.52)\times10^{0}$	16	84
0.73	$(2.08 \pm 0.08 \pm 0.18)\times10^{1}$	35	49	$(1.96 \pm 0.67 \pm 0.17)\times10^{0}$	34	54
0.91	$(1.90 \pm 0.05 \pm 0.12)\times10^{1}$	19	37	$(2.06 \pm 0.27 \pm 0.13)\times10^{0}$	19	43
1.11	$(1.74 \pm 0.03 \pm 0.09)\times10^{1}$	20	36	$(1.38 \pm 0.14 \pm 0.07)\times10^{0}$	19	44
1.33	$(1.48 \pm 0.02 \pm 0.06)\times10^{1}$	16	34	$(1.21 \pm 0.09 \pm 0.05)\times10^{0}$	15	36
1.58	$(1.21 \pm 0.01 \pm 0.04)\times10^{1}$	12	34	$(9.03 \pm 0.51 \pm 0.32)\times10^{-1}$	15	36
1.85	$(9.99 \pm 0.10 \pm 0.30)\times10^{0}$	13	34	$(7.25 \pm 0.33 \pm 0.22)\times10^{-1}$	18	35
2.15	$(8.27 \pm 0.07 \pm 0.22)\times10^{0}$	15	33	$(5.81 \pm 0.23 \pm 0.16)\times10^{-1}$	18	37
2.47	$(6.78 \pm 0.06 \pm 0.16)\times10^{0}$	20	40	$(4.33 \pm 0.16 \pm 0.11)\times10^{-1}$	27	47
2.82	$(5.24 \pm 0.04 \pm 0.11)\times10^{0}$	25	40	$(3.39 \pm 0.13 \pm 0.08)\times10^{-1}$	31	41
3.17	$(4.45 \pm 0.04 \pm 0.10)\times10^{0}$	21	39	$(2.64 \pm 0.10 \pm 0.06)\times10^{-1}$	26	48
3.54	$(3.53 \pm 0.03 \pm 0.08)\times10^{0}$	30	39	$(2.00 \pm 0.08 \pm 0.05)\times10^{-1}$	34	39
3.92	$(2.81 \pm 0.02 \pm 0.07)\times10^{0}$	32	38	$(1.65 \pm 0.06 \pm 0.04)\times10^{-1}$	33	43
4.32	$(2.21 \pm 0.02 \pm 0.05)\times10^{0}$	33	38	$(1.25 \pm 0.05 \pm 0.03)\times10^{-1}$	36	43
4.76	$(1.78 \pm 0.02 \pm 0.04)\times10^{0}$	34	37	$(1.02 \pm 0.04 \pm 0.03)\times10^{-1}$	36	45
5.24	$(1.41 \pm 0.01 \pm 0.03)\times10^{0}$	37	37	$(7.41 \pm 0.31 \pm 0.18)\times10^{-2}$	38	40
5.74	$(1.10 \pm 0.01 \pm 0.03)\times10^{0}$	38	38	$(5.63 \pm 0.25 \pm 0.14)\times10^{-2}$	37	40
6.26	$(8.87 \pm 0.08 \pm 0.21)\times10^{-1}$	38	38	$(4.76 \pm 0.21 \pm 0.12)\times10^{-2}$	39	39
6.81	$(6.98 \pm 0.07 \pm 0.17)\times10^{-1}$	40	38	$(3.63 \pm 0.17 \pm 0.09)\times10^{-2}$	36	41
7.39	$(5.52 \pm 0.06 \pm 0.13)\times10^{-1}$	41	38	$(2.92 \pm 0.14 \pm 0.08)\times10^{-2}$	40	40
7.99	$(4.45 \pm 0.05 \pm 0.11)\times10^{-1}$	43	38	$(2.59 \pm 0.13 \pm 0.07)\times10^{-2}$	37	43
8.62	$(3.52 \pm 0.04 \pm 0.09)\times10^{-1}$	43	38	$(2.02 \pm 0.10 \pm 0.05)\times10^{-2}$	39	40
9.28	$(2.80 \pm 0.03 \pm 0.07)\times10^{-1}$	44	39	$(1.60 \pm 0.09 \pm 0.04)\times10^{-2}$	38	42
9.96	$(2.33 \pm 0.03 \pm 0.06)\times10^{-1}$	45	39	$(1.28 \pm 0.07 \pm 0.03)\times10^{-2}$	34	39
10.67	$(1.78 \pm 0.02 \pm 0.04)\times10^{-1}$	44	40	$(1.08 \pm 0.07 \pm 0.03)\times10^{-2}$	37	42
11.41	$(1.48 \pm 0.02 \pm 0.04)\times10^{-1}$	44	41	$(8.39 \pm 0.57 \pm 0.24)\times10^{-3}$	38	41
12.19	$(1.21 \pm 0.02 \pm 0.03)\times10^{-1}$	44	41	$(6.54 \pm 0.47 \pm 0.18)\times10^{-3}$	35	41
12.99	$(9.66 \pm 0.16 \pm 0.24)\times10^{-2}$	44	42	$(5.84 \pm 0.43 \pm 0.17)\times10^{-3}$	38	41
13.82	$(8.16 \pm 0.14 \pm 0.21)\times10^{-2}$	46	42	$(4.90 \pm 0.37 \pm 0.14)\times10^{-3}$	37	38
14.69	$(6.56 \pm 0.12 \pm 0.17)\times10^{-2}$	47	42	$(3.42 \pm 0.31 \pm 0.10)\times10^{-3}$	34	43
15.59	$(5.55 \pm 0.11 \pm 0.14)\times10^{-2}$	47	45	$(2.97 \pm 0.27 \pm 0.09)\times10^{-3}$	38	44
16.52	$(4.48 \pm 0.09 \pm 0.12)\times10^{-2}$	48	42	$(3.12 \pm 0.27 \pm 0.09)\times10^{-3}$	34	41
17.48	$(3.86 \pm 0.08 \pm 0.10)\times10^{-2}$	46	44	$(2.43 \pm 0.22 \pm 0.07)\times10^{-3}$	37	42
18.48	$(3.23 \pm 0.07 \pm 0.08)\times10^{-2}$	45	44	$(1.93 \pm 0.19 \pm 0.06)\times10^{-3}$	34	42
19.51	$(2.68 \pm 0.06 \pm 0.07)\times10^{-2}$	47	45	$(1.71 \pm 0.17 \pm 0.05)\times10^{-3}$	32	44
20.58	$(2.11 \pm 0.06 \pm 0.06)\times10^{-2}$	48	45	$(1.76 \pm 0.17 \pm 0.06)\times10^{-3}$	34	41
21.68	$(1.89 \pm 0.05 \pm 0.05)\times10^{-2}$	47	46	$(1.26 \pm 0.15 \pm 0.04)\times10^{-3}$	35	46
22.83	$(1.55 \pm 0.04 \pm 0.04)\times10^{-2}$	48	46	$(1.08 \pm 0.12 \pm 0.03)\times10^{-3}$	32	46
24.01	$(1.32 \pm 0.04 \pm 0.03)\times10^{-2}$	47	48	$(1.14 \pm 0.13 \pm 0.04)\times10^{-3}$	39	46
25.25	$(1.12 \pm 0.04 \pm 0.03)\times10^{-2}$	49	49	$(8.86 \pm 1.06 \pm 0.29)\times10^{-4}$	31	43
26.56	$(8.95 \pm 0.30 \pm 0.24)\times10^{-3}$	51	48	$(6.62 \pm 0.88 \pm 0.21)\times10^{-4}$	31	48
27.95	$(7.63 \pm 0.27 \pm 0.20)\times10^{-3}$	44	51	$(6.43 \pm 0.83 \pm 0.22)\times10^{-4}$	36	47
29.43	$(6.63 \pm 0.24 \pm 0.18)\times10^{-3}$	50	51	$(4.66 \pm 0.68 \pm 0.16)\times10^{-4}$	33	51
31.00	$(5.45 \pm 0.22 \pm 0.15)\times10^{-3}$	52	53	$(4.65 \pm 0.66 \pm 0.16)\times10^{-4}$	35	49
32.66	$(4.95 \pm 0.20 \pm 0.14)\times10^{-3}$	50	51	$(3.02 \pm 0.53 \pm 0.10)\times10^{-4}$	30	49
34.43	$(3.88 \pm 0.17 \pm 0.11)\times10^{-3}$	47	55	$(2.47 \pm 0.44 \pm 0.08)\times10^{-4}$	38	47
36.32	$(3.14 \pm 0.15 \pm 0.09)\times10^{-3}$	55	58	$(2.41 \pm 0.41 \pm 0.09)\times10^{-4}$	42	56
38.62	$(2.89 \pm 0.12 \pm 0.08)\times10^{-3}$	52	54	$(1.68 \pm 0.30 \pm 0.06)\times10^{-4}$	30	48

TABLE B.18: Results for electron and positron flux in time interval: 05/Sep/2012 - 01/Oct/2012

Δt: **02/Oct/2012 - 28/Oct/2012**						
$\bar{E}$ (GeV)	$\Phi_{e-} \pm \sigma_{\text{stat}} \pm \sigma_{\text{sys}}$ (GeV^{-1} m^{-2} sr^{-1} s^{-1})	$\sigma^{\text{t}}_{\text{uc}}$ (%)	σ^{E}_{uc} (%)	$\Phi_{e+} \pm \sigma_{\text{stat}} \pm \sigma_{\text{sys}}$ (GeV^{-1} m^{-2} sr^{-1} s^{-1})	$\sigma^{\text{t}}_{\text{uc}}$ (%)	σ^{E}_{uc} (%)
0.57	$(2.42 \pm 0.18 \pm 0.27)\times10^{1}$	24	53	$(3.87 \pm 1.76 \pm 0.66)\times10^{0}$	16	84
0.73	$(2.07 \pm 0.09 \pm 0.18)\times10^{1}$	37	50	$(2.79 \pm 0.68 \pm 0.25)\times10^{0}$	36	55
0.91	$(1.77 \pm 0.05 \pm 0.11)\times10^{1}$	19	38	$(1.29 \pm 0.25 \pm 0.08)\times10^{0}$	19	43
1.11	$(1.65 \pm 0.03 \pm 0.08)\times10^{1}$	20	37	$(1.33 \pm 0.14 \pm 0.07)\times10^{0}$	19	44
1.33	$(1.47 \pm 0.02 \pm 0.06)\times10^{1}$	16	35	$(1.08 \pm 0.09 \pm 0.05)\times10^{0}$	15	36
1.58	$(1.19 \pm 0.02 \pm 0.04)\times10^{1}$	13	34	$(9.72 \pm 0.56 \pm 0.34)\times10^{-1}$	15	37
1.85	$(1.00 \pm 0.01 \pm 0.03)\times10^{1}$	13	34	$(6.36 \pm 0.34 \pm 0.19)\times10^{-1}$	18	35
2.15	$(8.21 \pm 0.08 \pm 0.21)\times10^{0}$	16	33	$(5.83 \pm 0.25 \pm 0.16)\times10^{-1}$	18	37
2.47	$(6.50 \pm 0.06 \pm 0.16)\times10^{0}$	20	43	$(4.21 \pm 0.17 \pm 0.11)\times10^{-1}$	27	49
2.82	$(5.27 \pm 0.05 \pm 0.12)\times10^{0}$	24	43	$(3.02 \pm 0.13 \pm 0.07)\times10^{-1}$	31	44
3.17	$(4.28 \pm 0.04 \pm 0.10)\times10^{0}$	20	42	$(2.74 \pm 0.11 \pm 0.07)\times10^{-1}$	26	50
3.54	$(3.45 \pm 0.03 \pm 0.08)\times10^{0}$	29	41	$(2.01 \pm 0.08 \pm 0.05)\times10^{-1}$	34	42
3.92	$(2.73 \pm 0.02 \pm 0.06)\times10^{0}$	31	40	$(1.58 \pm 0.07 \pm 0.04)\times10^{-1}$	33	45
4.32	$(2.20 \pm 0.02 \pm 0.05)\times10^{0}$	33	40	$(1.21 \pm 0.05 \pm 0.03)\times10^{-1}$	36	44
4.76	$(1.75 \pm 0.02 \pm 0.04)\times10^{0}$	34	40	$(9.69 \pm 0.41 \pm 0.25)\times10^{-2}$	36	46
5.24	$(1.40 \pm 0.01 \pm 0.03)\times10^{0}$	36	39	$(7.85 \pm 0.34 \pm 0.20)\times10^{-2}$	38	42
5.74	$(1.09 \pm 0.01 \pm 0.03)\times10^{0}$	37	40	$(6.04 \pm 0.27 \pm 0.15)\times10^{-2}$	37	42
6.26	$(8.54 \pm 0.08 \pm 0.21)\times10^{-1}$	38	40	$(4.47 \pm 0.21 \pm 0.11)\times10^{-2}$	38	40
6.81	$(6.90 \pm 0.07 \pm 0.17)\times10^{-1}$	39	40	$(3.92 \pm 0.18 \pm 0.10)\times10^{-2}$	36	42
7.39	$(5.42 \pm 0.06 \pm 0.13)\times10^{-1}$	41	39	$(3.00 \pm 0.15 \pm 0.08)\times10^{-2}$	40	41
7.99	$(4.36 \pm 0.05 \pm 0.11)\times10^{-1}$	43	39	$(2.44 \pm 0.13 \pm 0.06)\times10^{-2}$	37	43
8.62	$(3.43 \pm 0.04 \pm 0.08)\times10^{-1}$	43	39	$(2.11 \pm 0.11 \pm 0.06)\times10^{-2}$	39	40
9.28	$(2.83 \pm 0.04 \pm 0.07)\times10^{-1}$	44	39	$(1.44 \pm 0.09 \pm 0.04)\times10^{-2}$	38	42
9.96	$(2.28 \pm 0.03 \pm 0.06)\times10^{-1}$	45	39	$(1.10 \pm 0.07 \pm 0.03)\times10^{-2}$	34	39
10.67	$(1.78 \pm 0.03 \pm 0.04)\times10^{-1}$	44	40	$(1.07 \pm 0.07 \pm 0.03)\times10^{-2}$	37	42
11.41	$(1.50 \pm 0.02 \pm 0.04)\times10^{-1}$	44	40	$(8.01 \pm 0.58 \pm 0.23)\times10^{-3}$	38	40
12.19	$(1.18 \pm 0.02 \pm 0.03)\times10^{-1}$	44	40	$(6.75 \pm 0.50 \pm 0.18)\times10^{-3}$	35	41
12.99	$(9.76 \pm 0.17 \pm 0.25)\times10^{-2}$	44	41	$(5.32 \pm 0.42 \pm 0.15)\times10^{-3}$	38	41
13.82	$(8.20 \pm 0.15 \pm 0.21)\times10^{-2}$	46	41	$(4.99 \pm 0.39 \pm 0.14)\times10^{-3}$	37	37
14.69	$(6.54 \pm 0.13 \pm 0.17)\times10^{-2}$	47	41	$(4.00 \pm 0.33 \pm 0.11)\times10^{-3}$	34	43
15.59	$(5.32 \pm 0.11 \pm 0.14)\times10^{-2}$	48	44	$(4.16 \pm 0.33 \pm 0.13)\times10^{-3}$	38	44
16.52	$(4.54 \pm 0.10 \pm 0.12)\times10^{-2}$	48	41	$(2.54 \pm 0.25 \pm 0.07)\times10^{-3}$	34	40
17.48	$(3.73 \pm 0.09 \pm 0.10)\times10^{-2}$	47	43	$(2.44 \pm 0.24 \pm 0.07)\times10^{-3}$	38	41
18.48	$(3.32 \pm 0.08 \pm 0.09)\times10^{-2}$	46	43	$(2.35 \pm 0.22 \pm 0.07)\times10^{-3}$	35	41
19.51	$(2.63 \pm 0.07 \pm 0.07)\times10^{-2}$	48	43	$(2.07 \pm 0.20 \pm 0.06)\times10^{-3}$	32	43
20.58	$(2.17 \pm 0.06 \pm 0.06)\times10^{-2}$	49	43	$(1.45 \pm 0.16 \pm 0.05)\times10^{-3}$	35	40
21.68	$(1.80 \pm 0.05 \pm 0.05)\times10^{-2}$	47	44	$(1.43 \pm 0.15 \pm 0.05)\times10^{-3}$	36	45
22.83	$(1.49 \pm 0.04 \pm 0.04)\times10^{-2}$	49	45	$(1.10 \pm 0.12 \pm 0.03)\times10^{-3}$	32	45
24.01	$(1.32 \pm 0.04 \pm 0.03)\times10^{-2}$	48	46	$(7.84 \pm 1.01 \pm 0.26)\times10^{-4}$	39	45
25.25	$(1.12 \pm 0.04 \pm 0.03)\times10^{-2}$	50	47	$(7.65 \pm 1.00 \pm 0.25)\times10^{-4}$	32	41
26.56	$(9.19 \pm 0.31 \pm 0.25)\times10^{-3}$	51	45	$(7.87 \pm 0.95 \pm 0.25)\times10^{-4}$	31	46
27.95	$(8.17 \pm 0.28 \pm 0.21)\times10^{-3}$	45	49	$(6.54 \pm 0.82 \pm 0.23)\times10^{-4}$	37	46
29.43	$(6.76 \pm 0.25 \pm 0.18)\times10^{-3}$	51	49	$(5.04 \pm 0.71 \pm 0.17)\times10^{-4}$	34	50
31.00	$(5.92 \pm 0.23 \pm 0.16)\times10^{-3}$	52	51	$(3.85 \pm 0.63 \pm 0.13)\times10^{-4}$	35	47
32.66	$(4.98 \pm 0.20 \pm 0.13)\times10^{-3}$	51	49	$(4.61 \pm 0.63 \pm 0.16)\times10^{-4}$	31	48
34.43	$(3.93 \pm 0.18 \pm 0.11)\times10^{-3}$	48	53	$(3.35 \pm 0.57 \pm 0.11)\times10^{-4}$	39	45
36.32	$(3.50 \pm 0.16 \pm 0.10)\times10^{-3}$	55	56	$(1.45 \pm 0.31 \pm 0.05)\times10^{-4}$	41	54
38.62	$(3.03 \pm 0.13 \pm 0.08)\times10^{-3}$	52	51	$(3.23 \pm 0.43 \pm 0.10)\times10^{-4}$	30	46

TABLE B.19: Results for electron and positron flux in time interval: 02/Oct/2012 - 28/Oct/2012

Δt: **29/Oct/2012 - 24/Nov/2012**						
$\tilde{E}$ (GeV)	$\Phi_{e-} \pm \sigma_{\rm stat} \pm \sigma_{\rm sys}$ (GeV^{-1} m^{-2} sr^{-1} s^{-1})	$\sigma^{\rm t}_{\rm uc}$ (%)	$\sigma^{E}_{\rm uc}$ (%)	$\Phi_{e+} \pm \sigma_{\rm stat} \pm \sigma_{\rm sys}$ (GeV^{-1} m^{-2} sr^{-1} s^{-1})	$\sigma^{\rm t}_{\rm uc}$ (%)	$\sigma^{E}_{\rm uc}$ (%)
0.57	$(2.19 \pm 0.19 \pm 0.24)\times10^{1}$	29	55	$(5.29 \pm 14.72 \pm 0.91)\times10^{-1}$	19	84
0.73	$(2.06 \pm 0.09 \pm 0.18)\times10^{1}$	41	52	$(1.62 \pm 0.67 \pm 0.14)\times10^{0}$	40	57
0.91	$(1.91 \pm 0.05 \pm 0.12)\times10^{1}$	20	38	$(1.61 \pm 0.28 \pm 0.10)\times10^{0}$	19	43
1.11	$(1.77 \pm 0.03 \pm 0.09)\times10^{1}$	20	37	$(1.34 \pm 0.15 \pm 0.07)\times10^{0}$	19	44
1.33	$(1.47 \pm 0.02 \pm 0.06)\times10^{1}$	16	35	$(1.12 \pm 0.09 \pm 0.05)\times10^{0}$	15	36
1.58	$(1.23 \pm 0.02 \pm 0.04)\times10^{1}$	13	34	$(9.30 \pm 0.55 \pm 0.33)\times10^{-1}$	15	36
1.85	$(1.01 \pm 0.01 \pm 0.03)\times10^{1}$	13	34	$(6.94 \pm 0.35 \pm 0.21)\times10^{-1}$	18	35
2.15	$(8.40 \pm 0.08 \pm 0.22)\times10^{0}$	16	33	$(5.49 \pm 0.24 \pm 0.15)\times10^{-1}$	18	37
2.47	$(6.71 \pm 0.06 \pm 0.16)\times10^{0}$	20	42	$(4.60 \pm 0.18 \pm 0.12)\times10^{-1}$	27	49
2.82	$(5.30 \pm 0.05 \pm 0.12)\times10^{0}$	24	43	$(3.28 \pm 0.13 \pm 0.07)\times10^{-1}$	31	43
3.17	$(4.35 \pm 0.04 \pm 0.10)\times10^{0}$	21	42	$(2.65 \pm 0.10 \pm 0.06)\times10^{-1}$	26	49
3.54	$(3.51 \pm 0.03 \pm 0.08)\times10^{0}$	29	41	$(2.14 \pm 0.09 \pm 0.05)\times10^{-1}$	34	41
3.92	$(2.80 \pm 0.03 \pm 0.07)\times10^{0}$	32	40	$(1.57 \pm 0.07 \pm 0.04)\times10^{-1}$	33	45
4.32	$(2.21 \pm 0.02 \pm 0.05)\times10^{0}$	33	40	$(1.21 \pm 0.05 \pm 0.03)\times10^{-1}$	36	44
4.76	$(1.74 \pm 0.02 \pm 0.04)\times10^{0}$	34	40	$(10.00 \pm 0.43 \pm 0.26)\times10^{-2}$	36	46
5.24	$(1.38 \pm 0.01 \pm 0.03)\times10^{0}$	36	39	$(7.67 \pm 0.34 \pm 0.19)\times10^{-2}$	38	42
5.74	$(1.11 \pm 0.01 \pm 0.03)\times10^{0}$	37	40	$(6.04 \pm 0.27 \pm 0.15)\times10^{-2}$	37	42
6.26	$(8.65 \pm 0.09 \pm 0.21)\times10^{-1}$	38	40	$(4.68 \pm 0.22 \pm 0.12)\times10^{-2}$	38	41
6.81	$(6.99 \pm 0.07 \pm 0.17)\times10^{-1}$	39	40	$(3.51 \pm 0.18 \pm 0.09)\times10^{-2}$	36	43
7.39	$(5.51 \pm 0.06 \pm 0.14)\times10^{-1}$	41	40	$(2.55 \pm 0.14 \pm 0.07)\times10^{-2}$	40	42
7.99	$(4.22 \pm 0.05 \pm 0.10)\times10^{-1}$	43	40	$(2.51 \pm 0.13 \pm 0.07)\times10^{-2}$	37	44
8.62	$(3.47 \pm 0.04 \pm 0.09)\times10^{-1}$	42	40	$(1.91 \pm 0.11 \pm 0.05)\times10^{-2}$	39	41
9.28	$(2.76 \pm 0.04 \pm 0.07)\times10^{-1}$	44	40	$(1.47 \pm 0.09 \pm 0.04)\times10^{-2}$	38	43
9.96	$(2.21 \pm 0.03 \pm 0.06)\times10^{-1}$	45	40	$(1.37 \pm 0.08 \pm 0.04)\times10^{-2}$	34	40
10.67	$(1.80 \pm 0.03 \pm 0.05)\times10^{-1}$	44	41	$(9.45 \pm 0.65 \pm 0.27)\times10^{-3}$	37	42
11.41	$(1.47 \pm 0.02 \pm 0.04)\times10^{-1}$	44	42	$(7.34 \pm 0.55 \pm 0.21)\times10^{-3}$	38	42
12.19	$(1.18 \pm 0.02 \pm 0.03)\times10^{-1}$	44	42	$(7.01 \pm 0.52 \pm 0.19)\times10^{-3}$	35	42
12.99	$(9.43 \pm 0.17 \pm 0.24)\times10^{-2}$	44	43	$(5.14 \pm 0.42 \pm 0.15)\times10^{-3}$	38	42
13.82	$(7.85 \pm 0.15 \pm 0.20)\times10^{-2}$	46	43	$(4.62 \pm 0.40 \pm 0.13)\times10^{-3}$	37	39
14.69	$(6.72 \pm 0.13 \pm 0.17)\times10^{-2}$	47	43	$(3.64 \pm 0.34 \pm 0.10)\times10^{-3}$	34	44
15.59	$(5.34 \pm 0.11 \pm 0.14)\times10^{-2}$	48	46	$(3.63 \pm 0.32 \pm 0.11)\times10^{-3}$	38	45
16.52	$(4.56 \pm 0.10 \pm 0.12)\times10^{-2}$	48	43	$(2.68 \pm 0.26 \pm 0.08)\times10^{-3}$	34	42
17.48	$(3.74 \pm 0.09 \pm 0.10)\times10^{-2}$	46	45	$(1.99 \pm 0.22 \pm 0.06)\times10^{-3}$	37	43
18.48	$(3.07 \pm 0.08 \pm 0.08)\times10^{-2}$	45	45	$(1.79 \pm 0.20 \pm 0.06)\times10^{-3}$	35	42
19.51	$(2.65 \pm 0.07 \pm 0.07)\times10^{-2}$	47	45	$(1.66 \pm 0.19 \pm 0.05)\times10^{-3}$	32	44
20.58	$(2.16 \pm 0.06 \pm 0.06)\times10^{-2}$	48	45	$(1.38 \pm 0.16 \pm 0.04)\times10^{-3}$	35	41
21.68	$(1.90 \pm 0.05 \pm 0.05)\times10^{-2}$	47	46	$(1.26 \pm 0.14 \pm 0.04)\times10^{-3}$	35	46
22.83	$(1.51 \pm 0.05 \pm 0.04)\times10^{-2}$	49	47	$(1.16 \pm 0.14 \pm 0.04)\times10^{-3}$	32	46
24.01	$(1.31 \pm 0.04 \pm 0.03)\times10^{-2}$	47	48	$(8.91 \pm 1.13 \pm 0.30)\times10^{-4}$	39	47
25.25	$(1.04 \pm 0.04 \pm 0.03)\times10^{-2}$	50	50	$(1.11 \pm 0.12 \pm 0.04)\times10^{-3}$	33	44
26.56	$(9.05 \pm 0.32 \pm 0.25)\times10^{-3}$	51	48	$(5.50 \pm 0.80 \pm 0.18)\times10^{-4}$	31	48
27.95	$(8.25 \pm 0.29 \pm 0.22)\times10^{-3}$	44	51	$(6.75 \pm 0.86 \pm 0.24)\times10^{-4}$	37	47
29.43	$(6.69 \pm 0.26 \pm 0.18)\times10^{-3}$	51	51	$(4.92 \pm 0.78 \pm 0.16)\times10^{-4}$	34	51
31.00	$(5.47 \pm 0.23 \pm 0.15)\times10^{-3}$	52	54	$(3.25 \pm 0.60 \pm 0.11)\times10^{-4}$	36	49
32.66	$(4.77 \pm 0.21 \pm 0.13)\times10^{-3}$	51	52	$(2.97 \pm 0.52 \pm 0.10)\times10^{-4}$	31	50
34.43	$(3.95 \pm 0.18 \pm 0.11)\times10^{-3}$	48	55	$(3.35 \pm 0.51 \pm 0.11)\times10^{-4}$	39	47
36.32	$(3.48 \pm 0.17 \pm 0.10)\times10^{-3}$	56	58	$(2.41 \pm 0.46 \pm 0.09)\times10^{-4}$	42	56
38.62	$(2.63 \pm 0.12 \pm 0.07)\times10^{-3}$	53	55	$(2.31 \pm 0.38 \pm 0.08)\times10^{-4}$	33	49

TABLE B.20: Results for electron and positron flux in time interval: 29/Oct/2012 - 24/Nov/2012

Δt: **25/Nov/2012 - 21/Dec/2012**						
$\bar{E}$ (GeV)	$\Phi_{e-} \pm \sigma_{\text{stat}} \pm \sigma_{\text{sys}}$ (GeV^{-1} m^{-2} sr^{-1} s^{-1})	$\sigma^{\text{t}}_{\text{uc}}$ (%)	σ^{E}_{uc} (%)	$\Phi_{e+} \pm \sigma_{\text{stat}} \pm \sigma_{\text{sys}}$ (GeV^{-1} m^{-2} sr^{-1} s^{-1})	$\sigma^{\text{t}}_{\text{uc}}$ (%)	σ^{E}_{uc} (%)
0.57	$(2.13 \pm 0.17 \pm 0.23)\times10^{1}$	25	54	$(1.07 \pm 1.52 \pm 0.18)\times10^{0}$	16	84
0.73	$(2.00 \pm 0.08 \pm 0.17)\times10^{1}$	36	49	$(1.42 \pm 0.52 \pm 0.12)\times10^{0}$	35	54
0.91	$(1.79 \pm 0.04 \pm 0.11)\times10^{1}$	19	37	$(1.11 \pm 0.23 \pm 0.07)\times10^{0}$	19	42
1.11	$(1.59 \pm 0.03 \pm 0.08)\times10^{1}$	20	37	$(1.37 \pm 0.14 \pm 0.07)\times10^{0}$	19	44
1.33	$(1.39 \pm 0.02 \pm 0.06)\times10^{1}$	16	34	$(1.20 \pm 0.08 \pm 0.05)\times10^{0}$	15	36
1.58	$(1.18 \pm 0.01 \pm 0.04)\times10^{1}$	12	34	$(9.98 \pm 0.52 \pm 0.35)\times10^{-1}$	15	36
1.85	$(9.93 \pm 0.10 \pm 0.30)\times10^{0}$	13	34	$(7.48 \pm 0.32 \pm 0.23)\times10^{-1}$	18	35
2.15	$(8.29 \pm 0.07 \pm 0.22)\times10^{0}$	15	33	$(5.69 \pm 0.22 \pm 0.15)\times10^{-1}$	18	37
2.47	$(6.60 \pm 0.05 \pm 0.16)\times10^{0}$	20	41	$(4.04 \pm 0.16 \pm 0.10)\times10^{-1}$	27	48
2.82	$(5.25 \pm 0.04 \pm 0.12)\times10^{0}$	24	42	$(3.37 \pm 0.12 \pm 0.08)\times10^{-1}$	31	43
3.17	$(4.34 \pm 0.04 \pm 0.10)\times10^{0}$	21	41	$(2.56 \pm 0.10 \pm 0.06)\times10^{-1}$	26	49
3.54	$(3.50 \pm 0.03 \pm 0.08)\times10^{0}$	29	40	$(2.01 \pm 0.08 \pm 0.05)\times10^{-1}$	34	41
3.92	$(2.79 \pm 0.02 \pm 0.07)\times10^{0}$	32	39	$(1.59 \pm 0.06 \pm 0.04)\times10^{-1}$	33	44
4.32	$(2.24 \pm 0.02 \pm 0.05)\times10^{0}$	33	39	$(1.19 \pm 0.05 \pm 0.03)\times10^{-1}$	36	44
4.76	$(1.78 \pm 0.02 \pm 0.04)\times10^{0}$	34	39	$(9.63 \pm 0.39 \pm 0.25)\times10^{-2}$	36	46
5.24	$(1.39 \pm 0.01 \pm 0.03)\times10^{0}$	36	38	$(7.23 \pm 0.31 \pm 0.18)\times10^{-2}$	38	41
5.74	$(1.10 \pm 0.01 \pm 0.03)\times10^{0}$	37	39	$(5.55 \pm 0.25 \pm 0.14)\times10^{-2}$	37	41
6.26	$(8.75 \pm 0.08 \pm 0.21)\times10^{-1}$	38	39	$(4.38 \pm 0.20 \pm 0.11)\times10^{-2}$	38	40
6.81	$(7.00 \pm 0.07 \pm 0.17)\times10^{-1}$	39	39	$(3.69 \pm 0.17 \pm 0.10)\times10^{-2}$	36	42
7.39	$(5.50 \pm 0.06 \pm 0.13)\times10^{-1}$	41	39	$(2.98 \pm 0.14 \pm 0.08)\times10^{-2}$	40	41
7.99	$(4.50 \pm 0.05 \pm 0.11)\times10^{-1}$	43	39	$(2.33 \pm 0.12 \pm 0.06)\times10^{-2}$	37	43
8.62	$(3.52 \pm 0.04 \pm 0.09)\times10^{-1}$	43	39	$(1.92 \pm 0.10 \pm 0.05)\times10^{-2}$	39	40
9.28	$(2.80 \pm 0.03 \pm 0.07)\times10^{-1}$	44	39	$(1.55 \pm 0.09 \pm 0.04)\times10^{-2}$	38	42
9.96	$(2.30 \pm 0.03 \pm 0.06)\times10^{-1}$	45	39	$(1.17 \pm 0.07 \pm 0.03)\times10^{-2}$	34	39
10.67	$(1.85 \pm 0.03 \pm 0.05)\times10^{-1}$	44	40	$(9.87 \pm 0.64 \pm 0.28)\times10^{-3}$	37	42
11.41	$(1.43 \pm 0.02 \pm 0.04)\times10^{-1}$	44	40	$(7.59 \pm 0.53 \pm 0.22)\times10^{-3}$	38	41
12.19	$(1.21 \pm 0.02 \pm 0.03)\times10^{-1}$	44	40	$(7.18 \pm 0.50 \pm 0.20)\times10^{-3}$	35	41
12.99	$(9.70 \pm 0.16 \pm 0.25)\times10^{-2}$	44	41	$(5.71 \pm 0.42 \pm 0.17)\times10^{-3}$	38	41
13.82	$(8.32 \pm 0.15 \pm 0.21)\times10^{-2}$	46	41	$(4.89 \pm 0.39 \pm 0.14)\times10^{-3}$	37	38
14.69	$(6.62 \pm 0.12 \pm 0.17)\times10^{-2}$	47	41	$(3.86 \pm 0.31 \pm 0.11)\times10^{-3}$	34	43
15.59	$(5.54 \pm 0.11 \pm 0.14)\times10^{-2}$	47	44	$(3.36 \pm 0.29 \pm 0.10)\times10^{-3}$	38	44
16.52	$(4.50 \pm 0.09 \pm 0.12)\times10^{-2}$	48	42	$(3.07 \pm 0.26 \pm 0.09)\times10^{-3}$	34	41
17.48	$(3.84 \pm 0.08 \pm 0.10)\times10^{-2}$	47	43	$(2.21 \pm 0.21 \pm 0.07)\times10^{-3}$	37	42
18.48	$(3.08 \pm 0.07 \pm 0.08)\times10^{-2}$	46	44	$(2.22 \pm 0.21 \pm 0.07)\times10^{-3}$	35	41
19.51	$(2.56 \pm 0.06 \pm 0.07)\times10^{-2}$	47	44	$(2.12 \pm 0.19 \pm 0.06)\times10^{-3}$	32	43
20.58	$(2.17 \pm 0.06 \pm 0.06)\times10^{-2}$	48	44	$(1.45 \pm 0.15 \pm 0.05)\times10^{-3}$	34	40
21.68	$(1.83 \pm 0.05 \pm 0.05)\times10^{-2}$	47	45	$(1.15 \pm 0.13 \pm 0.04)\times10^{-3}$	35	45
22.83	$(1.47 \pm 0.04 \pm 0.04)\times10^{-2}$	49	45	$(1.11 \pm 0.13 \pm 0.03)\times10^{-3}$	32	45
24.01	$(1.28 \pm 0.04 \pm 0.03)\times10^{-2}$	47	47	$(8.01 \pm 1.03 \pm 0.27)\times10^{-4}$	39	46
25.25	$(1.13 \pm 0.04 \pm 0.03)\times10^{-2}$	49	48	$(8.04 \pm 0.98 \pm 0.26)\times10^{-4}$	31	42
26.56	$(9.37 \pm 0.31 \pm 0.25)\times10^{-3}$	51	46	$(7.16 \pm 0.89 \pm 0.23)\times10^{-4}$	31	47
27.95	$(8.02 \pm 0.28 \pm 0.21)\times10^{-3}$	44	50	$(6.50 \pm 0.83 \pm 0.23)\times10^{-4}$	37	46
29.43	$(6.57 \pm 0.24 \pm 0.18)\times10^{-3}$	51	50	$(5.44 \pm 0.72 \pm 0.18)\times10^{-4}$	34	50
31.00	$(5.93 \pm 0.22 \pm 0.16)\times10^{-3}$	52	52	$(5.07 \pm 0.67 \pm 0.17)\times10^{-4}$	35	48
32.66	$(4.47 \pm 0.19 \pm 0.12)\times10^{-3}$	51	51	$(4.47 \pm 0.64 \pm 0.15)\times10^{-4}$	31	49
34.43	$(3.91 \pm 0.17 \pm 0.11)\times10^{-3}$	47	54	$(3.34 \pm 0.51 \pm 0.11)\times10^{-4}$	38	45
36.32	$(3.49 \pm 0.16 \pm 0.10)\times10^{-3}$	54	56	$(2.42 \pm 0.45 \pm 0.09)\times10^{-4}$	40	54
38.62	$(2.98 \pm 0.12 \pm 0.08)\times10^{-3}$	52	52	$(2.59 \pm 0.37 \pm 0.08)\times10^{-4}$	30	47

TABLE B.21: Results for electron and positron flux in time interval: 25/Nov/2012 - 21/Dec/2012

Δt: **22/Dec/2012 - 17/Jan/2013**						
$\tilde{E}$ (GeV)	$\Phi_{e-} \pm \sigma_{\rm stat} \pm \sigma_{\rm sys}$ (GeV^{-1} m^{-2} sr^{-1} s^{-1})	$\sigma^{\rm t}_{\rm uc}$ (%)	$\sigma^{E}_{\rm uc}$ (%)	$\Phi_{e+} \pm \sigma_{\rm stat} \pm \sigma_{\rm sys}$ (GeV^{-1} m^{-2} sr^{-1} s^{-1})	$\sigma^{\rm t}_{\rm uc}$ (%)	$\sigma^{E}_{\rm uc}$ (%)
0.57	$(2.59 \pm 0.19 \pm 0.28)\times10^{1}$	23	53	$(1.60 \pm 1.75 \pm 0.27)\times10^{0}$	15	84
0.73	$(2.07 \pm 0.09 \pm 0.18)\times10^{1}$	37	50	$(2.08 \pm 0.58 \pm 0.18)\times10^{0}$	35	54
0.91	$(1.87 \pm 0.05 \pm 0.11)\times10^{1}$	19	37	$(1.58 \pm 0.25 \pm 0.10)\times10^{0}$	19	43
1.11	$(1.73 \pm 0.03 \pm 0.08)\times10^{1}$	20	37	$(1.49 \pm 0.14 \pm 0.08)\times10^{0}$	19	44
1.33	$(1.46 \pm 0.02 \pm 0.06)\times10^{1}$	16	34	$(1.18 \pm 0.08 \pm 0.05)\times10^{0}$	15	36
1.58	$(1.28 \pm 0.01 \pm 0.04)\times10^{1}$	12	33	$(9.35 \pm 0.50 \pm 0.33)\times10^{-1}$	15	36
1.85	$(1.04 \pm 0.01 \pm 0.03)\times10^{1}$	13	34	$(7.62 \pm 0.34 \pm 0.23)\times10^{-1}$	18	35
2.15	$(8.62 \pm 0.08 \pm 0.22)\times10^{0}$	15	33	$(6.10 \pm 0.23 \pm 0.16)\times10^{-1}$	18	37
2.47	$(7.04 \pm 0.06 \pm 0.17)\times10^{0}$	20	41	$(4.52 \pm 0.16 \pm 0.12)\times10^{-1}$	27	48
2.82	$(5.39 \pm 0.04 \pm 0.12)\times10^{0}$	25	41	$(3.38 \pm 0.12 \pm 0.08)\times10^{-1}$	31	42
3.17	$(4.54 \pm 0.04 \pm 0.10)\times10^{0}$	21	40	$(2.62 \pm 0.10 \pm 0.06)\times10^{-1}$	26	48
3.54	$(3.64 \pm 0.03 \pm 0.08)\times10^{0}$	29	39	$(2.23 \pm 0.08 \pm 0.05)\times10^{-1}$	34	40
3.92	$(2.97 \pm 0.02 \pm 0.07)\times10^{0}$	32	38	$(1.67 \pm 0.06 \pm 0.04)\times10^{-1}$	33	44
4.32	$(2.31 \pm 0.02 \pm 0.05)\times10^{0}$	33	38	$(1.34 \pm 0.05 \pm 0.03)\times10^{-1}$	36	43
4.76	$(1.87 \pm 0.02 \pm 0.04)\times10^{0}$	34	38	$(9.83 \pm 0.40 \pm 0.25)\times10^{-2}$	36	45
5.24	$(1.45 \pm 0.01 \pm 0.03)\times10^{0}$	37	38	$(7.81 \pm 0.32 \pm 0.19)\times10^{-2}$	38	40
5.74	$(1.14 \pm 0.01 \pm 0.03)\times10^{0}$	38	38	$(5.93 \pm 0.25 \pm 0.15)\times10^{-2}$	37	40
6.26	$(8.93 \pm 0.08 \pm 0.21)\times10^{-1}$	38	38	$(4.82 \pm 0.21 \pm 0.12)\times10^{-2}$	39	39
6.81	$(7.16 \pm 0.07 \pm 0.17)\times10^{-1}$	40	38	$(4.02 \pm 0.18 \pm 0.10)\times10^{-2}$	36	41
7.39	$(5.72 \pm 0.06 \pm 0.14)\times10^{-1}$	41	38	$(3.13 \pm 0.15 \pm 0.08)\times10^{-2}$	40	40
7.99	$(4.53 \pm 0.05 \pm 0.11)\times10^{-1}$	43	38	$(2.14 \pm 0.11 \pm 0.06)\times10^{-2}$	37	43
8.62	$(3.53 \pm 0.04 \pm 0.09)\times10^{-1}$	43	38	$(1.99 \pm 0.10 \pm 0.05)\times10^{-2}$	39	39
9.28	$(2.84 \pm 0.03 \pm 0.07)\times10^{-1}$	44	38	$(1.53 \pm 0.09 \pm 0.04)\times10^{-2}$	38	41
9.96	$(2.29 \pm 0.03 \pm 0.06)\times10^{-1}$	45	38	$(1.35 \pm 0.08 \pm 0.04)\times10^{-2}$	34	38
10.67	$(1.84 \pm 0.03 \pm 0.05)\times10^{-1}$	45	39	$(1.01 \pm 0.06 \pm 0.03)\times10^{-2}$	37	41
11.41	$(1.50 \pm 0.02 \pm 0.04)\times10^{-1}$	44	39	$(8.90 \pm 0.57 \pm 0.25)\times10^{-3}$	38	40
12.19	$(1.21 \pm 0.02 \pm 0.03)\times10^{-1}$	45	39	$(6.42 \pm 0.47 \pm 0.18)\times10^{-3}$	35	40
12.99	$(1.02 \pm 0.02 \pm 0.03)\times10^{-1}$	44	40	$(6.26 \pm 0.45 \pm 0.18)\times10^{-3}$	38	40
13.82	$(8.04 \pm 0.14 \pm 0.20)\times10^{-2}$	46	40	$(4.38 \pm 0.37 \pm 0.13)\times10^{-3}$	37	37
14.69	$(6.70 \pm 0.12 \pm 0.17)\times10^{-2}$	47	40	$(4.25 \pm 0.33 \pm 0.12)\times10^{-3}$	34	42
15.59	$(5.48 \pm 0.11 \pm 0.14)\times10^{-2}$	48	43	$(2.94 \pm 0.26 \pm 0.09)\times10^{-3}$	38	43
16.52	$(4.54 \pm 0.09 \pm 0.12)\times10^{-2}$	48	41	$(2.83 \pm 0.25 \pm 0.08)\times10^{-3}$	34	40
17.48	$(3.71 \pm 0.08 \pm 0.10)\times10^{-2}$	47	43	$(2.77 \pm 0.24 \pm 0.08)\times10^{-3}$	38	41
18.48	$(3.16 \pm 0.07 \pm 0.08)\times10^{-2}$	46	43	$(1.75 \pm 0.17 \pm 0.05)\times10^{-3}$	35	41
19.51	$(2.52 \pm 0.06 \pm 0.07)\times10^{-2}$	48	43	$(1.90 \pm 0.18 \pm 0.06)\times10^{-3}$	32	42
20.58	$(2.21 \pm 0.06 \pm 0.06)\times10^{-2}$	48	43	$(1.42 \pm 0.15 \pm 0.04)\times10^{-3}$	34	39
21.68	$(1.80 \pm 0.05 \pm 0.05)\times10^{-2}$	47	44	$(1.24 \pm 0.14 \pm 0.04)\times10^{-3}$	36	45
22.83	$(1.50 \pm 0.04 \pm 0.04)\times10^{-2}$	49	44	$(1.05 \pm 0.12 \pm 0.03)\times10^{-3}$	32	44
24.01	$(1.31 \pm 0.04 \pm 0.03)\times10^{-2}$	47	46	$(7.84 \pm 1.03 \pm 0.26)\times10^{-4}$	39	45
25.25	$(1.16 \pm 0.04 \pm 0.03)\times10^{-2}$	49	47	$(6.89 \pm 0.94 \pm 0.22)\times10^{-4}$	31	41
26.56	$(9.17 \pm 0.30 \pm 0.24)\times10^{-3}$	51	45	$(8.10 \pm 0.98 \pm 0.26)\times10^{-4}$	31	46
27.95	$(8.07 \pm 0.27 \pm 0.21)\times10^{-3}$	45	49	$(7.17 \pm 0.85 \pm 0.25)\times10^{-4}$	37	46
29.43	$(6.73 \pm 0.24 \pm 0.18)\times10^{-3}$	51	49	$(4.41 \pm 0.63 \pm 0.15)\times10^{-4}$	34	50
31.00	$(5.35 \pm 0.21 \pm 0.15)\times10^{-3}$	52	51	$(4.96 \pm 0.67 \pm 0.17)\times10^{-4}$	35	48
32.66	$(4.50 \pm 0.19 \pm 0.12)\times10^{-3}$	51	50	$(3.51 \pm 0.54 \pm 0.12)\times10^{-4}$	31	48
34.43	$(4.02 \pm 0.17 \pm 0.11)\times10^{-3}$	47	53	$(4.43 \pm 0.61 \pm 0.15)\times10^{-4}$	38	45
36.32	$(3.39 \pm 0.15 \pm 0.10)\times10^{-3}$	55	55	$(2.86 \pm 0.49 \pm 0.10)\times10^{-4}$	41	54
38.62	$(2.86 \pm 0.12 \pm 0.08)\times10^{-3}$	52	51	$(2.17 \pm 0.33 \pm 0.07)\times10^{-4}$	30	46

TABLE B.22: Results for electron and positron flux in time interval: 22/Dec/2012 - 17/Jan/2013

Δt: **18/Jan/2013 - 13/Feb/2013**						
$\bar{E}$ (GeV)	$\Phi_{e-} \pm \sigma_{\rm stat} \pm \sigma_{\rm sys}$ (GeV^{-1} m^{-2} sr^{-1} s^{-1})	$\sigma^{\rm t}_{\rm uc}$ (%)	$\sigma^{E}_{\rm uc}$ (%)	$\Phi_{e+} \pm \sigma_{\rm stat} \pm \sigma_{\rm sys}$ (GeV^{-1} m^{-2} sr^{-1} s^{-1})	$\sigma^{\rm t}_{\rm uc}$ (%)	$\sigma^{E}_{\rm uc}$ (%)
0.57	$(2.23 \pm 0.18 \pm 0.25)\times10^{1}$	27	54	$(1.48 \pm 1.23 \pm 0.25)\times10^{0}$	17	84
0.73	$(1.87 \pm 0.08 \pm 0.16)\times10^{1}$	41	53	$(2.29 \pm 0.66 \pm 0.20)\times10^{0}$	40	57
0.91	$(1.94 \pm 0.05 \pm 0.12)\times10^{1}$	19	37	$(1.32 \pm 0.26 \pm 0.08)\times10^{0}$	19	43
1.11	$(1.67 \pm 0.03 \pm 0.08)\times10^{1}$	20	37	$(1.58 \pm 0.15 \pm 0.08)\times10^{0}$	19	44
1.33	$(1.50 \pm 0.02 \pm 0.06)\times10^{1}$	16	34	$(1.29 \pm 0.09 \pm 0.05)\times10^{0}$	15	36
1.58	$(1.26 \pm 0.01 \pm 0.04)\times10^{1}$	12	33	$(9.65 \pm 0.53 \pm 0.34)\times10^{-1}$	15	36
1.85	$(1.05 \pm 0.01 \pm 0.03)\times10^{1}$	13	34	$(7.33 \pm 0.34 \pm 0.22)\times10^{-1}$	18	35
2.15	$(8.89 \pm 0.10 \pm 0.23)\times10^{0}$	15	33	$(6.22 \pm 0.24 \pm 0.17)\times10^{-1}$	18	37
2.47	$(6.99 \pm 0.06 \pm 0.17)\times10^{0}$	20	39	$(4.85 \pm 0.17 \pm 0.12)\times10^{-1}$	28	47
2.82	$(5.48 \pm 0.05 \pm 0.12)\times10^{0}$	25	39	$(3.90 \pm 0.13 \pm 0.09)\times10^{-1}$	31	40
3.17	$(4.65 \pm 0.04 \pm 0.10)\times10^{0}$	21	38	$(2.76 \pm 0.10 \pm 0.07)\times10^{-1}$	26	47
3.54	$(3.64 \pm 0.03 \pm 0.08)\times10^{0}$	30	38	$(2.13 \pm 0.08 \pm 0.05)\times10^{-1}$	34	38
3.92	$(2.92 \pm 0.02 \pm 0.07)\times10^{0}$	32	37	$(1.78 \pm 0.07 \pm 0.04)\times10^{-1}$	34	42
4.32	$(2.32 \pm 0.02 \pm 0.05)\times10^{0}$	33	37	$(1.40 \pm 0.05 \pm 0.03)\times10^{-1}$	36	42
4.76	$(1.84 \pm 0.02 \pm 0.04)\times10^{0}$	34	37	$(9.94 \pm 0.40 \pm 0.25)\times10^{-2}$	36	44
5.24	$(1.45 \pm 0.01 \pm 0.03)\times10^{0}$	37	36	$(7.96 \pm 0.33 \pm 0.20)\times10^{-2}$	38	40
5.74	$(1.14 \pm 0.01 \pm 0.03)\times10^{0}$	38	37	$(6.35 \pm 0.27 \pm 0.16)\times10^{-2}$	37	40
6.26	$(8.74 \pm 0.08 \pm 0.21)\times10^{-1}$	38	38	$(4.99 \pm 0.21 \pm 0.13)\times10^{-2}$	39	39
6.81	$(7.06 \pm 0.07 \pm 0.17)\times10^{-1}$	40	38	$(3.84 \pm 0.18 \pm 0.10)\times10^{-2}$	36	41
7.39	$(5.59 \pm 0.06 \pm 0.14)\times10^{-1}$	41	38	$(2.96 \pm 0.14 \pm 0.08)\times10^{-2}$	40	40
7.99	$(4.49 \pm 0.05 \pm 0.11)\times10^{-1}$	43	38	$(2.34 \pm 0.12 \pm 0.06)\times10^{-2}$	37	43
8.62	$(3.63 \pm 0.04 \pm 0.09)\times10^{-1}$	43	38	$(1.84 \pm 0.10 \pm 0.05)\times10^{-2}$	39	40
9.28	$(2.90 \pm 0.03 \pm 0.07)\times10^{-1}$	44	39	$(1.62 \pm 0.09 \pm 0.04)\times10^{-2}$	38	42
9.96	$(2.26 \pm 0.03 \pm 0.06)\times10^{-1}$	45	39	$(1.23 \pm 0.08 \pm 0.03)\times10^{-2}$	34	39
10.67	$(1.82 \pm 0.03 \pm 0.05)\times10^{-1}$	44	40	$(9.19 \pm 0.63 \pm 0.26)\times10^{-3}$	37	42
11.41	$(1.48 \pm 0.02 \pm 0.04)\times10^{-1}$	44	41	$(8.34 \pm 0.56 \pm 0.24)\times10^{-3}$	38	41
12.19	$(1.20 \pm 0.02 \pm 0.03)\times10^{-1}$	44	41	$(7.01 \pm 0.49 \pm 0.19)\times10^{-3}$	35	42
12.99	$(9.86 \pm 0.16 \pm 0.25)\times10^{-2}$	44	42	$(5.62 \pm 0.42 \pm 0.16)\times10^{-3}$	38	41
13.82	$(8.33 \pm 0.15 \pm 0.21)\times10^{-2}$	46	42	$(4.33 \pm 0.37 \pm 0.12)\times10^{-3}$	37	38
14.69	$(6.71 \pm 0.13 \pm 0.17)\times10^{-2}$	47	42	$(4.36 \pm 0.35 \pm 0.12)\times10^{-3}$	34	44
15.59	$(5.58 \pm 0.11 \pm 0.15)\times10^{-2}$	47	45	$(3.47 \pm 0.29 \pm 0.11)\times10^{-3}$	38	45
16.52	$(4.59 \pm 0.10 \pm 0.12)\times10^{-2}$	48	43	$(3.06 \pm 0.27 \pm 0.09)\times10^{-3}$	34	42
17.48	$(3.82 \pm 0.08 \pm 0.10)\times10^{-2}$	46	45	$(2.18 \pm 0.21 \pm 0.07)\times10^{-3}$	37	43
18.48	$(3.12 \pm 0.07 \pm 0.08)\times10^{-2}$	45	45	$(2.09 \pm 0.21 \pm 0.06)\times10^{-3}$	34	43
19.51	$(2.55 \pm 0.06 \pm 0.07)\times10^{-2}$	47	45	$(1.35 \pm 0.16 \pm 0.04)\times10^{-3}$	32	44
20.58	$(2.18 \pm 0.06 \pm 0.06)\times10^{-2}$	48	45	$(1.71 \pm 0.17 \pm 0.05)\times10^{-3}$	34	41
21.68	$(1.84 \pm 0.05 \pm 0.05)\times10^{-2}$	46	47	$(1.41 \pm 0.16 \pm 0.05)\times10^{-3}$	35	46
22.83	$(1.64 \pm 0.05 \pm 0.04)\times10^{-2}$	48	47	$(1.14 \pm 0.13 \pm 0.04)\times10^{-3}$	31	46
24.01	$(1.33 \pm 0.04 \pm 0.04)\times10^{-2}$	47	49	$(9.71 \pm 1.16 \pm 0.33)\times10^{-4}$	39	47
25.25	$(1.11 \pm 0.03 \pm 0.03)\times10^{-2}$	49	50	$(7.76 \pm 1.00 \pm 0.25)\times10^{-4}$	31	43
26.56	$(9.31 \pm 0.31 \pm 0.25)\times10^{-3}$	50	48	$(8.21 \pm 0.98 \pm 0.27)\times10^{-4}$	30	48
27.95	$(7.88 \pm 0.27 \pm 0.21)\times10^{-3}$	44	52	$(5.29 \pm 0.73 \pm 0.19)\times10^{-4}$	36	48
29.43	$(6.55 \pm 0.24 \pm 0.18)\times10^{-3}$	50	52	$(5.31 \pm 0.73 \pm 0.18)\times10^{-4}$	33	52
31.00	$(5.81 \pm 0.22 \pm 0.16)\times10^{-3}$	51	54	$(4.90 \pm 0.69 \pm 0.17)\times10^{-4}$	35	49
32.66	$(4.70 \pm 0.19 \pm 0.13)\times10^{-3}$	50	53	$(3.03 \pm 0.53 \pm 0.10)\times10^{-4}$	30	50
34.43	$(4.02 \pm 0.17 \pm 0.11)\times10^{-3}$	46	56	$(2.85 \pm 0.49 \pm 0.10)\times10^{-4}$	37	47
36.32	$(3.35 \pm 0.15 \pm 0.10)\times10^{-3}$	54	58	$(3.05 \pm 0.48 \pm 0.11)\times10^{-4}$	41	56
38.62	$(2.62 \pm 0.12 \pm 0.07)\times10^{-3}$	52	55	$(2.15 \pm 0.35 \pm 0.07)\times10^{-4}$	31	50

TABLE B.23: Results for electron and positron flux in time interval: 18/Jan/2013 - 13/Feb/2013

Δt: **14/Feb/2013 - 12/Mar/2013**						
$\tilde{E}$ (GeV)	$\Phi_{e-} \pm \sigma_{\rm stat} \pm \sigma_{\rm sys}$ (GeV^{-1} m^{-2} sr^{-1} s^{-1})	$\sigma^{\rm t}_{\rm uc}$ (%)	$\sigma^{E}_{\rm uc}$ (%)	$\Phi_{e+} \pm \sigma_{\rm stat} \pm \sigma_{\rm sys}$ (GeV^{-1} m^{-2} sr^{-1} s^{-1})	$\sigma^{\rm t}_{\rm uc}$ (%)	$\sigma^{E}_{\rm uc}$ (%)
0.57	$(2.47 \pm 0.19 \pm 0.27)\times10^{1}$	25	54	$(3.43 \pm 6.45 \pm 0.59)\times10^{-1}$	16	84
0.73	$(2.18 \pm 0.09 \pm 0.18)\times10^{1}$	36	49	$(2.03 \pm 0.66 \pm 0.18)\times10^{0}$	35	54
0.91	$(1.92 \pm 0.05 \pm 0.12)\times10^{1}$	19	37	$(2.04 \pm 0.27 \pm 0.13)\times10^{0}$	19	43
1.11	$(1.81 \pm 0.03 \pm 0.09)\times10^{1}$	20	37	$(1.64 \pm 0.15 \pm 0.08)\times10^{0}$	19	44
1.33	$(1.55 \pm 0.02 \pm 0.06)\times10^{1}$	16	34	$(1.31 \pm 0.09 \pm 0.05)\times10^{0}$	15	36
1.58	$(1.33 \pm 0.02 \pm 0.05)\times10^{1}$	12	33	$(1.01 \pm 0.05 \pm 0.04)\times10^{0}$	15	36
1.85	$(1.09 \pm 0.01 \pm 0.03)\times10^{1}$	13	34	$(7.92 \pm 0.35 \pm 0.24)\times10^{-1}$	18	35
2.15	$(9.05 \pm 0.08 \pm 0.24)\times10^{0}$	15	33	$(6.65 \pm 0.24 \pm 0.18)\times10^{-1}$	18	37
2.47	$(7.27 \pm 0.06 \pm 0.18)\times10^{0}$	20	42	$(4.98 \pm 0.17 \pm 0.13)\times10^{-1}$	27	49
2.82	$(5.61 \pm 0.05 \pm 0.12)\times10^{0}$	24	42	$(3.47 \pm 0.13 \pm 0.08)\times10^{-1}$	31	43
3.17	$(4.80 \pm 0.04 \pm 0.11)\times10^{0}$	21	41	$(2.93 \pm 0.11 \pm 0.07)\times10^{-1}$	26	49
3.54	$(3.72 \pm 0.03 \pm 0.09)\times10^{0}$	29	41	$(2.28 \pm 0.08 \pm 0.06)\times10^{-1}$	34	41
3.92	$(2.98 \pm 0.02 \pm 0.07)\times10^{0}$	32	40	$(1.71 \pm 0.07 \pm 0.04)\times10^{-1}$	33	44
4.32	$(2.37 \pm 0.02 \pm 0.06)\times10^{0}$	33	40	$(1.36 \pm 0.05 \pm 0.03)\times10^{-1}$	36	44
4.76	$(1.88 \pm 0.02 \pm 0.04)\times10^{0}$	34	39	$(1.11 \pm 0.04 \pm 0.03)\times10^{-1}$	36	46
5.24	$(1.47 \pm 0.01 \pm 0.04)\times10^{0}$	36	39	$(7.80 \pm 0.32 \pm 0.20)\times10^{-2}$	38	41
5.74	$(1.15 \pm 0.01 \pm 0.03)\times10^{0}$	37	39	$(6.26 \pm 0.26 \pm 0.16)\times10^{-2}$	37	41
6.26	$(9.03 \pm 0.08 \pm 0.22)\times10^{-1}$	38	40	$(4.67 \pm 0.21 \pm 0.12)\times10^{-2}$	38	40
6.81	$(7.20 \pm 0.07 \pm 0.18)\times10^{-1}$	39	40	$(3.78 \pm 0.17 \pm 0.10)\times10^{-2}$	36	42
7.39	$(5.74 \pm 0.06 \pm 0.14)\times10^{-1}$	41	39	$(3.27 \pm 0.15 \pm 0.09)\times10^{-2}$	40	41
7.99	$(4.48 \pm 0.05 \pm 0.11)\times10^{-1}$	43	39	$(2.58 \pm 0.12 \pm 0.07)\times10^{-2}$	37	44
8.62	$(3.50 \pm 0.04 \pm 0.09)\times10^{-1}$	43	39	$(1.91 \pm 0.10 \pm 0.05)\times10^{-2}$	39	41
9.28	$(2.88 \pm 0.03 \pm 0.07)\times10^{-1}$	44	39	$(1.38 \pm 0.08 \pm 0.04)\times10^{-2}$	38	42
9.96	$(2.26 \pm 0.03 \pm 0.06)\times10^{-1}$	45	39	$(1.25 \pm 0.08 \pm 0.03)\times10^{-2}$	34	40
10.67	$(1.76 \pm 0.02 \pm 0.04)\times10^{-1}$	44	41	$(1.05 \pm 0.07 \pm 0.03)\times10^{-2}$	37	42
11.41	$(1.48 \pm 0.02 \pm 0.04)\times10^{-1}$	44	41	$(9.95 \pm 0.60 \pm 0.28)\times10^{-3}$	38	41
12.19	$(1.23 \pm 0.02 \pm 0.03)\times10^{-1}$	44	41	$(7.38 \pm 0.49 \pm 0.20)\times10^{-3}$	35	42
12.99	$(9.94 \pm 0.16 \pm 0.25)\times10^{-2}$	44	42	$(5.78 \pm 0.43 \pm 0.17)\times10^{-3}$	38	41
13.82	$(8.15 \pm 0.14 \pm 0.21)\times10^{-2}$	46	42	$(4.41 \pm 0.36 \pm 0.13)\times10^{-3}$	37	38
14.69	$(6.56 \pm 0.12 \pm 0.17)\times10^{-2}$	47	42	$(4.23 \pm 0.33 \pm 0.12)\times10^{-3}$	34	44
15.59	$(5.68 \pm 0.11 \pm 0.15)\times10^{-2}$	47	45	$(3.38 \pm 0.30 \pm 0.10)\times10^{-3}$	38	44
16.52	$(4.58 \pm 0.10 \pm 0.12)\times10^{-2}$	48	42	$(2.43 \pm 0.23 \pm 0.07)\times10^{-3}$	34	41
17.48	$(3.81 \pm 0.08 \pm 0.10)\times10^{-2}$	46	44	$(2.31 \pm 0.22 \pm 0.07)\times10^{-3}$	37	42
18.48	$(3.14 \pm 0.07 \pm 0.08)\times10^{-2}$	46	44	$(1.95 \pm 0.20 \pm 0.06)\times10^{-3}$	34	42
19.51	$(2.73 \pm 0.07 \pm 0.07)\times10^{-2}$	47	44	$(1.57 \pm 0.16 \pm 0.05)\times10^{-3}$	32	43
20.58	$(2.21 \pm 0.06 \pm 0.06)\times10^{-2}$	48	44	$(1.42 \pm 0.15 \pm 0.04)\times10^{-3}$	34	41
21.68	$(1.89 \pm 0.05 \pm 0.05)\times10^{-2}$	47	46	$(1.31 \pm 0.14 \pm 0.04)\times10^{-3}$	35	46
22.83	$(1.55 \pm 0.04 \pm 0.04)\times10^{-2}$	48	46	$(9.95 \pm 1.20 \pm 0.31)\times10^{-4}$	32	45
24.01	$(1.32 \pm 0.04 \pm 0.03)\times10^{-2}$	47	47	$(6.37 \pm 0.90 \pm 0.21)\times10^{-4}$	39	46
25.25	$(1.12 \pm 0.03 \pm 0.03)\times10^{-2}$	49	48	$(8.10 \pm 0.98 \pm 0.26)\times10^{-4}$	31	42
26.56	$(9.36 \pm 0.31 \pm 0.25)\times10^{-3}$	51	47	$(5.10 \pm 0.76 \pm 0.16)\times10^{-4}$	30	47
27.95	$(7.84 \pm 0.27 \pm 0.21)\times10^{-3}$	44	50	$(8.39 \pm 0.92 \pm 0.29)\times10^{-4}$	36	47
29.43	$(6.55 \pm 0.24 \pm 0.18)\times10^{-3}$	51	50	$(5.53 \pm 0.73 \pm 0.18)\times10^{-4}$	34	51
31.00	$(5.67 \pm 0.22 \pm 0.16)\times10^{-3}$	52	52	$(4.81 \pm 0.64 \pm 0.16)\times10^{-4}$	35	48
32.66	$(4.44 \pm 0.19 \pm 0.12)\times10^{-3}$	51	51	$(4.80 \pm 0.63 \pm 0.16)\times10^{-4}$	31	49
34.43	$(4.19 \pm 0.18 \pm 0.11)\times10^{-3}$	47	54	$(2.64 \pm 0.43 \pm 0.09)\times10^{-4}$	37	45
36.32	$(3.47 \pm 0.16 \pm 0.10)\times10^{-3}$	54	56	$(2.85 \pm 0.49 \pm 0.10)\times10^{-4}$	40	54
38.62	$(2.97 \pm 0.12 \pm 0.08)\times10^{-3}$	52	52	$(2.19 \pm 0.34 \pm 0.07)\times10^{-4}$	30	47

TABLE B.24: Results for electron and positron flux in time interval: 14/Feb/2013 - 12/Mar/2013

Δt: **13/Mar/2013 - 08/Apr/2013**						
$\bar{E}$ (GeV)	$\Phi_{e-} \pm \sigma_{\text{stat}} \pm \sigma_{\text{sys}}$ ($\text{GeV}^{-1}\ \text{m}^{-2}\ \text{sr}^{-1}\ \text{s}^{-1}$)	$\sigma^{\text{t}}_{\text{uc}}$ (%)	σ^{E}_{uc} (%)	$\Phi_{e+} \pm \sigma_{\text{stat}} \pm \sigma_{\text{sys}}$ ($\text{GeV}^{-1}\ \text{m}^{-2}\ \text{sr}^{-1}\ \text{s}^{-1}$)	$\sigma^{\text{t}}_{\text{uc}}$ (%)	σ^{E}_{uc} (%)
0.57	$(2.15 \pm 0.18 \pm 0.24)\times10^{1}$	27	55	$(4.29 \pm 23.05 \pm 0.74)\times10^{-1}$	18	84
0.73	$(2.04 \pm 0.09 \pm 0.17)\times10^{1}$	38	51	$(1.54 \pm 0.59 \pm 0.14)\times10^{0}$	37	55
0.91	$(1.78 \pm 0.05 \pm 0.11)\times10^{1}$	19	37	$(1.80 \pm 0.27 \pm 0.11)\times10^{0}$	19	43
1.11	$(1.60 \pm 0.03 \pm 0.08)\times10^{1}$	20	37	$(1.46 \pm 0.15 \pm 0.07)\times10^{0}$	19	44
1.33	$(1.38 \pm 0.02 \pm 0.06)\times10^{1}$	16	35	$(1.26 \pm 0.09 \pm 0.05)\times10^{0}$	15	36
1.58	$(1.18 \pm 0.01 \pm 0.04)\times10^{1}$	13	34	$(9.16 \pm 0.54 \pm 0.32)\times10^{-1}$	15	36
1.85	$(9.82 \pm 0.10 \pm 0.29)\times10^{0}$	13	34	$(7.55 \pm 0.35 \pm 0.23)\times10^{-1}$	18	35
2.15	$(8.20 \pm 0.08 \pm 0.21)\times10^{0}$	16	33	$(5.61 \pm 0.24 \pm 0.15)\times10^{-1}$	18	37
2.47	$(6.43 \pm 0.06 \pm 0.16)\times10^{0}$	20	42	$(4.24 \pm 0.17 \pm 0.11)\times10^{-1}$	27	48
2.82	$(5.07 \pm 0.04 \pm 0.11)\times10^{0}$	24	42	$(3.29 \pm 0.13 \pm 0.07)\times10^{-1}$	31	43
3.17	$(4.30 \pm 0.04 \pm 0.10)\times10^{0}$	21	41	$(2.53 \pm 0.10 \pm 0.06)\times10^{-1}$	26	49
3.54	$(3.43 \pm 0.03 \pm 0.08)\times10^{0}$	29	40	$(1.92 \pm 0.08 \pm 0.05)\times10^{-1}$	34	41
3.92	$(2.74 \pm 0.02 \pm 0.06)\times10^{0}$	32	39	$(1.57 \pm 0.07 \pm 0.04)\times10^{-1}$	33	44
4.32	$(2.20 \pm 0.02 \pm 0.05)\times10^{0}$	33	39	$(1.24 \pm 0.05 \pm 0.03)\times10^{-1}$	36	44
4.76	$(1.73 \pm 0.02 \pm 0.04)\times10^{0}$	34	39	$(9.91 \pm 0.42 \pm 0.25)\times10^{-2}$	36	46
5.24	$(1.38 \pm 0.01 \pm 0.03)\times10^{0}$	36	38	$(7.60 \pm 0.33 \pm 0.19)\times10^{-2}$	38	41
5.74	$(1.07 \pm 0.01 \pm 0.03)\times10^{0}$	37	39	$(5.91 \pm 0.26 \pm 0.15)\times10^{-2}$	37	41
6.26	$(8.63 \pm 0.08 \pm 0.21)\times10^{-1}$	38	39	$(4.16 \pm 0.20 \pm 0.11)\times10^{-2}$	38	40
6.81	$(6.81 \pm 0.07 \pm 0.17)\times10^{-1}$	39	39	$(3.87 \pm 0.18 \pm 0.10)\times10^{-2}$	36	42
7.39	$(5.40 \pm 0.06 \pm 0.13)\times10^{-1}$	41	39	$(2.61 \pm 0.14 \pm 0.07)\times10^{-2}$	40	41
7.99	$(4.30 \pm 0.05 \pm 0.11)\times10^{-1}$	43	39	$(2.29 \pm 0.12 \pm 0.06)\times10^{-2}$	37	43
8.62	$(3.44 \pm 0.04 \pm 0.09)\times10^{-1}$	43	39	$(2.01 \pm 0.11 \pm 0.05)\times10^{-2}$	39	40
9.28	$(2.77 \pm 0.03 \pm 0.07)\times10^{-1}$	44	39	$(1.44 \pm 0.09 \pm 0.04)\times10^{-2}$	38	42
9.96	$(2.18 \pm 0.03 \pm 0.05)\times10^{-1}$	45	39	$(1.15 \pm 0.07 \pm 0.03)\times10^{-2}$	34	39
10.67	$(1.78 \pm 0.03 \pm 0.04)\times10^{-1}$	44	40	$(1.03 \pm 0.07 \pm 0.03)\times10^{-2}$	37	42
11.41	$(1.42 \pm 0.02 \pm 0.04)\times10^{-1}$	44	41	$(8.55 \pm 0.59 \pm 0.24)\times10^{-3}$	38	41
12.19	$(1.19 \pm 0.02 \pm 0.03)\times10^{-1}$	44	40	$(7.21 \pm 0.52 \pm 0.20)\times10^{-3}$	35	41
12.99	$(9.44 \pm 0.16 \pm 0.24)\times10^{-2}$	44	41	$(6.55 \pm 0.46 \pm 0.19)\times10^{-3}$	38	41
13.82	$(8.17 \pm 0.15 \pm 0.21)\times10^{-2}$	46	41	$(4.46 \pm 0.37 \pm 0.13)\times10^{-3}$	37	38
14.69	$(6.49 \pm 0.13 \pm 0.17)\times10^{-2}$	47	42	$(3.90 \pm 0.33 \pm 0.11)\times10^{-3}$	34	43
15.59	$(5.29 \pm 0.11 \pm 0.14)\times10^{-2}$	48	45	$(3.42 \pm 0.30 \pm 0.11)\times10^{-3}$	38	44
16.52	$(4.51 \pm 0.10 \pm 0.12)\times10^{-2}$	48	42	$(3.38 \pm 0.28 \pm 0.10)\times10^{-3}$	34	41
17.48	$(3.75 \pm 0.09 \pm 0.10)\times10^{-2}$	47	44	$(2.15 \pm 0.21 \pm 0.06)\times10^{-3}$	38	42
18.48	$(3.00 \pm 0.07 \pm 0.08)\times10^{-2}$	46	44	$(1.96 \pm 0.20 \pm 0.06)\times10^{-3}$	35	42
19.51	$(2.54 \pm 0.06 \pm 0.07)\times10^{-2}$	47	44	$(1.72 \pm 0.18 \pm 0.05)\times10^{-3}$	32	43
20.58	$(2.10 \pm 0.06 \pm 0.06)\times10^{-2}$	48	44	$(1.43 \pm 0.16 \pm 0.05)\times10^{-3}$	35	40
21.68	$(1.77 \pm 0.05 \pm 0.05)\times10^{-2}$	47	45	$(1.09 \pm 0.13 \pm 0.04)\times10^{-3}$	36	45
22.83	$(1.56 \pm 0.05 \pm 0.04)\times10^{-2}$	49	45	$(1.02 \pm 0.12 \pm 0.03)\times10^{-3}$	32	45
24.01	$(1.23 \pm 0.04 \pm 0.03)\times10^{-2}$	48	47	$(9.27 \pm 1.12 \pm 0.31)\times10^{-4}$	39	46
25.25	$(1.13 \pm 0.04 \pm 0.03)\times10^{-2}$	49	48	$(8.53 \pm 1.06 \pm 0.28)\times10^{-4}$	32	42
26.56	$(9.02 \pm 0.31 \pm 0.24)\times10^{-3}$	51	47	$(8.36 \pm 0.99 \pm 0.27)\times10^{-4}$	31	47
27.95	$(7.94 \pm 0.28 \pm 0.21)\times10^{-3}$	45	50	$(6.63 \pm 0.85 \pm 0.23)\times10^{-4}$	37	47
29.43	$(6.54 \pm 0.25 \pm 0.18)\times10^{-3}$	51	50	$(5.99 \pm 0.77 \pm 0.20)\times10^{-4}$	34	51
31.00	$(5.47 \pm 0.22 \pm 0.15)\times10^{-3}$	52	52	$(4.68 \pm 0.66 \pm 0.16)\times10^{-4}$	35	48
32.66	$(4.63 \pm 0.20 \pm 0.13)\times10^{-3}$	51	51	$(2.98 \pm 0.49 \pm 0.10)\times10^{-4}$	31	49
34.43	$(3.95 \pm 0.17 \pm 0.11)\times10^{-3}$	48	54	$(3.59 \pm 0.54 \pm 0.12)\times10^{-4}$	38	46
36.32	$(3.08 \pm 0.15 \pm 0.09)\times10^{-3}$	57	58	$(3.26 \pm 0.50 \pm 0.12)\times10^{-4}$	43	56
38.62	$(2.80 \pm 0.12 \pm 0.08)\times10^{-3}$	53	53	$(1.96 \pm 0.33 \pm 0.06)\times10^{-4}$	31	47

TABLE B.25: Results for electron and positron flux in time interval: 13/Mar/2013 - 08/Apr/2013

Δt: **09/Apr/2013 - 05/May/2013**						
$\bar{E}$ (GeV)	$\Phi_{e-} \pm \sigma_{\text{stat}} \pm \sigma_{\text{sys}}$ (GeV^{-1} m^{-2} sr^{-1} s^{-1})	$\sigma^{\text{t}}_{\text{uc}}$ (%)	σ^{E}_{uc} (%)	$\Phi_{e+} \pm \sigma_{\text{stat}} \pm \sigma_{\text{sys}}$ (GeV^{-1} m^{-2} sr^{-1} s^{-1})	$\sigma^{\text{t}}_{\text{uc}}$ (%)	σ^{E}_{uc} (%)
0.57	$(2.28 \pm 0.17 \pm 0.25)\times10^{1}$	25	54	$(-0.02 \pm 242.14 \pm 0.00)\times10^{0}$	16	84
0.73	$(1.93 \pm 0.08 \pm 0.17)\times10^{1}$	38	50	$(2.00 \pm 0.70 \pm 0.18)\times10^{0}$	37	55
0.91	$(1.84 \pm 0.05 \pm 0.11)\times10^{1}$	19	37	$(1.77 \pm 0.27 \pm 0.11)\times10^{0}$	19	43
1.11	$(1.68 \pm 0.03 \pm 0.08)\times10^{1}$	20	36	$(1.39 \pm 0.14 \pm 0.07)\times10^{0}$	19	44
1.33	$(1.46 \pm 0.02 \pm 0.06)\times10^{1}$	16	34	$(1.09 \pm 0.08 \pm 0.05)\times10^{0}$	15	36
1.58	$(1.24 \pm 0.01 \pm 0.04)\times10^{1}$	12	33	$(9.79 \pm 0.52 \pm 0.35)\times10^{-1}$	15	36
1.85	$(9.95 \pm 0.10 \pm 0.30)\times10^{0}$	13	34	$(7.44 \pm 0.33 \pm 0.23)\times10^{-1}$	18	35
2.15	$(8.32 \pm 0.07 \pm 0.22)\times10^{0}$	15	33	$(5.98 \pm 0.23 \pm 0.16)\times10^{-1}$	18	37
2.47	$(6.71 \pm 0.06 \pm 0.16)\times10^{0}$	20	41	$(4.56 \pm 0.17 \pm 0.12)\times10^{-1}$	27	48
2.82	$(5.21 \pm 0.04 \pm 0.11)\times10^{0}$	25	41	$(3.46 \pm 0.13 \pm 0.08)\times10^{-1}$	31	42
3.17	$(4.46 \pm 0.04 \pm 0.10)\times10^{0}$	21	40	$(2.61 \pm 0.10 \pm 0.06)\times10^{-1}$	26	48
3.54	$(3.57 \pm 0.03 \pm 0.08)\times10^{0}$	29	39	$(2.09 \pm 0.08 \pm 0.05)\times10^{-1}$	34	40
3.92	$(2.80 \pm 0.02 \pm 0.07)\times10^{0}$	32	38	$(1.66 \pm 0.06 \pm 0.04)\times10^{-1}$	33	43
4.32	$(2.19 \pm 0.02 \pm 0.05)\times10^{0}$	33	38	$(1.36 \pm 0.05 \pm 0.03)\times10^{-1}$	36	43
4.76	$(1.78 \pm 0.02 \pm 0.04)\times10^{0}$	34	37	$(1.03 \pm 0.04 \pm 0.03)\times10^{-1}$	36	45
5.24	$(1.38 \pm 0.01 \pm 0.03)\times10^{0}$	37	37	$(7.75 \pm 0.32 \pm 0.19)\times10^{-2}$	38	40
5.74	$(1.12 \pm 0.01 \pm 0.03)\times10^{0}$	38	38	$(5.94 \pm 0.25 \pm 0.15)\times10^{-2}$	37	40
6.26	$(8.83 \pm 0.08 \pm 0.21)\times10^{-1}$	38	38	$(4.77 \pm 0.21 \pm 0.12)\times10^{-2}$	39	39
6.81	$(6.95 \pm 0.07 \pm 0.17)\times10^{-1}$	40	38	$(3.39 \pm 0.16 \pm 0.09)\times10^{-2}$	36	41
7.39	$(5.46 \pm 0.06 \pm 0.13)\times10^{-1}$	42	37	$(2.87 \pm 0.14 \pm 0.07)\times10^{-2}$	40	40
7.99	$(4.46 \pm 0.05 \pm 0.11)\times10^{-1}$	43	38	$(2.44 \pm 0.12 \pm 0.06)\times10^{-2}$	37	42
8.62	$(3.50 \pm 0.04 \pm 0.09)\times10^{-1}$	43	37	$(1.81 \pm 0.10 \pm 0.05)\times10^{-2}$	39	39
9.28	$(2.85 \pm 0.03 \pm 0.07)\times10^{-1}$	44	38	$(1.49 \pm 0.09 \pm 0.04)\times10^{-2}$	38	41
9.96	$(2.28 \pm 0.03 \pm 0.06)\times10^{-1}$	45	37	$(1.29 \pm 0.08 \pm 0.03)\times10^{-2}$	34	38
10.67	$(1.85 \pm 0.03 \pm 0.05)\times10^{-1}$	45	39	$(9.97 \pm 0.65 \pm 0.28)\times10^{-3}$	38	41
11.41	$(1.45 \pm 0.02 \pm 0.04)\times10^{-1}$	45	39	$(8.02 \pm 0.55 \pm 0.23)\times10^{-3}$	39	39
12.19	$(1.19 \pm 0.02 \pm 0.03)\times10^{-1}$	45	39	$(7.43 \pm 0.50 \pm 0.20)\times10^{-3}$	35	40
12.99	$(9.75 \pm 0.16 \pm 0.24)\times10^{-2}$	44	40	$(6.51 \pm 0.46 \pm 0.19)\times10^{-3}$	38	40
13.82	$(8.01 \pm 0.14 \pm 0.20)\times10^{-2}$	46	40	$(4.11 \pm 0.36 \pm 0.12)\times10^{-3}$	37	36
14.69	$(6.49 \pm 0.12 \pm 0.17)\times10^{-2}$	48	40	$(4.56 \pm 0.34 \pm 0.13)\times10^{-3}$	35	42
15.59	$(5.41 \pm 0.11 \pm 0.14)\times10^{-2}$	48	43	$(3.01 \pm 0.28 \pm 0.09)\times10^{-3}$	38	43
16.52	$(4.48 \pm 0.09 \pm 0.12)\times10^{-2}$	48	40	$(2.65 \pm 0.24 \pm 0.08)\times10^{-3}$	34	40
17.48	$(3.76 \pm 0.08 \pm 0.10)\times10^{-2}$	47	42	$(2.21 \pm 0.22 \pm 0.07)\times10^{-3}$	38	41
18.48	$(3.03 \pm 0.07 \pm 0.08)\times10^{-2}$	46	42	$(2.19 \pm 0.21 \pm 0.07)\times10^{-3}$	35	40
19.51	$(2.59 \pm 0.06 \pm 0.07)\times10^{-2}$	48	42	$(1.59 \pm 0.17 \pm 0.05)\times10^{-3}$	32	42
20.58	$(2.23 \pm 0.06 \pm 0.06)\times10^{-2}$	49	42	$(1.30 \pm 0.15 \pm 0.04)\times10^{-3}$	35	39
21.68	$(1.80 \pm 0.05 \pm 0.05)\times10^{-2}$	47	44	$(1.30 \pm 0.14 \pm 0.04)\times10^{-3}$	36	44
22.83	$(1.59 \pm 0.04 \pm 0.04)\times10^{-2}$	49	44	$(9.15 \pm 1.08 \pm 0.28)\times10^{-4}$	32	44
24.01	$(1.31 \pm 0.04 \pm 0.03)\times10^{-2}$	48	45	$(8.65 \pm 1.07 \pm 0.29)\times10^{-4}$	39	45
25.25	$(1.13 \pm 0.04 \pm 0.03)\times10^{-2}$	50	46	$(6.79 \pm 0.88 \pm 0.22)\times10^{-4}$	31	41
26.56	$(9.73 \pm 0.31 \pm 0.26)\times10^{-3}$	51	45	$(8.90 \pm 1.00 \pm 0.28)\times10^{-4}$	30	46
27.95	$(8.52 \pm 0.28 \pm 0.22)\times10^{-3}$	45	48	$(5.55 \pm 0.76 \pm 0.19)\times10^{-4}$	37	46
29.43	$(6.54 \pm 0.24 \pm 0.17)\times10^{-3}$	51	49	$(4.47 \pm 0.65 \pm 0.15)\times10^{-4}$	34	50
31.00	$(5.40 \pm 0.21 \pm 0.15)\times10^{-3}$	52	51	$(4.56 \pm 0.64 \pm 0.15)\times10^{-4}$	35	47
32.66	$(4.79 \pm 0.19 \pm 0.13)\times10^{-3}$	51	49	$(3.62 \pm 0.55 \pm 0.12)\times10^{-4}$	31	48
34.43	$(4.03 \pm 0.17 \pm 0.11)\times10^{-3}$	48	52	$(3.51 \pm 0.55 \pm 0.12)\times10^{-4}$	38	44
36.32	$(3.16 \pm 0.15 \pm 0.09)\times10^{-3}$	56	56	$(2.97 \pm 0.48 \pm 0.11)\times10^{-4}$	42	54
38.62	$(2.65 \pm 0.12 \pm 0.07)\times10^{-3}$	53	52	$(3.35 \pm 0.42 \pm 0.11)\times10^{-4}$	31	46

TABLE B.26: Results for electron and positron flux in time interval: 09/Apr/2013 - 05/May/2013

Δt: **06/May/2013 - 01/Jun/2013**						
$\widetilde{E}$ (GeV)	$\Phi_{e-} \pm \sigma_{\text{stat}} \pm \sigma_{\text{sys}}$ (GeV^{-1} m^{-2} sr^{-1} s^{-1})	$\sigma^{\text{t}}_{\text{uc}}$ (%)	σ^{E}_{uc} (%)	$\Phi_{e+} \pm \sigma_{\text{stat}} \pm \sigma_{\text{sys}}$ (GeV^{-1} m^{-2} sr^{-1} s^{-1})	$\sigma^{\text{t}}_{\text{uc}}$ (%)	σ^{E}_{uc} (%)
0.57	$(1.96 \pm 0.17 \pm 0.22)\times10^{1}$	29	55	$(-0.01 \pm 1170.17 \pm 0.00)\times10^{0}$	19	84
0.73	$(1.64 \pm 0.08 \pm 0.15)\times10^{1}$	45	55	$(1.31 \pm 0.57 \pm 0.12)\times10^{0}$	44	59
0.91	$(1.63 \pm 0.04 \pm 0.10)\times10^{1}$	20	38	$(1.40 \pm 0.26 \pm 0.09)\times10^{0}$	19	43
1.11	$(1.42 \pm 0.03 \pm 0.07)\times10^{1}$	20	37	$(1.26 \pm 0.13 \pm 0.06)\times10^{0}$	20	44
1.33	$(1.25 \pm 0.02 \pm 0.05)\times10^{1}$	16	35	$(1.05 \pm 0.08 \pm 0.04)\times10^{0}$	16	36
1.58	$(1.06 \pm 0.01 \pm 0.04)\times10^{1}$	13	34	$(8.05 \pm 0.50 \pm 0.29)\times10^{-1}$	15	37
1.85	$(8.73 \pm 0.10 \pm 0.26)\times10^{0}$	13	34	$(6.33 \pm 0.32 \pm 0.19)\times10^{-1}$	18	35
2.15	$(7.19 \pm 0.07 \pm 0.19)\times10^{0}$	16	33	$(5.23 \pm 0.22 \pm 0.14)\times10^{-1}$	18	37
2.47	$(5.76 \pm 0.05 \pm 0.14)\times10^{0}$	20	42	$(3.82 \pm 0.15 \pm 0.10)\times10^{-1}$	27	49
2.82	$(4.53 \pm 0.04 \pm 0.10)\times10^{0}$	24	42	$(2.98 \pm 0.12 \pm 0.07)\times10^{-1}$	31	43
3.17	$(3.87 \pm 0.03 \pm 0.09)\times10^{0}$	21	41	$(2.37 \pm 0.10 \pm 0.06)\times10^{-1}$	26	49
3.54	$(3.13 \pm 0.03 \pm 0.07)\times10^{0}$	29	41	$(1.76 \pm 0.07 \pm 0.04)\times10^{-1}$	34	41
3.92	$(2.48 \pm 0.02 \pm 0.06)\times10^{0}$	32	40	$(1.45 \pm 0.06 \pm 0.04)\times10^{-1}$	33	45
4.32	$(1.99 \pm 0.02 \pm 0.05)\times10^{0}$	33	40	$(1.02 \pm 0.05 \pm 0.03)\times10^{-1}$	36	44
4.76	$(1.58 \pm 0.01 \pm 0.04)\times10^{0}$	34	39	$(8.56 \pm 0.38 \pm 0.22)\times10^{-2}$	36	46
5.24	$(1.25 \pm 0.01 \pm 0.03)\times10^{0}$	36	39	$(7.06 \pm 0.31 \pm 0.18)\times10^{-2}$	38	42
5.74	$(9.95 \pm 0.09 \pm 0.24)\times10^{-1}$	37	40	$(5.08 \pm 0.23 \pm 0.13)\times10^{-2}$	37	41
6.26	$(7.99 \pm 0.08 \pm 0.19)\times10^{-1}$	38	40	$(4.58 \pm 0.20 \pm 0.12)\times10^{-2}$	38	40
6.81	$(6.39 \pm 0.06 \pm 0.16)\times10^{-1}$	39	40	$(3.49 \pm 0.16 \pm 0.09)\times10^{-2}$	36	42
7.39	$(5.11 \pm 0.05 \pm 0.13)\times10^{-1}$	41	39	$(2.68 \pm 0.14 \pm 0.07)\times10^{-2}$	40	41
7.99	$(4.06 \pm 0.05 \pm 0.10)\times10^{-1}$	43	40	$(2.21 \pm 0.12 \pm 0.06)\times10^{-2}$	37	44
8.62	$(3.31 \pm 0.04 \pm 0.08)\times10^{-1}$	43	40	$(1.76 \pm 0.10 \pm 0.05)\times10^{-2}$	39	41
9.28	$(2.60 \pm 0.03 \pm 0.06)\times10^{-1}$	44	40	$(1.37 \pm 0.08 \pm 0.04)\times10^{-2}$	38	42
9.96	$(2.16 \pm 0.03 \pm 0.05)\times10^{-1}$	45	40	$(1.18 \pm 0.07 \pm 0.03)\times10^{-2}$	34	40
10.67	$(1.72 \pm 0.02 \pm 0.04)\times10^{-1}$	44	41	$(9.29 \pm 0.63 \pm 0.27)\times10^{-3}$	37	42
11.41	$(1.40 \pm 0.02 \pm 0.04)\times10^{-1}$	44	41	$(8.04 \pm 0.55 \pm 0.23)\times10^{-3}$	38	41
12.19	$(1.13 \pm 0.02 \pm 0.03)\times10^{-1}$	44	41	$(6.74 \pm 0.49 \pm 0.19)\times10^{-3}$	35	42
12.99	$(9.19 \pm 0.16 \pm 0.23)\times10^{-2}$	44	42	$(4.70 \pm 0.39 \pm 0.14)\times10^{-3}$	38	41
13.82	$(7.82 \pm 0.14 \pm 0.20)\times10^{-2}$	46	42	$(4.27 \pm 0.36 \pm 0.12)\times10^{-3}$	37	38
14.69	$(6.29 \pm 0.12 \pm 0.16)\times10^{-2}$	47	42	$(4.75 \pm 0.35 \pm 0.13)\times10^{-3}$	34	44
15.59	$(5.42 \pm 0.11 \pm 0.14)\times10^{-2}$	47	45	$(2.76 \pm 0.26 \pm 0.09)\times10^{-3}$	38	44
16.52	$(4.41 \pm 0.09 \pm 0.12)\times10^{-2}$	48	43	$(2.22 \pm 0.23 \pm 0.07)\times10^{-3}$	34	41
17.48	$(3.78 \pm 0.08 \pm 0.10)\times10^{-2}$	46	44	$(2.20 \pm 0.22 \pm 0.07)\times10^{-3}$	37	42
18.48	$(3.01 \pm 0.07 \pm 0.08)\times10^{-2}$	46	44	$(1.71 \pm 0.19 \pm 0.05)\times10^{-3}$	34	42
19.51	$(2.66 \pm 0.06 \pm 0.07)\times10^{-2}$	47	44	$(1.44 \pm 0.16 \pm 0.04)\times10^{-3}$	32	44
20.58	$(2.16 \pm 0.06 \pm 0.06)\times10^{-2}$	48	44	$(1.41 \pm 0.15 \pm 0.04)\times10^{-3}$	34	41
21.68	$(1.89 \pm 0.05 \pm 0.05)\times10^{-2}$	47	46	$(1.24 \pm 0.14 \pm 0.04)\times10^{-3}$	35	46
22.83	$(1.52 \pm 0.04 \pm 0.04)\times10^{-2}$	48	46	$(1.09 \pm 0.13 \pm 0.03)\times10^{-3}$	32	46
24.01	$(1.34 \pm 0.04 \pm 0.04)\times10^{-2}$	47	47	$(8.60 \pm 1.09 \pm 0.29)\times10^{-4}$	39	46
25.25	$(1.14 \pm 0.04 \pm 0.03)\times10^{-2}$	49	48	$(6.32 \pm 0.83 \pm 0.20)\times10^{-4}$	31	42
26.56	$(9.42 \pm 0.31 \pm 0.25)\times10^{-3}$	51	47	$(5.24 \pm 0.78 \pm 0.17)\times10^{-4}$	30	47
27.95	$(8.11 \pm 0.28 \pm 0.22)\times10^{-3}$	44	50	$(4.89 \pm 0.70 \pm 0.17)\times10^{-4}$	36	47
29.43	$(6.84 \pm 0.25 \pm 0.18)\times10^{-3}$	50	50	$(4.30 \pm 0.64 \pm 0.14)\times10^{-4}$	33	51
31.00	$(5.55 \pm 0.22 \pm 0.15)\times10^{-3}$	52	52	$(3.85 \pm 0.58 \pm 0.13)\times10^{-4}$	35	48
32.66	$(4.72 \pm 0.19 \pm 0.13)\times10^{-3}$	50	51	$(3.94 \pm 0.60 \pm 0.13)\times10^{-4}$	30	49
34.43	$(3.96 \pm 0.17 \pm 0.11)\times10^{-3}$	47	54	$(3.24 \pm 0.52 \pm 0.11)\times10^{-4}$	38	46
36.32	$(3.59 \pm 0.16 \pm 0.10)\times10^{-3}$	54	56	$(2.49 \pm 0.42 \pm 0.09)\times10^{-4}$	40	54
38.62	$(2.73 \pm 0.12 \pm 0.08)\times10^{-3}$	52	53	$(2.27 \pm 0.33 \pm 0.07)\times10^{-4}$	31	48

TABLE B.27: Results for electron and positron flux in time interval: 06/May/2013 - 01/Jun/2013

Δt: **02/Jun/2013 - 28/Jun/2013**						
$\tilde{E}$ (GeV)	$\Phi_{e-} \pm \sigma_{\rm stat} \pm \sigma_{\rm sys}$ (GeV^{-1} m^{-2} sr^{-1} s^{-1})	$\sigma^{\rm t}_{\rm uc}$ (%)	$\sigma^{E}_{\rm uc}$ (%)	$\Phi_{e+} \pm \sigma_{\rm stat} \pm \sigma_{\rm sys}$ (GeV^{-1} m^{-2} sr^{-1} s^{-1})	$\sigma^{\rm t}_{\rm uc}$ (%)	$\sigma^{E}_{\rm uc}$ (%)
0.57	$(1.64 \pm 0.15 \pm 0.18)\times10^{1}$	32	56	$(-0.01 \pm 674.38 \pm 0.00)\times10^{0}$	20	85
0.73	$(1.43 \pm 0.07 \pm 0.13)\times10^{1}$	47	57	$(2.06 \pm 0.53 \pm 0.19)\times10^{0}$	46	60
0.91	$(1.43 \pm 0.04 \pm 0.09)\times10^{1}$	20	38	$(1.65 \pm 0.25 \pm 0.10)\times10^{0}$	19	43
1.11	$(1.33 \pm 0.03 \pm 0.07)\times10^{1}$	20	37	$(1.16 \pm 0.13 \pm 0.06)\times10^{0}$	20	44
1.33	$(1.16 \pm 0.02 \pm 0.05)\times10^{1}$	16	35	$(8.38 \pm 0.73 \pm 0.35)\times10^{-1}$	16	36
1.58	$(9.98 \pm 0.13 \pm 0.35)\times10^{0}$	13	34	$(7.34 \pm 0.48 \pm 0.26)\times10^{-1}$	15	37
1.85	$(8.34 \pm 0.09 \pm 0.25)\times10^{0}$	13	34	$(5.80 \pm 0.30 \pm 0.18)\times10^{-1}$	18	35
2.15	$(6.81 \pm 0.07 \pm 0.18)\times10^{0}$	16	33	$(4.81 \pm 0.21 \pm 0.13)\times10^{-1}$	18	37
2.47	$(5.55 \pm 0.05 \pm 0.13)\times10^{0}$	20	40	$(3.45 \pm 0.15 \pm 0.09)\times10^{-1}$	28	47
2.82	$(4.44 \pm 0.04 \pm 0.10)\times10^{0}$	25	40	$(2.70 \pm 0.11 \pm 0.06)\times10^{-1}$	31	41
3.17	$(3.79 \pm 0.03 \pm 0.09)\times10^{0}$	21	39	$(2.27 \pm 0.09 \pm 0.06)\times10^{-1}$	26	48
3.54	$(3.08 \pm 0.03 \pm 0.07)\times10^{0}$	30	38	$(1.90 \pm 0.08 \pm 0.05)\times10^{-1}$	34	39
3.92	$(2.44 \pm 0.02 \pm 0.06)\times10^{0}$	32	38	$(1.28 \pm 0.06 \pm 0.03)\times10^{-1}$	33	43
4.32	$(1.93 \pm 0.02 \pm 0.05)\times10^{0}$	33	38	$(1.13 \pm 0.05 \pm 0.03)\times10^{-1}$	36	42
4.76	$(1.60 \pm 0.01 \pm 0.04)\times10^{0}$	34	37	$(8.93 \pm 0.38 \pm 0.23)\times10^{-2}$	36	45
5.24	$(1.27 \pm 0.01 \pm 0.03)\times10^{0}$	37	37	$(6.94 \pm 0.30 \pm 0.17)\times10^{-2}$	38	40
5.74	$(1.02 \pm 0.01 \pm 0.02)\times10^{0}$	38	38	$(5.57 \pm 0.25 \pm 0.14)\times10^{-2}$	37	40
6.26	$(7.90 \pm 0.08 \pm 0.19)\times10^{-1}$	38	38	$(4.20 \pm 0.20 \pm 0.11)\times10^{-2}$	39	39
6.81	$(6.37 \pm 0.06 \pm 0.15)\times10^{-1}$	40	38	$(3.60 \pm 0.17 \pm 0.09)\times10^{-2}$	36	41
7.39	$(5.15 \pm 0.05 \pm 0.13)\times10^{-1}$	41	38	$(2.69 \pm 0.14 \pm 0.07)\times10^{-2}$	40	40
7.99	$(4.09 \pm 0.05 \pm 0.10)\times10^{-1}$	43	38	$(2.14 \pm 0.11 \pm 0.06)\times10^{-2}$	37	43
8.62	$(3.24 \pm 0.04 \pm 0.08)\times10^{-1}$	43	38	$(1.80 \pm 0.10 \pm 0.05)\times10^{-2}$	39	40
9.28	$(2.59 \pm 0.03 \pm 0.06)\times10^{-1}$	44	39	$(1.44 \pm 0.08 \pm 0.04)\times10^{-2}$	38	41
9.96	$(2.13 \pm 0.03 \pm 0.05)\times10^{-1}$	45	39	$(1.28 \pm 0.08 \pm 0.03)\times10^{-2}$	34	39
10.67	$(1.73 \pm 0.02 \pm 0.04)\times10^{-1}$	44	40	$(9.05 \pm 0.63 \pm 0.26)\times10^{-3}$	37	41
11.41	$(1.41 \pm 0.02 \pm 0.04)\times10^{-1}$	44	40	$(6.84 \pm 0.50 \pm 0.19)\times10^{-3}$	38	41
12.19	$(1.16 \pm 0.02 \pm 0.03)\times10^{-1}$	44	40	$(6.27 \pm 0.48 \pm 0.17)\times10^{-3}$	35	41
12.99	$(9.49 \pm 0.16 \pm 0.24)\times10^{-2}$	44	41	$(5.50 \pm 0.43 \pm 0.16)\times10^{-3}$	38	41
13.82	$(7.92 \pm 0.14 \pm 0.20)\times10^{-2}$	46	42	$(4.13 \pm 0.35 \pm 0.12)\times10^{-3}$	37	38
14.69	$(6.56 \pm 0.12 \pm 0.17)\times10^{-2}$	47	42	$(3.89 \pm 0.32 \pm 0.11)\times10^{-3}$	34	43
15.59	$(5.31 \pm 0.11 \pm 0.14)\times10^{-2}$	47	45	$(3.92 \pm 0.32 \pm 0.12)\times10^{-3}$	38	44
16.52	$(4.33 \pm 0.09 \pm 0.11)\times10^{-2}$	48	42	$(2.57 \pm 0.25 \pm 0.08)\times10^{-3}$	34	41
17.48	$(3.71 \pm 0.08 \pm 0.10)\times10^{-2}$	46	44	$(2.64 \pm 0.23 \pm 0.08)\times10^{-3}$	37	42
18.48	$(3.15 \pm 0.07 \pm 0.08)\times10^{-2}$	45	44	$(1.78 \pm 0.19 \pm 0.05)\times10^{-3}$	34	42
19.51	$(2.55 \pm 0.06 \pm 0.07)\times10^{-2}$	47	45	$(2.12 \pm 0.19 \pm 0.06)\times10^{-3}$	32	44
20.58	$(2.11 \pm 0.06 \pm 0.06)\times10^{-2}$	48	45	$(1.01 \pm 0.13 \pm 0.03)\times10^{-3}$	34	41
21.68	$(1.80 \pm 0.05 \pm 0.05)\times10^{-2}$	47	46	$(1.02 \pm 0.12 \pm 0.03)\times10^{-3}$	35	46
22.83	$(1.55 \pm 0.04 \pm 0.04)\times10^{-2}$	48	46	$(1.32 \pm 0.14 \pm 0.04)\times10^{-3}$	32	46
24.01	$(1.26 \pm 0.04 \pm 0.03)\times10^{-2}$	47	48	$(8.63 \pm 1.05 \pm 0.29)\times10^{-4}$	39	46
25.25	$(1.13 \pm 0.04 \pm 0.03)\times10^{-2}$	49	49	$(6.04 \pm 0.86 \pm 0.20)\times10^{-4}$	31	43
26.56	$(9.11 \pm 0.31 \pm 0.25)\times10^{-3}$	51	47	$(7.18 \pm 0.90 \pm 0.23)\times10^{-4}$	31	47
27.95	$(7.32 \pm 0.26 \pm 0.20)\times10^{-3}$	44	51	$(4.90 \pm 0.70 \pm 0.17)\times10^{-4}$	37	47
29.43	$(6.22 \pm 0.24 \pm 0.17)\times10^{-3}$	51	51	$(4.31 \pm 0.65 \pm 0.14)\times10^{-4}$	34	51
31.00	$(5.55 \pm 0.22 \pm 0.15)\times10^{-3}$	52	53	$(3.62 \pm 0.60 \pm 0.12)\times10^{-4}$	35	49
32.66	$(4.59 \pm 0.19 \pm 0.13)\times10^{-3}$	50	52	$(3.87 \pm 0.59 \pm 0.13)\times10^{-4}$	31	50
34.43	$(3.71 \pm 0.17 \pm 0.10)\times10^{-3}$	48	55	$(4.04 \pm 0.58 \pm 0.14)\times10^{-4}$	38	47
36.32	$(3.30 \pm 0.15 \pm 0.09)\times10^{-3}$	55	58	$(2.69 \pm 0.47 \pm 0.10)\times10^{-4}$	41	55
38.62	$(2.45 \pm 0.11 \pm 0.07)\times10^{-3}$	53	55	$(3.54 \pm 0.44 \pm 0.12)\times10^{-4}$	32	49

TABLE B.28: Results for electron and positron flux in time interval: 02/Jun/2013 - 28/Jun/2013

Δt: **29/Jun/2013 - 25/Jul/2013**						
$\bar{E}$ (GeV)	$\Phi_{e-} \pm \sigma_{\rm stat} \pm \sigma_{\rm sys}$ (GeV^{-1} m^{-2} sr^{-1} s^{-1})	$\sigma^{\rm t}_{\rm uc}$ (%)	$\sigma^{E}_{\rm uc}$ (%)	$\Phi_{e+} \pm \sigma_{\rm stat} \pm \sigma_{\rm sys}$ (GeV^{-1} m^{-2} sr^{-1} s^{-1})	$\sigma^{\rm t}_{\rm uc}$ (%)	$\sigma^{E}_{\rm uc}$ (%)
0.57	$(1.53 \pm 0.14 \pm 0.17)\times10^{1}$	34	57	$(6.73 \pm 439.68 \pm 1.17)\times10^{-2}$	22	85
0.73	$(1.54 \pm 0.07 \pm 0.14)\times10^{1}$	45	55	$(1.77 \pm 0.59 \pm 0.16)\times10^{0}$	44	59
0.91	$(1.40 \pm 0.04 \pm 0.09)\times10^{1}$	20	38	$(1.44 \pm 0.24 \pm 0.09)\times10^{0}$	20	43
1.11	$(1.25 \pm 0.03 \pm 0.06)\times10^{1}$	20	37	$(1.24 \pm 0.13 \pm 0.06)\times10^{0}$	19	44
1.33	$(1.16 \pm 0.02 \pm 0.05)\times10^{1}$	16	35	$(9.98 \pm 0.79 \pm 0.42)\times10^{-1}$	16	36
1.58	$(9.76 \pm 0.13 \pm 0.34)\times10^{0}$	13	34	$(8.02 \pm 0.49 \pm 0.28)\times10^{-1}$	16	37
1.85	$(7.98 \pm 0.09 \pm 0.24)\times10^{0}$	13	34	$(6.17 \pm 0.31 \pm 0.19)\times10^{-1}$	18	35
2.15	$(6.92 \pm 0.07 \pm 0.18)\times10^{0}$	16	33	$(4.60 \pm 0.21 \pm 0.12)\times10^{-1}$	18	37
2.47	$(5.53 \pm 0.05 \pm 0.13)\times10^{0}$	20	42	$(3.65 \pm 0.15 \pm 0.09)\times10^{-1}$	27	48
2.82	$(4.45 \pm 0.04 \pm 0.10)\times10^{0}$	24	42	$(2.78 \pm 0.11 \pm 0.06)\times10^{-1}$	31	43
3.17	$(3.78 \pm 0.03 \pm 0.09)\times10^{0}$	21	41	$(2.33 \pm 0.09 \pm 0.06)\times10^{-1}$	26	49
3.54	$(2.97 \pm 0.03 \pm 0.07)\times10^{0}$	29	40	$(1.96 \pm 0.08 \pm 0.05)\times10^{-1}$	34	41
3.92	$(2.45 \pm 0.02 \pm 0.06)\times10^{0}$	32	39	$(1.46 \pm 0.06 \pm 0.04)\times10^{-1}$	33	44
4.32	$(2.00 \pm 0.02 \pm 0.05)\times10^{0}$	33	39	$(1.10 \pm 0.05 \pm 0.03)\times10^{-1}$	36	44
4.76	$(1.56 \pm 0.01 \pm 0.04)\times10^{0}$	34	39	$(8.60 \pm 0.38 \pm 0.22)\times10^{-2}$	36	46
5.24	$(1.24 \pm 0.01 \pm 0.03)\times10^{0}$	36	38	$(7.59 \pm 0.32 \pm 0.19)\times10^{-2}$	38	41
5.74	$(9.92 \pm 0.09 \pm 0.24)\times10^{-1}$	37	39	$(5.49 \pm 0.25 \pm 0.14)\times10^{-2}$	37	41
6.26	$(7.77 \pm 0.08 \pm 0.19)\times10^{-1}$	38	39	$(4.39 \pm 0.20 \pm 0.11)\times10^{-2}$	38	40
6.81	$(6.34 \pm 0.06 \pm 0.15)\times10^{-1}$	39	39	$(3.35 \pm 0.17 \pm 0.09)\times10^{-2}$	36	42
7.39	$(5.04 \pm 0.05 \pm 0.12)\times10^{-1}$	41	39	$(2.90 \pm 0.14 \pm 0.08)\times10^{-2}$	40	41
7.99	$(4.06 \pm 0.05 \pm 0.10)\times10^{-1}$	43	39	$(2.18 \pm 0.12 \pm 0.06)\times10^{-2}$	37	43
8.62	$(3.22 \pm 0.04 \pm 0.08)\times10^{-1}$	43	39	$(1.94 \pm 0.10 \pm 0.05)\times10^{-2}$	39	40
9.28	$(2.63 \pm 0.03 \pm 0.07)\times10^{-1}$	44	39	$(1.35 \pm 0.08 \pm 0.04)\times10^{-2}$	38	42
9.96	$(2.05 \pm 0.03 \pm 0.05)\times10^{-1}$	45	39	$(1.23 \pm 0.07 \pm 0.03)\times10^{-2}$	34	39
10.67	$(1.72 \pm 0.02 \pm 0.04)\times10^{-1}$	44	40	$(9.77 \pm 0.63 \pm 0.28)\times10^{-3}$	37	42
11.41	$(1.37 \pm 0.02 \pm 0.03)\times10^{-1}$	44	41	$(8.79 \pm 0.57 \pm 0.25)\times10^{-3}$	38	41
12.19	$(1.12 \pm 0.02 \pm 0.03)\times10^{-1}$	44	40	$(6.61 \pm 0.49 \pm 0.18)\times10^{-3}$	35	41
12.99	$(9.40 \pm 0.16 \pm 0.24)\times10^{-2}$	44	41	$(5.38 \pm 0.42 \pm 0.16)\times10^{-3}$	38	41
13.82	$(7.64 \pm 0.14 \pm 0.20)\times10^{-2}$	46	41	$(5.03 \pm 0.39 \pm 0.14)\times10^{-3}$	37	38
14.69	$(6.42 \pm 0.12 \pm 0.17)\times10^{-2}$	47	42	$(3.90 \pm 0.32 \pm 0.11)\times10^{-3}$	34	43
15.59	$(5.26 \pm 0.11 \pm 0.14)\times10^{-2}$	47	44	$(3.18 \pm 0.28 \pm 0.10)\times10^{-3}$	38	44
16.52	$(4.20 \pm 0.09 \pm 0.11)\times10^{-2}$	48	42	$(2.85 \pm 0.26 \pm 0.08)\times10^{-3}$	34	41
17.48	$(3.38 \pm 0.08 \pm 0.09)\times10^{-2}$	47	44	$(2.18 \pm 0.22 \pm 0.07)\times10^{-3}$	38	42
18.48	$(3.09 \pm 0.07 \pm 0.08)\times10^{-2}$	46	44	$(1.83 \pm 0.19 \pm 0.06)\times10^{-3}$	35	41
19.51	$(2.55 \pm 0.06 \pm 0.07)\times10^{-2}$	47	44	$(1.86 \pm 0.19 \pm 0.06)\times10^{-3}$	32	43
20.58	$(2.05 \pm 0.05 \pm 0.05)\times10^{-2}$	48	44	$(1.46 \pm 0.15 \pm 0.05)\times10^{-3}$	35	40
21.68	$(1.79 \pm 0.05 \pm 0.05)\times10^{-2}$	47	45	$(1.20 \pm 0.14 \pm 0.04)\times10^{-3}$	35	45
22.83	$(1.51 \pm 0.04 \pm 0.04)\times10^{-2}$	49	45	$(9.10 \pm 1.13 \pm 0.28)\times10^{-4}$	32	45
24.01	$(1.22 \pm 0.04 \pm 0.03)\times10^{-2}$	48	47	$(8.87 \pm 1.08 \pm 0.30)\times10^{-4}$	39	46
25.25	$(1.01 \pm 0.03 \pm 0.03)\times10^{-2}$	50	48	$(7.24 \pm 0.97 \pm 0.23)\times10^{-4}$	32	42
26.56	$(8.79 \pm 0.30 \pm 0.24)\times10^{-3}$	51	46	$(7.87 \pm 0.96 \pm 0.25)\times10^{-4}$	31	47
27.95	$(7.66 \pm 0.27 \pm 0.20)\times10^{-3}$	44	50	$(4.14 \pm 0.64 \pm 0.14)\times10^{-4}$	37	47
29.43	$(6.04 \pm 0.23 \pm 0.16)\times10^{-3}$	51	50	$(6.27 \pm 0.75 \pm 0.21)\times10^{-4}$	34	51
31.00	$(5.32 \pm 0.21 \pm 0.15)\times10^{-3}$	52	52	$(4.82 \pm 0.70 \pm 0.16)\times10^{-4}$	35	48
32.66	$(4.21 \pm 0.18 \pm 0.11)\times10^{-3}$	51	51	$(4.01 \pm 0.61 \pm 0.14)\times10^{-4}$	32	49
34.43	$(3.88 \pm 0.17 \pm 0.11)\times10^{-3}$	47	54	$(3.13 \pm 0.53 \pm 0.11)\times10^{-4}$	38	45
36.32	$(3.10 \pm 0.15 \pm 0.09)\times10^{-3}$	56	58	$(2.39 \pm 0.41 \pm 0.09)\times10^{-4}$	42	55
38.62	$(2.77 \pm 0.12 \pm 0.08)\times10^{-3}$	52	53	$(3.03 \pm 0.40 \pm 0.10)\times10^{-4}$	31	47

TABLE B.29: Results for electron and positron flux in time interval: 29/Jun/2013 - 25/Jul/2013

Δt: **26/Jul/2013 - 21/Aug/2013**						
$\bar{E}$ (GeV)	$\Phi_{e-} \pm \sigma_{\rm stat} \pm \sigma_{\rm sys}$ (GeV^{-1} m^{-2} sr^{-1} s^{-1})	$\sigma^{\rm t}_{\rm uc}$ (%)	$\sigma^{E}_{\rm uc}$ (%)	$\Phi_{e+} \pm \sigma_{\rm stat} \pm \sigma_{\rm sys}$ (GeV^{-1} m^{-2} sr^{-1} s^{-1})	$\sigma^{\rm t}_{\rm uc}$ (%)	$\sigma^{E}_{\rm uc}$ (%)
0.57	$(1.69 \pm 0.15 \pm 0.19)\times10^{1}$	30	56	$(1.59 \pm 1.49 \pm 0.27)\times10^{0}$	19	84
0.73	$(1.46 \pm 0.07 \pm 0.13)\times10^{1}$	45	55	$(1.07 \pm 0.56 \pm 0.10)\times10^{0}$	44	59
0.91	$(1.41 \pm 0.04 \pm 0.09)\times10^{1}$	20	38	$(1.49 \pm 0.24 \pm 0.09)\times10^{0}$	19	43
1.11	$(1.28 \pm 0.03 \pm 0.06)\times10^{1}$	20	37	$(1.16 \pm 0.13 \pm 0.06)\times10^{0}$	19	44
1.33	$(1.15 \pm 0.02 \pm 0.05)\times10^{1}$	16	35	$(9.93 \pm 0.75 \pm 0.41)\times10^{-1}$	16	36
1.58	$(9.79 \pm 0.13 \pm 0.34)\times10^{0}$	13	34	$(7.15 \pm 0.44 \pm 0.25)\times10^{-1}$	15	37
1.85	$(8.15 \pm 0.09 \pm 0.24)\times10^{0}$	13	34	$(6.22 \pm 0.30 \pm 0.19)\times10^{-1}$	18	35
2.15	$(6.82 \pm 0.07 \pm 0.18)\times10^{0}$	16	33	$(4.84 \pm 0.21 \pm 0.13)\times10^{-1}$	18	37
2.47	$(5.61 \pm 0.05 \pm 0.14)\times10^{0}$	20	42	$(4.07 \pm 0.16 \pm 0.11)\times10^{-1}$	27	48
2.82	$(4.49 \pm 0.04 \pm 0.10)\times10^{0}$	24	42	$(3.16 \pm 0.12 \pm 0.07)\times10^{-1}$	31	43
3.17	$(3.79 \pm 0.03 \pm 0.09)\times10^{0}$	21	41	$(2.51 \pm 0.10 \pm 0.06)\times10^{-1}$	26	49
3.54	$(3.10 \pm 0.03 \pm 0.07)\times10^{0}$	29	40	$(1.87 \pm 0.07 \pm 0.05)\times10^{-1}$	34	41
3.92	$(2.49 \pm 0.02 \pm 0.06)\times10^{0}$	32	39	$(1.42 \pm 0.06 \pm 0.04)\times10^{-1}$	33	44
4.32	$(1.98 \pm 0.02 \pm 0.05)\times10^{0}$	33	39	$(1.15 \pm 0.05 \pm 0.03)\times10^{-1}$	36	44
4.76	$(1.60 \pm 0.01 \pm 0.04)\times10^{0}$	34	39	$(8.68 \pm 0.37 \pm 0.22)\times10^{-2}$	36	46
5.24	$(1.30 \pm 0.01 \pm 0.03)\times10^{0}$	36	38	$(6.75 \pm 0.30 \pm 0.17)\times10^{-2}$	38	41
5.74	$(1.02 \pm 0.01 \pm 0.02)\times10^{0}$	38	39	$(5.71 \pm 0.25 \pm 0.15)\times10^{-2}$	37	41
6.26	$(8.06 \pm 0.08 \pm 0.19)\times10^{-1}$	38	39	$(4.37 \pm 0.20 \pm 0.11)\times10^{-2}$	38	40
6.81	$(6.65 \pm 0.07 \pm 0.16)\times10^{-1}$	39	39	$(3.70 \pm 0.17 \pm 0.10)\times10^{-2}$	36	42
7.39	$(5.16 \pm 0.05 \pm 0.13)\times10^{-1}$	41	39	$(2.56 \pm 0.14 \pm 0.07)\times10^{-2}$	40	41
7.99	$(4.13 \pm 0.05 \pm 0.10)\times10^{-1}$	43	39	$(2.33 \pm 0.12 \pm 0.06)\times10^{-2}$	37	43
8.62	$(3.39 \pm 0.04 \pm 0.08)\times10^{-1}$	43	39	$(1.92 \pm 0.10 \pm 0.05)\times10^{-2}$	39	40
9.28	$(2.68 \pm 0.03 \pm 0.07)\times10^{-1}$	44	39	$(1.29 \pm 0.08 \pm 0.04)\times10^{-2}$	38	42
9.96	$(2.16 \pm 0.03 \pm 0.05)\times10^{-1}$	45	39	$(1.26 \pm 0.08 \pm 0.03)\times10^{-2}$	34	39
10.67	$(1.76 \pm 0.02 \pm 0.04)\times10^{-1}$	44	40	$(1.06 \pm 0.07 \pm 0.03)\times10^{-2}$	37	42
11.41	$(1.40 \pm 0.02 \pm 0.04)\times10^{-1}$	44	40	$(7.95 \pm 0.54 \pm 0.23)\times10^{-3}$	38	41
12.19	$(1.20 \pm 0.02 \pm 0.03)\times10^{-1}$	44	40	$(7.06 \pm 0.50 \pm 0.19)\times10^{-3}$	35	41
12.99	$(9.51 \pm 0.16 \pm 0.24)\times10^{-2}$	44	41	$(6.10 \pm 0.44 \pm 0.18)\times10^{-3}$	38	41
13.82	$(7.77 \pm 0.14 \pm 0.20)\times10^{-2}$	46	41	$(4.28 \pm 0.37 \pm 0.12)\times10^{-3}$	37	38
14.69	$(6.49 \pm 0.12 \pm 0.17)\times10^{-2}$	47	41	$(3.35 \pm 0.31 \pm 0.09)\times10^{-3}$	34	43
15.59	$(5.36 \pm 0.11 \pm 0.14)\times10^{-2}$	47	44	$(3.23 \pm 0.29 \pm 0.10)\times10^{-3}$	38	44
16.52	$(4.53 \pm 0.10 \pm 0.12)\times10^{-2}$	48	42	$(2.73 \pm 0.25 \pm 0.08)\times10^{-3}$	34	41
17.48	$(3.47 \pm 0.08 \pm 0.09)\times10^{-2}$	47	44	$(2.34 \pm 0.23 \pm 0.07)\times10^{-3}$	38	42
18.48	$(2.94 \pm 0.07 \pm 0.08)\times10^{-2}$	46	44	$(1.50 \pm 0.17 \pm 0.05)\times10^{-3}$	35	41
19.51	$(2.56 \pm 0.06 \pm 0.07)\times10^{-2}$	47	44	$(1.79 \pm 0.17 \pm 0.05)\times10^{-3}$	32	43
20.58	$(1.98 \pm 0.05 \pm 0.05)\times10^{-2}$	49	44	$(1.72 \pm 0.17 \pm 0.05)\times10^{-3}$	35	40
21.68	$(1.79 \pm 0.05 \pm 0.05)\times10^{-2}$	47	45	$(1.06 \pm 0.13 \pm 0.03)\times10^{-3}$	36	45
22.83	$(1.58 \pm 0.04 \pm 0.04)\times10^{-2}$	49	45	$(1.11 \pm 0.12 \pm 0.03)\times10^{-3}$	32	45
24.01	$(1.23 \pm 0.04 \pm 0.03)\times10^{-2}$	48	47	$(8.57 \pm 1.08 \pm 0.29)\times10^{-4}$	39	46
25.25	$(1.06 \pm 0.03 \pm 0.03)\times10^{-2}$	50	48	$(4.49 \pm 0.75 \pm 0.14)\times10^{-4}$	32	42
26.56	$(9.11 \pm 0.30 \pm 0.24)\times10^{-3}$	51	46	$(7.16 \pm 0.89 \pm 0.23)\times10^{-4}$	31	47
27.95	$(7.67 \pm 0.27 \pm 0.20)\times10^{-3}$	45	50	$(5.72 \pm 0.77 \pm 0.20)\times10^{-4}$	37	46
29.43	$(6.64 \pm 0.24 \pm 0.18)\times10^{-3}$	51	50	$(3.34 \pm 0.58 \pm 0.11)\times10^{-4}$	34	50
31.00	$(5.23 \pm 0.21 \pm 0.14)\times10^{-3}$	52	52	$(4.02 \pm 0.61 \pm 0.14)\times10^{-4}$	36	48
32.66	$(4.72 \pm 0.19 \pm 0.13)\times10^{-3}$	51	50	$(4.27 \pm 0.63 \pm 0.15)\times10^{-4}$	31	49
34.43	$(4.04 \pm 0.17 \pm 0.11)\times10^{-3}$	47	54	$(3.33 \pm 0.53 \pm 0.11)\times10^{-4}$	38	45
36.32	$(3.39 \pm 0.15 \pm 0.10)\times10^{-3}$	55	56	$(2.29 \pm 0.39 \pm 0.08)\times10^{-4}$	41	54
38.62	$(2.79 \pm 0.12 \pm 0.08)\times10^{-3}$	52	53	$(2.63 \pm 0.38 \pm 0.09)\times10^{-4}$	31	47

TABLE B.30: Results for electron and positron flux in time interval: 26/Jul/2013 - 21/Aug/2013

Δt: **22/Aug/2013 - 17/Sep/2013**						
$\bar{E}$ (GeV)	$\Phi_{e-} \pm \sigma_{\text{stat}} \pm \sigma_{\text{sys}}$ ($\text{GeV}^{-1}\ \text{m}^{-2}\ \text{sr}^{-1}\ \text{s}^{-1}$)	$\sigma^{\text{t}}_{\text{uc}}$ (%)	σ^{E}_{uc} (%)	$\Phi_{e+} \pm \sigma_{\text{stat}} \pm \sigma_{\text{sys}}$ ($\text{GeV}^{-1}\ \text{m}^{-2}\ \text{sr}^{-1}\ \text{s}^{-1}$)	$\sigma^{\text{t}}_{\text{uc}}$ (%)	σ^{E}_{uc} (%)
0.57	$(1.36 \pm 0.14 \pm 0.16)\times10^{1}$	39	60	$(7.56 \pm 13.37 \pm 1.33)\times10^{-1}$	26	85
0.73	$(1.32 \pm 0.07 \pm 0.12)\times10^{1}$	53	61	$(6.79 \pm 6.04 \pm 0.65)\times10^{-1}$	52	64
0.91	$(1.30 \pm 0.04 \pm 0.08)\times10^{1}$	21	38	$(8.18 \pm 2.24 \pm 0.51)\times10^{-1}$	20	43
1.11	$(1.17 \pm 0.03 \pm 0.06)\times10^{1}$	21	37	$(1.30 \pm 0.14 \pm 0.07)\times10^{0}$	20	44
1.33	$(1.04 \pm 0.02 \pm 0.04)\times10^{1}$	16	35	$(9.75 \pm 0.79 \pm 0.41)\times10^{-1}$	16	36
1.58	$(9.07 \pm 0.13 \pm 0.32)\times10^{0}$	13	34	$(7.72 \pm 0.48 \pm 0.27)\times10^{-1}$	16	37
1.85	$(7.59 \pm 0.09 \pm 0.23)\times10^{0}$	13	34	$(5.64 \pm 0.30 \pm 0.17)\times10^{-1}$	18	35
2.15	$(6.50 \pm 0.07 \pm 0.17)\times10^{0}$	16	33	$(4.76 \pm 0.21 \pm 0.13)\times10^{-1}$	18	37
2.47	$(5.17 \pm 0.05 \pm 0.13)\times10^{0}$	20	41	$(3.44 \pm 0.15 \pm 0.09)\times10^{-1}$	27	48
2.82	$(4.26 \pm 0.04 \pm 0.09)\times10^{0}$	25	42	$(2.86 \pm 0.12 \pm 0.06)\times10^{-1}$	31	42
3.17	$(3.69 \pm 0.03 \pm 0.08)\times10^{0}$	21	40	$(2.27 \pm 0.09 \pm 0.06)\times10^{-1}$	26	49
3.54	$(2.96 \pm 0.03 \pm 0.07)\times10^{0}$	29	40	$(1.75 \pm 0.07 \pm 0.04)\times10^{-1}$	34	40
3.92	$(2.39 \pm 0.02 \pm 0.06)\times10^{0}$	32	39	$(1.46 \pm 0.06 \pm 0.04)\times10^{-1}$	33	44
4.32	$(1.94 \pm 0.02 \pm 0.05)\times10^{0}$	33	39	$(1.13 \pm 0.05 \pm 0.03)\times10^{-1}$	36	43
4.76	$(1.57 \pm 0.01 \pm 0.04)\times10^{0}$	34	38	$(8.68 \pm 0.39 \pm 0.22)\times10^{-2}$	36	45
5.24	$(1.27 \pm 0.01 \pm 0.03)\times10^{0}$	37	38	$(7.18 \pm 0.32 \pm 0.18)\times10^{-2}$	38	41
5.74	$(1.00 \pm 0.01 \pm 0.02)\times10^{0}$	38	38	$(5.35 \pm 0.25 \pm 0.14)\times10^{-2}$	37	40
6.26	$(8.09 \pm 0.08 \pm 0.19)\times10^{-1}$	38	39	$(4.85 \pm 0.21 \pm 0.12)\times10^{-2}$	39	39
6.81	$(6.50 \pm 0.07 \pm 0.16)\times10^{-1}$	40	39	$(3.59 \pm 0.17 \pm 0.09)\times10^{-2}$	36	41
7.39	$(5.15 \pm 0.06 \pm 0.13)\times10^{-1}$	41	38	$(3.01 \pm 0.15 \pm 0.08)\times10^{-2}$	40	40
7.99	$(4.10 \pm 0.05 \pm 0.10)\times10^{-1}$	43	38	$(2.24 \pm 0.12 \pm 0.06)\times10^{-2}$	37	43
8.62	$(3.32 \pm 0.04 \pm 0.08)\times10^{-1}$	43	38	$(1.74 \pm 0.10 \pm 0.05)\times10^{-2}$	39	40
9.28	$(2.68 \pm 0.03 \pm 0.07)\times10^{-1}$	44	38	$(1.52 \pm 0.09 \pm 0.04)\times10^{-2}$	38	41
9.96	$(2.13 \pm 0.03 \pm 0.05)\times10^{-1}$	45	38	$(1.21 \pm 0.07 \pm 0.03)\times10^{-2}$	34	39
10.67	$(1.76 \pm 0.03 \pm 0.04)\times10^{-1}$	45	39	$(1.01 \pm 0.07 \pm 0.03)\times10^{-2}$	37	41
11.41	$(1.40 \pm 0.02 \pm 0.04)\times10^{-1}$	44	40	$(7.90 \pm 0.58 \pm 0.22)\times10^{-3}$	38	40
12.19	$(1.18 \pm 0.02 \pm 0.03)\times10^{-1}$	45	40	$(7.04 \pm 0.50 \pm 0.19)\times10^{-3}$	35	41
12.99	$(9.35 \pm 0.16 \pm 0.24)\times10^{-2}$	44	41	$(5.83 \pm 0.44 \pm 0.17)\times10^{-3}$	38	40
13.82	$(7.77 \pm 0.14 \pm 0.20)\times10^{-2}$	46	41	$(4.11 \pm 0.36 \pm 0.12)\times10^{-3}$	37	37
14.69	$(6.22 \pm 0.12 \pm 0.16)\times10^{-2}$	47	41	$(3.43 \pm 0.31 \pm 0.10)\times10^{-3}$	35	43
15.59	$(5.08 \pm 0.11 \pm 0.13)\times10^{-2}$	48	44	$(2.93 \pm 0.29 \pm 0.09)\times10^{-3}$	38	44
16.52	$(4.15 \pm 0.09 \pm 0.11)\times10^{-2}$	48	41	$(3.01 \pm 0.27 \pm 0.09)\times10^{-3}$	34	40
17.48	$(3.80 \pm 0.09 \pm 0.10)\times10^{-2}$	47	43	$(2.54 \pm 0.24 \pm 0.08)\times10^{-3}$	38	41
18.48	$(3.15 \pm 0.08 \pm 0.08)\times10^{-2}$	46	43	$(2.09 \pm 0.21 \pm 0.06)\times10^{-3}$	35	41
19.51	$(2.49 \pm 0.06 \pm 0.06)\times10^{-2}$	48	43	$(1.84 \pm 0.18 \pm 0.06)\times10^{-3}$	32	43
20.58	$(2.14 \pm 0.06 \pm 0.06)\times10^{-2}$	49	43	$(1.62 \pm 0.16 \pm 0.05)\times10^{-3}$	35	40
21.68	$(1.80 \pm 0.05 \pm 0.05)\times10^{-2}$	47	45	$(1.23 \pm 0.14 \pm 0.04)\times10^{-3}$	36	45
22.83	$(1.54 \pm 0.05 \pm 0.04)\times10^{-2}$	49	45	$(1.29 \pm 0.14 \pm 0.04)\times10^{-3}$	32	45
24.01	$(1.30 \pm 0.04 \pm 0.03)\times10^{-2}$	48	46	$(9.58 \pm 1.14 \pm 0.32)\times10^{-4}$	39	45
25.25	$(1.05 \pm 0.03 \pm 0.03)\times10^{-2}$	50	48	$(9.92 \pm 1.13 \pm 0.32)\times10^{-4}$	32	42
26.56	$(9.84 \pm 0.32 \pm 0.26)\times10^{-3}$	51	45	$(7.19 \pm 0.90 \pm 0.23)\times10^{-4}$	31	46
27.95	$(7.51 \pm 0.27 \pm 0.20)\times10^{-3}$	45	49	$(5.79 \pm 0.81 \pm 0.20)\times10^{-4}$	37	46
29.43	$(6.89 \pm 0.25 \pm 0.18)\times10^{-3}$	51	49	$(5.33 \pm 0.74 \pm 0.18)\times10^{-4}$	34	50
31.00	$(5.47 \pm 0.22 \pm 0.15)\times10^{-3}$	53	52	$(5.19 \pm 0.72 \pm 0.18)\times10^{-4}$	36	48
32.66	$(5.03 \pm 0.20 \pm 0.14)\times10^{-3}$	51	49	$(4.14 \pm 0.61 \pm 0.14)\times10^{-4}$	31	48
34.43	$(3.62 \pm 0.17 \pm 0.10)\times10^{-3}$	49	54	$(3.37 \pm 0.55 \pm 0.11)\times10^{-4}$	39	46
36.32	$(3.50 \pm 0.16 \pm 0.10)\times10^{-3}$	55	56	$(2.78 \pm 0.49 \pm 0.10)\times10^{-4}$	41	54
38.62	$(2.72 \pm 0.12 \pm 0.08)\times10^{-3}$	53	53	$(2.72 \pm 0.41 \pm 0.09)\times10^{-4}$	32	47

TABLE B.31: Results for electron and positron flux in time interval: 22/Aug/2013 - 17/Sep/2013

Δt: **18/Sep/2013 - 14/Oct/2013**						
$\bar{E}$ (GeV)	$\Phi_{e-} \pm \sigma_{\text{stat}} \pm \sigma_{\text{sys}}$ (GeV^{-1} m^{-2} sr^{-1} s^{-1})	$\sigma^{\text{t}}_{\text{uc}}$ (%)	σ^{E}_{uc} (%)	$\Phi_{e+} \pm \sigma_{\text{stat}} \pm \sigma_{\text{sys}}$ (GeV^{-1} m^{-2} sr^{-1} s^{-1})	$\sigma^{\text{t}}_{\text{uc}}$ (%)	σ^{E}_{uc} (%)
0.57	$(1.16 \pm 0.12 \pm 0.13)\times10^{1}$	40	60	$(-0.01 \pm 0.00 \pm 0.00)\times10^{0}$	43	51
0.73	$(1.29 \pm 0.07 \pm 0.12)\times10^{1}$	50	59	$(6.66 \pm 4.58 \pm 0.62)\times10^{-1}$	49	62
0.91	$(1.11 \pm 0.04 \pm 0.07)\times10^{1}$	21	38	$(1.04 \pm 0.21 \pm 0.07)\times10^{0}$	20	43
1.11	$(1.10 \pm 0.02 \pm 0.05)\times10^{1}$	21	37	$(1.00 \pm 0.12 \pm 0.05)\times10^{0}$	20	44
1.33	$(1.01 \pm 0.02 \pm 0.04)\times10^{1}$	16	35	$(8.57 \pm 0.70 \pm 0.36)\times10^{-1}$	16	36
1.58	$(8.75 \pm 0.12 \pm 0.30)\times10^{0}$	13	34	$(7.61 \pm 0.46 \pm 0.27)\times10^{-1}$	16	37
1.85	$(7.54 \pm 0.09 \pm 0.23)\times10^{0}$	13	34	$(5.99 \pm 0.30 \pm 0.18)\times10^{-1}$	18	35
2.15	$(6.48 \pm 0.07 \pm 0.17)\times10^{0}$	16	33	$(4.81 \pm 0.21 \pm 0.13)\times10^{-1}$	18	37
2.47	$(5.32 \pm 0.05 \pm 0.13)\times10^{0}$	20	40	$(3.76 \pm 0.15 \pm 0.10)\times10^{-1}$	27	48
2.82	$(4.37 \pm 0.04 \pm 0.10)\times10^{0}$	25	41	$(2.94 \pm 0.12 \pm 0.07)\times10^{-1}$	31	42
3.17	$(3.69 \pm 0.03 \pm 0.08)\times10^{0}$	21	40	$(2.34 \pm 0.09 \pm 0.06)\times10^{-1}$	26	48
3.54	$(3.05 \pm 0.03 \pm 0.07)\times10^{0}$	29	39	$(1.83 \pm 0.07 \pm 0.04)\times10^{-1}$	34	40
3.92	$(2.45 \pm 0.02 \pm 0.06)\times10^{0}$	32	38	$(1.44 \pm 0.06 \pm 0.04)\times10^{-1}$	33	44
4.32	$(2.00 \pm 0.02 \pm 0.05)\times10^{0}$	33	39	$(1.22 \pm 0.05 \pm 0.03)\times10^{-1}$	36	43
4.76	$(1.62 \pm 0.01 \pm 0.04)\times10^{0}$	34	38	$(9.88 \pm 0.40 \pm 0.25)\times10^{-2}$	36	45
5.24	$(1.28 \pm 0.01 \pm 0.03)\times10^{0}$	37	38	$(7.27 \pm 0.31 \pm 0.18)\times10^{-2}$	38	41
5.74	$(1.01 \pm 0.01 \pm 0.02)\times10^{0}$	38	39	$(5.76 \pm 0.25 \pm 0.15)\times10^{-2}$	37	41
6.26	$(8.20 \pm 0.08 \pm 0.20)\times10^{-1}$	38	39	$(4.62 \pm 0.21 \pm 0.12)\times10^{-2}$	39	40
6.81	$(6.65 \pm 0.07 \pm 0.16)\times10^{-1}$	39	39	$(3.92 \pm 0.17 \pm 0.10)\times10^{-2}$	36	42
7.39	$(5.24 \pm 0.05 \pm 0.13)\times10^{-1}$	41	39	$(2.78 \pm 0.14 \pm 0.07)\times10^{-2}$	40	41
7.99	$(4.28 \pm 0.05 \pm 0.11)\times10^{-1}$	43	39	$(2.54 \pm 0.13 \pm 0.07)\times10^{-2}$	37	43
8.62	$(3.37 \pm 0.04 \pm 0.08)\times10^{-1}$	43	39	$(2.04 \pm 0.10 \pm 0.05)\times10^{-2}$	39	40
9.28	$(2.68 \pm 0.03 \pm 0.07)\times10^{-1}$	44	39	$(1.47 \pm 0.09 \pm 0.04)\times10^{-2}$	38	42
9.96	$(2.21 \pm 0.03 \pm 0.06)\times10^{-1}$	45	39	$(1.19 \pm 0.07 \pm 0.03)\times10^{-2}$	34	40
10.67	$(1.71 \pm 0.02 \pm 0.04)\times10^{-1}$	44	41	$(1.00 \pm 0.06 \pm 0.03)\times10^{-2}$	37	42
11.41	$(1.45 \pm 0.02 \pm 0.04)\times10^{-1}$	44	41	$(6.92 \pm 0.52 \pm 0.20)\times10^{-3}$	38	41
12.19	$(1.18 \pm 0.02 \pm 0.03)\times10^{-1}$	44	41	$(6.47 \pm 0.46 \pm 0.18)\times10^{-3}$	35	42
12.99	$(9.62 \pm 0.16 \pm 0.24)\times10^{-2}$	44	42	$(5.89 \pm 0.45 \pm 0.17)\times10^{-3}$	38	42
13.82	$(7.76 \pm 0.14 \pm 0.20)\times10^{-2}$	46	42	$(4.84 \pm 0.37 \pm 0.14)\times10^{-3}$	37	39
14.69	$(6.61 \pm 0.12 \pm 0.17)\times10^{-2}$	47	42	$(4.47 \pm 0.35 \pm 0.13)\times10^{-3}$	34	44
15.59	$(5.57 \pm 0.11 \pm 0.14)\times10^{-2}$	47	45	$(3.44 \pm 0.30 \pm 0.11)\times10^{-3}$	37	45
16.52	$(4.49 \pm 0.09 \pm 0.12)\times10^{-2}$	48	43	$(2.85 \pm 0.25 \pm 0.08)\times10^{-3}$	34	42
17.48	$(3.58 \pm 0.08 \pm 0.09)\times10^{-2}$	46	45	$(2.49 \pm 0.23 \pm 0.08)\times10^{-3}$	37	43
18.48	$(2.97 \pm 0.07 \pm 0.08)\times10^{-2}$	45	45	$(1.74 \pm 0.19 \pm 0.05)\times10^{-3}$	34	42
19.51	$(2.74 \pm 0.07 \pm 0.07)\times10^{-2}$	47	45	$(1.65 \pm 0.17 \pm 0.05)\times10^{-3}$	32	44
20.58	$(2.11 \pm 0.05 \pm 0.06)\times10^{-2}$	48	45	$(1.59 \pm 0.16 \pm 0.05)\times10^{-3}$	34	41
21.68	$(1.85 \pm 0.05 \pm 0.05)\times10^{-2}$	46	47	$(1.44 \pm 0.14 \pm 0.05)\times10^{-3}$	35	46
22.83	$(1.56 \pm 0.04 \pm 0.04)\times10^{-2}$	48	47	$(1.09 \pm 0.12 \pm 0.03)\times10^{-3}$	32	46
24.01	$(1.33 \pm 0.04 \pm 0.04)\times10^{-2}$	47	48	$(1.02 \pm 0.12 \pm 0.03)\times10^{-3}$	39	47
25.25	$(1.11 \pm 0.03 \pm 0.03)\times10^{-2}$	49	49	$(8.61 \pm 1.02 \pm 0.28)\times10^{-4}$	31	43
26.56	$(9.02 \pm 0.30 \pm 0.24)\times10^{-3}$	51	48	$(7.22 \pm 0.87 \pm 0.23)\times10^{-4}$	30	48
27.95	$(7.50 \pm 0.26 \pm 0.20)\times10^{-3}$	44	51	$(5.45 \pm 0.76 \pm 0.19)\times10^{-4}$	36	48
29.43	$(6.72 \pm 0.24 \pm 0.18)\times10^{-3}$	50	51	$(5.17 \pm 0.69 \pm 0.17)\times10^{-4}$	33	51
31.00	$(5.64 \pm 0.22 \pm 0.16)\times10^{-3}$	51	53	$(3.88 \pm 0.63 \pm 0.13)\times10^{-4}$	35	49
32.66	$(4.74 \pm 0.19 \pm 0.13)\times10^{-3}$	50	52	$(4.14 \pm 0.59 \pm 0.14)\times10^{-4}$	30	50
34.43	$(4.06 \pm 0.17 \pm 0.11)\times10^{-3}$	46	55	$(5.04 \pm 0.63 \pm 0.17)\times10^{-4}$	37	46
36.32	$(3.25 \pm 0.15 \pm 0.09)\times10^{-3}$	55	58	$(4.00 \pm 0.56 \pm 0.15)\times10^{-4}$	41	56
38.62	$(2.94 \pm 0.12 \pm 0.08)\times10^{-3}$	51	54	$(2.96 \pm 0.42 \pm 0.10)\times10^{-4}$	30	48

TABLE B.32: Results for electron and positron flux in time interval: 18/Sep/2013 - 14/Oct/2013

Δt: **15/Oct/2013 - 10/Nov/2013**						
$\widetilde{E}$ (GeV)	$\Phi_{e-} \pm \sigma_{\text{stat}} \pm \sigma_{\text{sys}}$ (GeV^{-1} m^{-2} sr^{-1} s^{-1})	$\sigma^{\text{t}}_{\text{uc}}$ (%)	σ^{E}_{uc} (%)	$\Phi_{e+} \pm \sigma_{\text{stat}} \pm \sigma_{\text{sys}}$ (GeV^{-1} m^{-2} sr^{-1} s^{-1})	$\sigma^{\text{t}}_{\text{uc}}$ (%)	σ^{E}_{uc} (%)
0.57	$(1.20 \pm 0.15 \pm 0.14)\times10^{1}$	48	64	$(-0.01 \pm 1538.77 \pm 0.00)\times10^{0}$	32	86
0.73	$(1.16 \pm 0.07 \pm 0.12)\times10^{1}$	62	68	$(1.33 \pm 0.48 \pm 0.14)\times10^{0}$	61	70
0.91	$(1.24 \pm 0.04 \pm 0.08)\times10^{1}$	22	39	$(1.35 \pm 0.27 \pm 0.08)\times10^{0}$	21	43
1.11	$(1.08 \pm 0.03 \pm 0.05)\times10^{1}$	22	37	$(1.02 \pm 0.14 \pm 0.05)\times10^{0}$	21	45
1.33	$(9.97 \pm 0.19 \pm 0.41)\times10^{0}$	17	35	$(8.63 \pm 0.79 \pm 0.36)\times10^{-1}$	16	37
1.58	$(8.91 \pm 0.13 \pm 0.31)\times10^{0}$	14	34	$(7.77 \pm 0.51 \pm 0.28)\times10^{-1}$	16	37
1.85	$(7.68 \pm 0.10 \pm 0.23)\times10^{0}$	13	34	$(5.74 \pm 0.32 \pm 0.17)\times10^{-1}$	18	35
2.15	$(6.49 \pm 0.07 \pm 0.17)\times10^{0}$	16	33	$(4.88 \pm 0.23 \pm 0.13)\times10^{-1}$	18	37
2.47	$(5.55 \pm 0.06 \pm 0.14)\times10^{0}$	20	43	$(4.18 \pm 0.17 \pm 0.11)\times10^{-1}$	27	50
2.82	$(4.41 \pm 0.04 \pm 0.10)\times10^{0}$	24	44	$(2.72 \pm 0.12 \pm 0.06)\times10^{-1}$	31	44
3.17	$(3.78 \pm 0.04 \pm 0.09)\times10^{0}$	20	43	$(2.54 \pm 0.10 \pm 0.06)\times10^{-1}$	26	50
3.54	$(3.10 \pm 0.03 \pm 0.07)\times10^{0}$	29	42	$(1.84 \pm 0.08 \pm 0.04)\times10^{-1}$	34	42
3.92	$(2.52 \pm 0.02 \pm 0.06)\times10^{0}$	31	41	$(1.59 \pm 0.07 \pm 0.04)\times10^{-1}$	33	45
4.32	$(1.99 \pm 0.02 \pm 0.05)\times10^{0}$	33	41	$(1.20 \pm 0.05 \pm 0.03)\times10^{-1}$	36	45
4.76	$(1.65 \pm 0.02 \pm 0.04)\times10^{0}$	34	40	$(8.52 \pm 0.40 \pm 0.22)\times10^{-2}$	36	47
5.24	$(1.31 \pm 0.01 \pm 0.03)\times10^{0}$	36	40	$(8.22 \pm 0.36 \pm 0.21)\times10^{-2}$	38	42
5.74	$(1.04 \pm 0.01 \pm 0.03)\times10^{0}$	37	40	$(5.75 \pm 0.27 \pm 0.15)\times10^{-2}$	37	42
6.26	$(8.12 \pm 0.09 \pm 0.20)\times10^{-1}$	38	40	$(4.67 \pm 0.23 \pm 0.12)\times10^{-2}$	38	41
6.81	$(6.59 \pm 0.07 \pm 0.16)\times10^{-1}$	39	40	$(3.51 \pm 0.18 \pm 0.09)\times10^{-2}$	36	43
7.39	$(5.27 \pm 0.06 \pm 0.13)\times10^{-1}$	41	39	$(2.82 \pm 0.15 \pm 0.07)\times10^{-2}$	40	42
7.99	$(4.23 \pm 0.05 \pm 0.10)\times10^{-1}$	43	40	$(2.32 \pm 0.13 \pm 0.06)\times10^{-2}$	37	44
8.62	$(3.40 \pm 0.04 \pm 0.08)\times10^{-1}$	43	39	$(2.17 \pm 0.12 \pm 0.06)\times10^{-2}$	39	41
9.28	$(2.73 \pm 0.04 \pm 0.07)\times10^{-1}$	44	40	$(1.59 \pm 0.10 \pm 0.04)\times10^{-2}$	38	42
9.96	$(2.24 \pm 0.03 \pm 0.06)\times10^{-1}$	45	39	$(1.32 \pm 0.08 \pm 0.03)\times10^{-2}$	34	40
10.67	$(1.74 \pm 0.03 \pm 0.04)\times10^{-1}$	44	40	$(9.73 \pm 0.69 \pm 0.28)\times10^{-3}$	37	42
11.41	$(1.47 \pm 0.02 \pm 0.04)\times10^{-1}$	44	41	$(8.98 \pm 0.63 \pm 0.26)\times10^{-3}$	38	41
12.19	$(1.20 \pm 0.02 \pm 0.03)\times10^{-1}$	44	41	$(6.89 \pm 0.54 \pm 0.19)\times10^{-3}$	35	41
12.99	$(9.52 \pm 0.18 \pm 0.24)\times10^{-2}$	44	41	$(5.20 \pm 0.45 \pm 0.15)\times10^{-3}$	38	41
13.82	$(8.01 \pm 0.16 \pm 0.20)\times10^{-2}$	46	41	$(5.19 \pm 0.43 \pm 0.15)\times10^{-3}$	37	38
14.69	$(6.47 \pm 0.13 \pm 0.17)\times10^{-2}$	47	42	$(4.36 \pm 0.37 \pm 0.12)\times10^{-3}$	35	43
15.59	$(5.36 \pm 0.12 \pm 0.14)\times10^{-2}$	48	45	$(3.06 \pm 0.31 \pm 0.09)\times10^{-3}$	39	45
16.52	$(4.24 \pm 0.10 \pm 0.11)\times10^{-2}$	48	42	$(2.98 \pm 0.29 \pm 0.09)\times10^{-3}$	34	41
17.48	$(3.53 \pm 0.09 \pm 0.09)\times10^{-2}$	47	44	$(2.04 \pm 0.24 \pm 0.06)\times10^{-3}$	38	42
18.48	$(3.07 \pm 0.08 \pm 0.08)\times10^{-2}$	46	44	$(2.17 \pm 0.22 \pm 0.07)\times10^{-3}$	35	41
19.51	$(2.56 \pm 0.07 \pm 0.07)\times10^{-2}$	48	44	$(1.53 \pm 0.19 \pm 0.05)\times10^{-3}$	33	43
20.58	$(2.20 \pm 0.06 \pm 0.06)\times10^{-2}$	49	44	$(1.56 \pm 0.18 \pm 0.05)\times10^{-3}$	35	40
21.68	$(1.83 \pm 0.05 \pm 0.05)\times10^{-2}$	47	45	$(1.42 \pm 0.15 \pm 0.05)\times10^{-3}$	36	45
22.83	$(1.52 \pm 0.05 \pm 0.04)\times10^{-2}$	49	45	$(1.23 \pm 0.15 \pm 0.04)\times10^{-3}$	33	45
24.01	$(1.32 \pm 0.04 \pm 0.03)\times10^{-2}$	48	47	$(9.05 \pm 1.19 \pm 0.30)\times10^{-4}$	40	46
25.25	$(1.13 \pm 0.04 \pm 0.03)\times10^{-2}$	51	48	$(6.87 \pm 1.01 \pm 0.22)\times10^{-4}$	33	42
26.56	$(9.46 \pm 0.34 \pm 0.25)\times10^{-3}$	52	46	$(8.03 \pm 1.02 \pm 0.26)\times10^{-4}$	31	47
27.95	$(7.97 \pm 0.30 \pm 0.21)\times10^{-3}$	45	49	$(4.87 \pm 0.80 \pm 0.17)\times10^{-4}$	37	46
29.43	$(6.98 \pm 0.27 \pm 0.19)\times10^{-3}$	52	50	$(5.45 \pm 0.80 \pm 0.18)\times10^{-4}$	35	50
31.00	$(5.93 \pm 0.25 \pm 0.16)\times10^{-3}$	53	52	$(4.48 \pm 0.71 \pm 0.15)\times10^{-4}$	36	48
32.66	$(4.91 \pm 0.22 \pm 0.13)\times10^{-3}$	52	51	$(4.08 \pm 0.63 \pm 0.14)\times10^{-4}$	32	49
34.43	$(4.09 \pm 0.19 \pm 0.11)\times10^{-3}$	49	54	$(3.74 \pm 0.60 \pm 0.13)\times10^{-4}$	39	46
36.32	$(3.70 \pm 0.18 \pm 0.11)\times10^{-3}$	57	57	$(1.88 \pm 0.39 \pm 0.07)\times10^{-4}$	42	55
38.62	$(2.94 \pm 0.13 \pm 0.08)\times10^{-3}$	54	53	$(2.49 \pm 0.40 \pm 0.08)\times10^{-4}$	33	47

TABLE B.33: Results for electron and positron flux in time interval: 15/Oct/2013 - 10/Nov/2013

Δt	ϕ^{e-} (GV)	$\sigma_{fromFit}$ (GV)	$\sigma_{sys}^{par\_corr}$ (GV)	$\sigma_{sys}^{bin-to-bin\ corr}$ (GV)
01/Jul/2011-28/Jul/2011	1.2198	0.0016	0.0289	0.0201
28/Jul/2011-24/Aug/2011	1.2329	0.0016	0.0292	0.0204
24/Aug/2011-20/Sep/2011	1.2224	0.0015	0.0289	0.0204
20/Sep/2011-17/Oct/2011	1.2546	0.0016	0.0297	0.0208
17/Oct/2011-13/Nov/2011	1.2309	0.0015	0.0292	0.0204
13/Nov/2011-10/Dec/2011	1.2249	0.0016	0.0290	0.0203
10/Dec/2011-06/Jan/2012	1.2274	0.0016	0.0291	0.0204
06/Jan/2012-02/Feb/2012	1.2469	0.0016	0.0295	0.0205
02/Feb/2012-29/Feb/2012	1.2579	0.0016	0.0298	0.0207
29/Feb/2012-27/Mar/2012	1.3494	0.0018	0.0319	0.0219
27/Mar/2012-23/Apr/2012	1.2870	0.0016	0.0305	0.0206
23/Apr/2012-20/May/2012	1.2655	0.0016	0.0299	0.0206
20/May/2012-16/Jun/2012	1.2910	0.0015	0.0306	0.0201
16/Jun/2012-13/Jul/2012	1.3084	0.0017	0.0309	0.0208
13/Jul/2012-09/Aug/2012	1.3905	0.0019	0.0329	0.0217
09/Aug/2012-05/Sep/2012	1.3987	0.0018	0.0331	0.0211
05/Sep/2012-02/Oct/2012	1.3677	0.0017	0.0323	0.0206
02/Oct/2012-29/Oct/2012	1.3805	0.0017	0.0326	0.0209
29/Oct/2012-25/Nov/2012	1.3705	0.0018	0.0324	0.0208
25/Nov/2012-22/Dec/2012	1.3782	0.0017	0.0326	0.0204
22/Dec/2012-18/Jan/2013	1.3461	0.0016	0.0318	0.0202
18/Jan/2013-14/Feb/2013	1.3440	0.0017	0.0318	0.0204
14/Feb/2013-13/Mar/2013	1.3248	0.0016	0.0313	0.0201
13/Mar/2013-09/Apr/2013	1.3904	0.0018	0.0329	0.0209
09/Apr/2013-06/May/2013	1.3697	0.0017	0.0324	0.0206
06/May/2013-02/Jun/2013	1.4655	0.0019	0.0347	0.0218
02/Jun/2013-29/Jun/2013	1.4858	0.0019	0.0351	0.0216
29/Jun/2013-26/Jul/2013	1.4946	0.0019	0.0353	0.0218
26/Jul/2013-22/Aug/2013	1.4822	0.0018	0.0351	0.0212
22/Aug/2013-18/Sep/2013	1.5163	0.0019	0.0359	0.0214
18/Sep/2013-15/Oct/2013	1.5107	0.0019	0.0357	0.0209
15/Oct/2013-11/Nov/2013	1.5006	0.0020	0.0355	0.0208

TABLE B.34: The obtained value for electrons solar modulation potentials in each time interval.

Δt	ϕ^{e+} (GV)	$\sigma_{fromFit}$ (GV)	$\sigma_{sys}^{par\_corr}$ (GV)	$\sigma_{sys}^{bin-to-bin\ corr}$ (GV)
01/Jul/2011-28/Jul/2011	0.9544	0.0070	0.0148	0.0185
28/Jul/2011-24/Aug/2011	0.9585	0.0072	0.0148	0.0190
24/Aug/2011-20/Sep/2011	0.9359	0.0067	0.0145	0.0185
20/Sep/2011-17/Oct/2011	0.9911	0.0072	0.0154	0.0191
17/Oct/2011-13/Nov/2011	0.9508	0.0067	0.0147	0.0186
13/Nov/2011-10/Dec/2011	0.9284	0.0071	0.0144	0.0180
10/Dec/2011-06/Jan/2012	0.9173	0.0069	0.0142	0.0180
06/Jan/2012-02/Feb/2012	0.9332	0.0069	0.0145	0.0184
02/Feb/2012-29/Feb/2012	0.9480	0.0071	0.0147	0.0186
29/Feb/2012-27/Mar/2012	1.0436	0.0079	0.0162	0.0200
27/Mar/2012-23/Apr/2012	0.9701	0.0070	0.0150	0.0183
23/Apr/2012-20/May/2012	0.9833	0.0072	0.0152	0.0185
20/May/2012-16/Jun/2012	0.9764	0.0069	0.0151	0.0184
16/Jun/2012-13/Jul/2012	0.9951	0.0072	0.0154	0.0187
13/Jul/2012-09/Aug/2012	1.0911	0.0085	0.0169	0.0199
09/Aug/2012-05/Sep/2012	1.0810	0.0075	0.0167	0.0190
05/Sep/2012-02/Oct/2012	1.0601	0.0072	0.0164	0.0186
02/Oct/2012-29/Oct/2012	1.0789	0.0078	0.0167	0.0188
29/Oct/2012-25/Nov/2012	1.0730	0.0078	0.0166	0.0188
25/Nov/2012-22/Dec/2012	1.0776	0.0073	0.0167	0.0188
22/Dec/2012-18/Jan/2013	1.0431	0.0070	0.0162	0.0183
18/Jan/2013-14/Feb/2013	1.023	0.0069	0.0158	0.0180
14/Feb/2013-13/Mar/2013	1.0086	0.0067	0.0156	0.0179
13/Mar/2013-09/Apr/2013	1.0731	0.0077	0.0166	0.0191
09/Apr/2013-06/May/2013	1.0503	0.0071	0.0163	0.0184
06/May/2013-02/Jun/2013	1.1496	0.0083	0.0178	0.0202
02/Jun/2013-29/Jun/2013	1.1785	0.0084	0.0183	0.0200
29/Jun/2013-26/Jul/2013	1.1520	0.0082	0.0179	0.0197
26/Jul/2013-22/Aug/2013	1.1410	0.0078	0.0177	0.0193
22/Aug/2013-18/Sep/2013	1.1656	0.0083	0.0181	0.0193
18/Sep/2013-15/Oct/2013	1.1482	0.0078	0.0178	0.0185
15/Oct/2013-11/Nov/2013	1.1367	0.0084	0.0176	0.0186

TABLE B.35: The obtained value for electrons solar modulation potentials in each time interval.

Bibliography

[1] B. Bertucci. Overview of direct CR measurements. *Talk at* International Symposium on Very High Energy Cosmic Ray Interactions, 2014.

[2] V. Vagelli. Measurement of the cosmic $(e^+ + e^-)$ flux from 0.5 GeV to 1 TeV with the Alpha Magnetic Spectrometer (AMS-02) on the International Space Station. 2014.

[3] K.A. Olive et al. Particle Data Group. *Chin. Phys. C*, 38, 2014.

[4] E. Fermi. On the Origin of the Cosmic Radiation. *Phys. Rev.*, 75:1169–1174, 1949.

[5] M. Ackermann *et al.* Detection of the Characteristic Pion-Decay Signature in Supernova Remnants. *Science*, 339(6121):807–811.

[6] Malcolm S. Longair. High Energy Astrophysics. 2011.

[7] Berezinsky, Veniamin, Gazizov, Askhat, and Grigorieva, Svetlana. On astrophysical solution to ultrahigh energy cosmic rays. *Phys. Rev. D*, 74:043005, 2006.

[8] K. Greisen. End to the Cosmic-Ray Spectrum? *Phys. Rev. Lett.*, 16:748–750, 1966.

[9] A. W. Strong, I. V. Moskalenko and V. S. Ptuskin. Cosmic-Ray Propagation and Interactions in the Galaxy. *Annual Review of Nuclear and Particle Science*, 57:285–327, 2007.

[10] R. Beck. Galactic and extragalactic magnetic fields a concise review. *Astrophys. Space Sci. Trans.*, 5:43–47, 2009.

[11] G. Brunetti *et al.* Alfvénic reacceleration of relativistic particles in galaxy clusters: MHD waves, leptons and hadrons. *Monthly Notices of the Royal Astronomical Society*, 350:1174–1194, 2004.

[12] GALPROP code. http://galprop.stanford.edu, 1998.

[13] DRAGON code. http://dragon.hepforge.org/DRAGON/Home.html, 1992.

[14] Craig L. Sarazin. The Energy Spectrum of Primary Cosmic-Ray Electrons in Clusters of Galaxies and Inverse Compton Emission. *The Astrophysical Journal*, 520:529–547, 1999.

[15] G. Kopp, G. Lawrence, G. Rottman. The Total Irradiance Monitor (TIM): Science Results. *The Solar Radiation and Climate Experiment (SORCE)*, pages 129–139, 2005.

[16] Jokipii, J. R., Thomas, B. T. *Astrophys. J. 243, 1115.*, 1981.

[17] Potgieter, M. S., Moraal, H. *Astophys. J. 294, 425.*, 1985.

[18] Duldig, M. L. *Publications of the Astronomical Society of Australia*, 18:12–40, 2001.

[19] Singh Y. P., Badruddin. *Solar Phys.234, 339*, 2006.

[20] Heber, B. *Space Sci. Rev., doi:10.1007/s11214-011-9784-x.*, 2011.

[21] L. J. Gleeson and W. I. Axford. Cosmic Rays in the interplanetary medium. *The Astrophysical Journal*, 149, 1967.

[22] McDonald, F. B., Nand Lal, McGuire, R. E. *J. Geophys. Res. 98, 124.*, 1993.

[23] Potgieter, M. S. *Leahy, D. A., Hicks, R. B., Venkatesan, D. (eds.), Proc. 23rd Int. Cosmic Ray Conf., Invited, Rapporteur and Highlight Papers, World Scientific, Singapore, 213.*, 1994.

[24] McKibben, R. B., Connel, J. J., Lopate C., Simpson, J. A., Zhang, M. *Space Sci. Rev. 72, 367.*, 1995.

[25] Van Allen, J. A. *Geophys. Res. Lett. 27, 2453.*, 2000.

[26] Badruddin, Singh, M., Singh, Y. P. *Astron. Astrophys. 466, 677.*, 2007.

[27] Parker, E.N. Dynamics of the Interplanetary Gas and Magnetic Fields. *Astrophys. J.*, 128:664–676, 1958.

[28] L. J. Gleeson and W. I. Axford. Solar modulation of galactic cosmic rays. *The Astrophysical Journal*, 154, 1968.

[29] C. C. IAGA Working Group V-MOD: Finlay, S. Maus, C. D. Beggan, and et al. International geomagnetic reference field: the eleventh generation. *Geophysical Journal International, 183(3):1216-1230*, 2010.

[30] N. A. Tsyganenko. A model of the near magnetosphere with a dawn-dusk asymmetry. *Journal of Geophysical Research, 107(A8)*, 2002.

[31] Oxford C.Stoermer, The PolarAurora. 1955 and references therein.

[32] G.Lemaitre and U.R.Raoand M.A.Shea M.S.Vailarta, Phys. Rev. 49 (1936) 719. K.G.McCracken. *Mass. Inst. Tech. TechnicalReport No. 77*, 1962.

[33] U.R.Raoand M.A.Shea. K.G.McCracken.

[34] C.Z. Stormer. *Astroph.*, 1:237, 1930.

[35] C.Z. Stormer. The Polar Aurora. 1955.

[36] J.A. Hinton. The status of the HESS project. *New Astron.Rev.*, 48:331–337, 2004.

[37] Daniel Ferenc. The MAGIC gamma-ray observatory . *Nuclear Instruments and Methods in Physics Research A*, 553(1–2):274 – 281, 2005.

[38] J. Nishimura. *Astrophys. J.*, 238:394, 1980.

[39] J. Nishimura *et al. Adv. Space Res.*, 26:1827, 2000.

[40] Torii *et al. Adv. Space Res.*, 26:1823, 2000.

[41] D. Muller *et al. Astrophys. J.*, 186:841, 1973.

[42] T. A. Prince *et al. Astrophys. J.*, 227:676, 1979.

[43] K. K. Tang *et al. Astrophys. J.*, 278:881, 1984.

[44] D. Muller and K. K. Tang *et al. Astrophys. J.*, 312:183, 1987.

[45] B. Bertucci. *Int.J.Mod.Phys.*, A17:1613–1624, 2002.

[46] J. Chang *et al.* An excess of cosmic ray electrons at energies of 300-800 GeV. *Nature*, 456(7220):362–365, 2008.

[47] M. Ackermann *et al.* Fermi LAT observations of cosmic-ray electrons from 7 GeV to 1 TeV. *Phys. Rev. D*, 82(9):092004, 2010.

[48] F. Aharonian *et al.* Energy Spectrum of Cosmic-Ray Electrons at TeV Energies. *Physical Review Letters*, 101(26):261104, 2008.

[49] F. Aharonian *et al.* Probing the ATIC peak in the cosmic-ray electron spectrum with H.E.S.S. *Astron. Astrophys.*, 508:561–564, 2009.

[50] R. L. Golden *et al.* Measurement of the Positron to Electron Ratio in the Cosmic Rays above 5 GeV. *Astrophysical Journal*, 457:103–106, 1996.

[51] M. Boezio *et al.* The Cosmic-Ray Electron and Positron Spectra Measured at 1 AU during Solar Minimum Activity. *The Astrophysical Journal*, 532(1): 653, 2000.

[52] S. Torii *et al.* The Energy Spectrum of Cosmic-Ray Electrons from 10 to 100 GeV Observed with a Highly Granulated Imaging Calorimeter. *The Astrophysical Journal*, 559:973, 2001.

[53] K. Yoshida *et al.* Cosmic-ray electron spectrum above 100 GeV from PPB-BETS experiment in Antarctica. *Advances in Space Research*, 42:1670–1675, 2008.

[54] S. W. Barwick *et al.* The Energy Spectra and Relative Abundances of Electrons and Positrons in the Galactic Cosmic Radiation. *The Astrophysical Journal*, 498(2):779, 1998.

[55] M. A. DuVernois *et al.* Cosmic-Ray Electrons and Positrons from 1 to 100 GeV: Measurements with HEAT and Their Interpretation. *The Astrophysical Journal*, 559(1):296, 2001.

[56] C. Grimani *et al.* Measurements of the absolute energy spectra of cosmic-ray positrons and electrons above 7 GeV. *Astronomy and Astrophysics*, 392: 287–294, 2002.

[57] R. L. Golden *et al.* Observations of cosmic ray electrons and positrons using an imaging calorimeter. *Astrophysical Journal*, 436:769–775, 1994.

[58] J. Alcaraz *et al.* Leptons in near Earth orbit. *Physics Letters B*, 484:10–22, 2000.

[59] M. Aguilar *et al.* Cosmic-ray positron fraction measurement from 1 to 30 GeV with AMS-01. *Physics Letter B*, 646:145–154, 2007.

[60] O. Adriani *et al.* Cosmic-Ray Electron Flux Measured by the PAMELA Experiment between 1 and 625 GeV. *Physical Review Letters*, 106:201101, 2011.

[61] O. Adriani *et al.* An anomalous positron abundance in cosmic rays with energies 1.5-100 GeV. *Nature*, 458:607–609, 2009.

[62] M. Ackermann *et al.* Measurement of Separate Cosmic-Ray Electron and Positron Spectra with the Fermi Large Area Telescope. *Phys. Rev. Lett.*, 108 (1):011103, 2012.

[63] Fanselow. *Astrophysical Journal*, 158:771, 1969.

[64] A. Yamamoto *et al.* The BESS Program. *Nuclear Physics B - Proceedings Supplements*, 166:62 – 67, 2007.

[65] L. Accardo *et al.* High Statistics Measurement of the Positron Fraction in Primary Cosmic Rays of 0.5-500 GeV with the Alpha Magnetic Spectrometer on the International Space Station. *Phys. Rev. Lett.*, 113:121101, 2014.

[66] M. Aguilar *et al.* First Result from the Alpha Magnetic Spectrometer on the International Space Station: Precision Measurement of the Positron Fraction in Primary Cosmic Rays of 0.5-350 GeV. *Phys. Rev. Lett.*, 110:141102, 2013.

[67] M. Aguilar *et al.* Electron and Positron Fluxes in Primary Cosmic Rays Measured with the Alpha Magnetic Spectrometer on the International Space Station. Phys. Rev. Lett., 113:121102, 2014.

[68] Cholis, Ilias and Hooper, Dan. Dark matter and pulsar origins of the rising cosmic ray positron fraction in light of new data from the AMS. *Phys. Rev. D*, 88:023013, 2013.

[69] Kopp, Joachim. Constraints on dark matter annihilation from AMS-02 results. *Phys. Rev. D*, 88:076013, 2013.

[70] Bergström, Lars, Bringmann, Torsten, Cholis, Ilias, Hooper, Dan, and Weniger, Christoph. New Limits on Dark Matter Annihilation from Alpha Magnetic Spectrometer Cosmic Ray Positron Data. *Phys. Rev. Lett.*, 111: 171101, 2013.

[71] Blum, Kfir, Katz, Boaz, and Waxman, Eli. AMS-02 Results Support the Secondary Origin of Cosmic Ray Positrons. *Phys. Rev. Lett.*, 111:211101, 2013.

[72] V. M. Balebanov *et al.* AMS proposal to DOE. *Nuclear Instruments and Methods A*, 350(1–2):351 – 367, 1994.

[73] M. Aguilar *et al.* The Alpha Magnetic Spectrometer (AMS) on the International Space Station: Part I – results from the test flight on the space shuttle. *Physics Reports*, 366:331–405, (2002).

[74] P. Chardonnet *et al.* Production of anti-matter in our galaxy. *Physics Letters B*, 409:313–320, (1997).

[75] Mayorov, A.G. *et al.* The search for antihelium in cosmic rays using data from the PAMELA experiment. *Bulletin of the Russian Academy of Sciences: Physics*, 75(3), 2011.

[76] M. Aguilar *et al.* Precision Measurement of the Proton Flux in Primary Cosmic Rays from Rigidity 1 GV to 1.8 TV with the Alpha Magnetic Spectrometer on the International Space Station. *Phys. Rev. Lett.*, 114:171103, 2015.

[77] M. Aguilar *et al.* Precision Measurement of the Helium Flux in Primary Cosmic Rays of Rigidities 1.9 GV to 3 TV with the Alpha Magnetic Spectrometer on the International Space Station. *Phys. Rev. Lett.*, 115:211101, 2015.

[78] A. Castellina , F. Donato. Diffusion coefficient and acceleration spectrum from direct measurements of charged cosmic ray nuclei. *Astroparticle Physics*, (24): 146–159, 2005.

[79] B. Alpat *et al.* "the internal alignment and position resolution of the AMS-02 silicon tracker determined with cosmic-ray muons ". *Nucl. Instrum. Methods Phys. Res., Sect. A*, 613(2):207–217, 2010.

[80] K. Lubelsmeyer *et al.* Upgrade of the Alpha Magnetic Spectrometer (AMS-02) for long term operation on the International Space Station (ISS). *Nucl. Instrum. Methods Phys. Res., Sect. A*, 654(1):639, 2011.

[81] J. van Es. AMS02 TRACKER THERMAL CONTROL SYSTEM OVERVIEW AND SPIN-OFF FOR FUTURE SPACECRAFT COOLING SYSTEM DEVELOPMENTS . *Proc. of IAC C2.7.1*, 2009.

[82] L. Amati *et al.* The TOF counters of the AMS-02 experiment: space qualification tests and beam test results. *Nuclear Physics B (Proc.Suppl.)*, 150: 276–280, 2006.

[83] T. Bruch and W. Wallraff. The Anti-Coincidence Counter shield of the AMS tracker. *Nuclear Instruments and Methods in Physics Research A*, 572:505–507, 2007.

[84] W. Sun and Z. Weng. Measurement of the absolute charge of cosmic ray nuclei with the AMS Transition Radiation Detector. *ICRC 2013 proceedings*, 2013.

[85] K. Andeen M. Heil and F. Spada. Operations and Alignment of the AMS-02 Transition Radiation Detector. *ICRC 2013 proceedings*, 2013.

[86] C. Adlo *et al.* The AMS-02 lead-scintillating fibres Electromagnetic Calorimeter. *Nuclear Instruments and Methods in Physics Research A*, 714:147–154, 2013.

[87] F. Cervelli *et al.* "a reduced scale e.m. calorimeter prototype for the AMS-02 experiment ". *Nuclear Instruments and Methods in Physics Research Section A: Accelerators, Spectrometers, Detectors and Associated Equipment*, 490 (1–2):132 – 139, 2002.

[88] F. Cadoux *et al.* "the AMS-02 electromagnetic calorimeter ". *Nuclear Physics B - Proceedings Supplements*, 113(1–3):159 – 165, 2002.

[89] L. Basara. Energy Calibration with MIP in space and charge measurement with AMS02 Electromagnetic Calorimeter. ICRC 2013 proceedings, 2013.

[90] Grindhammer, G. and Peters, S. The Parameterized Simulation of Electromagnetic Showers in Homogeneous and Sampling Calorimeters. *ArXiv High Energy Physics - Experiment e-prints*, 2000.

[91] S. Di Falco. Performance of the AMS-02 Electromagnetic Calorimeter in Space. *In ICRC 2013 proceedings*, 2013.

[92] M. Vecchi. A 3-dimensional electromagnetic shower characterization and its application to AMS-02 pointing capability. *In ICRC 2013 proceedings*, 2013.

[93] C. H. Lin. Trigger Logic Design Specifications. *Internal Note*, 2008.

[94] Lin, C. Trigger Logic Design Specifications. *Internal AMS-02 note*, 2005.

[95] A. Kounine and V. Koutsenko. Flight Software for xDR and JINx nodes in AMS-02 . *AMS internal notes.*, 2011.

[96] The AMS Collaboration. AMS on ISS: Application of particle physics technology to manned interplanetary flight . to be published on Nuclear and Instruments Methods. *AMS collaboration internal report.*

[97] R. Brun *et al.* Root web page, 2001. URL http://root.cern.ch/.

[98] Vitali Choutko and the Ams Collaboration. Parallelization of the event processing in the AMS experiment. *Journal of Physics: Conference Series*, 219 (3):032032, 2010.

[99] Vitali Choutko *et al.* Computing Strategy of the AMS-02 Experiment. *AMS collaboration internal report*, 2015.

[100] M. Aguilar et al. Precision Measurement of the $(e^+ + e^-)$ Flux in Primary Cosmic Rays from 0.5 GeV to 1 TeV with the Alpha Magnetic Spectrometer on the International Space Station. *Phys. Rev. Lett.*, 113(221102), 2014.

[101] J.D. Sullivan. Geometric factor and directional response of single and multi-element particle telescopes . *Nuclear Instruments and Methods*, 95(1):5 – 11, 1971.

[102] Q. Yan, V. Choukto. AMS RTI. *AMS collaboration internal report*, 2013.

[103] William R. Leo. Techniques for Nuclear and Particle Physics Experiments. 1994.

[104] G. Grindhammer and S. Peters. The Parameterized Simulation of Electromagnetic Showers in Homogeneous and Sampling Calorimeters. *ArXiv High Energy Physics - Experiment e-prints*, 1993.

[105] B. P. Roe *et al.* "Boosted decision trees as an alternative to artificial neural networks for particle identification". *Nuclear Instruments and Methods in Physics Research A*, 543:577–584, (2005).

[106] C. Corti M. Incagli and V. Vagelli. A study for an ECAL standalone classification algorithm using the Boosted Decision Tree (BDT) technique. *AMS internal notes.*, 2014.

[107] M. Heil *et al.* Operations and Alignment of the AMS-02 Transition Radiation Detector. *In ICRC 2013 proceedings*, 2013.

[108] M. Duranti. Measurement of the Atmospheric Muon Flux on Ground with the AMS-02 Detector. 2011.

[109] Root Cern Guide. The RooFit method. URL https://root.cern.ch/drupal/content/roofit.

[110] W. Verkerke and D. Kirkby. The RooFit toolkit for data modeling. *ArXiv Physics e-prints*, eprint: physics/0306116, 2003.

[111] Lafferty, G D and Wyatt, T R. Where to stick your data points: the treatment of measurements within wide bins. *Nucl. Instrum. Methods Phys. Res., A*, 355 (CERN-PPE-94-72. MAN-HEP-94-3):541–547. 17 p, 1994.

[112] NOAA / NWS Space Weather Prediction Center. Solar Cycle Progression, Retrieved 2015-07-06. URL www.swpc.noaa.gov.

[113] D. Gaggero and L. Maccione. Model independent interpretation of recent CR lepton data after AMS-02 . *JCAP12(2013)011*, 12:11, 2013.

[114] A. Ghelfi, L. Derome. Time dependence of fluxes. *AMS collaboration internal report*, 2015.

[115] O. Adriani *et al.* Time Dependence of the e^- Flux Measured by PAMELA during the July 2006–December 2009 Solar Minimum. *The Astrophysical Journal*, 810(2):142, 2015.

List of Figures

List of Tables

Ringraziamenti

Se ho potuto iniziare il mio viaggio verso la fisica, che spero vivamente non si concluda con il dottorato, è stato solo grazie ai miei genitori. Quindi il primo ringraziamento va soprattutto a loro che mi hanno sostenuto non solo dal punto di vista economico ma anche e soprattuto morale, consigliandomi sulla scelta degli studi da intraprendere ma sempre rispettando le mie decisioni.

Grazie al gruppo di AMS di Perugia all'interno del quale ho potuto iniziare e accrescere la mia esperienza lavorativa. In particolare grazie a Bruna che, fin dalla laurea triennale e nonostante i numerosi impegni, ha sempre trovato del tempo per seguire il mio lavoro. La ringrazio soprattutto perché è riuscita a trasmettermi la passione per quello che faccio. Grazie a Matteo per tutto il tempo che ha speso nel seguire questo lavoro di tesi, per tutte le lunghe e costruttive discussioni avute e per aver pazientemente letto la mia tesi "in order to" aiutarmi a correggerla. Grazie a Valerio per avermi sempre aiutato nel risolvere dubbi e per aver letto la mia tesi correggendo il mio "terribile" inglese. Grazie ad Emanuele Fiandrini per le sue delucidazioni sulla parte teorica (dove purtroppo sono carente).

E "last but not least"...

Grazie a mia sorella che si è presa un gatto ed è risaputo che i gatti sono anti-stress e anche che sotto tesi di anti-stress ce ne vogliono parecchi...

Grazie a Emanuele che non mi ha mai ostacolato nelle scelte fatte ma anzi mi ha sempre supportato e consigliato (e poi anche perché mi ha aiutato a sistemare la bibliografia all'ultimo momento).

Grazie a chi ha condiviso con me l'aula dottorandi, in particolare a Marta con la quale ci concedevamo quei 5-10 minuti di pausa persi in chiacchiere (scusa Marta, dopo questa affermazione perderemo il lavoro :D) che aiutavano ad allentare la tensione e riprendere piú efficientemente il lavoro.

Grazie a tutti gli amici del pacchetto perché, nonostante la distanza, sono sempre stati pronti a darmi una mano.